# 6. SITE 994[1]

Shipboard Scientific Party[2]

## HOLE 994A

**Position:** 31°47.141′N, 75°32.751′W

**Start hole:** 2108 hr, 7 November 1995

**End hole:** 2345 hr, 7 November 1995

**Time on hole:** 9.5 hr (0.40 days)

**Seafloor (drill pipe measurement from rig floor, mbrf):** 2808.6

**Total depth (drill pipe measurement from rig floor, mbrf):** 2845

**Distance between rig floor and sea level (m):** 10.9

**Water depth (drill pipe measurement from sea level, m):** 2797.6

**Penetration (mbsf):** 36.4

**Coring totals:**
Type: APC
Number: 4
Cored: 36.4 m
Recovered: 37.3 m (102.4%)

**Formation:**
Unit I: 0–13.31 mbsf; Holocene to late Pleistocene; gray nannofossil-rich clay and nannofossil clay
Unit II: 13.3–36.4 mbsf; late Pleistocene to late Pliocene; greenish gray nannofossil-rich clay and nannofossil clay

## HOLE 994B

**Position:** 31°47.139′N, 75°32.740′W

**Start hole:** 0030 hr, 8 November 1995

**End hole:** 0045 hr, 8 November 1995

**Time on hole:** 1.0 hr (0.04 days)

**Seafloor (drill pipe measurement from rig floor, mbrf):** 2808.6

**Total depth (drill pipe measurement from rig floor, mbrf):** 2815.5

**Distance between rig floor and sea level (m):** 11.0

**Water depth (drill pipe measurement from sea level, m):** 2797.6

**Penetration (mbsf):** 6.9

**Coring totals:**
Type: APC
Number: 1
Cored: 6.9 m
Recovered: 6.94 m (100.6%)

**Formation:**
Unit I: 0-6.9 mbsf; Holocene to late Pleistocene; gray nannofossil-rich clay and nannofossil clay

## HOLE 994C

**Position:** 31°47.139′N, 75°32.753′W

**Start hole:** 0115 hr, 8 November 1995

**End hole:** 0110 hr, 15 November 1995

**Time on hole:** 168.50 hr (7.02 days)

**Seafloor (drill pipe measurement from rig floor, mbrf):** 2810.1

**Total depth (drill pipe measurement from rig floor, mbrf):** 3513.6

**Distance between rig floor and sea level (m):** 11.0

**Water depth (drill pipe measurement from sea level, m):** 2799.1

**Penetration (mbsf):** 703.5

**Coring totals:**
Type: APC
Number: 17
Cored: 156.4 m
Recovered: 160.48 m (102.6%)

Type: XCB
Number: 57
Cored: 537.1 m
Recovered: 332.63 m (61.9%)

Type: PCS
Number: 10
Cored: 10.0 m
Recovered: 1.28 m (12.8%)

**Formation:**
Unit I: 0–13.32 mbsf; Holocene to late Pleistocene; gray nannofossil-rich clay and nannofossil clay
Unit II: 13.32–160.12 mbsf; late Pleistocene to late Pliocene; greenish gray nannofossil-rich clay and nannofossil clay
Unit III: 160.12–703.5 mbsf; late Miocene; dark greenish gray diatom-bearing nannofossil-rich clay

## HOLE 994D

**Position:** 31°47.142′N, 75°32.750′W

**Start hole:** 0300 hr, 15 November 1995

**End hole:** 0345 hr, 20 November 1995

**Time on hole:** 122.50 hr (5.10 days)

**Seafloor (drill pipe measurement from rig floor, mbrf):** 2810.1

**Total depth (drill pipe measurement from rig floor, mbrf):** 3480.1

**Distance between rig floor and sea level (m):** 11.1

**Water depth (drill pipe measurement from sea level, m):** 2799.1

---

[1]Paull, C.K., Matsumoto, R., Wallace, P.J., et al., 1996. *Proc. ODP, Init. Repts.*, 164: College Station, TX (Ocean Drilling Program).

[2]Shipboard Scientific Party is given in the list of participants that precedes the Table of Contents.

**Penetration (mbsf):** 670.0

**Coring totals**:

Type: APC
Number: 1
Cored: 9.5 m
Recovered: 10.12 m (106.5%)

Type: XCB
Number: 8
Cored: 76.7 m
Recovered: 59.31 m (77.3%)

**Formation:**

Cores were recovered only from limited intervals (see "Operations" section, this chapter); lithologies are similar to those in Hole 994C.

**Principal results:** Site 994 is the reference site on a transect of holes that extends from an area on the southern flank of the Blake Ridge where a BSR is not detectable to an area where an extremely well-developed BSR exists. A BSR is not observed under Site 994.

At Site 994, we cored a 700-m-thick sequence of sediments composed of clay and calcareous nannofossils. Three major lithologic units are identified, based on downward decreasing contents of calcareous nannoplankton. Unit I (0–14 mbsf; late Pleistocene) has the highest nannofossil contents (as much as 45%) correlating with the lightest gray colors of any sediment recovered at the site. Unit II (14–160 mbsf; late Pleistocene to late Pliocene) consists of decimeter- to meter-thick layers of dark greenish gray nannofossil-rich clay and more carbonate-rich greenish gray nannofossil clay. Nannofossil contents average 25%, with values of 40% and higher in the lighter colored beds. Unit III (160–703.5 mbsf), which extends to the bottom of the hole and comprises the remainder of the Pliocene to uppermost Miocene, consists of a monotonous succession of dark greenish gray diatom-bearing nannofossil-rich clay, with average $CaCO_3$ contents of 20%. Within most of the section (from 180 to 703.5 mbsf), grain densities are homogeneous. The sedimentation rates increase with depth. The average rates for the Quaternary, upper Pliocene, and lower Pliocene are ~70, 90, and 140 m/m.y., respectively. Rates increase to ~300 m/m.y. for the uppermost Miocene at the base of the hole. Within the same interval, wet bulk density and strength increase linearly, whereas water contents gradually decrease as a function of depth. The lithologic homogeneity of sediments at Site 994 makes it an ideal reference section for comparative gas hydrate studies.

The section obtained in Hole 994C contains a continuous record spanning from Holocene to latest Miocene (~6 Ma) in age. All nannofossil zones and subzones were present, and no obvious hiatuses were identified. Measurement of discrete paleomagnetic samples allowed determination of approximate positions for the Brunhes/Matuyama (27–65 mbsf) and Gauss/Matuyama (150 mbsf) magnetochron boundaries and for the Olduvai subchron (95–115 mbsf). Estimated sedimentation rates increased consistently downsection, reaching a maximum of 400 m/m.y.

Sediments in many cores were very gassy. Most cores underwent extensive gas-driven self-extrusion that sometimes split the liners near the shoe. One core burst its liner within the core barrel on the drill floor. Disruption of the cores from gas expansion began occurring at ~60 mbsf. Poor recovery below 190 mbsf is largely a result of vigorous degassing. The gas is mostly methane with small amounts of $CO_2$. Methane/ethane ratios generally increase with depth to values of several hundred, suggesting a small but increasing contribution of thermogenic gas with depth.

The interstitial-water chloride profiles from Holes 994C and 994D contain numerous anomalous low-chloride spikes superimposed on a trend of generally decreasing concentrations of chloride. Chloride values typical of seawater values (~560 mM) at the top of the section decrease to ~90% of seawater (~500 mM) at 300–400 mbsf. A slight increase in chloride toward the bottom of the hole is present. The lowest concentration of chloride measured in the spikes is 438 mM. In the interval from 100 to 450 mbsf, these spikes were found in 50% of the interstitial-water samples, and they are particularly abundant and well developed at 380–440 mbsf. Detailed studies of Hole 994D revealed that each of the anomalous low-chloride spikes extends over less than 1.5 m. The spikes are interpreted as evidence for the presence of gas hydrate, which melts and dilutes the interstitial water during coring and core processing.

Gas hydrate was recovered in two cores. Section 164-994C-31X-7 (259 mbsf) contained several white nodules of hydrate that ranged in volume from ~4 to 25 $cm^3$. The gas composition of the hydrate was 98.78% methane, 1.22% $CO_2$, 86 ppm ethane, and 2 ppm propane. Volumetric calculations show that the hydrate has at least 80% of its cages occupied by gas. In Section 164-994D-4X-1 (261 mbsf), a piece of hydrate <1 $cm^3$ was found. In the general region where solid hydrate was recovered from the cores, the physical properties data do not reveal significant changes in any measured trend. Many cores recovered from 240 to 430 mbsf contained anomalously cold zones (measured after recovery using temperature probes on the catwalk) that may indicate gas hydrate decomposition within these cores (although hydrate was not visually observed) or that these sections were cooled by vigorous gas expansion.

Fourteen in situ temperature measurements were attempted between 0 and 445 mbsf in Hole 994C. Based on data from eight successful Adara and WSTP deployments, the average geothermal gradient in the uppermost 320 m, where successful measurements were made, is estimated at 35.4°C/km. Average heat flow is 35 $mW/m^2$ over the depth range of the measurements, but 44.3 $mW/m^2$ within the upper 110 m of the hole.

Rock-magnetic studies indicate an anomalous interval of high greigite content from 20 to 200 mbsf superimposed on a continuous sequence of magnetite to pyrite reduction. The anomalous interval corresponds to a zone of downhole decreasing interstitial-water chloride content. This rock-magnetic signature is similar to that found during Leg 146 within the gas hydrate zone at Site 889.

A suite of wireline logs, including natural gamma, bulk density, neutron porosity, electrical resistivity, *P*-wave sonic, *S*-wave sonic, and geochemical logs, was run. In addition, several measurements with the geochemical tool in the inelastic mode were made in an attempt, for the first time in ODP history, to determine carbon/oxygen ratios. Initial analysis of the electrical resistivity and sonic logs shows dramatic changes in *P*-wave velocity and electrical resistivity in two important regions. The first corresponds to the zone just below 220 mbsf from which gas hydrate was recovered. In this zone, *P*-wave velocity and electrical resistivity have pronounced positive spikes. The second region is near the predicted base of the hydrate stability field at 420 mbsf, where *P*-wave velocity and electrical resistivity decrease sharply. In contrast, the bulk density log does not show changes at corresponding depths. The relatively constant bulk density throughout this interval suggests that the rise in electrical resistivity and *P*-wave velocity is not entirely caused by changes in porosity and may reflect increasing amounts of gas hydrate with depth in this zone.

Vertical seismic profiling was conducted between 110 and 650 mbsf during five lowerings of the three-component WHOI borehole seismometer in Hole 994D. Difficulties with the clamping arm restricted the acquisition to two walkaway profiles at 650 and 482 mbsf and 8 zero-offset (ZO) clamps over the same depth range. ZO air gun shots were fired with the tool suspended in the hole at 20-m intervals from 570 to 110 mbsf. A stacked record section shows clear first arrivals from 650 to 250 mbsf. A preliminary *P*-wave velocity model shows velocities generally increase with depth to a high of 1840 m/s at 540 mbsf. A pronounced low-velocity zone (less than 1550 m/s) occurs near the base of the hole (550–650 mbsf). The low-velocity zone may be due to the presence of free-gas bubbles dispersed in the sediments at this depth. Average velocity estimates from the *P*-wave sonic and vertical seismic profiling generally agree to within ±100 m/s. Differences in detail between the profiles are presumably attributable to the different resolution of the two methods.

## BACKGROUND AND OBJECTIVES

Sites 994, 995, and 997 comprise a transect of holes that penetrate below the base of gas hydrate stability within the same stratigraphic interval over a relatively short distance (9.6 km). A BSR is not ob-

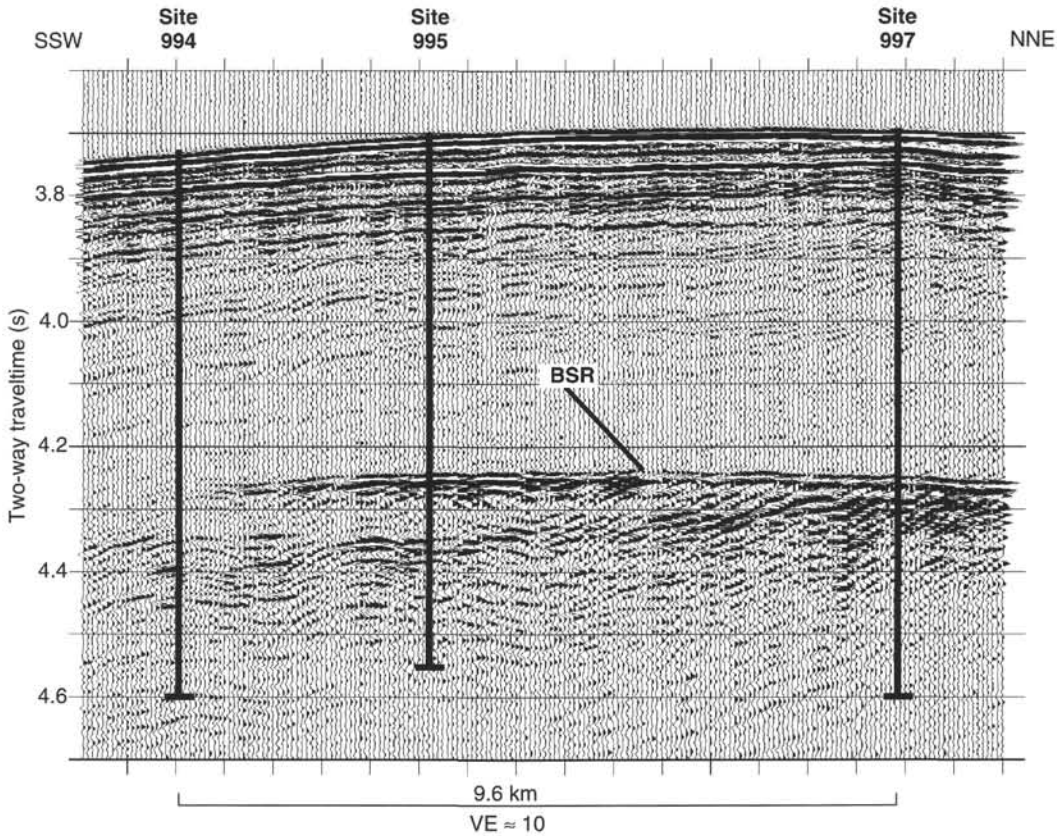


Figure 1. Seismic Profile CH-06-92 Line 31 along which Sites 994, 995, and 997 were drilled. Note that Site 994 is not associated with a distinct BSR although a very strong BSR occurs at 4.24 s sub-bottom at Site 995. The location of the profile is shown in Figure 6. VE = vertical exaggeration.

served at Site 994, a modest BSR occurs at 995, and a strong BSR is seen at Site 997 (Fig. 1).

Since the early 1970s, BSRs have been identified in numerous places around the world (Kvenvolden et al., 1993). They have been reported to have some of the following attributes, as summarized in the "Introduction" chapter (this volume):

1. Sub-bottom depths that vary with total water depth approximately as the gas hydrate phase boundary should;
2. Anomolously high seismic velocities for the burial depth ($V_p$ >2.0 km/s) in the units directly above the BSR;
3. Reversals in the polarity of the $V_p$ wavelets at the BSR indicating a lower velocity medium beneath the BSR;
4. Velocities that are less than seawater (<1500 m/s) in a zone directly beneath the BSR, which may indicate the presence of free gas;
5. A blanking or transparent zone above the BSR in which there is a very low impedance contrast; and
6. Generally high reflectivity in a zone as much as several hundred meters thick beneath the BSR.

Based on this evidence, BSRs are generally thought to indicate the presence of gas hydrate in the subsurface. However, the actual relationship between the BSR and gas hydrate needs to be calibrated.

## BSRs and the Blake Ridge

The Blake Ridge is a pronounced topographic feature on the North American Continental Rise (Fig. 2). The crest of the ridge extends more than 500 km downslope to the southeast from water depths of 2000 to 4800 m, approximately perpendicular to the general trend of the continental margin and continental rise. The crest of the entire ridge is generally straight, and the northeastern flanks of the ridge tend to be steeper than its southern flank. The upper ridge is referred to here as the Blake Ridge, whereas the region below 3000 m water depth is commonly called the Blake Outer Ridge.

The orientation of magnetic lineations (Klitgord and Behrendt, 1979) and seismic reflection profiles (e.g., Tucholke and Mountain, 1979; Shipley et al., 1979) indicate that the Blake Ridge overlies normal oceanic crust and is not associated with a distinct basement feature (Fig. 3). The Blake Ridge is thought to be a large sediment drift (Tucholke et al., 1977) that formed since the Eocene and overlies essentially horizontal pre-Neogene sedimentary sequences (Tucholke and Mountain, 1979).

The existence of a strong BSR on the crest of the Blake Ridge (Markl et al., 1970) has been known since the late 1960s (Fig. 4). Before any drilling had occurred, the origin of the BSR was thought to be related to a temperature- and pressure-dependent diagenetic change. During DSDP Leg 11, three holes (102, 103, and 104) were drilled on the Blake Outer Ridge to establish the nature of this reflector (Fig. 4). Hole 102 on the crest of the Blake Outer Ridge penetrated ~650 m through the Quaternary and into upper Miocene sediments thought to be well below the BSR. Because of the highly gassy nature of these hemipelagic sediments and the coincidence of the BSR depth with the predicted depth at which gas hydrate should become unstable, it was highly suspected that the BSR corresponds to the base of the gas hydrate stability zone (Shipboard Scientific Party, 1972). However, it could not be ruled out that the BSR was caused by diagenetic boundaries such as carbonate nodules and lenses.

Further drilling on the Blake Outer Ridge occurred at Site 533 during DSDP Leg 76 (Sheridan, Gradstein, et al., 1983) (Fig. 5). Total thicknesses of 151 m of Quaternary and 219 m of Pliocene mate-

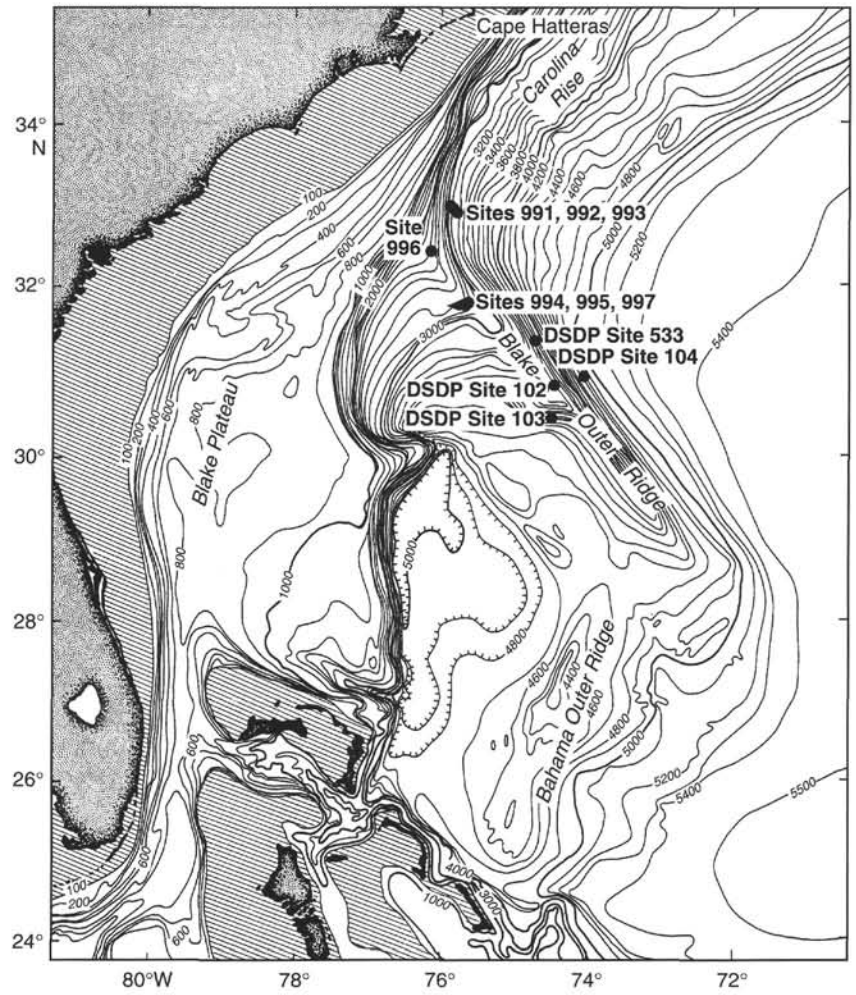


Figure 2. Bathymetry of the southeastern North American continental margin showing the location of Sites 994, 995, and 997 with respect to the Blake Ridge. DSDP sites in the region are indicated.

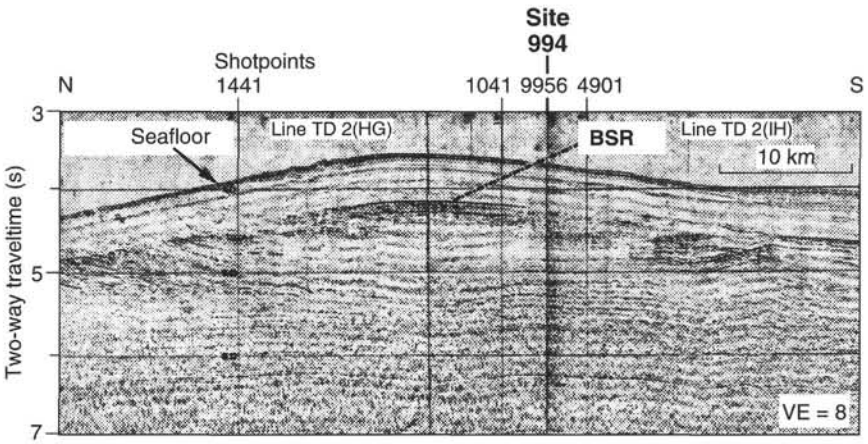


Figure 3. Multichannel seismic reflection profile (TD-2) across the flanks of the Blake Ridge showing that the stratigraphic units below 5 s sub-bottom are continuous beneath the ridge. A prominent BSR is identified. The location of Site 994 is projected onto the line. See Figure 6 for the location of the profile. VE = vertical exaggeration.

rials were recovered. Hole 533A terminated at only 399.5 mbsf, more than 200 m above the estimated base of gas hydrate stability in that area. Nevertheless, the presence of gas hydrate at Site 533 was demonstrated by the recovery of gas hydrate–bearing samples at 263.5 mbsf. Interstitial-water chemistry and degassing patterns from the pressurized core barrel (Kvenvolden et al., 1983) demonstrated that gas hydrate is common in these hemipelagic sediments. However, because Site 533 drilling was more than 200 m above the BSR, the nature and origin of the BSR remained unsolved. Also, the data were inadequate for assessing how extensive or pervasive the gas hydrate deposits are in this region.

Since the existence of gas hydrate in marine sediments was substantiated by drilling during Leg 76, the scientific community has developed an increased interest in understanding the amounts of gas hydrate stored in marine sediments (Kvenvolden, 1988). The major objective of returning to the Blake Ridge for more drilling was to understand better the amounts of gas that are stored in these sections. Because drilling at all the sites on the Blake Ridge penetrated below

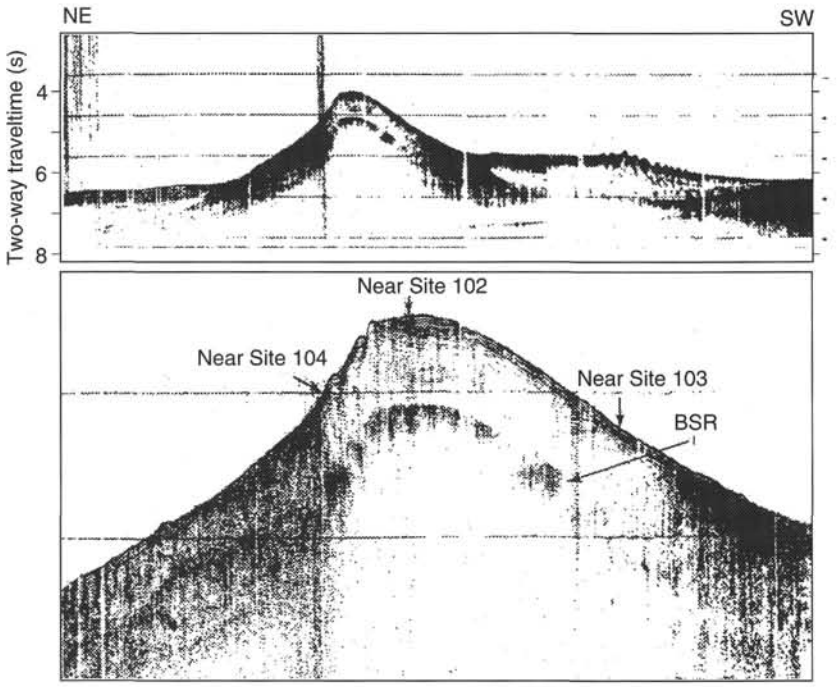


Figure 4. Single-channel seismic reflection profile across the Blake Outer Ridge along which DSDP Sites 102, 103, and 104 were located (from Shipboard Scientific Party, 1972; after Markl et al., 1970).

the base of gas hydrate stability, they provide critical information on the amounts of gas and gas hydrate in the sediments as well as the nature of the BSR itself.

The Blake Ridge transect of Sites 994, 995, and 997 was selected because it is an area where the BSR and seismic blanking are especially distinct (Figs. 1, 3, 6). Understanding the causes of variations in sediment gas hydrate contents and BSR development was a major objective of drilling during Leg 164. Site 994 on the southern flanks of the Blake Ridge is part of a transect of holes that extends from an area where a BSR is not detectable to an area where an extremely well-developed and distinct BSR exists (Figs. 1, 3). However, the geology and topography along this transect are relatively simple (Figs.1, 3), which provides an opportunity to assess the basic properties of gas hydrate–bearing sediments and to understand lateral hydrate variations caused by local lithologic, chemical, and hydrologic factors.

According to the most recent and closest geophysical data on the velocity of the sedimentary section above the BSR near Site 994 (e.g., ≤1950 m/s; Katzman et al., 1994), the depth of the base of gas hydrate stability at Site 994 is estimated to be ~450 mbsf. However, higher velocity estimates exist in the region (see "Introduction" chapter, this volume). A geothermal gradient of 36°C/km was measured at Site 533 (Gradstein and Sheridan, 1983). Recent heat-flow measurements near Site 994 indicate a surface temperature gradient of 46.9°C/km (Ruppel et al., 1995). Both the *P*-wave velocities and temperature gradient in the Blake Ridge sediments need to be refined. The gas composition and crystal structure of natural gas hydrate also should be determined to refine the pressure-temperature conditions for gas hydrate stability.

## OPERATIONS

### Transit to Hole 994A

The 135-km sea voyage to Site 994 required 6.5 hr at an average speed of 11.2 kt. The Datasonics 354M beacon (S/N 779, 14.0 kHz) was dropped on Global Positioning System (GPS) coordinates at 1408 hr on 7 November.

### Hole 994A

The operational plan at Site 994 (prospectus site BRH-4) called for two short holes from which sediments would be sampled for microbiological studies, followed by an APC/XCB hole to 750 mbsf. The same APC/XCB bit and BHA that had been used at Sites 991, 992, and 993 were run. The first APC core attempt had full recovery and no mudline. The pipe was moved up 5 m, and Hole 994A was spudded at 2108 hr on 7 November (Table 1). The seafloor was 2797.6 m below sea level (mbsl), based on recovery of the mudline. Cores 164-994A-1H through 4H were taken from 0 to 36.4 mbsf. During this time a Force 9 storm hit with rain and continuous lightning, 55-kt winds, and 15-ft seas. The ship was forced 55 m off location, resulting in a yellow (2% of water depth) warning light. Coring operations, however, continued unabated. After the coring objective was reached, the hole was terminated, and the pipe cleared the seafloor at 2350 hr on 7 November.

### Hole 994B

Hole 994B was drilled to obtain a single mudline core. Hole 994B was spudded at 0030 hr on 8 November, without moving the ship from the position of Hole 994A. The seafloor was 2797.6 mbsl, based on recovery of a mudline. Core 164-994B-1H was taken from 0 to 6.9 mbsf, and the hole was then terminated.

### Hole 994C

The ship was moved 10 m south, and Hole 994C was spudded at 0115 hr on 8 November. The seafloor was 2799.1 mbsl, based on recovery. Seventeen APC cores, 164-994C-1H through 19H, were taken from 0 to 158.4 mbsf, with PCS cores taken at 164-994C-9P and 18P. Cores were oriented from 164-994C-3H. The Adara temperature tool was run with a 10-min burial at Cores 164-994C-4H, 6H, 10H, 13H, 16H, and 20H. When liners were removed from the core barrel, some gas pockets were noted in the cores and occasional liner splits had occurred, but no special precautions were taken because of low total gas volumes and pressures.

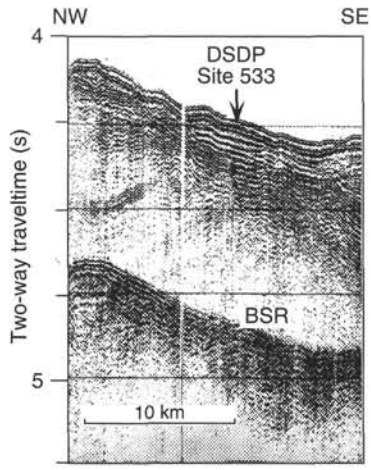


Figure 5. Single-channel seismic reflection profile across the Blake Outer Ridge along which DSDP Site 533 was located (from Sheridan, Gradstein, et al., 1983).

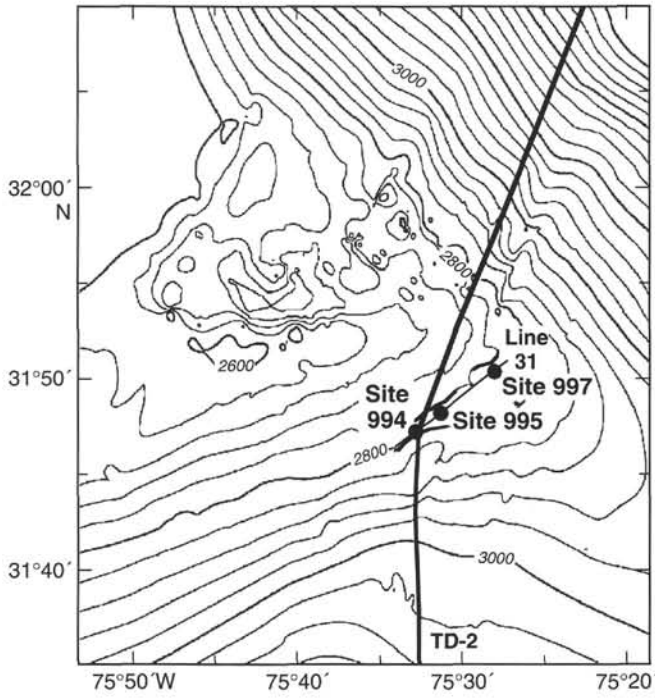


Figure 6. Bathymetry of the Blake Ridge around Sites 994, 995, and 997. The locations of multichannel seismic Profile CH-06-92 Line 31 (Fig. 1) and multichannel seismic Profile TD-2 (Fig. 3) are indicated.

The Fisseler Water Sampler was run at 51.0 mbsf and again at 100.4 mbsf. For both runs, the sampler was buried with 10,000 lb setdown weight for a 10-min sample period. When retrieved after each run, the 2-µm screen filter on the sampler was clogged with clay. Water recovered from both runs was determined by analysis to be a mixture of borehole water and water that is loaded into the tool for operational reasons before the run.

Fifty-seven XCB cores (164-994C-20X through 84X) were taken from 158.4 to 703.5 mbsf, with 537.1 m cored and 332.63 m recovered (61.9% recovery). Cores 164-944C-28X and 29X had very low recovery, and mud was found on the check valve, indicating that it had been blown out of the top of the liner. Core 164-944C-30X had enough gas pressure in the inner core barrel to blow out and fall down the V-door slide.

Ten PCS cores were taken at Hole 994C, with a total of 10.0 m cored and 1.28 m recovered (12.8% recovery). The PCS retained greater than 75% of hydrostatic pressure upon retrieval in nine of these runs and greater than 98% of hydrostatic pressure in six of the nine runs. It recovered more than 15 cm of sediment in seven of these runs. The new PCS push-in type shoes (see "Explanatory Notes" chapter, this volume) were run twice (Cores 164-994C-36P and 45P), and the new PCS rotary auger-type bit was run eight times. Coring parameters were varied in an effort to maximize recovery. After drilling to 703.5 mbsf, a sepiolite/seawater mud sweep was circulated, and a wiper trip was made to 76.0 mbsf to condition the hole for logging. On the first run (run 1) of the Quad-combo logging tool, borehole bridging prevented logging Hole 994C below 450 mbsf. The GST was then run; however, it was unable to pass a bridge at 330.0 mbsf. A second run (run 2) of the Quad-combo tool was attempted in Hole 994C, but the tool failed to fully exit the pipe, and only temperature data were collected. Hole 994C was terminated at 0110 hr on 15 November when the bit cleared the seafloor.

## Hole 994D

The ship was moved 20 m north-northeast, and Hole 994D was spudded at 0300 hr on 15 November to provide a more in-gage hole for VSP clamping and downhole logging. The seafloor was 2799.1 mbsl, based on Hole 994C. An 11 $^{7}/_{16}$ -in hole was drilled from 0 to 100.0 mbsf. One core (164-994D-1H) was taken from 100.0 to 109.6 mbsf. The hole was drilled with a center bit from 109.6 to 241.8 mbsf. Four cores (164-994D-2X through 5X) were taken from 241.8 to 280.3 mbsf. The hole was then drilled with a center bit from 280.3 to 376.7 mbsf. Four cores (164-994D-6X through 9X) were taken from 376.7 to 415.0 mbsf, after which the hole was drilled with a center bit to 670.0 mbsf. A 35-bbl sepiolite mud sweep was circulated and a wiper trip was made to 70 mbsf to condition the hole for logging. The hole was reamed from 508 to 670 mbsf, with 22 m of fill on bottom (clay pushed to the bottom without circulation or rotation). The sediments from 240 to 300 mbsf and below 450 mbsf were elastic, and reaming was ineffective because the hole closed in quickly after the bit was withdrawn. The hole was displaced with sepiolite/seawater mud. At 0515 hr on 16 November, the *Cape Hatteras* arrived on location from Beaufort, N.C., in order to conduct a two-ship walkaway VSP (W-VSP) experiment (see "Geophysics" section, this chapter).

The initial attempt to run the VSP log with the pipe at 494.5 mbsf was unsuccessful because of tight hole conditions. The drill pipe was pulled to 75 mbsf and the conical side-entry sub (CSES) was inserted so that the drill pipe could be used to push through constrictions that logging tools could not pass. The CSES was picked up in 4.75 hr, and drill pipe was run to 661 mbsf with as much as 35,000 lb drag. The VSP tool was deployed and pushed through the XCB bit by pumping; however, the logging cable was damaged, and the tool had to be pulled together with the CSES and drill pipe. The cable was reheaded, and the VSP tool was deployed again using the CSES and drill pipe. This time, the Gearhart fitting on the pendant rotated, damaging the conductors in the Gearhart head. After retrieval, the Gearhart head was repaired. Just before the fourth deployment, the VSP tool was found to have an electrical leakage. The backup WHOI tool was deployed in its place and run through the CSES and drill pipe to 650 mbsf, after which the first walkaway VSP began with the *Cape Hatteras*. The VSP tool stuck at 635 mbsf on its second clamping and was worked free; however, the clamping arm drive train was damaged. The VSP tool was retrieved through the CSES.

While the two VSP tools were repaired, a modified Quad-combo logging tool (without the CNT-G) was run to 628 mbsf using the CSES. The first VSP tool was rerun with the CSES to 650 mbsf, after which the *Cape Hatteras* conducted a W-VSP. The VSP clamping

**Table 1. Coring summary for Site 994.**

| Core | Date (Nov. 1995) | Time (UTC) | Depth (mbsf) | Length cored (m) | Length recovered (m) | Recovery (%) |
|---|---|---|---|---|---|---|
| 164-994A- | | | | | | |
| 1H | 8 | 0225 | 0.0–7.9 | 7.9 | 7.93 | 100.0 |
| 2H | 8 | 0315 | 7.9–17.4 | 9.5 | 9.84 | 103.0 |
| 3H | 8 | 0405 | 17.4–26.9 | 9.5 | 9.86 | 104.0 |
| 4H | 8 | 0445 | 26.9–36.4 | 9.5 | 9.66 | 101.0 |
| Coring totals | | | | 36.4 | 37.29 | 102.4 |
| 164-994B- | | | | | | |
| 1H | 8 | 0545 | 0.0–6.9 | 6.9 | 6.94 | 100.6 |
| Coring totals | | | | 6.9 | 6.94 | 100.6 |
| 164-994C- | | | | | | |
| 1H | 8 | 0630 | 0.0–4.4 | 4.4 | 4.40 | 100.0 |
| 2H | 8 | 0730 | 4.4–13.9 | 9.5 | 9.70 | 102.0 |
| 3H | 8 | 0825 | 13.9–23.4 | 9.5 | 9.32 | 98.1 |
| 4H | 8 | 0925 | 23.4–32.9 | 9.5 | 9.50 | 100.0 |
| 5H | 8 | 1050 | 32.9–42.4 | 9.5 | 9.79 | 103.0 |
| 6H | 8 | 1230 | 42.4–51.9 | 9.5 | 10.34 | 108.8 |
| 7H | 8 | 1500 | 51.9–61.4 | 9.5 | 9.89 | 104.0 |
| 8H | 8 | 1550 | 61.4–70.9 | 9.5 | 9.94 | 104.0 |
| 9P | 8 | 1640 | 70.9–71.9 | 1.0 | 0.23 | 23.0 |
| 10H | 8 | 1745 | 71.9–81.4 | 9.5 | 10.30 | 108.4 |
| 11H | 8 | 1835 | 81.4–90.9 | 9.5 | 10.16 | 106.9 |
| 12H | 8 | 1940 | 90.9–100.4 | 9.5 | 10.13 | 106.6 |
| 13H | 8 | 2250 | 100.4–109.9 | 9.5 | 10.21 | 107.5 |
| 14H | 8 | 2350 | 109.9–119.4 | 9.5 | 9.88 | 104.0 |
| 15H | 9 | 0050 | 119.4–128.9 | 9.5 | 10.07 | 106.0 |
| 16H | 9 | 0210 | 128.9–138.4 | 9.5 | 10.03 | 105.6 |
| 17H | 9 | 0300 | 138.4–147.9 | 9.5 | 10.02 | 105.5 |
| 18P | 9 | 0405 | 147.9–148.9 | 1.0 | 0.00 | 0.0 |
| 19H | 9 | 0500 | 148.9–158.4 | 9.5 | 6.80 | 71.6 |
| 20X | 9 | 0700 | 158.4–164.8 | 6.4 | 7.25 | 113.0 |
| 21X | 9 | 0800 | 164.8–174.4 | 9.6 | 6.94 | 72.3 |
| 22X | 9 | 0905 | 174.4–184.0 | 9.6 | 9.14 | 95.2 |
| 23X | 9 | 1000 | 184.0–193.6 | 9.6 | 7.41 | 77.2 |
| 24X | 9 | 1100 | 193.6–203.3 | 9.7 | 4.24 | 43.7 |
| 25X | 9 | 1305 | 203.3–212.9 | 9.6 | 7.80 | 81.2 |
| 26X | 9 | 1410 | 212.9–222.5 | 9.6 | 4.44 | 46.2 |
| 27P | 9 | 1500 | 222.5–223.5 | 1.0 | 0.07 | 7.0 |
| 28X | 9 | 1555 | 223.5–232.1 | 8.6 | 0.00 | 0.0 |
| 29X | 9 | 1705 | 232.1–241.7 | 9.6 | 2.27 | 23.6 |
| 30X | 9 | 2010 | 241.7–251.3 | 9.6 | 7.42 | 77.3 |
| 31X | 9 | 2130 | 251.3–260.9 | 9.6 | 9.74 | 101.0 |
| 32X | 9 | 2250 | 260.9–270.6 | 9.7 | 2.47 | 25.4 |
| 33X | 10 | 0025 | 270.6–280.2 | 9.6 | 5.78 | 60.2 |
| 34X | 10 | 0130 | 280.2–289.8 | 9.6 | 0.23 | 2.4 |
| 35X | 10 | 0430 | 289.8–299.4 | 9.6 | 3.95 | 41.1 |
| 36P | 10 | 0545 | 299.4–300.4 | 1.0 | 0.23 | 23.0 |
| 37X | 10 | 0650 | 300.4–309.0 | 8.6 | 0.49 | 5.7 |
| 38X | 10 | 0815 | 309.0–318.6 | 9.6 | 2.20 | 22.9 |
| 39X | 10 | 1110 | 318.6–328.3 | 9.7 | 1.30 | 13.4 |
| 40X | 10 | 1230 | 328.3–337.9 | 9.6 | 5.01 | 52.2 |
| 41X | 10 | 1400 | 337.9–347.6 | 9.7 | 9.17 | 94.5 |
| 42X | 10 | 1700 | 347.6–357.2 | 9.6 | 6.64 | 69.1 |
| 43X | 10 | 1825 | 357.2–366.8 | 9.6 | 5.53 | 57.6 |
| 44X | 10 | 2015 | 366.8–376.5 | 9.7 | 3.18 | 32.8 |
| 45P | 10 | 2115 | 376.5–377.5 | 1.0 | 0.00 | 0.0 |
| 46X | 10 | 2245 | 377.5–386.1 | 8.6 | 5.77 | 67.1 |
| 47X | 11 | 0140 | 386.1–395.6 | 9.5 | 6.65 | 70.0 |
| 48P | 11 | 0235 | 395.6–396.6 | 1.0 | 0.15 | 15.0 |
| 49X | 11 | 0410 | 396.6–405.2 | 8.6 | 8.43 | 98.0 |
| 50X | 11 | 0545 | 405.2–414.8 | 9.6 | 3.88 | 40.4 |
| 51X | 11 | 0655 | 414.8–424.5 | 9.7 | 2.83 | 29.2 |
| 52X | 11 | 1005 | 424.5–434.1 | 9.6 | 4.12 | 42.9 |
| 53P | 11 | 1055 | 434.1–435.1 | 1.0 | 0.15 | 15.0 |
| 54X | 11 | 1215 | 435.1–443.7 | 8.6 | 5.24 | 60.9 |
| 55X | 11 | 1450 | 443.7–453.4 | 9.7 | 4.95 | 51.0 |
| 56X | 11 | 1615 | 453.4–463.0 | 9.6 | 5.11 | 53.2 |
| 57X | 11 | 1745 | 463.0–472.6 | 9.6 | 4.99 | 52.0 |
| 58X | 11 | 1915 | 472.6–482.3 | 9.7 | 4.05 | 41.7 |
| 59X | 11 | 2040 | 482.3–491.9 | 9.6 | 5.93 | 61.8 |
| 60P | 11 | 2120 | 491.9–492.9 | 1.0 | 0.28 | 28.0 |
| 61X | 11 | 2300 | 492.9–501.5 | 8.6 | 9.73 | 113.0 |
| 62X | 12 | 0025 | 501.5–511.1 | 9.6 | 8.01 | 83.4 |
| 63X | 12 | 0210 | 511.1–520.7 | 9.6 | 8.93 | 93.0 |
| 64X | 12 | 0400 | 520.7–530.4 | 9.7 | 7.83 | 80.7 |
| 65X | 12 | 0530 | 530.4–540.1 | 9.7 | 9.03 | 93.1 |
| 66P | 12 | 0630 | 540.1–541.1 | 1.0 | 0.22 | 22.0 |
| 67X | 12 | 0835 | 541.1–549.7 | 8.6 | 8.90 | 103.0 |
| 68X | 12 | 1035 | 549.7–559.3 | 9.6 | 9.17 | 95.5 |
| 69X | 12 | 1210 | 559.3–568.9 | 9.6 | 8.67 | 90.3 |
| 70P | 12 | 1310 | 568.9–569.9 | 1.0 | 0.20 | 20.0 |
| 71X | 12 | 1445 | 569.9–578.5 | 8.6 | 4.47 | 52.0 |
| 72X | 12 | 1620 | 578.5–588.1 | 9.6 | 2.94 | 30.6 |
| 73X | 12 | 1805 | 588.1–597.7 | 9.6 | 8.20 | 85.4 |
| 74X | 12 | 1955 | 597.7–607.4 | 9.7 | 5.94 | 61.2 |
| 75X | 12 | 2145 | 607.4–617.0 | 9.6 | 9.23 | 96.1 |
| 76X | 12 | 2350 | 617.0–626.6 | 9.6 | 9.45 | 98.4 |
| 77X | 13 | 0145 | 626.6–636.2 | 9.6 | 7.77 | 80.9 |
| 78X | 13 | 0355 | 636.2–645.8 | 9.6 | 5.83 | 60.7 |
| 79X | 13 | 0615 | 645.8–655.4 | 9.6 | 8.24 | 85.8 |
| 80X | 13 | 0825 | 655.4–665.0 | 9.6 | 9.30 | 96.9 |
| 81X | 13 | 1035 | 665.0–674.6 | 9.6 | 8.55 | 89.0 |
| 82X | 13 | 1235 | 674.6–684.2 | 9.6 | 1.74 | 18.1 |
| 83X | 13 | 1500 | 684.2–693.8 | 9.6 | 3.28 | 34.1 |
| 84X | 13 | 1750 | 693.8–703.5 | 9.7 | 9.80 | 101.0 |
| Coring totals | | | | 703.5 | 501.47 | 71.3 |
| 164-994D- | | | | | | |
| 1H | 15 | 1050 | 100.0–109.5 | 9.5 | 10.12 | 106.5 |
| 2X | 15 | 1745 | 241.8–251.4 | 9.6 | 7.09 | 73.8 |
| 3X | 15 | 1850 | 251.4–261.0 | 9.6 | 9.02 | 93.9 |
| 4X | 15 | 1955 | 261.0–270.6 | 9.6 | 5.99 | 62.4 |
| 5X | 15 | 2110 | 270.6–280.2 | 9.6 | 7.93 | 82.6 |
| 6X | 16 | 0505 | 376.7–386.2 | 9.5 | 7.66 | 80.6 |
| 7X | 16 | 0700 | 386.2–395.8 | 9.6 | 6.52 | 67.9 |
| 8X | 16 | 0845 | 395.8–405.4 | 9.6 | 7.29 | 75.9 |
| 9X | 16 | 1030 | 405.4–415.0 | 9.6 | 7.81 | 81.3 |
| Coring totals | | | | 86.2 | 69.43 | 80.5 |

Notes: UTC = Universal Time Coordinated. An expanded version of this coring summary table that includes lengths and depths of sections, sampling comments, and locations of water-sampling temperature probe (WSTP) measurements is included on CD-ROM in the back pocket of this volume.

arm failed after three clampings, and the *Cape Hatteras* was released at 1110 hr on 19 November. The ZO-VSP was continued to 113 mbsf by suspending the tool in the hole at 20-m intervals and confirming arrivals on the geophone using the oscilloscope in the Underway Geophysics Lab. After the ZO-VSP was completed, the bit was washed in the last 30 m. The LDEO-SST was then run to 615 mbsf, and logs were taken successfully. The CSES was pulled back to the moonpool, and the logging tool was retrieved. Hole 994D was then terminated, and the bit cleared the seafloor at 0340 hr on 20 November. The bit was pulled 100 m above the seafloor for the move in DP mode to Site 995.

## LITHOSTRATIGRAPHY

### Introduction

Of the four holes drilled at Site 994, Hole 994C was continuously cored to 703.5 mbsf and used to establish the lithostratigraphy for the Holocene to uppermost Miocene section of the Blake Ridge at this site. Only short intervals of uppermost Pleistocene to Holocene sediments were recovered from Holes 994A and 994B. Nine cores from three intervals within the Pliocene section were recovered from Hole 994D (Fig. 7). Three lithologic units are recognized in Hole 994C, based on sediment composition, primarily variations in the nannofossil and total carbonate contents. Color reflectance measurements in the 400–700 nm range downhole also exhibit changes corresponding to unit boundaries (Fig. 7).

### *Unit I*

Interval: 164-994C-1H-1, 0 cm, through 2H-6, 142 cm
Age: Holocene to late Pleistocene/(?)Holocene
Depth: 0–13.32 mbsf

Unit I consists of interbeds of light gray to gray (5Y 7/1 to 6/1) nannofossil clay and greenish gray to gray (5 GY 5/1 to 5Y 5/1) nannofossil-rich clay with individual beds as much as 1.20 m thick. The

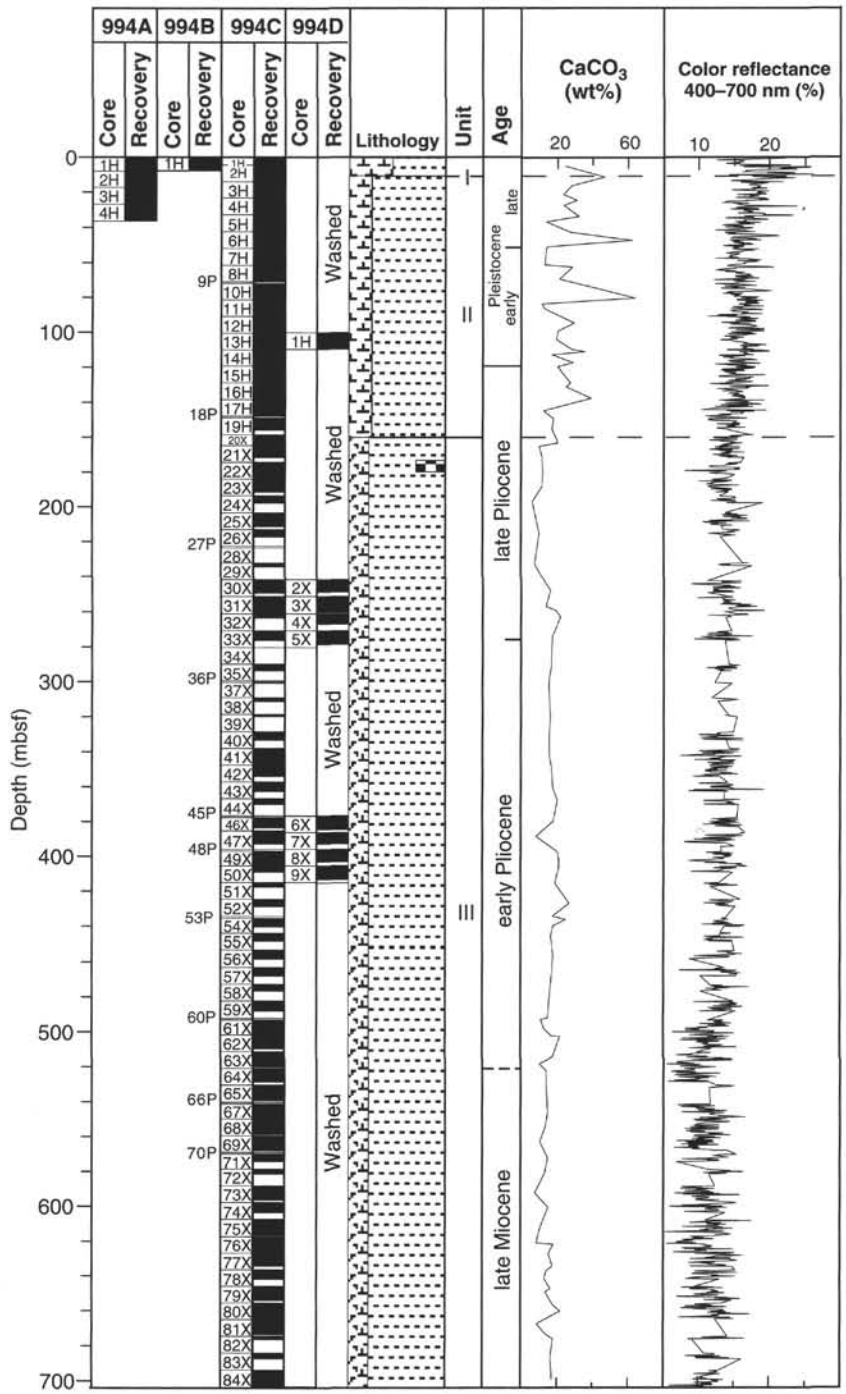


Figure 7. Composite stratigraphic section for Site 994 showing core recovery, a simplified summary of lithology, lithologic unit boundaries, and age. Also shown are total carbonate contents expressed as $CaCO_3$ weight percentage (see "Organic Geochemistry" section, this chapter) and average color reflectance of sediments across the visible spectrum (VIS 400–700 nm) down Hole 994C. Lithologic symbols are explained in Figure 2 of the "Explanatory Notes" chapter (this volume).

subtle color differences are caused by variations in biogenic carbonate content. This unit is subdivided into two subunits to discriminate the distinctive brown to reddish brown interval of oxidized sediments at the top of the section.

*Subunit IA*

The uppermost 20 cm of the section (interval 164-994C-1H, 0–20 cm; 0–0.2 mbsf) consists of reddish brown (5YR 5/3) bioturbated foraminifer-bearing nannofossil silty clay. A 2-cm-thick darker band occurs near the base of this subunit from 0.16 to 0.18 mbsf (Fig. 8). Subunit IA is 15 cm thick in Hole 994A (interval 164-994A-1H-1, 0–15 cm; 0–0.15 mbsf), and the color is brown (10YR 5/3).

*Subunit IB*

Subunit IB extends from 0.20 to 13.32 mbsf (interval 164-994C-1H-1, 20 cm, through 2H-6, 142 cm) and consists of alternating

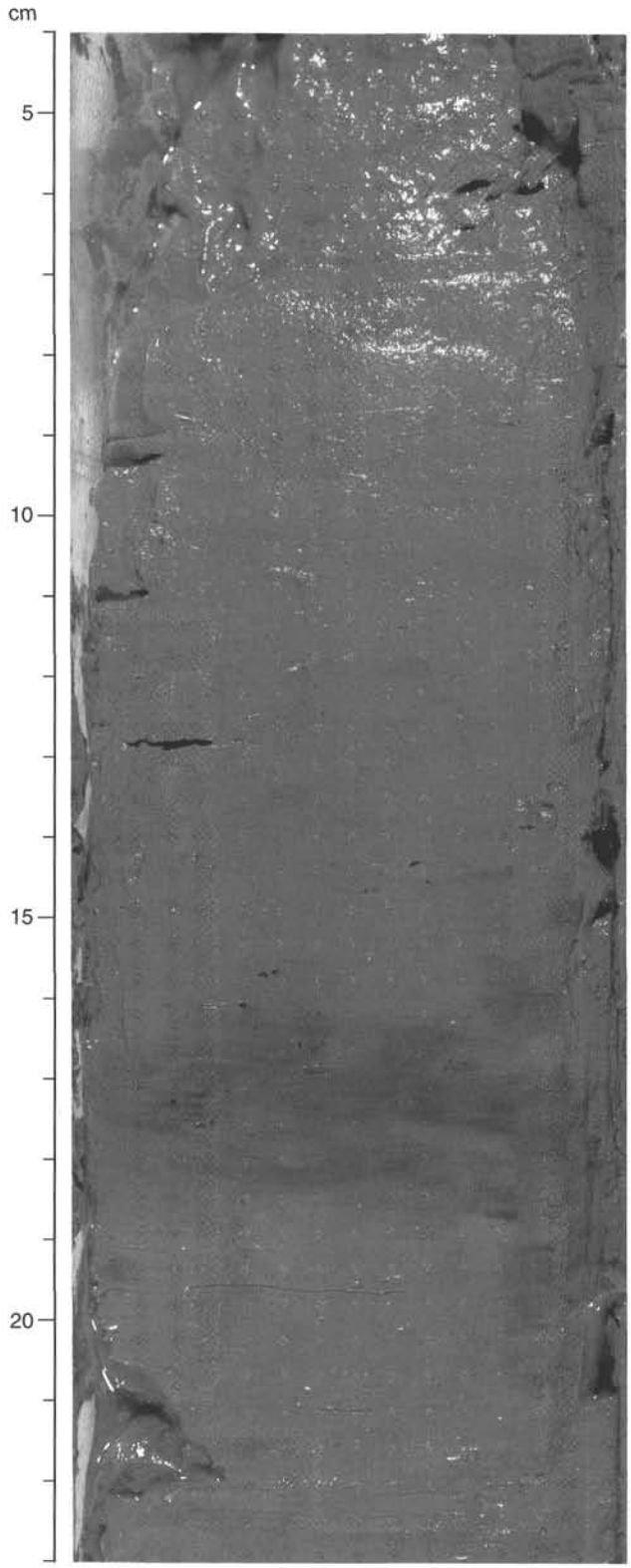


Figure 8. Reddish brown foraminifer-bearing nannofossil clay (Subunit IA) at the top of Core 164-994C-1H that shows a darker band of ferromanganese oxide hydroxide (16–18 cm) near the base of the subunit (interval 164-994C-1H-1, 4–23 cm; 0.04–0.23 mbsf).

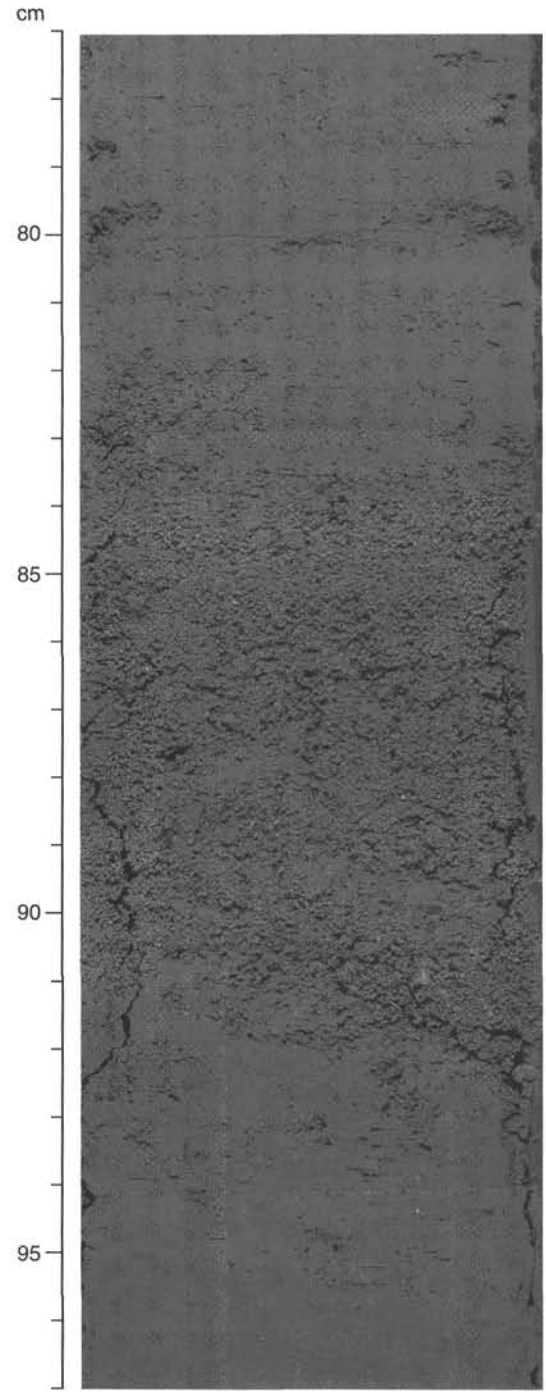


Figure 9. Coarse-graded bed of sand-sized foraminifers within greenish gray nannofossil-rich clay (interval 164-994C-5H-5, 77–97 cm; 37.67–37.87 mbsf). Grain size increases upward from the base (reverse grading) to ~86 cm and then decreases upward (normal grading) to the top of the bed.

greenish gray to gray (5GY 6/1 to 5Y 5/1) bioturbated nannofossil clay and darker gray (5Y 5/1 to 4/1) foraminifer-bearing nannofossil-rich clay with minor burrowing. Bioturbation is most intensive at the contacts between lithologic and/or color changes as evidenced by infilling of burrows with the overlying sediment. *Zoophycos* is abundant. Total carbonate content (expressed as weight percentage $CaCO_3$) is 24 to 47 wt% (Fig. 7).

Coarse beds of foraminifer ooze as much as 18 cm thick occur in both the darker and lighter clays, and they commonly exhibit irregular,

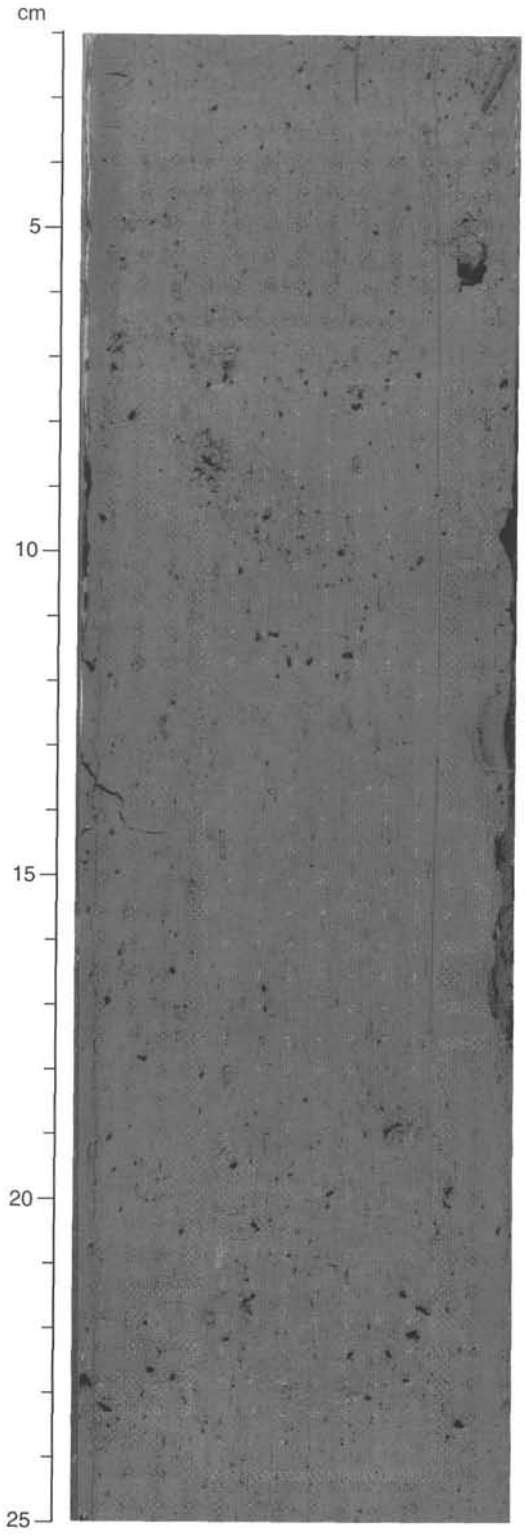


Figure 10. Mousse-like sediment surface that possibly indicates degassing or hydrate decomposition (interval 164-994C-10H-CC, 2–25 cm; 81.80–82.03 mbsf).

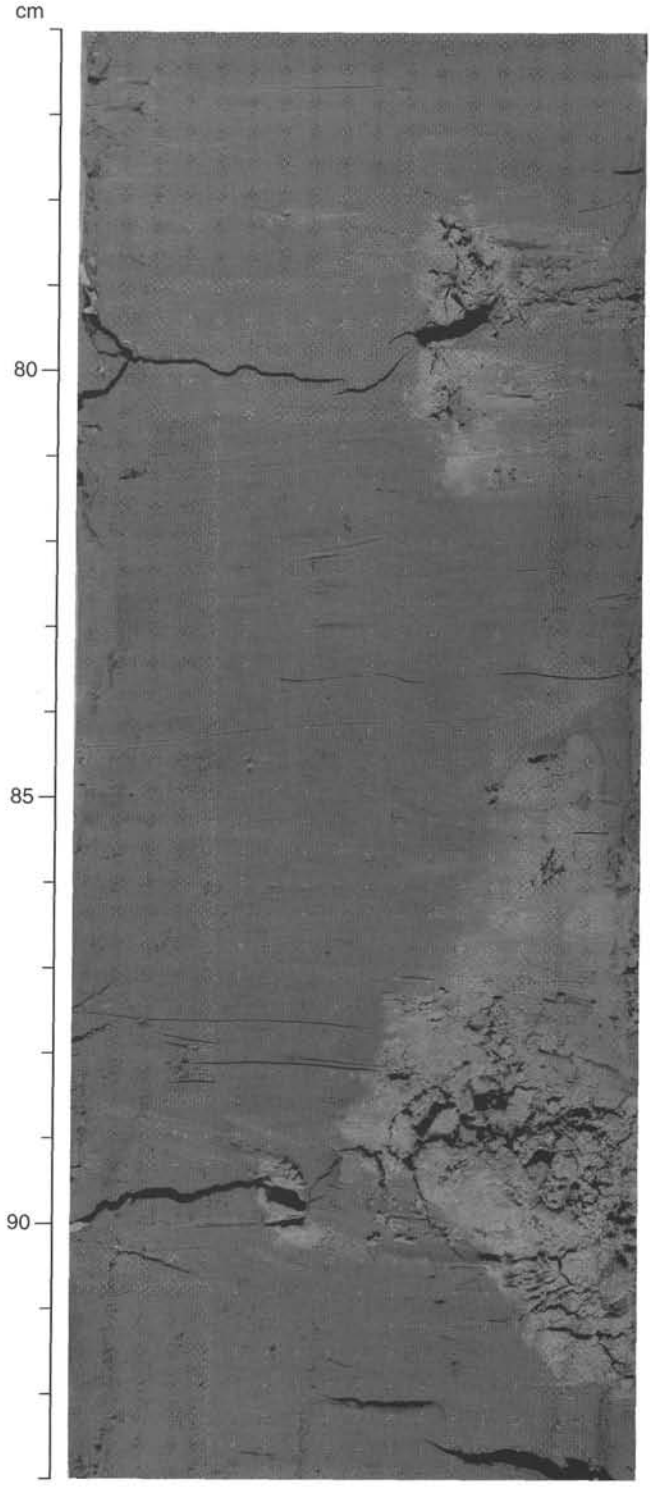


Figure 11. Irregular, semilithified brownish gray dolomite-rich nodules in greenish gray nannofossil-rich silty clay (interval 164-994C-5H–6, 76–93 cm; 41.16–41.23 mbsf).

scoured bases. Coarse foraminifer ooze also occurs as burrow infillings, and some of these burrows are surrounded by glauconite-rich rims in the adjacent mud. A 16-cm-thick bed of weak red (2.5 YR 5/2) foraminifer- and nannofossil-rich clay occurs in interval 164-994C-2H-1, 46–62 cm (4.86–5.02 mbsf). This bed appears to be normally graded with downward-increasing foraminifer content and a sharp base.

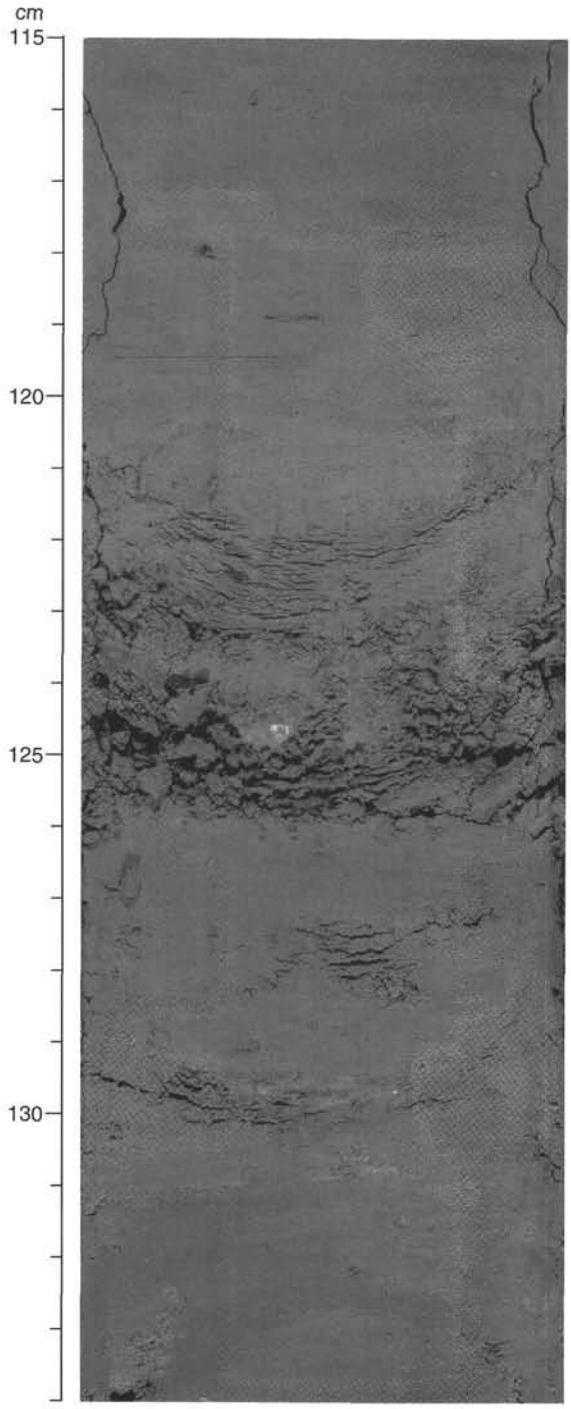


Figure 12. Light brownish gray dolomite-rich diagenetic bed (interval 164-994C-10H-1, 115–134 cm; 73.05–73.24 mbsf).

### *Unit II*

Interval: 164-994C-2H-6, 142 cm, through 20X-2, 22 cm
Age: late Pleistocene to late Pliocene
Depth: 13.32–160.12 mbsf

Unit II consists of greenish gray (5GY 5/1) nannofossil-rich clay with interbeds of lighter colored greenish gray (5GY 6/1) nannofossil clay. The nannofossil clay beds range in thickness from 10 to 130 cm and exhibit gradational upper and lower contacts. These rhythmic alternations are different from those of Unit I in that the lighter colored clay beds are thinner and less common, color variations between beds are more subtle, and terrigenous red muds are absent. Total carbonate content ranges from 12 to 64 wt% with the highest contents in beds of dolomite (Fig. 7). The sediments are generally mottled by slight to intense bioturbation.

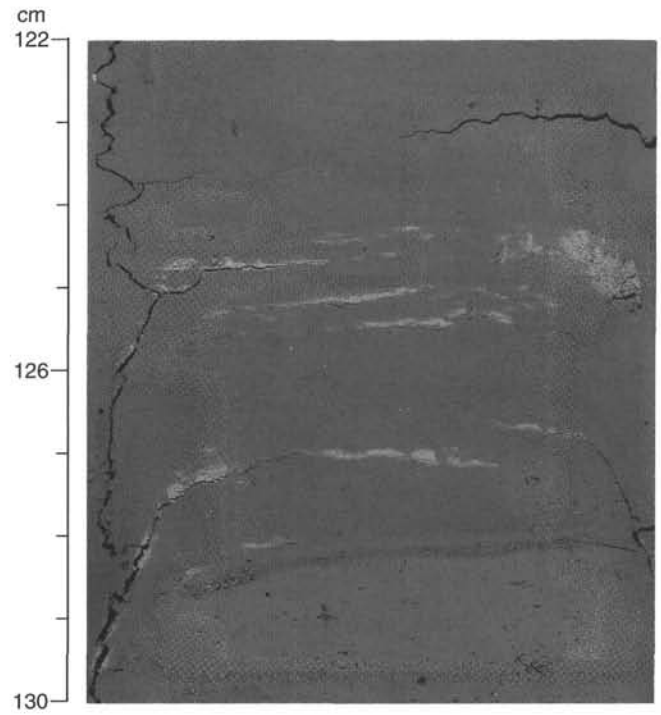


Figure 13. Thin dolomite-rich laminae at base of dark greenish gray nannofossil-rich clay (interval 164-994C-12H-5, 122–130 cm; 98.12–98.20 mbsf).

In Cores 164-994C-3H and 4H and 164-994A-3H and 4H, some of the light-colored beds show a distinct light greenish color (5G 7/1 to 6/1) that is probably caused by the presence of disseminated glauconite. Discrete coarse beds of foraminifer ooze as much as 15 cm thick occur in Unit II from 13.3 to 80 mbsf. These beds decrease in abundance down this interval and are rare below 80 mbsf. A 10-cm-thick foraminifer ooze bed in interval 164-994C-5H-5, 84–94 cm (37.74–37.84 mbsf), exhibits both reverse and normal grading; particle size increases gradually from the base upward to the middle of the bed and then decreases toward the top of the bed (Fig. 9).

A soupy texture occurs in interval 164-994C-4H-5, 90 cm, through 4H-7, 50 cm (30.5–32.7 mbsf). Vuggy surfaces on split cores of silty, clayey sediment suggest localized degassing (Fig. 10; interval 164-994C-10H-CC, 0–25 cm [81.78–82.03 mbsf]).

Light brownish gray (10YR 6/2), 10- to 20-cm-thick beds and/or soft nodules of silt-sized anhedral and subhedral dolomite crystals occur in Sections 164-994C-5H-6, 84–92 cm (41.24–41.32 mbsf) (Fig. 11); 6H-4, 65–73 cm (47.25–47.33 mbsf); 8H-5, 103–112 cm (68.43–68.52 mbsf); 10H-1, 119–133 cm (73.09–73.23 mbsf) (Fig. 12); and 10H-6, 95–100 cm (80.35–80.40 mbsf). Thin laminae of dolomite are very rare (interval 994C-12H-5, 124–127 cm; 98.14–98.17 mbsf) (Fig. 13).

### *Unit III*

Interval: 164-994C-20X-2, 22 cm, through 84X-CC, 36 cm
Age: late Pliocene to late Miocene
Depth: 160.12–703.5 mbsf

Unit III consists of a 540-m-thick monotonous succession of bioturbated dark greenish gray to dark gray (5GY 4/1 to 5Y 4/1) diatom-bearing nannofossil-rich clay and claystone. The total carbonate content of Unit III ranges from 6 to 27 wt% (Fig. 7). Primary sedimentary structures and bioturbation structures, if present, are difficult to discern because of the "biscuit" structure produced by XCB drilling disturbances.

The upper portion of Unit III from 160 to ~500 mbsf consists of dark greenish gray to greenish gray (5GY 4/1 to 5Y 4/1) nannofossil- and diatom-rich clays. A 6-m-thick interval (164-994C-22X-1, 20 cm, through 22X-4, 136 cm; 174.6–179.4 mbsf) of clay conglomerate near the top of the unit contains clay clasts that are as much as 5 cm long and are commonly deformed (Fig. 14). Increasing compaction and lithification downhole cause gradual transition of the clay to predominantly claystone by 500 mbsf. The lower portion of Unit III below ~500 mbsf consists of dark greenish gray to dark gray (5GY 4/1 to 5Y 4/1) diatom-bearing nannofossil-rich claystone. The lithologies of the upper and lower portions of Unit III are similar, except for the higher compaction, fissile texture, and lithification of the claystone.

High-angle to vertical fractures occur downhole from interval 164-994C-62X-5, 45 cm (507.95 mbsf), downward. Individual fractures, continuous across several successive drilling biscuits, are common, suggesting that they are primary structures, not drilling disturbance. Similar fractures occur in Leg 150 cores, and a few of these are filled with pyrite-cemented quartz sands, which clearly indicates that the fractures are primary structures (Mountain, Miller, Blum, et al., 1994).

## Sediment Composition Based on Smear-Slide and XRD Analyses

The dominant mineral components of Unit I are clay minerals, calcite, and quartz (Fig. 15). Feldspars, dolomite, and pyrite are minor components (Table 2). The biogenic calcareous constituents consist of nannofossils and minor amounts of foraminifers (Fig. 15). Siliceous fossils are present as diatoms and rare sponge spicules. Clay minerals and nannofossils make up the bulk of the clay-sized fraction. Quartz and feldspars dominate the silt fraction, but their abundances shown by XRD data indicate that quartz and feldspars also are present within the clay-sized fraction (Fig. 16). Sand-sized particles generally comprise less than 5% of the sediment and are composed largely of foraminifers. Concentrations of sand-sized foraminifers reach as much as 50% in foraminiferal ooze beds. Disseminated dolomite rhombs (15–30 μm) make up a few percent of the bulk mineralogy (Fig 16). According to the d-spacing of the (104) diffraction peak at 2.888–2.887 Å, the dolomite falls into the range of stoichiometric dolomite (Table 2). Pyrite is low in abundance (<5 wt%), and glauconite occurs locally within burrows.

Clay minerals, calcite, and quartz also are the dominant mineral components in Unit II (Figs. 15, 16; Table 2). Feldspars, dolomite, siderite, and pyrite are minor components, although dolomite is dominant in nodules and thin beds. Nannofossil abundances are generally less than in Unit I. Foraminifer concentrations are locally as much as 55% in foraminiferal ooze beds. Dolomite rhombs, 5–15 μm in diameter, are widely disseminated, but generally they make up only a few percent of the bulk sediment composition. Trends in the d-spacing of the (104) peak indicate a general increase in either calcium or iron content of the dolomite with depth (Table 2). In the diagenetic carbonate horizons listed above, micrometer-sized particles are associated with larger subhedral crystals of 10–20 μm diameter. According to the d-spacing of the (104) and (116) diffraction peaks at 2.897 and 1.792 Å, respectively, the dolomite is a ferroan dolomite (Table 2). Siderite first occurs at 120 mbsf but remains low in abundance throughout Unit II. Diatoms may reach 15% but, on average, remain below 5%. As in Unit I, quartz and feldspars generally occur in the

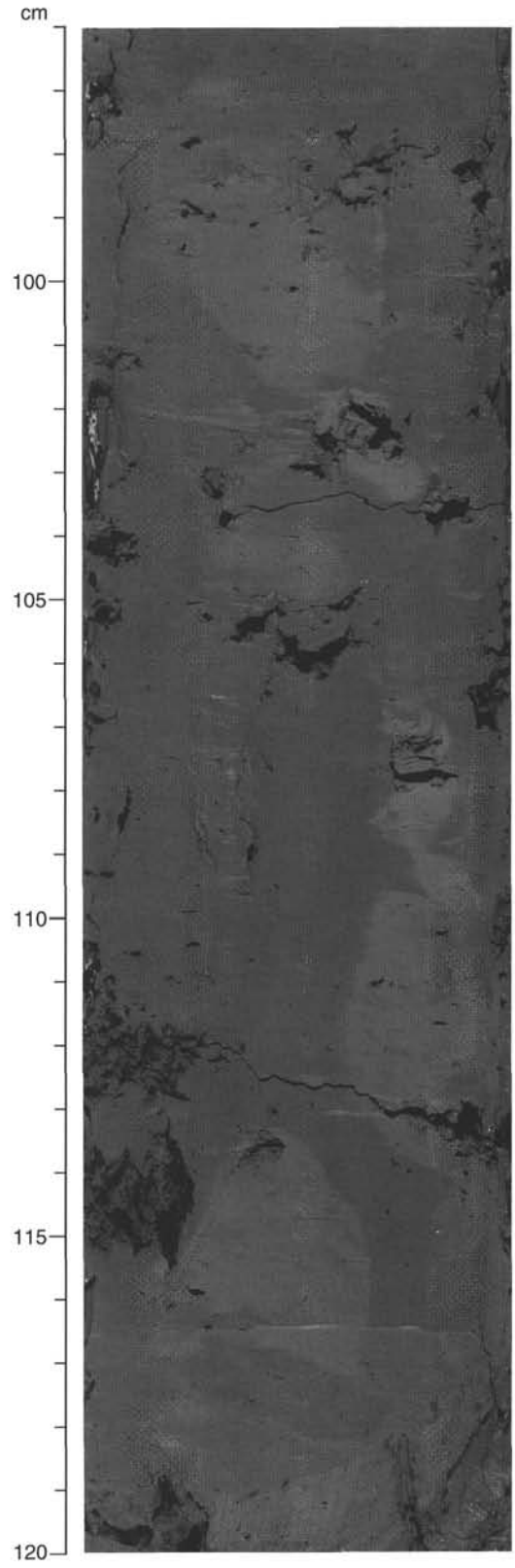


Figure 14. Debris-flow deposit showing rounded, slightly deformed clay clasts (interval 164-994C-22X-3, 96–120 cm; 177.76–178.00 mbsf).

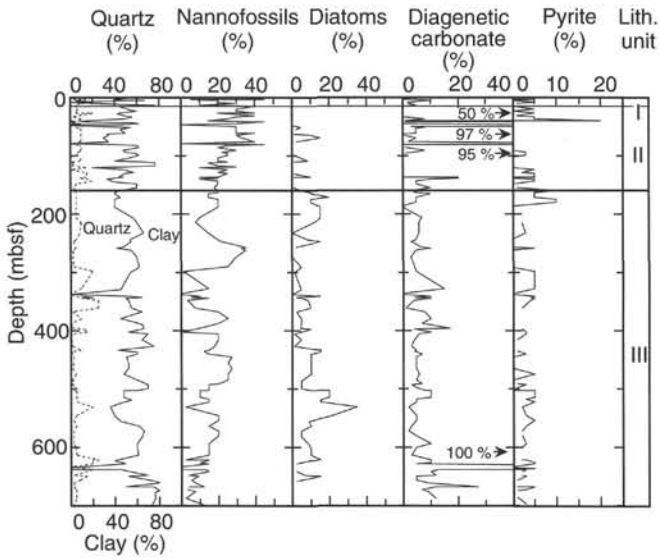


Figure 15. Downhole mineralogical variation of the major sediment constituents, based on visual estimation in smear slides.

silt-sized fraction, which also contains siliceous fossils and foraminifers. The clay-sized fraction is dominated by clay minerals and nannofossils, but it also includes quartz and feldspars.

In Unit III, clay minerals, calcite, and quartz are the major mineral components, whereas dolomite, siderite, pyrite, and feldspars constitute minor components (Figs. 15, 16; Table 2). Nannofossils and diatoms are the major biogenic components and vary widely in abundance; however, these components show overall downward decreasing and increasing trends, respectively (Fig. 15). Clay minerals, together with nannofossils, make up the bulk of the clay-sized fraction; quartz is mostly silt size. Diagenetic carbonate rhombs, similar in shape to those observed in Unit II, are widely disseminated throughout the sediment, and abundances range from 5% to 10%, according to smear-slide estimations (Fig. 15). XRD analyses indicate that downhole decreases in dolomite are generally compensated by increases in siderite (Fig. 16). Variable dolomite composition is exhibited by shifts in the d-spacing of the (104) peak, which ranges from 2.886 to 2.910 Å. There is, however, no significant downhole trend in the d-space variation of dolomite (Table 2). On the basis of smear-slide estimates, pyrite consistently comprises ~5% of the bulk sediment. Siderite nodules and laminae are rare in Unit III.

## Discussion

Site 994 is located on the Blake Ridge at a water depth of ~2799 m (see "Background and Objectives" section, this chapter). The Blake Ridge is a classic contourite ridge or sediment-drift deposit created by sediment deposition from the thermohaline-induced Western Boundary Undercurrent (WBUC), a strong contour current flowing southward along the U.S. continental rise (Heezen, et al., 1966; Markl and Bryan, 1983). In the vicinity of Site 994, there has been no strong input of coarse terrigenous sediment from the shelf via submarine canyons; thus, sediments tend to be fine grained. Hemipelagic accumulation of biogenic and terrigenous sediments has been modified by reworking and redeposition by the WBUC. Mass-transport deposits are rare (e.g., a 6-m-thick debris-flow deposit near the top of Unit III).

The alternation of nannofossil-rich and nannofossil clays with significant differences in carbonate content in the upper 160 m (Units I and II) of the section apparently reflects fluctuations in WBUC intensity, terrigenous input, and/or carbonate productivity, all of which were probably forced by glacial-interglacial climatic fluctuations. The higher carbonate nannofossil-rich clays apparently reflect times of less terrigenous dilution and/or greater nannofossil productivity, presumably during interglacial phases. In contrast, increased terrigenous sediment was transported to the area by the WBUC during glacial phases. The thin, reddish brown nannofossil clay of Subunit IA apparently provides evidence of these climatic fluctuations. Subunit IA is similar to other brownish, relatively high-carbonate intervals of approximately Holocene age that were cored previously in this region (e.g., Heezen et al., 1966) and elsewhere throughout the Atlantic. At most of these locations, this brownish, oxidized interval records the decrease of terrigenous sediment supply to the Atlantic in response to Holocene sea-level rise (see Damuth, 1977, and references therein).

Distinctive features clearly indicative of contour-current deposition are only observed in lithologic Units I and II (0–160 mbsf). Evidence for long-distance transport of continental slope sediments by the WBUC to Site 994 is clearly provided by the weak red bed of foraminifer-rich terrigenous mud in Unit I (interval 164-994C-2H-1, 46–62 cm; 4.86–5.02 mbsf), which is presumed equivalent to the "rose-colored lutites" previously described by Heezen et al. (1966). These red sediments were derived from erosion of carboniferous red beds in Eastern Canada during glacial periods, injected into the WBUC on the continental rise off Nova Scotia, and transported southward to the Blake Ridge (Needham et al., 1969). In addition, the reverse-graded beds of foraminifer ooze (e.g., Fig. 9) indicate winnowing of fine sediments by the WBUC.

## GAS HYDRATE

Although a BSR does not occur in the seismic reflection profiles that cross Site 994 several pieces of gas hydrate were recovered at 259.90 mbsf in Hole 994C and disseminated gas hydrate was observed at almost the same depth in Hole 994D. Despite these limited occurrences of gas hydrate we infer, based on chemical and logging data, that disseminated gas hydrate occurs intermittently throughout a zone extending between ~195 and ~450 mbsf. We conclude that this disseminated hydrate had largely dissociated during core recovery and was so fine grained that it was difficult to visually detect.

### Initial Core Inspection

#### *Hole 994C*

Gas hydrate was found in interval 164-994C-31X-7, 10–50 cm (259.90–260.30 mbsf). During initial core inspection on the catwalk, a nodular-like white area, ~5 cm in diameter, was observed through the core liner. The sediment around the white material was anomalously cold (<5°C) compared to typical catwalk core temperatures (~12°C). The material was thought to be solid gas hydrate, so the core was immediately cut at the location of the hydrate. Sections (~20 cm long) were subsequently cut off above and below this initial cut. Five large pieces of gas hydrate (20–50 $cm^3$) and one small piece (~2 $cm^3$) were recovered from near both ends of the first cut section. Thus, we estimate that all the gas hydrate samples came from a zone that was <10 cm thick. The sediments in this section (164-994C-31X-7) and the uppermost 20 cm of the next core (Section 164-994C-32X-1) were slightly soupy. The soupy nature could be caused by the melting of gas hydrate, although drilling disturbance also is possible.

Although all the pieces of gas hydrate were embedded in clay, the hydrate to clay boundary appeared to be sharp rather than transitional. The gas hydrate samples appeared white with a soapy luster. They were irregularly shaped, with rounded edges, and tended to be flattened parallel to the core. Because of disturbance of the host sediments, it is unclear whether the gas hydrate originally occurred as nodules, fracture fillings, or layers. However, because the surface curvature of one large sample matched the shape of the core liner, it

**Table 2. Main diffraction peak areas, d-values, and weight percentage proportions for minerals identified in samples from Hole 994C.**

| Core, section, interval (cm) | Depth (mbsf) | Dolomite d-value (Å) | Dolomite peak area | Calcite d-value (Å) | Calcite peak area | Quartz peak area | Clay peak area | Feldspar peak area | Pyrite peak area | Siderite peak area | Quartz* (wt%) | Calcite* (wt%) | Dolomite* (wt%) |
|---|---|---|---|---|---|---|---|---|---|---|---|---|---|
| 164-994C- | | | | | | | | | | | | | |
| 2H-1, 47–48 | 4.87 | 2.887 | 1,955 | 3.036 | 12,969 | 21,653 | 2,726 | 4,597 | 1,534 | | 16 | 26 | 2 |
| 2H-5, 96–97 | 11.36 | 2.895 | 678 | 3.036 | 22,890 | 22,604 | 2,441 | 4,074 | 1,631 | | 17 | 63 | 0 |
| 3H-2, 66–67 | 16.06 | 2.890 | 1,930 | 3.036 | 14,805 | 11,245 | 2,439 | 4,988 | 1,249 | | 8 | 31 | 2 |
| 3H-5, 129–130 | 21.19 | 2.899 | 1,770 | 3.037 | 15,492 | 13,905 | 2,539 | 5,368 | 2,789 | | 10 | 34 | 2 |
| 4H-1, 89–90 | 24.29 | 2.891 | 3,178 | 3.034 | 13,096 | 13,840 | 2,372 | 8,259 | 1,573 | | 10 | 26 | 3 |
| 4H-3, 89–90 | 27.29 | 2.888 | 2,842 | 3.031 | 12,325 | 21,927 | 2,578 | 3,877 | 674 | | 16 | 24 | 3 |
| 5H-1, 70–71 | 33.60 | 2.901 | 2,980 | 3.035 | 15,143 | 13,841 | 2,570 | 2,049 | 3,061 | | 10 | 33 | 3 |
| 5H-3, 69–70 | 36.59 | 2.888 | 4,208 | 3.037 | 10,756 | 33,135 | 2,609 | 6,074 | 1,831 | | 25 | 20 | 4 |
| 6H-1, 26–27 | 42.66 | 2.889 | 3,882 | 3.034 | 7,084 | 32,139 | 2,786 | 4,269 | 2,652 | | 24 | 11 | 4 |
| 6H-4, 72–73 | 47.32 | 2.896 | 19,612 | 3.037 | 16,241 | 10,000 | 1,827 | 4,873 | 1,284 | | 7 | 36 | 21 |
| 6H-6, 121–122 | 50.81 | 2.892 | 1,644 | 3.033 | 8,182 | 13,434 | 2,617 | 5,214 | 1,865 | | 10 | 13 | 2 |
| 7H-1, 24–25 | 52.14 | 2.901 | 1,235 | 3.038 | 7,716 | 11,567 | 2,751 | 5,360 | 2,960 | | 9 | 12 | 1 |
| 7H-7, 20–21 | 61.10 | 2.891 | 2,861 | 3.034 | 6,014 | 16,345 | 2,504 | 8,012 | 2,414 | | 12 | 9 | 3 |
| 8H-1, 101–102 | 62.41 | 2.898 | 2,843 | 3.036 | 17,025 | 8,849 | 2,837 | 2,034 | 1,884 | | 7 | 39 | 3 |

Note: * = percentages (wt%) for quartz, calcite, and dolomite are calculated using the calibration curves described in the "Lithostratigraphy" section of the "Explanatory Notes" chapter (this volume).

**Only part of this table is produced here. The entire table appears on the CD-ROM (back pocket).**

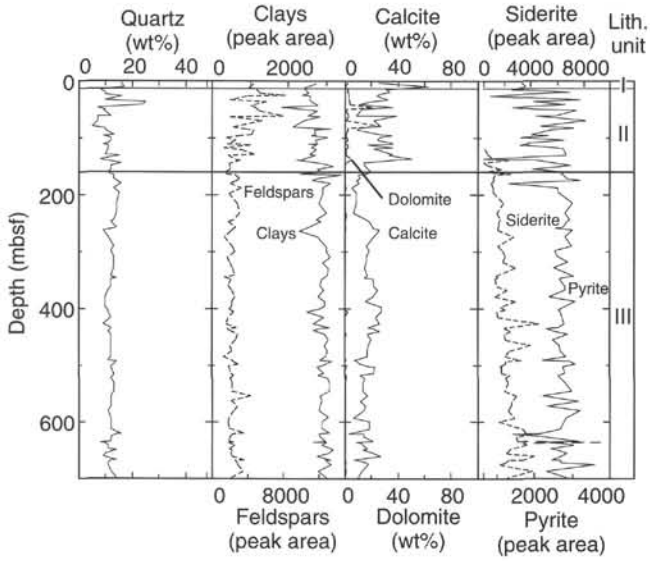


Figure 16. Downhole mineralogical variation of the major sediment constituents, based on XRD analysis.

suggests that the recovered core was only part of the original subsurface gas hydrate deposit that was broken into pieces during coring and recovery. One piece appeared to contain millimeter-scale clay laminations.

### *Hole 994D*

Hole 994D was spot-cored in an attempt to recover more gas hydrate from two horizons where strong indications of the presence of gas hydrate were observed in Hole 994C. Four cores were taken from 241.8 to 280.2 mbsf, and another four cores from 376.7 to 415.0 mbsf. The upper of these zones was where gas hydrate was sampled in Hole 994C. Both zones correspond with the strong negative chloride anomalies in Hole 994C (see "Inorganic Geochemistry" section, this chapter). Gas hydrate samples were observed in Sections 164-994D-4X-1 and 2 (~261 mbsf). Upon recovery, these sections were noted to be cold to the touch, and small white spots (<1 mm across) were visible through the core liner. The core section was immediately cut off and split horizontally. Intensively disturbed, soupy, dark greenish gray nannofossil-rich clay in Section 164-994D-4X-1 contained a few white specks (<1 mm in diameter) of gas hydrate, among which a single ~1 $cm^3$ piece of hydrate was collected and stored in liquid nitrogen and later decomposed for gas analysis (see description below).

Under close hand-lens inspection of the freshly split surface of sediment in Section 164-994D-4X-2, a tiny white speck <1 mm long was seen. However, the white speck disappeared within a few minutes. It is uncertain whether the white material was gas hydrate or water-ice formed by endothermic dissociation of gas hydrate, but the observation that the entire lengths of Sections 164-994D-4X-1 and 2 were anomalously cool more than 30 min after core recovery suggests that significant amounts of gas hydrate were once contained in these sections, probably as disseminated, minute accumulations.

Some differences between the behavior of the gas hydrate pieces that were recovered and the gas hydrate inferred from the proxy data are notable. While the larger pieces of hydrate were sampled and placed into various pressure vessels and the decomposition chamber, conspicuous changes in the characteristics of the hydrate were not observed. Specifically, none of the people involved in the handling of the gas hydrate pieces observed significant changes during the 5- to 10-min period while viewing the materials. In contrast, it is inferred that for most of the samples for which shipboard thermal anomalies, pore-water chloride anomalies, and downhole-logging data suggest the presence of gas hydrate before coring, the gas hydrate had decomposed before the cores reached the catwalk. We suggest that the rate of gas hydrate decomposition is a function of the surface area/volume ratio of the gas hydrate pieces. Thus, larger nodules persist much longer, but finely disseminated gas hydrate decomposes before it arrives on the catwalk of the ship.

## Composition of Gas Hydrate

A sample of gas hydrate from 164-994C-31X-7 was stored in liquid nitrogen for 20 hr before being placed in a hydrate dissociation chamber for volumetric analyses (Fig. 17). These results and those of the shipboard chemical analyses are given in Table 3. Methane usually forms structure I gas hydrate, which contains 8 mol of methane in small (12-sided polyhedral) and large (14-sided polyhedral) cages per 46 mol of water molecules, the formula being expressed as $CH_4 \times 5.75H_2O$. However, the addition of a small amount (>0.5 mol%) of propane would cause the hydrate structure to change to structure II (Sloan, 1990) in which small (12-sided polyhedral) cages are occupied by methane and a small number of large (16-sided polyhedral) cages by propane, the formula being roughly expressed as $CH_4 \times 8.5H_2O$. Hence, the volumetric ratio of gas to water of structure I

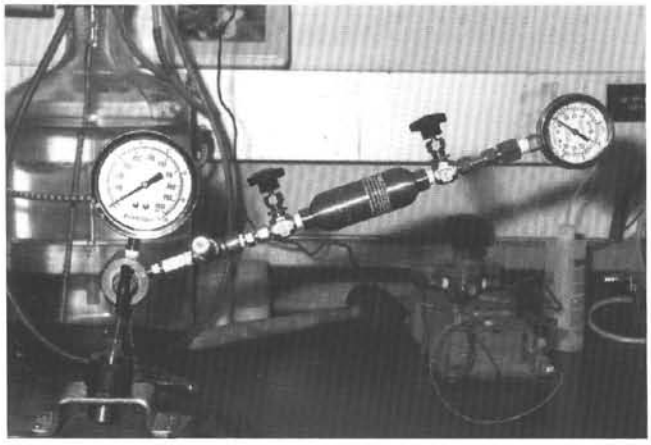

Figure 17. Gas hydrate dissociation chamber used to collect gas and water samples for shipboard analysis.

**Table 3. Results of gas and geochemical analyses of gas hydrate from Site 994.**

| Hole, core, section, interval (cm): | 994C-31X-7, 10–30 | 994D-4X-1, 5–6 |
|---|---|---|
| Equilibrium pressure at 21.3°C (psi): | 465 | NM |
| Total volume of gas ($cm^3$): | 617 (STP) | 2 (est.) |
| Gas composition: | | |
| $CH_4$ (%) | 98.78 | 12.69 |
| $C_2$ (ppmv) | 86 | 29 |
| $C_3$ (ppmv) | 2 | 0.3 |
| $CO_2$ (%) | 1.22 | 1.22 |
| Total volume of water ($cm^3$): | 4.0 | <0.5 (est.) |
| Volumetric ratio of $CH_4$ to $H_2O$: | 154 | 4–6 (est.) |
| Composition of water: | | NM |
| Chloride (mM/L) | 57.18 | |
| Sulfate (mM/L) | 1.9 | |
| $K^+$ (mM/L) | 2.4 | |
| $Mg^{2+}$ (mM/L) | 2.9 | |
| $Ca^{2+}$ (mM/L) | 2.4 | |

Notes: NM = not measured, STP = standard temperature and pressure, and est. = estimated. For Sample 164-994D-4X-1, 5–6 cm, a very small sample of gas hydrate was placed in a helium evacuated syringe and allowed to dissociate at 21°C. The estimated 2 $cm^3$ of evolved gas that was injected onto the gas chromatograph was not sufficient to fill the sample loops and resulted in volumetrically low gas concentrations. The balance of the gas was helium added during the measuring process and the gas in the sample loops before sample injection. Gas compositions are normalized to methane.

methane hydrate is ~216, whereas that of structure II methane hydrate with minor amounts of propane is ~146. Gas hydrate recovered from Hole 994C consists of methane (~99%) with minor to trace amounts of $CO_2$ (1.22%), ethane (86 ppmv), and propane (2 ppmv), and the volumetric ratio of methane to water is 154 (Table 3). The $Cl^-$ concentration (57.18 mM) of the water collected from the dissociation chamber indicates that the sample was a mixture of ~10% pore water, with 90% freshwater derived from gas hydrate dissociation, assuming that the pore-water $Cl^-$ concentration is the same as that of seawater. Taking this value (10% pore-water contamination), the gas:water volumetric ratio of the sample exceeds 170. This evidence indicates that Hole 994C hydrate is a structure I methane hydrate with a cage occupancy of ~80%, which is more than any previously reported cage-occupancy values from natural marine gas hydrate (Sloan, 1990). The $C_1/C_2$ ratio of gas from the hydrate sample is 11500, three times higher than that of the headspace gas of the host sediment (Section 164-994C-31X-5) (see "Organic Geochemistry" section, this chapter).

## Core Slab Temperature Measurements

In an attempt to detect small pieces of gas hydrate that were not exposed on split core surfaces, as well as to observe homogeneously disseminated gas hydrate, we conducted high-resolution temperature measurements of split surfaces (see "Explanatory Notes" chapter, this volume). Each measurement was made from top to bottom of 29 20-cm-long split cores from Hole 994C and six full-length sections of six cores (164-994D-1H, 2X, 3X, 5X, 7X, and 8X). Measurements were made within 10–15 min of the time that the core arrived on the rig floor. For the "normal" samples without any heat-absorbing sources, a slight increase (~1.5°C) of the average surface temperature was detected over the time the measurements were made. Also overprinted was a slight positive temperature gradient toward the core liners. These warming effects are clearly shown in the interval 164-994C-2H-6, 130–150 cm (13.0–13.2 mbsf), as a background-temperature pattern (Fig. 18), which demonstrates an upcore inclined trough in the temperature values.

Anomalously cold temperatures were observed in interval 164-994C-63X-6, 130–150 cm (517.9–518.1 mbsf), within nannofossil-rich diatom-rich clay of lithologic Unit III (Fig. 19). The average surface temperature was rather constant, ranging from 16.6° to 18.4°C, whereas a very cold spot with a temperature of 9°C was detected at 134 cm (4 cm below the top of the measured section), an anomaly of ~8°C. Shown as a sharp depression in the three-dimensional isothermal surface plot in Figure 19, this cold spot was a maximum of 3 cm wide because only two temperature probes detected the anomaly. Most of the other measurements showed rather uneven surface-temperature distributions, but negative temperature anomalies of more than 2°C were rare.

Distinct thermal anomalies also were observed on a split 1.5-m section (164-994D-8X-2; 397.3–398.65 mbsf) (Fig. 20). Contrary to the downcore temperature increases observed in "normal" samples as they warmed, the surface temperature of this section decreased downcore from 14.0°C at the top to less than 10°C in the lower half, then increased to 12.0°C at the bottom. Furthermore, several cold spots with a maximum temperature anomaly of 3.0°C were detected. The overall temperature anomaly pattern observed in this section strongly suggests that several spots in the lower part of the section had been cooled because of gas hydrate decomposition.

## Downhole Profile of Core Temperatures

In addition to the high-resolution temperature measurements, temperatures were measured with handheld temperature probes that were inserted into small holes drilled through the core liners on the catwalk. Temperatures also were measured using a probe that penetrated as much as 10 cm into the end of the core section through the end cap while the core was inside one of the gas-collection chambers (see "Explanatory Notes" chapter, this volume). A composite of all the available core temperature data that was collected after the cores were recovered is shown in Figure 21. This record shows that core temperatures were not uniform shortly after recovery nor did they increase with depth, reflecting different initial temperatures along a geothermal gradient. Instead, the measured core temperatures in the zone between 150 and 430 mbsf are generally lower and also show more scatter than the temperature of the cores that were collected from either above or below this zone. This anomaly is interpreted to result from the cooling that samples from this depth zone experienced during gas hydrate decomposition or through the adiabatic expansion of gas during core recovery.

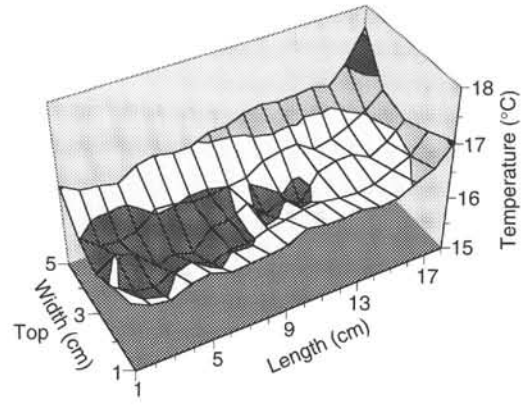


Figure 18. Three-dimensional isothermal surface plot of surface temperatures of a 20-cm-long split sample (164-994C-2H-6, 130–150 cm). No distinct temperature anomaly is observed.

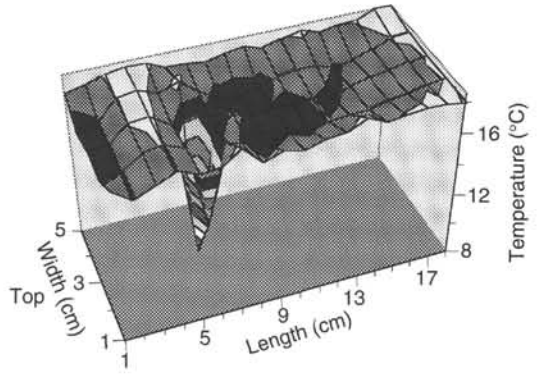


Figure 19. Three-dimensional isothermal surface plot of surface temperatures of a 20-cm-long split sample (164-994C-63X-6, 130–150 cm). A sharp depression between 5 and 6 cm from the top of the sample appears to suggest a dissociation of gas hydrate in sediments below, although no distinct features were observed on the surface.

### Gas Volume Measurements

The volume of gas that evolved from core sections while they warmed to room temperature was measured by placing whole-core sections in a sealed gas-collection chamber (see "Explanatory Notes" chapter, this volume). Table 4 gives the total measured volume of gas evolved from individual core sections. Also given are the calculated volumes of gas that were evolved per liter of interstitial water, based on measured water contents (see "Physical Properties" section, this chapter).

Measurable volumes of evolved gas (Fig. 22A) first occur in core sections that come from below the base of the sulfate reduction zone (>21 mbsf; see "Inorganic Geochemistry" section, this chapter). The general pattern is of increasing gas volume downhole throughout the APC cores. These are minimum values because the cores expanded considerably before they were received on the catwalk and were observed to release gas before they could be placed in the chambers. The volume of gas in these cores dropped abruptly when APC coring was terminated and XCB coring started (i.e., Section 164-994C-20X-1), suggesting that the lower gas volume below 144 mbsf is a result of the XCB coring process. However, the volume of gas and concentration of methane in the gas measured with gas-collection tubes in the upper 144 m is small in comparison with the amount of methane required to saturate water under in situ conditions (Fig. 22B). To have methane bubbles at the base of the gas hydrate stability zone, gas saturation needs to be achieved within the pore waters (Paull et al., 1994). Because this site is not associated with a BSR, pore-water methane saturation at the base of the gas hydrate stability field may not occur. Cores with anomolously low temperatures did not evolve more gas, suggesting that if cooling was from gas hydrate decomposition, it had occurred before the core sections were placed into the gas-collection chambers.

## BIOSTRATIGRAPHY

Four holes were drilled at this site, but nannofossils were studied only for Holes 994A and 994C.

### Hole 994A

Four APC cores were retrieved from this hole, and only core-catcher samples were examined for nannofossil biostratigraphy. Sample 164-994A-1H-CC contains dominant small *Gephyrocapsa* and abundant *Emiliania huxleyi*. This flora is assignable to the lower to middle portions of Zone CN15 (0.085–0.27 Ma). Samples 164-994A-2H-CC through 4H-CC contain common to abundant *Pseudoemiliania lacunosa* together with few to common *Gephyrocapsa oceanica*. This is the character of Subzone CN14a flora; therefore, the entire section correlatable to Subzone CN14b must be contained within Core 164-994A-2H.

### Hole 994C

Out of 84 cores drilled at this hole, 10 were PCS cores (drilling interval = ~1 m) with generally low recovery. For the remaining 17 APC and 57 XCB cores, all core-catcher samples and selected section samples were studied during the shipboard examination of biostratigraphy. A continuous sequence of zones and subzones was observed from the Holocene to the upper Miocene (Fig. 23). Nannofossils are abundant throughout the examined samples, except for three cores of early Pliocene age (Cores 164-994C-22X through 24X). Preservation of nannofossils is consistently good for the upper sequences down to Sample 164-994C-21X-CC (171.74 mbsf) and becomes generally moderate with some well-preserved intervals intercalated for the remainder of the hole. Dissolution of nannofossils is weak even in the moderately preserved nannofloras, and overgrowth was not observed until Sample 164-994C-63X-CC (520.0 mbsf), which is very close to the Pliocene/Miocene boundary (Fig. 23). Discoasters are slightly overgrown in 60% of Miocene samples examined, but moderate to advanced overgrowth was not observed even for discoasters. Placoliths, meanwhile, show no sign of recrystallization in any of the samples that were examined. This lack of overgrowth, despite the continuous presence of methane in the middle to lower sections of Hole 994C, is inconsistent with the notion that carbonate cementation is induced by methane. Ascidian spicules are present in many samples, but they are generally rare and are more scarce than at the three previous sites on the Cape Fear Diapir. Site 994 is located farther seaward than the Cape Fear Diapir sites, and the lack of spicules indicates that significant downflow of upper continental shelf sediment did not occur. Although not severe, reworking of nannofossils is persistent, and Cretaceous and Eocene forms constitute the majority of obviously reworked specimens.

#### *Pleistocene*

The upper 14 cores of this hole contain Pleistocene nannofloras. The mudline sample, Sample 164-994C-1H-1, 0–1 cm, contains dominant *E. huxleyi*, indicating Holocene or the latest Pleistocene age (<0.085 Ma). Sample 164-994C-1H-3, 16–17 cm, and 1H-CC

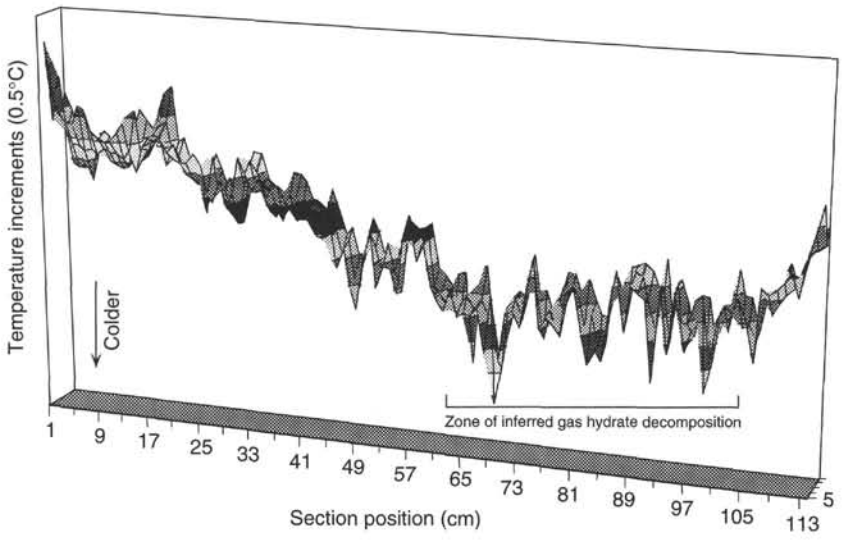


Figure 20. Three-dimensional isothermal surface plot of surface temperatures from a 1.5-m split-core section (interval 164-994D-8X-2, 0–135 cm). Downcore decreasing temperatures and several cold spots in the lower part of the section strongly suggest that significant amounts of gas hydrate dissociated in this sample. Each shaded increment corresponds to a 0.5°C temperature change.

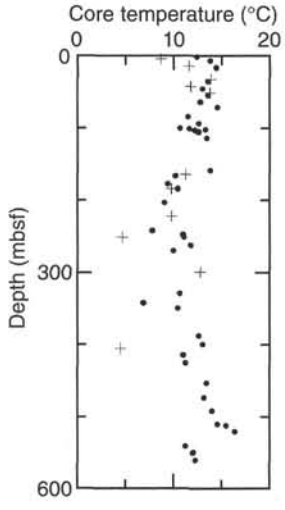


Figure 21. Core temperatures measured on catwalk shortly after core recovery at Site 994. Plus signs = temperatures measured at catwalk. Solid circles = initial temperature when the core sections were placed into the gas-collection chambers.

also contains abundant *E. huxleyi,* and the entire Core 164-994C-1H was assigned to Zone CN15. Samples 164-994C-2H-1, 4–5 cm, through 2H-CC yield abundant small to medium forms of genera *Gephyrocapsa* and *Reticulofenestra. E. huxleyi* does not occur, and except for the rare reworked specimens, *P. lacunosa* also was absent. This sample, therefore, belongs to Subzone CN14b.

Samples 164-994C-3H-1, 4–5 cm, through 6H-1, 4–5 cm, were assigned to lower upper Pleistocene Subzone CN14a. *P. lacunosa* is common in all samples examined, and the highest occurrence of *Reticulofenestra asanoi* was observed in Sample 164-994C-5H-CC, implying that the datum event of 0.88 Ma (last occurrence [LO] of this taxon) lies within the lower sections of Core 164-994C-5H.

Samples 164-994C-6H-2, 94–95 cm, through 15H-2, 45–47 cm, were assigned to Subzone CN13b. Small *Gephyrocapsa* dominate the flora, and medium to large *Gephyrocapsa* are very rare or absent between Samples 164-994C-6H-2, 94–95 cm, and 994C-7H-CC. This is a clear indication of the "small *Gephyrocapsa* Zone" of Gartner (1977) corresponding to the uppermost portion of Subzone CN13b. The first occurrence (FO) of *R. asanoi* (1.02–1.17 Ma) is likely to occur within Core 164-994C-7H. The LOs of *Helicosphaera sellii* (1.26–1.44 Ma) and *Calcidiscus macintyrei* (1.60–1.64 Ma) are likely to be in Cores 164-994C-8H and 11H, respectively. *Gephyrocapsa caribbeanica* was missing in many section samples of Core 164-994C-13H and 14H, and its FO (1.8 Ma) was tentatively identified in Section 164-994C-15H-2. Reworked specimens of *Discoaster brouweri* are frequent in Cores 164-994C-13H through 15H, and the LO of this taxon (2.0 Ma) was tentatively identified between Samples 164-994C-15H-7, 45–47 cm, and 16H-2, 77–79 cm. Thus, all the important Quaternary datum events were observed in a sequential order, and the Pliocene/Pleistocene boundary lies either within Core 164-994C-14H or 15H.

### *Pliocene*

Because no medium-size *Gephyrocapsa* or discoasters occur, Samples 164-994C-15H-3, 45–47 cm, through 15H-6, 75–76 cm, belong to Subzone CN13a of the uppermost Pliocene (1.8–2.0 Ma). Small *Gephyrocapsa, Reticulofenestra minuta,* and *P. lacunosa* are the major components of the nannoflora, and reworked Pliocene discoasters are rare. Common to abundant occurrences of *Umbilicosphaera* sp. A in downcore samples seems to terminate within this subzone, and this may be another useful datum event to identify the Pliocene/Pleistocene boundary.

The LOs of *D. brouweri* and *Reticulofenestra pseudoumbilica* occur in Samples 164-994C-16H-2, 77–79 cm, and 34X-CC, respectively. The interval between these samples was assigned to Zone CN12. As a result of reworking of zonal marker discoasters, however, precise identification of subzone boundaries was difficult for this late Pliocene zone.

The LO of *Discoaster pentaradiatus* (CN12d/CN12c subzonal boundary, 2.4 Ma) was tentatively placed at Sample 164-994C-17H-3, 77–79 cm. *Coccolithus pelagicus* is generally common downward from the lower part of Subzone CN12d.

Rare specimens of *Discoaster surculus* observed in Samples 164-994C-17H-CC and 19H-2, 77–79 cm, were considered as reworked, and the taxon's LO (CN12c/CN12b subzonal boundary, 2.5 Ma) was tentatively placed between the latter sample and Sample 164-994C-19H-4, 77–79 cm. *P. lacunosa, R. minuta, Reticulofenestra minutula, Reticulofenestra producta,* and *Umbilicosphaera* sp. A are the major species observed in Subzone CN12b. The highest occurrence of *Discoaster tamalis* was observed in Sample 164-994C-21X-1, 77–79 cm, and this sample marks the CN12b/CN12a subzonal boundary (2.8 Ma).

**Table 4. Volumes of gas collected from whole-core sections (≤1.5 m in length) warmed to room temperature inside gas-collection chambers.**

| Core, section | Depth (mbsf) | Insertion temperature (C°) | Gas evolved (mL) | Gas/pore water ratio (mL/L) |
|---|---|---|---|---|
| 164-994C- | | | | |
| 1H-2 | 1.50 | 12.4 | 0 | 0 |
| 2H-3 | 7.40 | 13.8 | 0 | 0 |
| 3H-3 | 16.90 | 14.4 | 0 | 0 |
| 5H-3 | 35.90 | 13.6 | 225 | 71 |
| 6H-3 | 45.40 | 13.0 | 835 | 221 |
| 7H-3 | 54.90 | 13.6 | 565 | 152 |
| 8H-3 | 64.40 | 12.8 | 1140 | 313 |
| 10H-1 | 71.90 | 14.6 | 310 | 84 |
| 11H-3 | 84.40 | 11.5 | 680 | 230 |
| 12H-3 | 93.90 | 12.6 | 270 | 84 |
| 13H-2 | 101.90 | 13.3 | 840 | 238 |
| 14H-4 | 114.40 | 13.5 | 610 | 188 |
| 15H-2 | 120.90 | — | 950 | 349 |
| 16H-3 | 131.90 | — | 510 | 189 |
| 17H-4 | 142.90 | — | 1340 | 454 |
| 20X-1 | 158.40 | 13.8 | 0 | 0 |
| 21X-2 | 166.30 | 10.2 | 0 | 0 |
| 22X-2 | 177.40 | 9.4 | 440 | 128 |
| 23X-1 | 184.00 | 10.5 | 13 | 3 |
| 25X-1 | 203.30 | 9.1 | 170 | 57 |
| 30X-5 | 247.62 | 11.0 | 190 | 68 |
| 31X-4 | 251.80 | 11.1 | 0 | 0 |
| 40X-2 | 329.80 | 10.7 | 240 | 95 |
| 41X-4 | 342.41 | 6.9 | 150 | 57 |
| 42X-2 | 349.10 | 10.5 | 140 | 57 |
| 47X-2 | 387.50 | 12.6 | 150 | 62 |
| 49X-4 | 400.10 | 13.0 | 100 | 33 |
| 50X-1 | 414.80 | 11.0 | 155 | 65 |
| 52X-1 | 424.50 | 11.2 | 77 | 30 |
| 56X-1 | 453.40 | 13.4 | 0 | 0 |
| 58X-2 | 474.10 | 13.2 | 140 | 54 |
| 61X-3 | 492.90 | 14.0 | 130 | 49 |
| 62X-3 | 511.40 | 14.6 | 100 | 38 |
| 63X-3 | 513.10 | 15.5 | 230 | 89 |
| 64X-1 | 520.70 | 16.4 | 0 | 0 |
| 67X-1 | 541.10 | 11.3 | 150 | 59 |
| 68X-2 | 550.30 | 12.0 | 160 | 62 |
| 69X-2 | 560.80 | 12.3 | 140 | 45 |
| 71X-1 | 571.10 | — | 150 | 56 |
| 164-994D- | | | | |
| 1H-1 | 100.00 | 10.7 | 390 | 119 |
| 1H-2 | 101.50 | 11.7 | 325 | 99 |
| 1H-3 | 103.00 | 12.2 | 860 | 263 |
| 1H-4 | 104.50 | 12.5 | 1345 | 412 |
| 1H-5 | 106.00 | 12.6 | 1570 | 481 |
| 2X-2 | 242.90 | 7.8 | 0 | 0 |
| 3X-3 | 262.50 | 11.8 | 0 | 0 |
| 4X-3 | 270.60 | 10.0 | 0 | 0 |

Note: — = not available.

Small *Gephyrocapsa,* which is abundant through the Quaternary and uppermost Pliocene floras, is rare or even absent between Samples 164-994C-17H-CC and 29X-CC, corresponding to Subzone CN12c to the upper part of Subzone CN12a. But it again becomes an important component of nannoflora in the lower part of Subzone CN12a. The temporary disappearance of small *Gephyrocapsa* is likely to reflect an environmental change that occurred here during a portion of the late Pliocene (~2.2–3.2 Ma). *Sphenolithus abies* is very rare in Samples 164-994C-32X-CC and 33X-CC, and these specimens are likely to be reworked. This species is common in Sample 164-994C-34X-CC, but no *R. pseudoumbilica* was found. Therefore, the age of this sample is likely to be from 3.62 Ma (LO of *S. abies*) to 3.65 Ma (LO of *R. pseudoumbilica*).

Sample 164-994C-38X-1, 91–93 cm, still contains rare *D. tamalis,* and the interval between the top of Core 164-994C-35X and this sample was assigned to lower Pliocene Subzone CN11b. Subzone CN11a was identified between Samples 164-994C-38X-CC and 46X-4, 77–79 cm. The FO of small *Gephyrocapsa* was recognized at the upper part of this subzone in Sample 164-994C-40X-CC. As was observed at Site 991, the FO of typical *P. lacunosa* occurs at the middle part of this subzone, and the FO of *P.* cf. *lacunosa* was recognized at the lower part of this subzone.

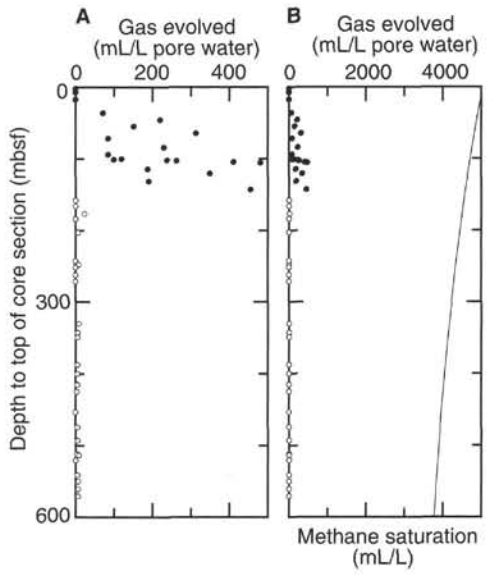


Figure 22. **A.** Plot of the volume of gas that evolved per liter of pore water from 1.5-m whole-core sections as they warmed to room temperature. The total amount of gas was corrected by the total volume and porosity of core. Solid circles = measurements on APC cores. Open circles = XCB core measurements. **B.** The same data plotted on a scale to include the methane saturation curve (solid line). The gas saturation curve is based on Duan et al. (1992), assuming a 2800-m water depth, 3.5°C bottom-water temperature, 45°C/km thermal gradient, and pore water with 35% NaCl.

Samples 164-994C-46X-CC through 72X-1, 77–79 cm, belong to Zone CN10 of the lower Pliocene to the uppermost Miocene (4.4–5.6 Ma). Because *Discoaster asymmetricus* is rare in these samples, the boundary of Subzones CN10d/10c was not determinable. The LO of *Ceratolithus acutus* is in Sample 164-994C-56X-1, 77–79 cm. Samples 164-994C-46X-CC through 55X-CC, therefore, were assigned to Subzones CN10c–10d. Although rare *Amaurolithus delicatus* and *Amaurolithus tricorniculatus* are consistently present throughout these samples, *Ceratolithus rugosus* is rare, and it is sporadic in the lower samples. The FO of a taxon referable to *Ceratolithus cristatus* was recognized in Sample 164-994C-52X-CC.

Samples 164-994C-56X-1, 77–79 cm, through 64X-CC were tentatively assigned to Subzone CN10b, and the Pliocene/Miocene boundary lies within the lower part of this interval. Small to large forms of the genus *Reticulofenestra* are abundant, and *D. brouweri, D. pentaradiatus, D. surculus, S. abies,* and *Umbilicosphaera* sp. A are common members of the flora. The occurrence of rare *C. acutus,* whose FO defines the lower boundary of Subzone CN10b, is consistent, whereas the related taxon, *Ceratolithus armatus,* occurs only in the upper part of this subzone. Rare specimens of *Ceratolithus atlanticus,* which show a large morphologic diversity, also were observed in some samples of this subzone.

### *Miocene*

Samples 164-994C-65X-6, 77–79 cm, through 72X-1, 77–79 cm, contain nannoflora of uppermost Miocene Subzone CN10a. Except the absences of *C. acutus* and *C. atlanticus,* the floral assemblage is similar to that of the lowermost Pliocene Subzone CN10b. The rare *Discoaster berggrenii* in Sample 164-994C-69X-CC was considered reworked.

Samples 164-994C-72X-2, 77–79 cm, through 84X-CC are assignable to upper upper Miocene Subzone CN9b. The major components of the nannoflora in this subzone are the small to medium forms of the genus *Reticulofenestra,* such as *R. minuta, R. minutula,* and *R.*

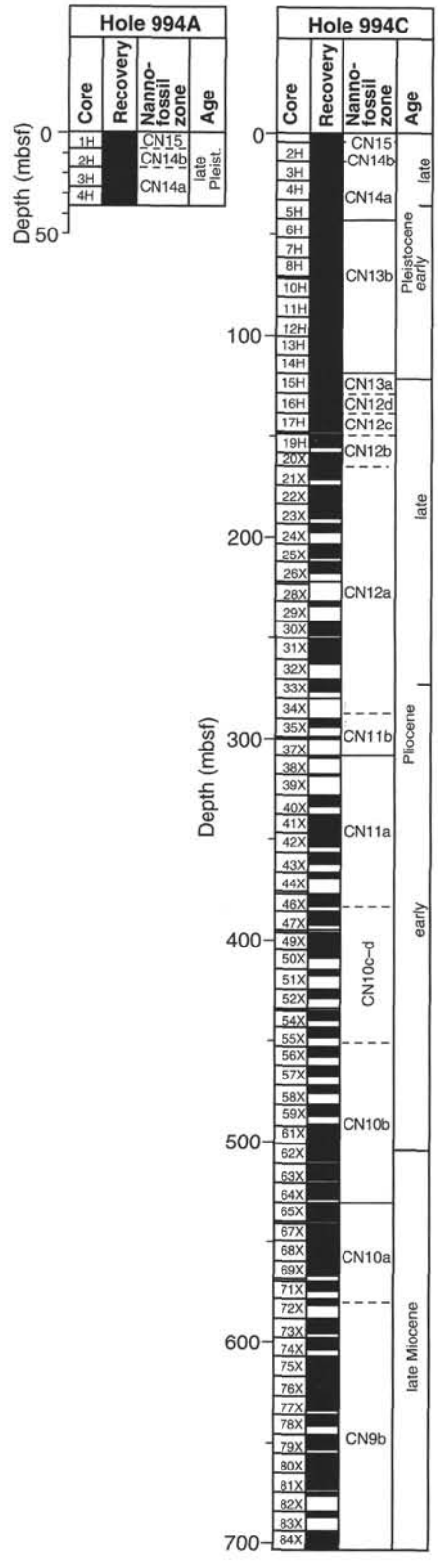


Figure 23. Biostratigraphic summaries of Holes 994A and 994C. Dashed lines indicate that zonal boundaries are ambiguous because of reworking.

*producta.* As explained in the "Explanatory Notes" chapter (this volume), the continuous occurrence of dominant to abundant *Florisphaera profunda* has not been mentioned in the previous descriptions of floral assemblages in this report. This species, which recently has proven to be the most important nannofossil taxon for late Cenozoic paleoceanography (Molfino and McIntyre, 1990), becomes a subordinate member of the nannoflora below the upper part of this Subzone CN9b.

Rare *Amaurolithus amplificus* occurs in the lowest two cores of this hole, and the LO of this taxon (5.9 Ma) was placed between Samples 164-994C-82X-CC and 83X-1, 85–87 cm. Assuming the same sedimentation rate for the upper Miocene sequence, the age of the oldest sediment recovered from this hole is ~6.0 Ma.

### Sedimentation Rate

Sedimentation rates calculated from the calcareous nannofossil datum events increase with depth (Fig. 24). Rates in the Quaternary sequence for the upper (0–0.46 Ma), middle (0.46–0.98 Ma), and lower (0.98–1.8 Ma) sections are ~30, 55, and 98 m/m.y., respectively (Fig. 24). The average rate for the entire Quaternary sequence is 68 m/m.y, and it increases to 89 m/m.y. for the upper Pliocene sequence. The rate further increases to 140 m/m.y. for the lower Pliocene and to 303 m/m.y. for the uppermost Miocene sequence.

These rates are too high for pelagic sedimentation, especially for the Pliocene and Miocene sequences. Because ascidian spicules and reworked nannofossils are not present in great abundances in the studied materials, direct downslope redeposition caused by gravity flows seems unlikely to be the major source of the reworked material at this site. Thus, a significant proportion of the sediments recovered at this site are likely to be drifted sediments, supporting the popular notion of thick contourite deposition at the Blake Ridge. (e.g., Tucholke and Carpenter, 1977). As was the case at the Cape Fear Diapir sites (991, 992, and 993), many of the reworked nannofossils observed at this site are Cretaceous and Eocene forms that may originally have been derived from either land sections or exposed submarine canyons. The occurrence of reworked Neogene specimens is fairly common; however, because of the small age difference between the original deposition and reworking, precise estimation of their numbers was difficult. Therefore, most of the materials that accumulated in the sediment drift must be unconsolidated surface sediments of the time.

## PALEOMAGNETISM

### Magnetostratigraphy

Paleomagnetic measurements at Hole 994C were conducted with the pass-through cryogenic magnetometer, following the procedures outlined in the "Explanatory Notes" chapter (this volume). We measured the NRM on the cores that were taken with the APC (Cores 164–994C-1H through 19H) and demagnetized them under alternating fields of 10 and 20 mT to determine the direction of the stable component of remanence. To supplement magnetostratigraphic results from the routine demagnetization, discrete samples were AF demagnetized in 5-mT steps up to 50 mT. Routine measurement of remanence was abandoned for the subsequent XCB cores (164-994C-20X through 84X) because they were highly biscuited and obviously disturbed during drilling.

The intensity of NRM fluctuates between 50 and 0.1 mA/m through the sedimentary section (Fig. 25). The NRM declination is very scattered, and the inclination is generally steeply downward (near +90°), suggesting that a core-barrel overprint acquired during coring is present.

After demagnetization at 20 mT, intensity is more constant downhole than the NRM intensity and is generally less than 1 mA/m below

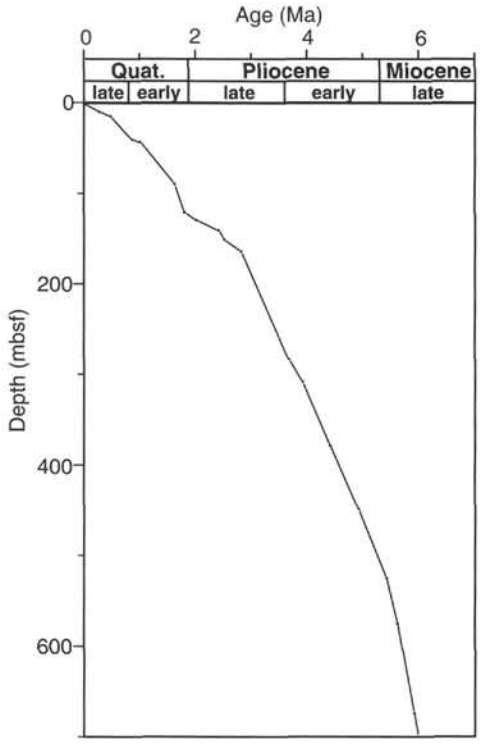


Figure 24. Age-depth relationships of biostratigraphic markers of calcareous nannofossils from Hole 994C.

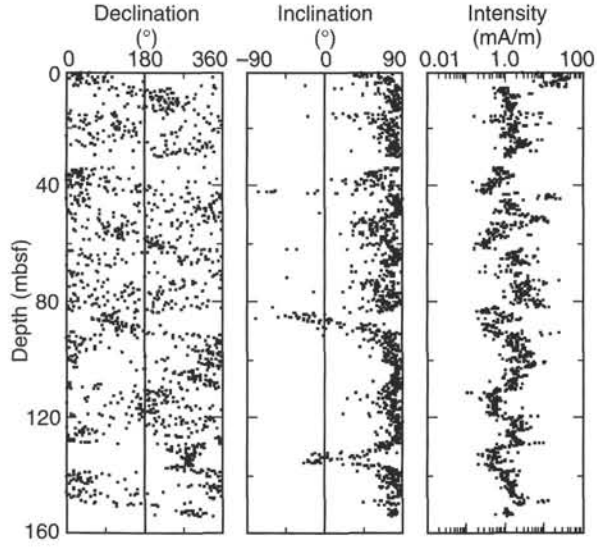


Figure 25. NRM declination (referred to arbitrary core coordinates), inclination, and intensity for Hole 994C.

5 mbsf (Fig. 26). The inclination after 20-mT demagnetization shifts toward lower inclinations and shows obvious negative and positive intervals through the section. The decrease in intensity and inclination suggests that the demagnetization has removed the core-barrel overprint. The declination after 20-mT demagnetization is less scattered than that of NRM. Before Tensor tool orientation, demagnetized declinations are generally grouped around 180° relative to the x-axis direction defined by the double-line fiducial mark in the center

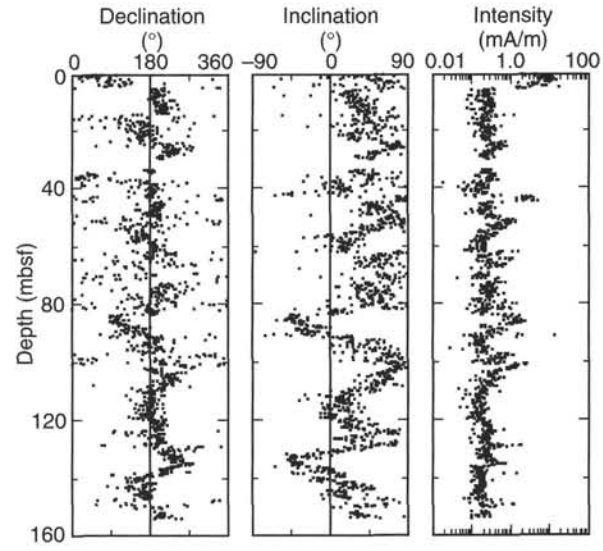


Figure 26. Declination (core coordinates), inclination, and intensity after 20-mT demagnetization for Hole 994C.

of the core liner on the archive half of the cores. Orientation of declination relative to geographic north (see "Explanatory Notes" chapter, this volume) produces a distinct break at the top of each core (Fig. 27); this is most readily explained by an inability of the y-axis sensor in the cryogenic magnetometer to respond to the very weak remanence surviving after demagnetization (see "Explanatory Notes" chapter, this volume).

Progressive AF demagnetization of discrete samples shows that the steeply inclined drilling-induced components can be removed from most samples, leaving a stable component of remanence at 5–10 mT (Fig. 27). After the removal of the overprint, typical progressive demagnetization up to 50 mT follows a linear demagnetization path converging on the origin of the Zijderveld plot (Fig. 28A). This indicates a single, stable component that is interpreted as the primary remanence, from which magnetic polarity can be determined. Some samples display three components of remanence (Fig. 28B). In order of increasing AF stability these are (1) a steep, positive inclination component that is demagnetized at 5 mT, (2) a lower inclination, normally polarized component demagnetized at 15 mT, and (3) the most stable component, which converges on the origin of the Zijderveld plot. We interpret the three components as a drilling-induced overprint, a viscous remanent magnetization (VRM), and the primary remanence, respectively. The stepwise demagnetization of the discrete samples suggests that a magnetostratigraphy can be constructed for the APC-cored interval in Hole 994C.

Rock-magnetic analysis (see below) indicates authigenic growth of magnetite between the seafloor and ~2 mbsf, followed by reduction of magnetite and authigenesis of magnetic sulfides. It is likely that the primary remanence identified in the demagnetization studies is carried by SD or pseudo-single-domain (PSD) magnetite, although SD and/or PSD magnetic sulfides also may contribute. Both SD magnetite and magnetic sulfides in this sequence are dominantly authigenic. Bioturbation, which is observed throughout the sequence at Site 994, is likely to have disrupted the original detrital remanence (DRM). Consequently, although DRM may make some contribution, the primary remanence at Site 994 is probably postdepositional (PDRM). The lag between sediment deposition and acquisition of PDRM is not clear, but the PDRM probably is dominated by magnetite produced between 0 and 2 mbsf. Consequently, the magnetostratigraphy at Site 994 may be offset downhole from the depositional history (i.e., nannofossil biostratigraphy) by as much as 2 m.

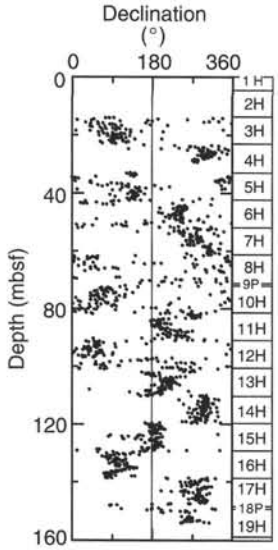


Figure 27. Declination data oriented to geographic coordinates with the Tensor tool after 20-mT demagnetization for Hole 994C.

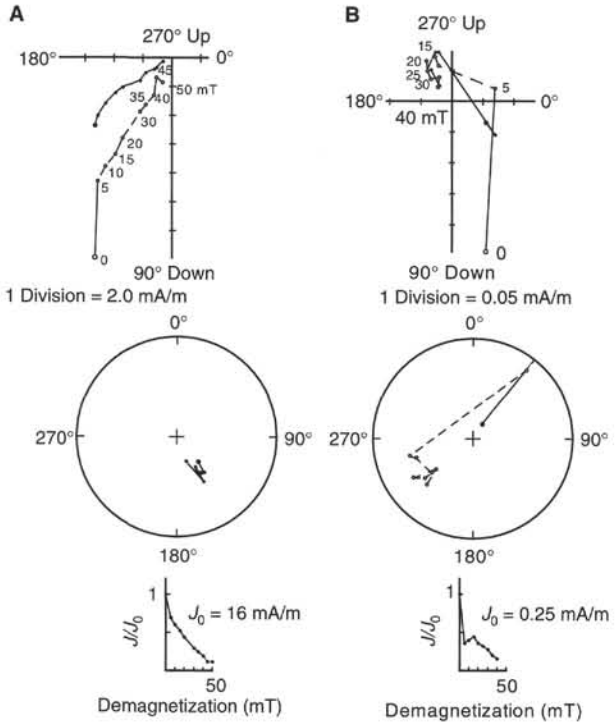


Figure 28. Representative Zijderveld, stereo, and intensity demagnetization plots for (**A**) Sample 164-994C-1H-2, 39–41 cm (1.90 mbsf), and (**B**) Sample 164-994C-15H-6, 42–44 cm (126.66 mbsf). Demagnetization increases in 5-mT steps to 40 mT for (A) and 50 mT for (B). Zijderveld plot: Solid circles = projection on the horizontal plane; open circles = projection on the vertical plane. Stereo plot: solid circles = the lower hemisphere. Declination is with respect to core coordinates.

Polarity determined from the analysis of discrete samples does not correlate well with the inclination data obtained from the 20-mT demagnetization of continuous core sections in the cryogenic magnetometer (Fig. 29). Apparently, the cryogenic magnetometer record does not reveal the primary magnetization. The difference between the discrete sample and pass-through data may result from increased

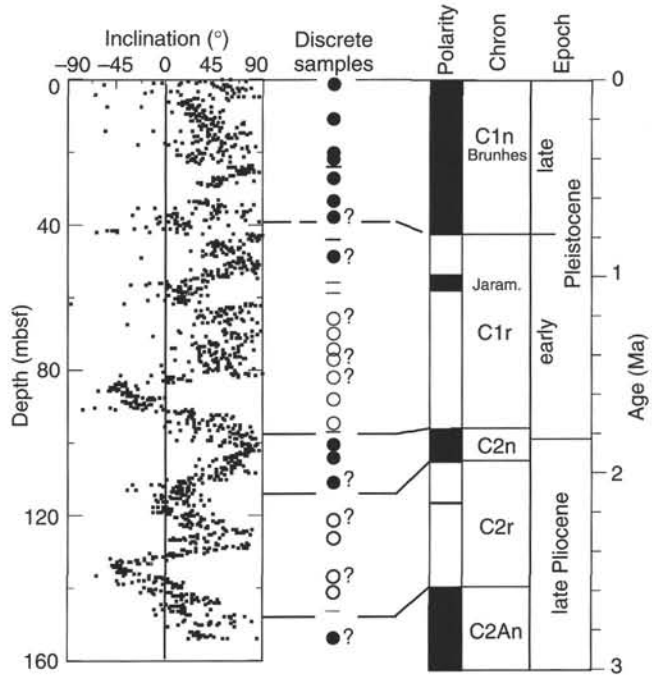


Figure 29. Inclination after 20-mT demagnetization with pass-through magnetometer and polarity data determined from Zijderveld diagram analysis of discrete samples from Hole 994C, correlated to the revised geomagnetic polarity time scale of Cande and Kent (1995). Solid circles and zones = normal polarity, open circles and zones = reverse polarity, question marks = less certain polarity, and bars = unsuccessful analyses.

overprinting in the outer part of cores (Collot, Greene, Stokking, et al., 1992) in combination with the insensitivity of the cryogenic y-axis to the low magnetizations that were observed during Leg 164 (see "Explanatory Notes" chapter, this volume).

Analysis of the discrete samples indicates that the sedimentary section from 0 to 155 mbsf includes three normal-polarity zones and two reverse-polarity zones. With the constraint of the nannofossil datums (see "Biostratigraphy" section, this chapter) these polarity zones are correlated to the polarity chrons C1n (Brunhes), C1r, C2n, C2r, and C2An, in descending order, although there is an uncertainty in the depth of each polarity boundary as a result of the difficulty in establishing the polarity of many of the discrete samples (Fig. 29). The polarity boundary between C1n and C1r (Brunhes/Matuyama boundary) is poorly constrained, falling somewhere between 27 and 65 mbsf, and the position of the Jaramillo normal chron (C1r.1n) could not be determined. According to the nannofossil biostratigraphy (see "Biostratigraphy" section, this chapter), the C1n/C1r boundary should lie at ~38 mbsf.

## Magnetic Susceptibility

Measurement of magnetic susceptibility of whole-core sections from Hole 994C using the MST produced a noisy record, with anomalously high values at the top of some cores resulting from rust contamination and frequent intervals of low susceptibility corresponding to gas voids and the removal of whole-round samples (Fig. 30). Despite this, a systematic downhole trend is apparent. An initial increase in susceptibility from the mudline to ~2 mbsf is seen in all three holes at Site 994, presumably reflecting bacterial authigenesis of magnetite. Maximum susceptibilities are reached at ~2–3 mbsf (~60–70 × $10^{-5}$ in Holes 994A and 994B, and ~40 × $10^{-5}$ in Hole 994C; all susceptibilities are in volume-normalized SI terms). Susceptibility declines sharply at 3–4 mbsf, probably as a result of bacterially mediated reduction of magnetite to iron sulfides. Susceptibility declines to

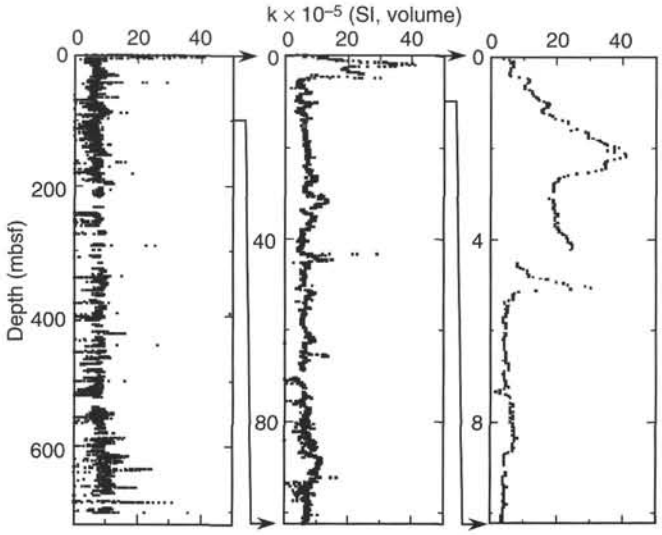


Figure 30. Susceptibility determined on the MST in Hole 994C.

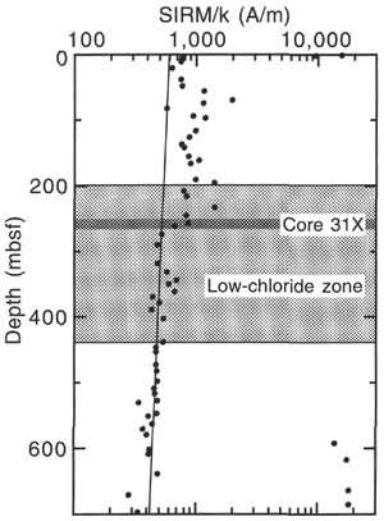


Figure 31. SIRM/k vs. sub-bottom depth, Hole 994C. A log-linear line along the background trend is indicated. Shaded interval = the approximate limits of the zone of low chlorinity in interstitial-water samples. Darker shaded interval = the extent of Core 164-994C-31X in which hydrate was recovered on the catwalk.

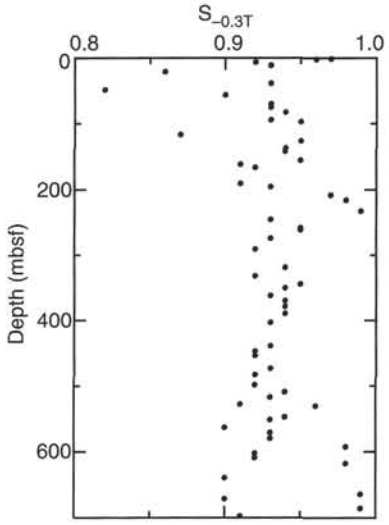


Figure 32. $S_{-0.3T}$ vs. sub-bottom depth, Hole 994C.

~6–8 × $10^{-5}$ by 5–6 mbsf. Superimposed on this diagenetic trend is a series of smaller spikes (e.g., at ~0.5 and 1 mbsf), recognizable in all three holes, that presumably represents depositional laminae enriched in magnetite.

Susceptibility continues downhole with a background value of ~6–8 × $10^{-5}$, with cyclic variations between 4 and 12 × $10^{-5}$ on a 1- to 5-m scale reflecting alternations in magnetic mineralogy. Variations in susceptibility on this scale could be driven by variations in detrital magnetite input (representing climate-driven changes in sediment provenance) or in the supply of organic material to the sediments. Changes in organic supply appear in the susceptibility record through shifts in the extent of magnetite authigenesis and reduction.

Below ~560 mbsf (within the upper Miocene part of the sequence) susceptibility increases to ~10–12 × $10^{-5}$. This increase in susceptibility may reflect a decrease in the degree of magnetite reduction through this interval.

## Rock Magnetism

### *Isothermal Remanence*

SIRM at 1.2 T, normalized for susceptibility (i.e., the SIRM/k ratio), displays a roughly log-linear decrease downhole (Fig. 31), which is best defined below ~260 mbsf. The SIRM/k ratio increases with an increase in the proportion of the total magnetic mineralogy composed of greigite or SD magnetite (Thompson and Oldfield, 1986; Roberts, 1994; Reynolds et al., 1994), and so is effectively an index of the extent of reduction of iron below the initial zone of authigenic magnetite growth. The log-linear decrease in SIRM/k implies a continued reduction of iron oxides and sulfides throughout the sequence at a rate that decreases with depth.

Superimposed on the log-linear trend of SIRM/k with sub-bottom depth is a series of anomalies. High SIRM/k values (15.7 and 9.5 $kAm^{-1}$) occur in the first 2 m of Core 164-994C-1H, just above the interval of enhanced susceptibility near the seafloor; these values would suggest a magnetic assemblage dominated by magnetite with an average grain size of 5–10 µm (i.e., in the PSD range). Perhaps surprisingly, the $S_{-0.3T}$ ratio, which is an index of the proportion of the magnetic mineralogy that has coercivities higher than the saturation coercivity of magnetite (see "Explanatory Notes" chapter, this volume), is only 0.96–0.97 in this interval. This $S_{-0.3T}$ ratio is only slightly higher than the general background value of ~0.9–0.95 found throughout the interval cored in Hole 994C (Fig. 32). It is not clear whether the relatively low $S_{-0.3T}$ ratio in this interval results from the presence of substantial proportions of detrital hematite within the first few meters or whether magnetic sulfide generation has already commenced within this zone.

A second set of anomalously high SIRM/k values occur below 600 mbsf within the zone of enhanced susceptibility in the upper Miocene sequence. Samples with SIRM/k >9 kA/m (i.e., similar values to those seen above the zone of magnetite reduction in the first core) alternate with samples that lie on the log-linear trend, with SIRM/k of 0.2–0.3 kA/m. The $S_{-0.3T}$ ratio for the high SIRM/k samples below 600 mbsf is also high (≥0.98), suggesting that magnetite dominates the magnetic mineralogy, and this is confirmed by pARM and demagnetization of anhysteretic remanence (dARM) studies (see below).

Variable, moderately high values of SIRM/k (Fig. 31), lying above the general log-linear trend, occur in an almost continuous sequence between 20 and 260 mbsf. Intriguingly, the lower limit of this

interval corresponds to the base of Core 164-994C-31X, the only core from Hole 994C in which gas hydrate was visibly recovered. This sub-bottom depth also represents an important geochemical datum (see "Inorganic Geochemistry" section, this chapter). Interstitial-water chemistry defines a linear trend of chloride-concentration, declining downhole from the seafloor to ~260 mbsf. A second linear chloride concentration trend is defined by interstitial-water analyses between 700 and 460 mbsf, and it can be extended uphole as a background through the interval in which hydrate dissociation during core recovery produces anomalously low chloride concentrations. The two linear trends intercept at 260 mbsf.

Similar interstitial-water profiles were reported for the pair of Sites 889 and 890 during Leg 146 (Shipboard Scientific Party, 1994). At Site 889, a sub-bottom depth of ~130–150 mbsf marked the intersection of a chloride-concentration trend that declined downhole from the seafloor with a constant low-chloride interval. This depth also marked the lower limit of an interval of anomalously high SIRM/k values at Sites 889 and 890 (Housen and Musgrave, 1996).

In Hole 994C, other intervals of scattered SIRM/k above the log-linear trend occur between ~325 and 365 mbsf, and possibly between 400 and 440 mbsf, within the zone from ~200 to 440 mbsf defined by low interstitial-water chlorinity. The sizes of the three positive SIRM/k anomalies within the low-chloride zone decline with depth. Below the base of the low-chloride zone, SIRM/k remains almost constant to ~530 mbsf.

### *Anhysteretic Remanence*

Acquisition of pARM and dARM indicates a moderately broad, slightly left-skewed coercivity spectrum in Samples 164-994C-1H-1, 89–91 cm (0.90 mbsf), and 1H-2, 39–41 cm (1.90 mbsf) (Fig. 33A), as would be typical of a mixture of grain sizes of a mineral with coercivity in the magnetite range. The peak coercivity is 25–35 mT, suggesting the dominant magnetite grain size is in the MD to PSD range, typical of detrital magnetites. Microbial magnetite usually has been reported in the single-domain size range. Hence, it is likely that detrital magnetite comprises a significant proportion of the magnetic mineralogy in the first meter below seafloor.

Samples immediately below the near-seafloor zone of high susceptibility (e.g., Sample 164-994C-2H-2, 39–41 cm, at 6.30 mbsf; Fig. 33B) have broad coercivity spectra, without a clearly defined central peak; this coercivity distribution could be explained either as the result of a mix of SD magnetite and one or more other magnetic minerals, or as a very wide range of magnetite grain sizes.

Samples 164-994C-3H-2, 39–41 cm (15.80 mbsf), 5H-4, 39–41 cm (37.80 mbsf), and 10H-2, 89–91 cm (74.30 mbsf), have strongly left-skewed coercivity spectra with a single peak at 15 mT (Fig. 33C). These samples appear to be dominated by a single low-coercivity magnetic phase, suggesting that almost all remaining SD magnetite has been lost in this interval.

Sample 164-994C-19H-6, 92–94 cm (155.07 mbsf), displays a broader coercivity spectrum, with a wide peak shifted upward toward 25 mT (Fig. 33D). Broadening of the stability spectra appears to continue with depth through the interval of high SIRM/k above 260 mbsf. For example, in Sample 164-30X-3, 29–31 cm (245.0 mbsf), pARM and dARM intervals are high from 5 to 50 mT, and there appear to be two distinct peaks in coercivity, one at 15–20 mT and the other at 35–40 mT (Fig. 33E). The coercivity trend through the interval of high SIRM/k from ~50 to 260 mbsf is most easily explained by a downhole increase in the proportion of a distinct, higher coercivity phase or grain-size population.

Downhole broadening and splitting of the coercivity spectrum peak reverses below 260 mbsf, where SIRM/k drops toward the background log-linear trend. Samples 164-994C-33X-2, 34–36 cm (272.24 mbsf), and 40X-2, 102–104 cm (330.83 mbsf), show a more narrow, single-coercivity peak centered on 25–35 mT (Fig. 33F).

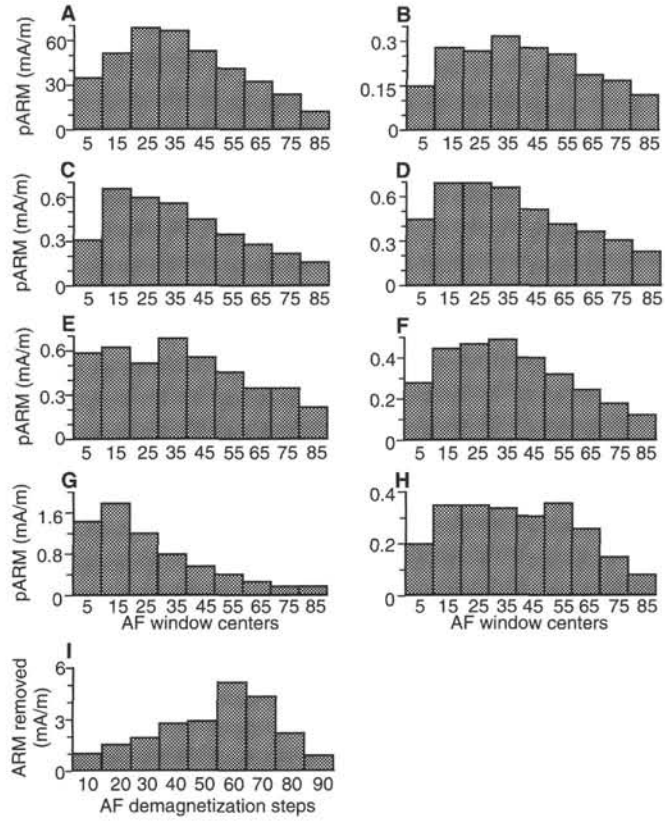


Figure 33. Coercivity plots of samples from Hole 994C, illustrated either by pARM in 10-mT-wide windows (A–H), or by dARM acquired at 90 mT (I). **A.** Sample 164-994C-1H-1, 89–91 cm (0.90 mbsf). **B.** Sample 164-994C-2H-2, 39–41 cm (6.30 mbsf). **C.** Sample 164-3H-2, 39–41 cm (15.80 mbsf). **D.** Sample 164-994C-19H-6, 92–94 cm (155.07 mbsf). **E.** Sample 164-994C-30X-3, 29–31 cm (245.0 mbsf). **F.** Sample 164-994C-33X-2, 34–36 cm (272.24 mbsf). **G.** Sample 164-994C-41X-5, 93–95 cm (344.21 mbsf). **H.** Sample 164-994C-61X-4, 59–61 cm (498.00 mbsf). **I.** Sample 164-994C-80X-7, 97–99 cm (664.39 mbsf).

SIRM/k increases again between 325 and 365 mbsf; coercivity in Sample 164-994C-41X-5, 93–95 cm (344.21 mbsf), becomes strongly left skewed, with a large increase in the 15-mT coercivity window (Fig. 33G).

Below 400 mbsf, coercivity spectra broaden again, indicating an increased proportion of a population of magnetic grains with high coercivities (e.g., Sample 164-994C-49X-5, 89–91 cm, at 402.22 mbsf, and Sample 164-994C-61X-4, 59–61 cm, at 498.0 mbsf; Fig. 33H).

Sample 164-994C-80X-7, 97–99 cm (664.39 mbsf), one of the set of samples below 590 mbsf that gave an anomalously high SIRM/k value, has a simple coercivity spectrum with a peak at 60 mT, suggesting that SD magnetite has survived in these samples (Fig. 33I).

## Summary of Rock-Magnetic Analysis

Magnetic susceptibility, SIRM/k, and anhysteretic coercivity define a relatively simple background pattern of (1) initial detrital magnetite deposition, (2) authigenic (presumably microbial) generation of SD magnetite and magnetic sulfides within the first few meters below seafloor, and (3) further reduction to remove most magnetite (and almost all magnetite in the fine-grained, SD range) below ~4 mbsf, followed by an apparently highly uniform continued reduction of the magnetic iron mineralogy toward pyrite downhole. Superim-

posed on this are two sets of anomalies. Anomalously high SIRM/k values between 20 and 260 mbsf correlate with an interval of downhole-decreasing interstitial-water chloride concentration in a manner closely analogous to Sites 889 and 890 from Leg 146. High SIRM/k in the interval of downhole-decreasing chlorinity at Sites 889 and 890 was associated with the presence of substantial proportions of greigite, demonstrated through a variety of shore-based rock-magnetic analyses (Housen and Musgrave, 1996). A zone of constant low chloride concentration at the base of the interval of decreasing chloride at Sites 889 and 890 has been interpreted as resulting from in situ melting of hydrate from a "fossil gas hydrate zone" at the end of the last glacial (Shipboard Scientific Party, 1994). Previous rock-magnetic studies indicated an abrupt change in coercivity properties at the predicted depth for the base of the "fossil hydrate zone" at Site 889 (Housen and Musgrave, 1996). Shore-based rock-magnetic studies may clarify whether comparison with Sites 889 and 890 is well founded.

Alternating high and low SIRM/k values below 590 mbsf are superimposed on generally higher susceptibility in the upper Miocene sequence below 560 mbsf. We suggest that the higher susceptibility interval represents a zone of decreased magnetite reduction in which further periodic decreases in reduction pushed the iron diagenesis sequence back to the point where substantial quantities of SD magnetite survived burial.

## DOWNHOLE TOOLS AND SAMPLING

### Pressure Core Sampler

The PCS was deployed 10 times during coring at Hole 994C (Table 5). The PCS retained >75% of hydrostatic pressure upon retrieval in nine of these runs and recovered >15 cm of sediment in seven of these runs (Table 5). Although no PCS run recovered a complete 1-m core of sediment, PCS operations at Site 994 must be considered a success given previous difficulties in recovering cores with this tool (e.g., Davis, Mottl, Fisher, et al., 1992; Behrmann, Lewis, Musgrave, et al., 1992; Westbrook, Carson, Musgrave, et al., 1994).

There may be several reasons for the success of the PCS at Site 994. Application of new cutting shoes, a different ball-valve assembly, and/or high pump pressures (to 2000 psi) on the rig (see "Downhole Tools and Sampling" section, "Explanatory Notes" chapter, this volume) are likely explanations. Operation in firm, homogenous clay also may have contributed to the success.

Observed pressures for Cores 164-994C-45P, 48P, 60P, and 66P were unexpected because they exceed hydrostatic pressure (Table 5). Possible explanations for these high pressures include an abnormally pressurized formation, dissociation of gas hydrate within the PCS during and after coring, or warming of gases inside the PCS after core recovery.

#### *Sample Collection*

Cores recovered by the PCS were placed in a "mounting sleeve" upon arrival at the PCS sampling station. Ice was then placed in the sleeve and around the PCS for all cores from Site 994. The purpose of the ice bath was to keep pressures low in the event of substantial hydrate recovery and to maintain similar temperature conditions for all PCS experiments at Site 994 (see discussion below). A potential and untested ramification of cooling the PCS is that gas hydrate may actually form inside the PCS if sufficient dissolved $CH_4$ is available.

Gas sample collection from the PCS cores at Site 994 is best termed experimental. The PCS was connected to one of several PCS manifolds (PCS-Ms) (see "Downhole Tools and Sampling" section, "Explanatory Notes" chapter, this volume). After a certain length of time (5–1100 min), a valve on the PCS was opened briefly to allow a small volume of gas into the PCS-M. Repeated opening and closing of the valve on the PCS released pressure from the PCS and gas

**Table 5. Description of PCS deployment at Site 994.**

| Core | Depth (mbsf) | Pressure: Expected (psig) | Pressure: Observed (psig) | Hydrostatic (%) | Cutting shoe | Core recovered (cm) | Manifold design |
|---|---|---|---|---|---|---|---|
| 164-994C- | | | | | | | |
| 9P | 70.9 | 4210 | 1500 | 36 | Auger | 23 | PCS-M2 |
| 18P | 147.9 | 4323 | 3260 | 75 | Auger | 0 | PCS-M2 |
| 27P | 222.5 | 4433 | 3657 | 83 | Auger | 7 | PCS-M2 |
| 36P | 299.4 | 4545 | 4436 | 98 | Push-in | 23 | PCS-M3A |
| 45P | 376.5 | 4658 | 4985 | 107 | Push-in | 0 | PCS-M3A |
| 48P | 395.6 | 4686 | 4940 | 105 | Auger | 15 | PCS-M3A |
| 53P | 434.1 | 4743 | 5030 | 106 | Auger | 15 | PCS-M3A |
| 60P | 491.9 | 4828 | 5166 | 107 | Auger | 28 | PCS-M3A |
| 66P | 540.1 | 4898 | 5206 | 106 | Auger | 22 | PCS-M3A |
| 70P | 568.9 | 4941 | 4266 | 86 | Auger | 20 | PCS-M3B |

Notes: The water depth at Hole 994C is 2799 m. Expected pressure is the hydrostatic pressure, assuming a pressure gradient of 1.467 psi/m. Observed pressure is that first recorded at the PCS sampling station.

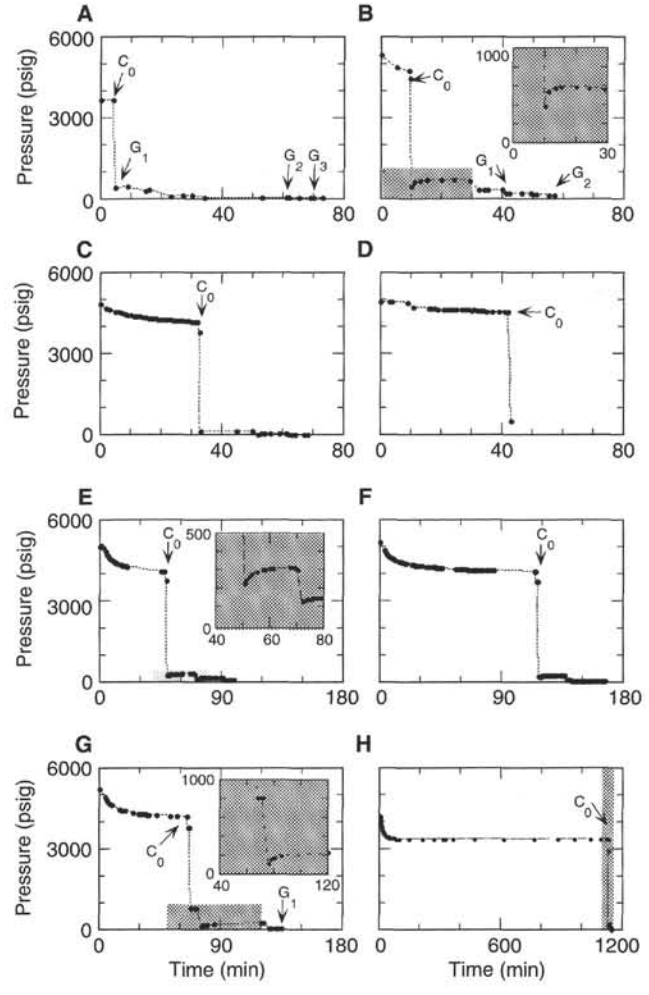


Figure 34. Time-pressure plots (after Kvenvolden et al., 1983) that show the pressure in the PCS with respect to time. **A.** Core 164-994C-27P (4434–35 psi). **B.** Core 164-994C-36P (4436–120 psi). **C.** Core 164-994C-45P (4688–14 psi). **D.** Core 164-994C-48P (4688–500 psi). **E.** Core 164-994C-53P (5030–102 psi). **F.** Core 164-994C-60P (5166–29 psi). **G.** Core 164-994C-66P (5206–41 psi). **H.** Core 164-994C-70P (4266–14 psi). The initial, near-exponential drop in pressure reflects cooling of the PCS on ice. The first pronounced drop in pressure ($C_0$) represents the initial opening of the PCS into the manifold. Note the increase in pressure (insets in B, E, and G) that occurs after pressure in the PCS is dropped below 200 to 800 psi. G = the time at which gas samples were collected.

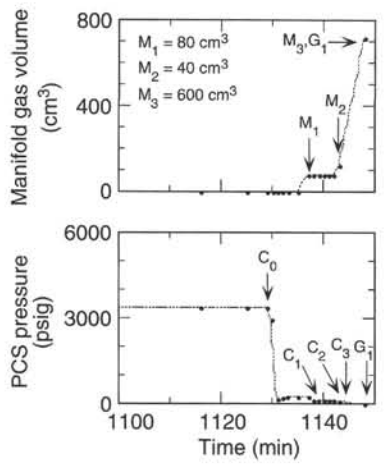


Figure 35. Time-pressure-volume plot of Core 164-994C-70P. The volume represents the cumulative gas volume collected in the manifold bubbling chamber (see "Downhole Tools and Sampling" section, "Explanatory Notes" chapter, this volume). C = time of manifold opening, M = time of manifold gas volume change, and G = time of gas sampling. Note that the volume increments increase with decreasing pressure (see text for discussion).

into the PCS-M. Samples of gas (or liquid) at any PCS pressure could be taken via the PCS-M, although few samples actually were collected because of a variety of technical problems (discussed in "Downhole Tools and Sampling" section, "Explanatory Notes" chapter, this volume). Manifold collection procedures for individual PCS cores are shown in PCS time-pressure plots (Fig. 34A–H, after Kvenvolden et al., 1983) or PCS time-pressure-volume plots (Fig. 35). The PCS eventually was depressurized and opened. Interstitial-water samples were taken from whole-round intervals of sediment when possible.

The time it took the PCS tool to reach 0°C from its initial temperature (>0°C) after being placed in an ice bath can be determined from the time-pressure plots. Initial pressures in the PCS drop rapidly when ice is placed around the tool, and they continue to decrease along a roughly exponential curve with respect to time. The pressure eventually remains constant when the temperature within the PCS equilibrates with ambient temperature (in the case of ice, 0°C). Core 164-994C-70P was kept in ice for 1130 min before releasing the first gas into the PCS-M. The time in which pressure-temperature conditions in Core 164-994C-70P equilibrated with the ice bath was ~210 min (Fig. 34H). Only Core 164-994C-70P was allowed to sit in ice for this length of time. However, it also is clear that pressure-temperature conditions approach near equilibrium with an ice bath after ~45–60 minutes. The initial opening of Cores 164-994C-53P, 60P, and 66P occurred after 45 min in an ice bath (Fig. 34E–G).

### *Gas Release Experiments and Preliminary Analyses*

The first PCS core (164-994C-9P) contained 10–23 cm of sediment slurry at only 36% of hydrostatic pressure; the second PCS core (164-994C-18P) contained only water. Waters and gases from these cores were not investigated because the chemistry laboratory was overwhelmed with other samples and because the cores were less than ideal.

Gas and water analyses for the remaining eight PCS cores taken from Site 994 are presented in Tables 6 and 7, respectively. Gas compositions are mixtures of air ($N_2$ and $O_2$), $CO_2$, $CH_4$, and trace amounts of other hydrocarbons. There also are relatively high amounts of two unidentified gases in most PCS gas samples (not presented in Table 6). The retention times for these two unidentified gases on the GC column are between that of *n*-pentane and *n*-hexane for the first gas and between *n*-hexane and *n*-heptane for the second gas. The retention times did not match those of any gases in the shipboard standards that contain alkanes, alkenes, and cyclics up to $C_7$ or of headspace gas from the grease used in the PCS. The origin and composition of these two gases are unknown at present.

All waters obtained from the PCS (via the PCS-M or core squeezing) contain appreciable amounts of seawater (as evident by the nonzero $SO_4^{2-}$ concentrations; Table 7). The sample obtained through the PCS-M is mostly seawater and largely reflects borehole water that was collected by the PCS. The PCS-M sample also had an oily film. Interstitial waters from the PCS cores have higher $SO_4^{2-}$ concentrations than adjacent APC and XCB cores (see "Inorganic Geochemistry" section, this chapter). This result may be related to the size of PCS cores and/or the time of PCS sampling. Cores from the PCS are narrower (~4.2 cm) than those from the APC or XCB, and they typically remained surrounded by seawater (borehole water within the PCS) for more than 2 hr before being removed from the PCS.

The $Cl^-$ concentration (443 mM) and salinity (30‰) of interstitial water from Core 164-994C-66P (541.1 mbsf) is of interest. This water is fresher than seawater and pore water from surrounding XCB cores (especially when corrected for seawater contamination) but is from a depth (541 mbsf) significantly lower than the $Cl^-$ anomalies observed in interstitial waters from APC and XCB cores (see "Inorganic Geochemistry" section, this chapter).

Time-pressure plots for eight PCS cores (Fig. 34A–H) have three features in common: (1) an initial time interval over which pressure in the PCS decreases in a roughly exponential pattern; (2) a pronounced drop in pressure when the PCS is first opened to the manifold; and (3) a late time interval over which pressure fluctuates with time. The initial exponential decrease in pressure is on the order of 800 to 1000 psi, and it is caused by the decrease in temperature in the ice bath.

The significant drop in pressure upon opening the PCS to the manifold likely represents the release of a small volume of air that exists in the PCS (perhaps as headspace). Two observations support this interpretation. First, the pronounced drop is associated with only a small volume of gas (80 $cm^3$ for Core 164-994C-70P; Fig. 34). Second, initial gas samples have significantly more air (Table 6) than subsequent samples from Cores 164-994C-27P and 36P. Even though seawater flows through the PCS on its descent to the seafloor (i.e., the ball valve is open), a potential source of air in the manifold and gas samples would be air trapped in certain mandrels of the PCS during deployment.

Most of the gas released from the PCS is $CH_4$ (Table 6), and most of this $CH_4$ appears to be released at low pressure. The $CH_4$ content of gas increased with respect to sampling time, and the volume of gas released from Core 164-994-70P increased with decreasing pressure (Table 6; Figs. 34A, B and 35).

At pressures below some threshold value, a drop in PCS pressure (via venting into the manifold) is followed by an increase in pressure (e.g., Fig. 34). The threshold pressure is between 800 and 200 psi for Core 164-994C-66P (Fig. 34G). This observation, in conjunction with the discussion above, strongly suggests that significant quantities of $CH_4$ are released after the $CH_4$ hydrate equilibrium pressure (at 0°C) is surpassed. Kvenvolden et al. (1983) made a similar observation with the pressure core barrel—a predecessor to the PCS—and attributed this phenomenon to the dissociation of gas hydrate. An alternative explanation is that $CH_4$ is degassing from the fluid in the core barrel (i.e., the threshold pressure is the saturation point of $CH_4$ in fluid at 0°C).

## Water Sampling Tools

The Fisseler tool was deployed twice at Site 994 (Table 8). Neither deployment was successful.

The WSTP was deployed seven times at Site 994 (Table 8). Three of the WSTP runs were sampled for gas analyses (Table 6). An unexpected observation was that the overflow water for WSTP Sample

**Table 6. Gas composition of PCS and WSTP samples, Hole 994C.**

| Core | Depth (mbsf) | $C_1$ (ppmv) | $C_2$ (ppmv) | $C_3$ (ppmv) | $i$-$C_4$ (ppmv) | $n$-$C_4$ (ppmv) | $i$-$C_5$ (ppmv) | $n$-$C_5$ (ppmv) | $i$-$C_6$ (ppmv) | $n$-$C_6$ (ppmv) | $N_2$ (vol%) | $O_2$ (vol%) | $CO_2$ (ppmv) | Total (vol%) | $C_1/C_2$ |
|---|---|---|---|---|---|---|---|---|---|---|---|---|---|---|---|
| PCS | | | | | | | | | | | | | | | |
| 164-994C- | | | | | | | | | | | | | | | |
| 27P ($G_1$) | 222.5 | 104 | | | | | | | | | 76 | 19 | 2,090 | 95.2 | |
| 27P ($G_2$) | 222.5 | 231,900 | 21 | 6 | 2 | 0.7 | 2.6 | | 1.5 | 0.5 | 60 | 13 | 1,780 | 96.4 | 11,043 |
| 27P ($G_3$) | 222.5 | 393,800 | 40 | 11 | 3.5 | 1.4 | 0.4 | | 1.2 | 0.4 | 51 | 9 | 4,800 | 99.9 | 9,845 |
| 36P ($G_1$) | 299.4 | 128,200 | 15 | | | | | | | | 64 | 16 | 6,480 | 93.5 | 8,547 |
| 36P ($G_2$) | 299.4 | 225,000 | | 5 | 1.2 | 0.3 | | | 0.4 | | | | | | |
| 66P | 540.1 | 228,400 | 109 | 10 | 1 | | | | | | 56 | 14 | 5,550 | 93.4 | 2,095 |
| 70P | 568.9 | 789,800 | 474 | 26 | 2.6 | 2 | 1.9 | 0.7 | 0.3 | 0.2 | 11 | 2 | 5,320 | 92.6 | 1,666 |
| WSTP | | | | | | | | | | | | | | | |
| 164-994C- | | | | | | | | | | | | | | | |
| 39X, coil | 318.6 | 950 | | | | | | | | | 76 | 19 | 1,050 | 95.2 | |
| 39X, overflow | 318.6 | 259,200 | 32 | 1 | 0.5 | | | | | | 58 | 18 | 5,740 | 102.5 | 8,100 |
| 39X, overflow | 318.6 | 187,800 | 23 | 4 | 0.5 | 0.3 | | | | | 60 | 18 | 5,530 | 97.3 | 8,165 |
| 42X, coil | 347.6 | 5,500 | | | | | | | | | 76 | 19 | 1,170 | 95.7 | |

Notes: PCS = pressure core sampler, and WSTP = water-sampling temperature probe. G = gas sample. Gas samples taken from the PCS are not replicates because they are sampled at different times during manifold operation (see Fig. 34). However, two replicate gas samples supposedly were taken from the overflow water of WSTP Sample 164-994C-39X. It is unclear why these samples have different absolute gas concentrations. The total amount of gas likely is not 100% because concentrations of $N_2$ and $O_2$ are poorly calibrated. There also are significant quantities of an unidentified gas in the PCS samples.

**Table 7. Chemistry of water samples from the PCS and WSTP, surface seawater, and drilling mud filtrate at Site 994.**

| Core, interval (cm) | Depth (mbsf) | Sample | pH (g/kg) | Alk (mM) | Sal (mM) | $Cl^-$ (mM) | $Mg^{2+}$ (mM) | $Ca^{2+}$ (mM) | $SO_4^{2-}$ (mM) | $NH_4^+$ (mM) | $K^+$ (mM) | $Sr^{2+}$ (μM) |
|---|---|---|---|---|---|---|---|---|---|---|---|---|
| PCS | | | | | | | | | | | | |
| 164-994C- | | | | | | | | | | | | |
| 36P, 0–23 | 300.4 | IW | 7.5 | 59.36 | 33.0 | 503 | 25.9 | 3.5 | 11.07 | 14.5 | 13.3 | 90.0 |
| 53P, 8–12 | 435.1 | IW | 7.62 | 91.56 | 34.0 | 507 | 15.9 | 3.3 | 3.65 | 23.4 | 13.6 | |
| 66P, 0–20 | 541.1 | IW | | | 30.0 | 443 | 14.9 | 3.8 | 4.9 | 20.4 | 11.9 | 100.0 |
| 66P | 541.1 | Manifold | | | | 540 | 45.1 | 9.8 | 24.1 | | 11.8 | |
| 70P, 0–20 | 569.9 | IW | 7.8 | 42.3 | 33.8 | 537 | 23.8 | 4.8 | 12.7 | 23.9 | 14.2 | 103.0 |
| WSTP | | | | | | | | | | | | |
| 164-994C- | | | | | | | | | | | | |
| 25X | 203.3 | | | | | 603 | 54.2 | 10.4 | 28.96 | 3.2 | 12.3 | 98.0 |
| 39X | 318.6 | | | | | 594 | 55.1 | 11.2 | 29.11 | 2.1 | 10.7 | 98.0 |
| 42X | 347.6 | | | | | 578 | 53.8 | 10.6 | 28.99 | 2.2 | 10.8 | 94.0 |
| 47X | 386.1 | | | | | 584 | 55.2 | 10.9 | 29.77 | 4.8 | 10.5 | 89.0 |
| Surface seawater | | | | | | 581 | 55.8 | 11.2 | 29.77 | 0.0 | 10.5 | 95.0 |
| Drilling mud filtrate | | | | | | 551 | 54.9 | 7.8 | 27.8 | 0.0 | 10.1 | 89.0 |

Notes: Alk = alkalinity, and Sal = salinity. PCS = pressure core sampler, IW = interstitial water (see "Explanatory Notes" chapter, this volume), and WSTP = water-sampling temperature probe. Depths for samples from the PCS are placed at the top of the core and not from the interval.

**Table 8. Description of FWS and WSTP deployment at Site 994.**

| Core | Tool | Depth (mbsf) | Water type (mL) | |
|---|---|---|---|---|
| | | | Coil | Overflow |
| 164-994C- | | | | |
| 7H | FWS | 51.9 | NR | NR |
| 13H | FWS | 100.4 | NR | NR |
| 25X | WSTP | 203.3 | 25 | 1100 |
| 30X | WSTP | 241.7 | Mostly gas | NR |
| 35X | WSTP | 299.4 | 25 | 1100 |
| 39X | WSTP | 318.6 | NR | NR |
| 42X | WSTP | 347.6 | 10 | 1150 |
| 47X | WSTP | 386.1 | 10 | 350 |
| 55X | WSTP | 443.7 | 10 | 400 |

Notes: Tool abbreviations: FWS = Fisseler Water Sampler, and WSTP = water-sampling temperature probe. NR = not recorded.

164-994C-39X contained substantial quantities (18%–25%) of $CH_4$, whereas the coil sample contained air (>97%).

Four of the WSTP runs were sampled for chemical analyses. These analyses are presented in Table 7. Spectrophotometric color measurements (see "Downhole Tools and Sampling" section, "Explanatory Notes" chapter, this volume) showed that samples from the other three WSTP runs did not contain any formation water.

One objective at Site 994 was to determine the $Cl^-$ content of in situ interstitial water (see "Inorganic Geochemistry" section, this chapter). On the basis of $SO_4^{2-}$ concentrations (Table 7), the four WSTP samples that were analyzed contain between 97.3% and 100% seawater. The concentrations of $Na^+$, $K^+$, $Ca^{2+}$, $Mg^{2+}$, and $Sr^{2+}$ (Table 7) also are consistent with high proportions of seawater. The $Cl^-$ concentrations of the in situ water in the WSTP samples can be estimated by correcting for the amount of seawater contamination. The small proportion of in situ interstitial water actually collected precludes this approach because of large uncertainties in the corrected $Cl^-$ values (relative standard deviations greater than 50%). However, two of the four WSTP samples (164-994C-25X and 39X) have $Cl^-$ concentrations (603 and 594 mM) that are significantly higher than that of surface seawater (582 mM). Because it is impossible to explain these $Cl^-$ values via the mixing of seawater and formation water of low salinity, the possibility of high salinity formation waters warrants consideration.

## ORGANIC GEOCHEMISTRY

The shipboard organic geochemistry program at Site 994 included analyses of volatile hydrocarbons; determinations of inorganic carbon, total nitrogen, total carbon, and total sulfur; Rock-Eval pyroly-

sis; and gas hydrate decomposition analyses (for a description of methods see "Explanatory Notes" chapter, this volume).

## Volatile Hydrocarbons

### *Headspace Gas*

Concentrations of methane ($C_1$), ethane ($C_2$), and propane ($C_3$) were measured from every core using the standard ODP headspace-sampling technique. The $C_1$ headspace concentration increases rapidly from 11 to 29,000 ppmv between 9 and 46 mbsf. Below this depth, $C_1$ concentrations decrease steadily to values of ~3000 ppm down to a depth of 310 mbsf. The headspace concentration of $C_1$ remains constant at greater depths. $C_2$ headspace concentrations are low (1–2 ppm) in the upper 400 mbsf and increase to values of 40 ppmv between 400 and 700 mbsf (Table 9; Fig. 36).

Thirty-six samples of headspace gas also were taken from the uppermost four cores at Hole 994A and analyzed for $C_1$ content (Table 10). The objective of this high-resolution gas sampling was to delineate the base of the $SO_4^{2-}$ reduction zone to within a meter for shore-based investigations (see "Inorganic Geochemistry" section, this chapter).

### *Free-Gas Samples*

Free gases were removed from within the core liner by attaching a 60-mL syringe to the valve-block assembly. Concentrations of $C_1$, $C_2$, higher molecular weight hydrocarbons, and carbon dioxide ($CO_2$) were measured using the Natural Gas Analyzer. Air contamination occurs during the sampling of free gas. Hence, the measurements of hydrocarbons were more varied than those measured by the headspace method, and only gas ratios can be directly interpreted.

There is a decrease in the $C_1/C_2$ ratio with depth, from 30,000 to 800 (Fig. 36), whereas the concentrations of the higher molecular weight hydrocarbon gases remain nearly constant. In the depth range from 32.80 to 163.70 mbsf, the $C_1/CO_2$ ratios are ~50; below that depth, they decrease to ~10. The $C_1/CO_2$ ratio has a distinct maximum of 142 at a depth of 272.69 mbsf (Table 11; Fig. 37).

### *Gas-Collection Chamber Samples*

Compositions of gas released from the gas-collection chambers (GCC) are presented in Tables 12 and 13. The $C_1$ concentrations measured in GCC gases are ~1 order of magnitude higher than the corresponding $C_1$ headspace concentrations (Table 12). However, the trends with depth are similar. The $C_2$ concentrations increase with depth from 16 ppm at 45.10 mbsf to a maximum value of 109 ppm at 618.50 mbsf, and the $C_1/C_2$ ratio decreases from 19,050 at the top of the hole to 890 at the bottom (Fig. 36). Hydrocarbons $C_3$ through $C_6$ are present, but no depth trend is observed.

Experiments were carried out to measure the compositions of gases released from 1.5-m whole-round core sections as a function of the degassing time. Five sections from Core 164-994D-1H (100.0–107.5 mbsf) were placed into the GCC, and gases were collected at various times, from 2 min to ~4 hr. Results are given in Table 13. Concentrations of $C_1$ and $CO_2$ increase with the degassing time. This likely is a function of purging original air from the chamber. No systematic change of the $C_1/C_2$ ratio was observed.

## Organic Carbon, Total Nitrogen, and Total Sulfur

The TOC content of the sediment from 0 to 160 mbsf averages 0.7% (Table 14; Fig. 38) with a maximum value of 1.84% at 612 mbsf. Average TOC content of sediment from 160 to 699 mbsf is 1.4%. Nitrogen contents correlate well with TOC contents. Some samples from the uppermost parts of Hole 994C were not included in this analysis because their carbon and nitrogen contents are within the

**Table 9. Composition of headspace gas in sediment from Hole 994C.**

| Core, section | Depth (mbsf) | $C_1$ (ppmv) | $C_2$ (ppmv) | $C_3$ (ppmv) | $C_1/C_2$ | $C_1/C_{2+}$ | $C_1$ (μL/kg wet sediment) |
|---|---|---|---|---|---|---|---|
| 164-994C- | | | | | | | |
| 2H-4 | 8.90 | 11 | | | | | 40 |
| 3H-4 | 18.40 | 1,950 | 0.5 | | 3,900 | | 6,050 |
| 4H-7 | 32.00 | 26,000 | 2.0 | | 13,000 | 13,000 | 68,700 |
| 5H-2 | 35.85 | 13,900 | 0.9 | | 15,400 | | 52,700 |
| 6H-3 | 46.55 | 29,200 | 2.0 | | 14,600 | | 86,100 |
| 7H-5 | 57.90 | 23,400 | 1.0 | | 23,400 | 23,400 | 78,500 |
| 8H-4 | 65.90 | 25,800 | 2.0 | | 12,900 | 12,900 | 90,700 |
| 10H-5 | 77.90 | 14,500 | 1.2 | 1.0 | 12,100 | 6,600 | 42,000 |
| 11H-4 | 85.90 | 17,400 | 1.0 | | 17,400 | 17,400 | 38,900 |
| 12H-4 | 95.40 | 12,000 | | | | | 41,000 |

Notes: $C_1$ through $C_6$ = the alkanes: methane, ethane, propane, butane, pentane, and hexane. Iso- and normal configurations of butane, pentane, and hexane are designated with *i*- and *n*- prefixes. $C_1/C_2$ = the methane/ethane ratio, $C_1/C_{2+}$ = the ratio of methane/Σ ($C_2$ through $C_6$).

**Only part of this table is produced here. The entire table appears on the CD-ROM (back pocket).**

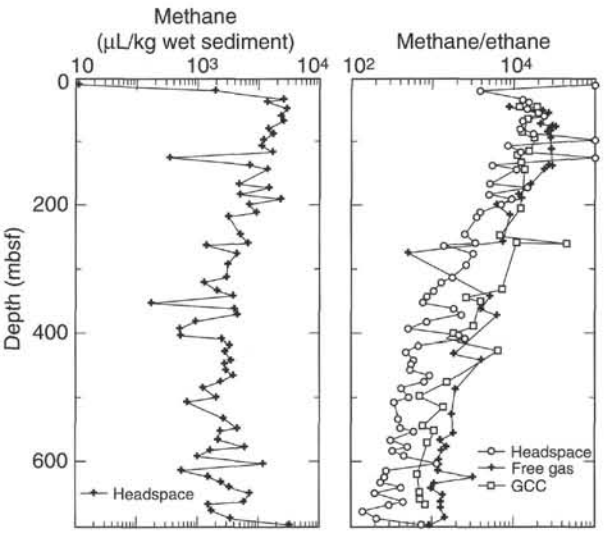


Figure 36. Concentrations of $C_1$ and $C_2$ and $C_1/C_2$ ratios in sediment, headspace gas, free gas, and gas from the GCC.

**Table 10. Methane concentrations from the four uppermost cores.**

| Core, section, interval (cm) | Depth (mbsf) | $CH_4$ (μM) |
|---|---|---|
| 164-994A- | | |
| 1H-1, 140–150 | 1.40 | |
| 1H-2, 140–150 | 2.90 | 1 |
| 1H-3, 140–150 | 4.40 | |
| 1H-4, 140–150 | 5.90 | |
| 1H-5, 140–150 | 7.40 | |
| 2H-1, 140–150 | 9.30 | |
| 2H-2, 115–130 | 10.55 | 2 |
| 2H-2, 140–150 | 10.80 | |
| 2H-3, 115–130 | 12.05 | 2 |
| 2H-3, 140–150 | 12.30 | |

Note: The dense sampling scheme was designed to delineate the base of the sulfate reduction zone, which occurred at ~20.4 m.

**Only part of this table is produced here. The entire table appears on the CD-ROM (back pocket).**

**Table 11. Composition of free gas collected in syringes from sediments at Site 994.**

| Core, section | Depth (mbsf) | $O_2$ (ppmv) | $N_2$ (ppmv) | $C_1$ (ppmv) | $CO_2$ (ppmv) | $C_2$ (ppmv) | $H_2S$ (ppmv) | $C_3$ (ppmv) | *i*-$C_4$ (ppmv) | *n*-$C_4$ (ppmv) | *i*-$C_5$ (ppmv) | *n*-$C_5$ (ppmv) | *i*-$C_6$ (ppmv) | *n*-$C_6$ (ppmv) | $C_1/C_2$ | $C_1/C_{2+}$ |
|---|---|---|---|---|---|---|---|---|---|---|---|---|---|---|---|---|
| 164-994C- | | | | | | | | | | | | | | | | |
| 4H-7 | 32.80 | 137,000 | 58,000 | 237,100 | 5,500 | | | 4 | 1 | 5 | | 0 | 1 | 2 | | 19,000 |
| 4H-2 | 25.70 | 183,000 | 774,000 | 1,600 | 800 | | | | | | | | | | | |
| 5H-6 | 41.20 | 191,000 | 70,000 | 63,000 | 2,400 | 6 | | 4 | 2 | 2 | 0 | 0 | 1 | 1 | 11,500 | 3,800 |
| 6H-6 | 50.40 | 76,000 | 240,000 | 630,300 | 1,200 | 28 | | 17 | 4 | 1 | 1 | 0 | 1 | 2 | 22,500 | 11,800 |
| 6H-2 | 44.40 | 138,000 | 575,000 | 244,000 | 4,200 | 28 | | 4 | 1 | 2 | | | 1 | 4 | 8,710 | 6,070 |
| 7H-2 | 54.20 | 14,000 | 76,000 | 880,700 | 16,600 | 33 | | 18 | 3 | | | | | | 26,700 | 16,300 |
| 8H-7 | 71.20 | 99,000 | 371,000 | 484,900 | 8,100 | 23 | | 11 | 2 | | | | | | 21,100 | 13,500 |
| 10H-2 | 74.20 | 26,000 | 114,000 | 829,400 | 22,700 | 28 | | 18 | 4 | | | | | | 29,600 | 16,600 |
| 10H-3 | 75.70 | 31,000 | 138,000 | 845,300 | 24,400 | 26 | | 19 | 4 | | | | | 2 | 32,500 | 16,600 |
| 10H-4 | 77.20 | 30,000 | 105,000 | 842,400 | 12,500 | 30 | | 19 | 4 | | | | | | 28,100 | 15,900 |

Notes: Oxygen ($O_2$) and nitrogen ($N_2$) concentrations are included as a guide to the amount of air contamination in each sample. $C_1$ through $C_7$ = the alkanes: methane, ethane, propane, butane, pentane, hexane, and heptane. Iso- and normal configurations of butane, pentane, and hexane are designated with *i*- and *n*- prefixes. $C_1/C_2$ = the methane/ethane ratio, and $C_1/C_{2+}$ = the ratio methane/$\Sigma$ ($C_2$ through $C_6$).

**Only part of this table is produced here. The entire table appears on the CD-ROM (back pocket).**

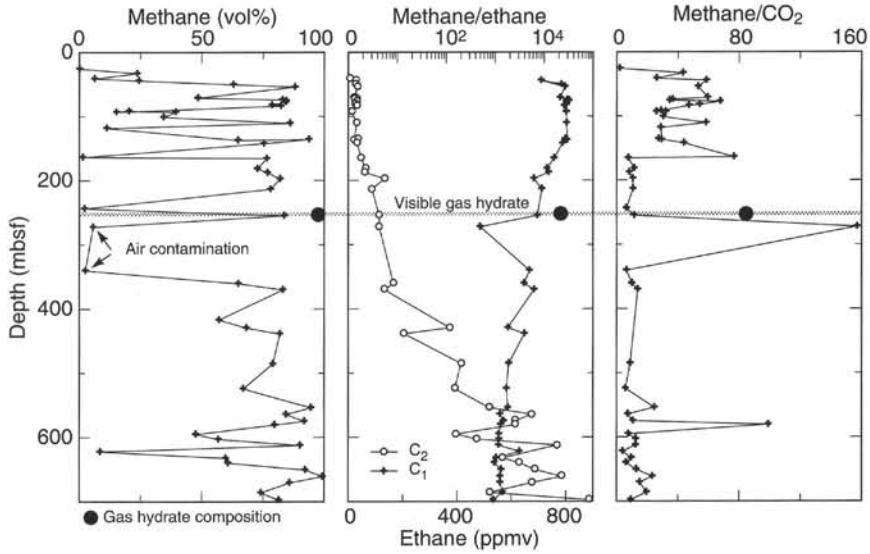


Figure 37. $C_1$ and $C_2$ concentrations and $C_1/C_2$ and $C_1/CO_2$ ratios of free gas collected in vacutainers from Site 994. Below a depth of 258.9 mbsf where a gas hydrate nodule was found, the concentration of $C_1$ is reduced, that of $C_2$ is enriched, and that of $CO_2$ is depleted, relative to the gas hydrate composition. "Air contamination" highlights measurements where significant quantities of atmospheric gas diluted free gas recovered from the core.

error of the determination (Table 14). The C/N ratios of samples from 27.29 to 200 mbsf generally are greater than 10, whereas in samples below 200 mbsf C/N ratios are mostly less than 10. Measured hydrogen indices (HI) from Rock-Eval pyrolysis range from 86 to 297 (Table 15). The calculated HI (see Langford and Blanc-Valleron, 1990) is 198. Oxygen indices (OI) are between 108 and 238. The average $T_{max}$ is 414°C (Table 15). The total sulfur content varies from 0.02% to 1.79%.

## Discussion

The $C_1/C_2$ ratios indicate that the methane is largely of microbial origin (Schoell, 1980). The $C_1$ concentrations measured in headspace gas are heavily influenced by coring technique (APC or XCB), time of exposure of cores to atmospheric pressure, stage of sediment diagenesis (lithification and water content), and analytical procedures (e.g., desorption conditions). Therefore, volumes determined by this method do not represent in situ concentrations. However, this standardized procedure allows three general depth zones of gas distribution to be differentiated. The $C_1$ concentration of the headspace gas within the sulfate reduction zone (0–21 mbsf) is relatively low (e.g., 40 µL/kg at 8.9 mbsf). A middle zone of sediment has the highest concentrations of $C_1$ (90,700 µL/kg at 65.9 mbsf). Sediment below this depth has lower $C_1$ concentrations in headspace gas. Similar $C_1$ concentration vs. depth profiles have been observed at other ODP sites associated with sedimentary gas hydrate (e.g., Kvenvolden and Kastner, 1990). $C_1$ is largely microbially generated within the zone of methanogenesis below the sulfate reduction zone. Taking the $C_1$ headspace concentrations as a guide, the most active zone of $C_1$ generation may extend from 20.4 mbsf down to ~209.3 mbsf. In this zone, a tenfold increase in alkalinity was measured (see "Inorganic Geochemistry" section, this chapter). Some portion of that $C_1$ migrates upward where it is oxidized, whereas sediment below the zone of more active methanogenesis contains a largely residual pool of $C_1$.

Concentrations of the $C_4$ through $C_6$ hydrocarbons in free-gas samples are mostly below 10 ppm for each compound. Because of this low concentration and the preference of the isoalkanes over the *n*-alkanes, these compounds are more likely of diagenetic rather than thermogenic origin (e.g., Schaefer and Leythaeuser, 1984).

The large volumes of gas recovered from the PCS (see "Downhole Tools and Sampling" section, this chapter) clearly demonstrate that the headspace gas concentrations do not reflect the in situ gas volumes.

Preliminary CNS analysis of the organic matter from Site 994 sediment indicates a marine origin (C/N ratios near 10). Conversely, low HI values (mostly <200 mg/gC), and high OI values (mostly >150 mg/gC) from Rock-Eval pyrolysis suggest a terrestrial type III kerogen. A slight increase of the marine character of the organic matter with depth may be deduced both from Rock-Eval and C/N data. These analyses indicate that the organic matter is of a mixed terrestrial and marine origin. Similar results were noted by Katz (1983) in sediment collected from the Blake Ridge during DSDP Leg 76. The

**Table 12. Composition of gas released from gas-collection chambers, Hole 994A.**

| Core, section | Depth (mbsf) | $O_2$ (ppmv) | $N_2$ (ppmv) | $C_1$ (ppmv) | $CO_2$ (ppmv) | $C_2$ (ppmv) | $C_3$ (ppmv) | *i*-$C_4$ | *n*-$C_4$ | *i*-$C_5$ | *n*-$C_5$ | $C_1/C_2$ | $C_1/C_{2+}$ |
|---|---|---|---|---|---|---|---|---|---|---|---|---|---|
| 164-994A- | | | | | | | | | | | | | |
| 5H-3 | 35.90 | 50,000 | 199,000 | 41,000 | | | | | | | | | |
| 6H-3 | 45.10 | 130,000 | 538,000 | 246,000 | 5,400 | 13 | | | | | | 19,100 | 19,100 |
| 6H-3 | 45.10 | 136,000 | 575,000 | 245,000 | 5,400 | 13 | | | | | | 18,200 | 18,200 |
| 6H-3 | 45.10 | 109,000 | 461,000 | 244,000 | 9,700 | 16 | 4 | 1 | | | | 15,300 | 11,600 |
| 7H-3 | 54.90 | 139,000 | 584,000 | 240,000 | 5,700 | 7 | 4 | 1 | | | | 34,200 | 20,000 |
| 8H-3 | 64.40 | 118,000 | 490,000 | 349,000 | 9,000 | 14 | 8 | 2 | | | | 25,000 | 14,600 |
| 8H-5 | 67.40 | 126,000 | 522,000 | 298,000 | 9,700 | 14 | 6 | 1 | | | | 21,300 | 14,200 |
| 10H-1 | 71.90 | 157,000 | 652,000 | 156,000 | 6,400 | 7 | 3 | 1 | | | | 22,200 | 14,200 |
| 11H-3 | 84.40 | 133,000 | 549,000 | 269,000 | 10,400 | 16 | 5 | 1 | | | | 16,800 | 12,200 |
| 12H-3 | 93.90 | 155,000 | 645,000 | 161,000 | 6,600 | 5 | 3 | 1 | | | | 32,200 | 17,900 |
| 13H-2 | 101.90 | 135,000 | 561,000 | 260,000 | 13,800 | 8 | 5 | 2 | | | | 32,500 | 17,300 |
| 14H-4 | 114.40 | 150,000 | 621,000 | 181,000 | 11,300 | 6 | 4 | 2 | | | | 30,100 | 15,100 |
| 15H-2 | 120.26 | 125,000 | 535,000 | 286,000 | 21,100 | 11 | 9 | 4 | 1 | 1 | | 26,000 | 11,000 |
| 16H-3 | 131.90 | 119,000 | 493,000 | 333,000 | 22,300 | 13 | 8 | 3 | 1 | 1 | 1 | 25,600 | 12,300 |
| 17H-4 | 142.90 | 98,000 | 407,000 | 432,000 | 37,600 | 14 | 10 | 4 | 1 | 2 | 1 | 30,800 | 13,500 |
| 25X-1 | 203.30 | 85,000 | 370,000 | 206,000 | 16,700 | 8 | 5 | 2 | | 2 | | 25,700 | 12,100 |
| 30X-5 | 246.83 | 140,000 | 616,000 | 182,000 | 35,700 | 14 | 7 | 3 | 1 | 2 | | 13,000 | 6,730 |
| 31X-6 | 258.80 | 27,000 | 102,000 | 177,000 | 900 | | 1 | 1 | | 2 | | | 44,300 |
| 31X-5 | 257.30 | 8,000 | 26,000 | 939,000 | | 86 | 2 | | | | | 10,900 | 10,700 |
| 40X-2 | 329.80 | 152,000 | 621,000 | 120,000 | 9,300 | 11 | 4 | 1 | | | 1 | 10,900 | 7,080 |
| 41X-4 | 341.77 | 153,000 | 635,000 | 64,000 | 12,400 | 12 | 10 | 1 | | 2 | | 5,360 | 2,570 |
| 42X-2 | 349.10 | 150,000 | 622,000 | 123,000 | 24,100 | 24 | 5 | | | 1 | 2 | 5,140 | 3,850 |
| 47X-2 | 387.60 | 147,000 | 622,000 | 105,000 | 17,400 | 28 | 2 | 1 | | 1 | 1 | 3,760 | 3,190 |
| 49X-2 | 398.10 | 134,000 | 585,000 | 105,000 | 27,200 | 50 | 2 | 1 | | 3 | 2 | 2,100 | 1,810 |
| 50X-2 | 406.70 | 152,000 | 648,000 | 87,000 | 22,300 | 27 | 25 | 2 | | 2 | 2 | 3,220 | 1,500 |
| 52X-1 | 424.50 | 149,000 | 672,000 | 140,000 | 8,300 | 12 | 5 | 2 | | 1 | 2 | 11,700 | 6,380 |
| 58X-2 | 474.10 | 160,000 | 671,000 | 66,000 | 20,100 | 39 | 2 | 1 | | 1 | 1 | 1,690 | 1,490 |
| 61X-3 | 495.90 | 152,000 | 629,000 | 60,000 | 28,100 | 67 | 4 | 1 | 13 | 2 | 1 | 900 | 685 |
| 63X-3 | 513.18 | 153,000 | 645,000 | 101,000 | 36,900 | 67 | 4 | 1 | 1 | 1 | 1 | 1,500 | 1,340 |
| 67X-2 | 542.45 | 149,000 | 668,000 | 79,000 | 42,200 | 91 | 7 | 1 | 1 | 1 | 2 | 870 | 768 |
| 68X-2 | 550.30 | 146,000 | 616,000 | 73,000 | 34,100 | 62 | 4 | 1 | 1 | 1 | | 1,180 | 1,060 |
| 69X-2 | 560.71 | 138,000 | 591,000 | 98,000 | 42,100 | 85 | 12 | 1 | 1 | 1 | | 1,150 | 976 |
| 71X-1 | 569.90 | 148,000 | 621,000 | 77,000 | 24,600 | 70 | 17 | | 1 | 1 | | 1,100 | 870 |
| 76X-2 | 618.50 | 153,000 | 640,000 | 78,000 | 28,800 | 109 | 7 | 1 | 1 | 1 | | 715 | 655 |
| 79X-2 | 646.88 | 156,000 | 655,000 | 69,000 | 23,900 | 90 | 5 | 1 | 1 | 1 | | 764 | 701 |
| 80X-3 | 657.41 | 147,000 | 605,000 | 77,000 | 23,100 | 97 | 7 | 1 | 1 | 1 | | 789 | 715 |
| 81X-2 | 665.34 | 159,000 | 664,000 | 78,000 | 24,500 | 88 | 5 | 1 | 1 | 1 | 0 | 889 | 814 |

Notes: Total gas volumes released from the chambers are reported in Table 4. Analyses were conducted on subsamples of the total gas volume. Oxygen ($O_2$) and nitrogen ($N_2$) concentrations are included as a guide to the amount of air contamination in each sample. $C_1$ through $C_6$ = the alkanes: methane, ethane, propane, butane, pentane, and hexane. Iso- and normal configurations of butane, pentane, and hexane are designated with *i*- and *n*- prefixes. $C_1/C_2$ = the methane/ethane ratio, and $C_1/C_{2+}$ = the ratio of methane/$\Sigma$ ($C_2$ through $C_6$).

**Table 13. Composition of gas released from gas-collection chambers after various degassing periods, Hole 994D.**

| Core, section | Depth (mbsf) | Time elapsed | | | $O_2$ (ppmv) | $N_2$ (ppmv) | $C_1$ (ppmv) | $CO_2$ (ppmv) | $C_2$ (ppmv) | $C_3$ (ppmv) | *i*-$C_4$ (ppmv) | *n*-$C_4$ (ppmv) | *i*-$C_5$ (ppmv) | *n*-$C_5$ (ppmv) | $C_1/C_2$ | $C_1/C_{2+}$ |
|---|---|---|---|---|---|---|---|---|---|---|---|---|---|---|---|---|
| | | Hours | Min. | Sec. | | | | | | | | | | | | |
| 164-994D- | | | | | | | | | | | | | | | | |
| 1H-1 | 100.00 | 0 | 14 | 25 | 137,000 | 556,000 | 135,600 | 143,300 | 19 | 4 | 1 | 0.2 | 2.3 | 0.5 | 7,130 | 5,100 |
| 1H-1 | 100.00 | 0 | 14 | 50 | 145,000 | 590,000 | 162,200 | 7,200 | 33 | 5 | 1.3 | 0.5 | 0.7 | 0.8 | 4,920 | 3,930 |
| 1H-1 | 100.00 | 4 | 2 | 15 | 110,000 | 455,000 | 256,500 | 8,100 | 13 | 6 | 1.7 | 0.4 | 1.6 | 0.6 | 19,700 | 11,000 |
| 1H-1 | 100.00 | 4 | 2 | 30 | 109,000 | 449,000 | 282,200 | 8,700 | 16 | 6 | 1.7 | | 0.6 | 0.5 | 17,600 | 11,400 |
| 1H-2 | 101.50 | 0 | 17 | 12 | 118,000 | 479,000 | 269,700 | 14,200 | 32 | 7 | 1.8 | 0.4 | 0.8 | | 8,430 | 6,420 |
| 1H-2 | 101.50 | 0 | 17 | 45 | 113,000 | 462,000 | 273,200 | 14,800 | 40 | 7 | 2.4 | 0.5 | 0.7 | 0.5 | 6,830 | 5,350 |
| 1H-3 | 103.00 | 0 | 4 | 0 | 96,000 | 392,000 | 387,500 | 23,700 | 26 | 7 | 2.2 | | | | 14,900 | 11,100 |
| 1H-3 | 103.00 | 0 | 4 | 10 | 89,000 | 36,000 | 401,900 | 24,700 | 28 | 10 | 2.5 | 0.5 | 0.6 | 0.3 | 14,500 | 9,780 |
| 1H-3 | 103.00 | 0 | 39 | 0 | 63,000 | 259,000 | 607,500 | 36,200 | 36 | 15 | 3.9 | 1.1 | 0.9 | | 16,900 | 10,700 |
| 1H-3 | 103.00 | 0 | 42 | 0 | 58,000 | 239,000 | 500,000 | 26,900 | 20 | 9 | 2.7 | 0.6 | 0.8 | 0.3 | 25,000 | 15,000 |
| 1H-4 | 104.50 | 0 | 1 | 50 | 178,000 | 710,000 | 13 | 700 | | | | | | | | |
| 1H-4 | 104.50 | 0 | 1 | 55 | 92,000 | 369,000 | 454,100 | 20,500 | 21 | 11 | 2.5 | 0.6 | 0.6 | 0.6 | 21,600 | 12,500 |
| 1H-4 | 104.50 | 0 | 21 | 50 | 57,000 | 231,000 | 619,500 | 31,900 | 40 | 17 | 3.7 | 0.8 | 1.1 | 0.6 | 15,500 | 9,800 |
| 1H-4 | 104.50 | 0 | 22 | 10 | 59,000 | 241,000 | 627,400 | 34,200 | 31 | 15 | 3.5 | 0.8 | 0.9 | | 20,200 | 12,300 |
| 1H-5 | 106.00 | 0 | 9 | 45 | 105,000 | 426,000 | 343,200 | 17,900 | 18 | 7 | 2.2 | | 0.5 | | 19,100 | 12,500 |
| 1H-5 | 106.00 | 0 | 9 | 55 | 106,000 | 431,000 | 345,900 | 18,300 | 15 | 7 | 1.9 | 0.3 | 0.5 | 0.4 | 23,100 | 13,800 |
| 1H-5 | 106.00 | 0 | 27 | 15 | 90,000 | 371,000 | 382,600 | 19,000 | 13 | 9 | 2.7 | | 0.8 | 0.3 | 29,400 | 14,800 |
| 1H-5 | 106.00 | 0 | 27 | 45 | 89,000 | 365,000 | 374,300 | 21,500 | 12 | 8 | 2.8 | 0.4 | 0.6 | 0.3 | 31,200 | 15,500 |
| 1H-5 | 106.00 | 1 | 15 | 30 | 59,000 | 248,000 | 573,000 | 27,800 | 28 | 13 | 3.7 | 0.5 | 1 | 0.3 | 20,500 | 12,300 |
| 1H-5 | 106.00 | 1 | 15 | 40 | 62,000 | 262,000 | 582,500 | 28,600 | 28 | 13 | 3.8 | 0.5 | 1 | 0.4 | 20,800 | 12,500 |
| 1H-5 | 106.00 | 3 | 58 | 40 | 40,000 | 173,000 | 709,100 | 29,900 | 35 | 20 | 4.5 | 0.6 | 1 | 0.6 | 20,300 | 11,500 |
| 1H-5 | 106.00 | 3 | 59 | 0 | 41,000 | 178,000 | 708,100 | 29,500 | 36 | 19 | 4.6 | 0.7 | 1.1 | 0.6 | 19,700 | 11,400 |

Notes: Oxygen ($O_2$) and nitrogen ($N_2$) concentrations are included as a guide to the amount of air contamination in each sample. $C_1$ through $C_6$ = the alkanes: methane, ethane, propane, butane, pentane, and hexane. Iso- and normal configurations of butane, pentane, and hexane are designated with *i*- and *n*- prefixes. $C_1/C_2$ = the methane/ethane ratio, and $C_1/C_{2+}$ = the ratio of methane/$\Sigma$ ($C_2$ through $C_6$). Min. = minutes, and Sec. = seconds. Total gas volumes released from the chambers are reported in Table 4.

**Table 14. Carbonate, carbon, nitrogen, and sulfur contents in sediments from Site 994.**

| Core, section, interval (cm) | Depth (mbsf) | $CaCO_3$ (wt%) | Organic carbon (wt%) | Total nitrogen (wt%) | C/N | Total sulfur (wt%) |
|---|---|---|---|---|---|---|
| 164-994C- | | | | | | |
| 2H-1, 47–48 | 4.87 | 24.4 | 0.34 | 0.00 | NA | 0.02 |
| 2H-5, 96–97 | 11.36 | 46.8 | NA | NA | NA | NA |
| 3H-5, 130–131 | 21.20 | 23.4 | 0.44 | 0.01 | NA | 0.51 |
| 3H-2, 67–68 | 16.07 | 28.2 | NA | NA | NA | NA |
| 4H-1, 89–90 | 24.29 | 31.3 | NA | NA | NA | NA |
| 4H-3, 89–90 | 27.29 | 23.0 | 0.39 | 0.02 | NA | 0.48 |
| 5H-1, 70–71 | 33.60 | 32.2 | NA | NA | NA | NA |
| 5H-3, 69–70 | 36.59 | 13.7 | 0.38 | 0.02 | NA | 1.58 |
| 6H-1, 26–27 | 42.66 | 27.6 | NA | NA | NA | NA |
| 6H-4, 72–73 | 47.32 | 62.1 | NA | NA | NA | NA |

Note: NA = not analyzed.

**Only part of this table is produced here. The entire table appears on the CD-ROM (back pocket).**

average $T_{max}$ value of 414°C is indicative of immature organic matter. Therefore, substantial amounts of thermogenic hydrocarbons are not expected to be generated in situ.

## INORGANIC GEOCHEMISTRY

Site 994, located on the Blake Ridge near a prominent BSR, was the first of several deep (~750 m) sites planned for high-resolution interstitial-water sampling (see "Background and Objectives" section, this chapter). The primary reasons for this unprecedented ODP water sampling strategy were twofold: (1) to establish detailed chemical profiles in uppermost cores for a variety of shore-based investigations (e.g., microbiology studies) and (2) to document downcore variability in pore-water $Cl^-$ concentrations within a gas hydrate–bearing pelagic sequence. Previous works (e.g., Hesse and Harrison, 1981; Kvenvolden and Barnard, 1983; Kvenvolden and Kastner, 1990; Froelich et al., 1995) have demonstrated that interstitial waters within gas hydrate–bearing sediments are notably deficient in $Cl^-$ relative to seawater and have ascribed this freshening to hydrate dissociation during transport of cores to the surface. However, the range and variability of such freshening is poorly constrained because interstitial waters previously have been sampled at low resolution (<1 sample per core).

A total of 128 whole-round samples were taken from Holes 994A (22 samples), 994B (three samples), 994C (71 samples), and 994D (32 samples) for interstitial-water analyses. These samples (Table 16) span the entire sedimentary sequence from Site 994 at a resolution of at least one sample per core. There were three intervals (0–35, 243–277, and 378–413 mbsf) in which sampling resolution was increased to one sample per 1.5-m section. Samples of surface seawater, drilling mud filtrate, and four WSTP (or Barnes Tool) interstitial-water runs also were collected at Site 994. The analyses of these samples, as well as water samples recovered from PCS runs at Site 994, are presented in the "Downhole Tools and Sampling" section (this chapter).

The high-resolution sampling strategy at Site 994 necessitated certain deviations from routine interstitial-water analyses because, at times, the rate of sample collection was significantly faster than the rate at which samples could be processed. One consequence was that some whole-round intervals from Hole 994D were stored in a refrigerator for as long as 36 hr before being squeezed. The outer rims of the stored samples were removed immediately after core cutting, and the samples were tightly wrapped in thick-walled plastic bags before refrigeration.

### Chloride

The high-resolution interstitial-water $Cl^-$ profile increases from 555 and 557 mM in the shallowest samples to a subsurface maximum of 560 mM at 12 mbsf (Fig. 39A, B). The gradient over this initial depth interval is 0.36 mM/m. Between 12 and 195 mbsf, $Cl^-$ decreases nearly linearly to 510 mM. Chloride concentrations then become highly variable in the depth range from 195 to 456 mbsf. "Background" $Cl^-$ values are 515 to 525 mM; however, superimposed on this general trend are $Cl^-$ concentrations of significantly lower values. These $Cl^-$ excursions are found in the same depth range at both Holes 994C and 994D, and the number and magnitude of the anomalies are particularly well developed at ~400 mbsf. The lowest $Cl^-$ concentration measured is 447 mM at 388 mbsf (Sample 164-994D-7X-2, 135–150 cm). Chloride increases slightly from 515 to 530 mM (~610 mbsf) just below the zone of $Cl^-$ excursions and then decreases to 525 mM at the base of Hole 994C (697 mbsf). The overall gradient in this lowest depth interval (456 to 697 mbsf) is ~0.06 mM/m.

### Sulfate

Sulfate decreases with depth from a value of 25.6 mM at 1.4 mbsf to negligible concentrations at 21–26 mbsf (Figs. 40, 41). The $SO_4^{2-}$ gradient over the first 21 m is approximately linear at 1.37 mM/m, and there may be concave-down curvature near the base of the $SO_4^{2-}$ reduction zone (Fig. 40). Below 21 mbsf, $SO_4^{2-}$ concentrations vary from 0 to 3.2 mM (Fig. 40).

### Alkalinity

Alkalinity increases with depth through the $SO_4^{2-}$ reduction zone to a subsurface maximum of 104.25 mM at 352 mbsf (Fig. 40). This alkalinity increase is linear between ~40 and 216 mbsf, where alkalinity reaches 92.15 mM. Below 352 mbsf, alkalinity decreases to ~55 mM at 700 mbsf. Alkalinity values at Hole 994D are offset relative to those at Hole 994C from the same depth.

### Ammonium

Ammonium increases downhole to a subsurface maximum of 28 mM at ~510 mbsf and then declines to 21 mM at the hole bottom (Fig. 40). Most of the $NH_4^+$ results from Hole 994D are within 1 standard deviation (5.9%) of the results at corresponding depths from Hole 994C.

### Potassium

Although the concentrations of $K^+$ fluctuate considerably, there is a general downhole increase to ~150 mbsf followed by a decrease to 697 mbsf (Fig. 40). Hole 994D interstitial-water samples are on average enriched in $K^+$ by ~3 mM relative to corresponding samples from Hole 994C.

### Calcium, Magnesium, and Strontium

Concentrations of $Ca^{2+}$ decrease sharply to ~2.5 mM at 25 mbsf and continue to decrease to 0.83 mM at 132 mbsf (Fig. 40). Below this depth, $Ca^{2+}$ increases irregularly to a level of 5 mM at the bottom of 994C.

Concentrations of $Mg^{2+}$ decrease downhole until 392 mbsf and then do not vary systematically with depth (Fig. 40). Concentrations of $Mg^{2+}$ decrease most rapidly in the uppermost interval from 0 to 26 mbsf. This is roughly the same depth interval as the $SO_4^{2-}$ reduction zone.

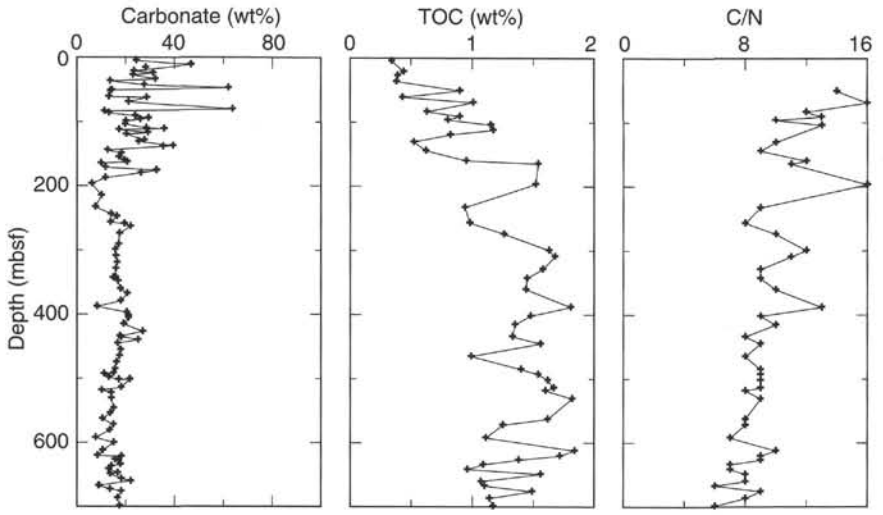


Figure 38. Total organic carbon, total nitrogen, and C/N ratios in sediments from Site 994. A C/N ratio of 10 or lower is indicative of marine organic matter; ratios higher than 20 are representative of terrestrial organic matter.

**Table 15. Rock-Eval analysis of sediment from Hole 994C.**

| Core, section, interval (cm) | Depth (mbsf) | $T_{max}$ | $S_1$ | $S_2$ | $S_3$ | PI | HI | OI |
|---|---|---|---|---|---|---|---|---|
| 164-994C- | | | | | | | | |
| 6H-6, 121–122 | 50.81 | 393 | 0.28 | 1.43 | 2.15 | 0.16 | 158 | 238 |
| 8H-6, 33–34 | 69.23 | 405 | 0.52 | 2.04 | 2.10 | 0.20 | 201 | 207 |
| 11H-7, 53–54 | 90.93 | 400 | 0.37 | 1.32 | 2.35 | 0.22 | 146 | 261 |
| 13H-3, 70–71 | 104.10 | 417 | 0.22 | 1.41 | 2.19 | 0.14 | 122 | 190 |
| 14H-2, 102–103 | 112.42 | 416 | 0.18 | 1.27 | 1.85 | 0.12 | 108 | 158 |
| 17H-5, 16–17 | 144.56 | 384 | 0.23 | 1.06 | 1.68 | 0.18 | 170 | 270 |
| 20X-2, 33–34 | 160.23 | 404 | 0.23 | 1.38 | 2.21 | 0.14 | 145 | 232 |
| 24X-3, 30–31 | 196.90 | 406 | 0.22 | 1.37 | 1.86 | 0.14 | 90 | 122 |
| 29X-1, 80–81 | 232.90 | 398 | 0.17 | 1.13 | 1.83 | 0.13 | 120 | 194 |
| 31X-4, 105–106 | 256.85 | 404 | 0.30 | 1.43 | 1.83 | 0.17 | 145 | 186 |
| 33X-3, 55–56 | 273.94 | 406 | 0.22 | 1.37 | 1.86 | 0.14 | 90 | 122 |
| 36P-1, 10–11 | 299.50 | 421 | 0.29 | 2.10 | 2.16 | 0.12 | 128 | 132 |
| 38X-1, 26–27 | 309.26 | 398 | 0.17 | 1.13 | 1.83 | 0.13 | 120 | 194 |
| 41X-4, 147–148 | 343.24 | 404 | 0.30 | 1.43 | 1.83 | 0.17 | 145 | 186 |
| 43X-3, 94–95 | 360.62 | 411 | 0.34 | 1.89 | 2.34 | 0.15 | 150 | 185 |
| 47X-2, 51–52 | 388.11 | 415 | 0.33 | 1.57 | 1.96 | 0.17 | 87 | 108 |
| 49X-5, 66–67 | 401.98 | 415 | 0.69 | 4.12 | 2.34 | 0.14 | 278 | 158 |
| 53P-1, 1–2 | 434.11 | 421 | 0.41 | 2.78 | 2.36 | 0.13 | 209 | 177 |
| 55X-2, 53–54 | 445.34 | 422 | 0.42 | 3.49 | 2.17 | 0.11 | 224 | 139 |
| 57X-2, 64–65 | 464.90 | 409 | 0.39 | 1.80 | 1.99 | 0.18 | 182 | 201 |
| 59X-3, 82–83 | 485.40 | 412 | 0.56 | 3.18 | 2.10 | 0.15 | 227 | 150 |
| 61X-1, 10–11 | 493.00 | 413 | 0.68 | 3.76 | 2.28 | 0.15 | 244 | 148 |
| 63X-3, 79–80 | 513.97 | 421 | 0.45 | 3.27 | 2.47 | 0.12 | 196 | 148 |
| 65X-6, 59–60 | 530.99 | 422 | 0.55 | 5.09 | 2.29 | 0.10 | 280 | 126 |
| 69X-3, 70–71 | 562.91 | 419 | 0.48 | 3.37 | 2.32 | 0.12 | 208 | 143 |
| 71X-2, 74–75 | 572.14 | 419 | 0.35 | 2.34 | 2.11 | 0.13 | 187 | 169 |
| 73X-4, 66–67 | 592.33 | 420 | 0.40 | 2.32 | 1.77 | 0.15 | 209 | 159 |
| 75X-4, 67–69 | 612.37 | 427 | 0.32 | 2.88 | 1.96 | 0.10 | 157 | 107 |
| 77X-1, 32–33 | 626.92 | 424 | 0.26 | 2.11 | 1.78 | 0.11 | 153 | 129 |
| 79X-3, 70–71 | 649.08 | 420 | 0.51 | 3.94 | 2.12 | 0.11 | 253 | 136 |
| 81X-3, 54–56 | 667.38 | 417 | 0.28 | 2.04 | 1.64 | 0.12 | 185 | 149 |
| 82X-2, 13–14 | 676.23 | 420 | 0.37 | 2.88 | 2.02 | 0.11 | 193 | 136 |
| 84X-4, 73–74 | 699.03 | 421 | 0.25 | 1.90 | 1.98 | 0.12 | 162 | 169 |

Notes: $T_{max}$ = temperature (°C) at which the maximum amount of hydrocarbons is generated from the kerogen during pyrolysis; $S_1$ = quantity of free hydrocarbons in the rock samples, in mg/g rock; $S_2$ = quantity of hydrocarbons produced by kerogen cracking, in mg/g rock; $S_3$ = quantity of organic $CO_2$ produced during pyrolysis of the rock, in mg/g rock; PI = production index, calculated as $S_1/S_1+S_2$; HI = hydrogen index, calculated as $S_2$/TOC; and OI = oxygen index, calculated as $S_3$/TOC.

Concentrations of $Sr^{2+}$ increase rapidly to a pronounced maximum of 123 µM at 32 mbsf and then decrease to a minimum of 43 µM at 132 mbsf (Fig. 40). Below this depth, $Sr^{2+}$ increases irregularly to its maximum concentration of 139 µM at total depth.

Interstitial-water samples from Hole 994D are slightly depleted in $Mg^{2+}$ and considerably depleted in $Ca^{2+}$ and $Sr^{2+}$ relative to samples from similar depth from Hole 994C.

## Phosphate and Dissolved Silica

Phosphate reaches a subsurface maximum of 150 µM at 120–140 mbsf (Fig. 40), below which $PO_4^{3-}$ decreases to near 0 µM in the deepest samples. Interstitial-water samples at Hole 994D are considerably enriched in $PO_4^{3-}$ relative to samples from similar depth at Hole 994C.

Dissolved silica increases irregularly from ~200 µM in the shallowest samples to almost 1200 µM at 500 mbsf, below which depth concentrations decrease to 640 µM at total depth (Fig. 40). Interstitial waters at Hole 994D are considerably depleted in dissolved silica compared to those at Hole 994C.

## Preliminary Interpretations

At Site 994, the interstitial-water profiles are broadly similar to those observed at other DSDP/ODP sites drilled in or near gas hydrate–bearing sediments (e.g., Hesse et al., 1985; Kastner et al.,

**Table 16. Interstitial water data for Site 994.**

| Core, section, interval (cm) | Water (mL) | Depth (mbsf) | pH | Alk (mM) | Sal (g/kg) | $Cl^-$ (mM) | $Cl^{-*}$ (mM) | $Mg^{2+}$ (mM) | $Ca^{2+}$ (mM) | $SO_4^{2-}$ (mM) | $PO_4^{3-}$ (µM) | $NH_4^+$ (µM) | $SiO_2$ (µM) | $K^+$ (µM) | $Sr^{2+}$ (µM) |
|---|---|---|---|---|---|---|---|---|---|---|---|---|---|---|---|
| 164-994A | | | | | | | | | | | | | | | |
| 1H-1, 140–150 | 40 | 1.40 | 7.7 | 5.0 | 34.0 | 555 | 555 | 49.5 | 9.4 | 25.6 | 29 | 470 | 469 | 12.6 | 93 |
| 1H-2, 140–150 | 40 | 2.90 | 8.2 | 5.2 | 34.0 | 557 | 557 | 46.9 | 8.5 | 23.9 | 33 | 800 | 693 | 12.0 | 93 |
| 1H-3, 140–150 | 40 | 4.40 | 7.6 | 6.0 | 34.0 | 557 | 557 | 48.1 | 8.4 | 22.6 | 32 | 770 | 693 | 12.6 | 93 |
| 1H-4, 140–150 | 40 | 5.90 | 7.6 | 6.5 | 34.0 | 558 | 558 | 46.6 | 8.6 | 23.2 | 37 | 730 | 697 | 12.0 | 93 |
| 1H-5, 140–150 | 40 | 7.40 | 7.7 | 7.2 | 34.0 | 557 | 557 | 45.3 | 7.2 | 20.6 | 23 | 1,050 | 606 | 12.1 | 96 |
| 2H-1, 140–150 | 40 | 9.30 | 7.8 | 8.7 | 33.0 | 560 | 560 | 40.9 | 5.2 | 14.4 | 33 | 1,360 | 611 | 12.6 | 97 |
| 2H-2, 140–150 | 40 | 10.80 | 8.0 | 9.8 | 33.0 | 559 | 559 | 39.3 | 4.6 | 12.9 | 36 | 1,450 | 506 | 12.6 | 97 |
| 2H-3, 140–150 | 40 | 12.30 | 7.9 | 10.3 | 32.5 | 560 | 560 | 38.3 | 4.0 | 11.1 | 49 | 1,510 | 585 | 12.4 | 100 |
| 2H-4, 140–150 | 40 | 13.80 | 8.0 | 11.7 | 32.5 | 559 | 559 | 36.1 | 3.7 | 9.2 | 49 | 1,740 | 615 | 12.5 | 100 |
| 2H-5, 140–150 | 40 | 15.30 | 8.0 | 13.0 | 32.0 | 556 | 556 | 34.3 | 3.3 | 6.7 | 59 | 1,650 | 707 | 12.1 | 99 |

Notes: Alk = alkalinity, and Sal = salinity. $Cl^{-*}$ = values are corrected for seawater contamination (see text). All other concentrations are uncorrected.

***Only part of this table is produced here. The entire table appears on the CD-ROM (back pocket).***

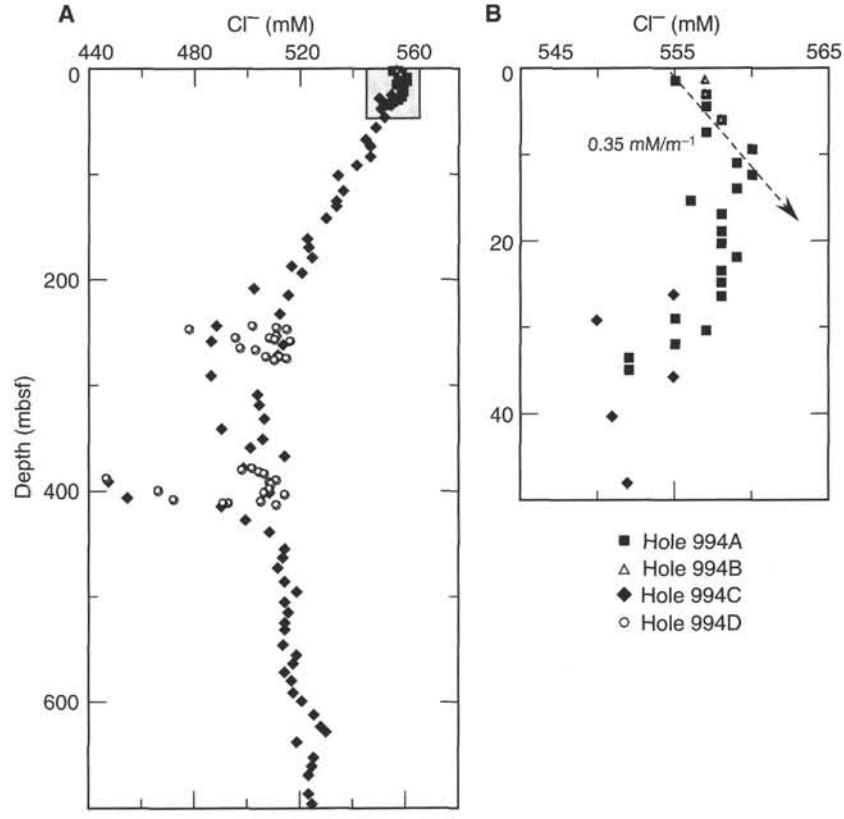


Figure 39. **A.** The concentration of chloride vs. depth for interstitial waters at Site 994. The shaded area in (A) is expanded in (B). **B.** Detailed profile of chloride values for the upper 50 m at Site 994. The gradient in the first 12 m is 0.35 mM/m, as illustrated by the dashed line. Values have not been corrected for seawater contamination (see text).

1990; Westbrook, Carson, Musgrave, et al., 1994; Froelich et al., 1995). However, whereas most previous drilling of gas hydrate–bearing sediments was in active margin settings, Site 994 is located on a passive margin and in remarkably uniform lithology.

Four topics concerning interstitial-water chemistry at Site 994 are discussed in the following paragraphs: (1) the $Cl^-$ profile and gas hydrate, (2) the contamination of samples by drilling, (3) the focused $SO_4^{2-}$ consumption, and (4) the effects of sample storage.

### *Chloride Gradients*

Variations in the downhole $Cl^-$ profile are similar to those observed at other ODP sites that contain gas hydrate. Most of these variations are suggested to represent the effects of gas hydrate formation and dissociation in an open system (Hesse and Harrison, 1981; Jenden and Geiskes, 1983; Kvenvolden and Barnard, 1983; Hesse et al., 1985; Kastner et al., 1990; Kvenvolden and Kastner, 1990; Ussler and Paull, 1995). Dissolved ions are excluded from a gas hydrate lattice during gas hydrate formation, such that a gas hydrate lattice contains little (if any) salt, and the salinity of surrounding water is increased. In a closed system, the salinity of surrounding water will return to its original value upon hydrate dissociation. However, in an open system, excluded ions will diffuse away from zones where gas hydrate is forming toward regions of lower salinity. Residual saline pore waters also may be expelled by porosity reduction caused by sediment compaction. If water samples are recovered from gas hydrate zones after gas hydrate dissociation during core recovery and sampling, the salinity of the water will be less than the salinity before gas hydrate formation.

There are three possible explanations for the increasing $Cl^-$ gradient between 0 and 12 mbsf. The first explanation is that it represents $Cl^-$ diffusion from deeper, more saline interstitial waters (Kvenvolden and Kastner, 1990). These high-salinity interstitial waters would be generated during hydrate formation and ion exclusion. The

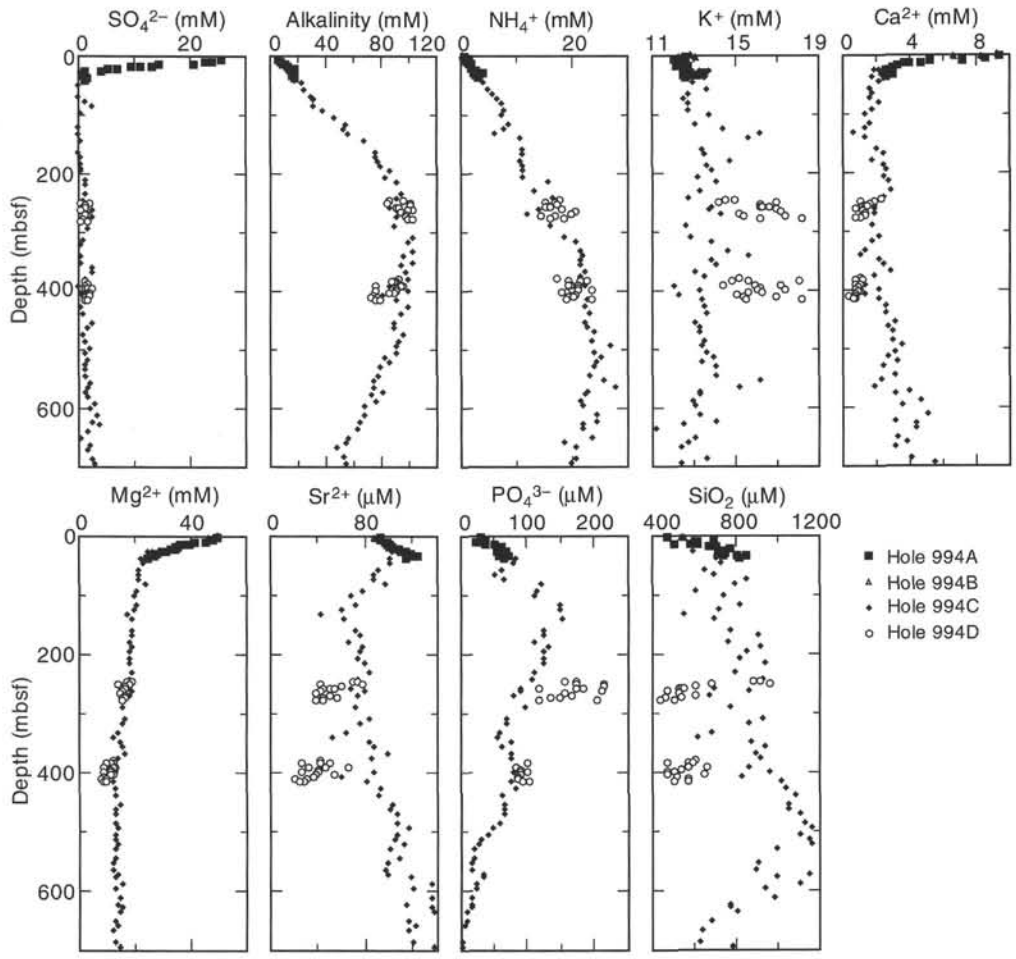


Figure 40. The concentration vs. depth for various dissolved species in interstitial waters at Site 994. Concentrations have not been corrected for seawater contamination (see text).

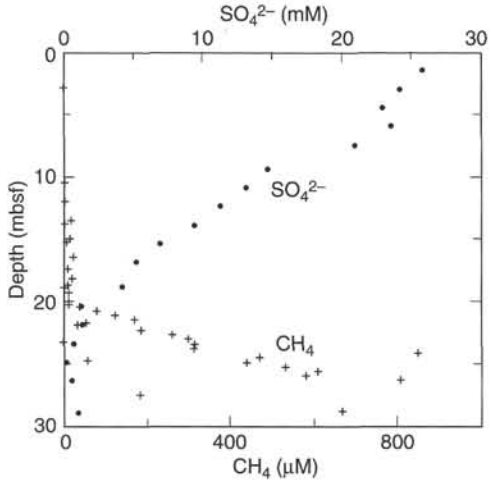


Figure 41. Downhole sulfate and methane profiles in the uppermost 30 mbsf at Site 994. The methane profile is from data presented in Table 10. At ~20.5 mbsf, the sulfate concentrations decrease to near 0, and methane concentrations begin to increase rapidly downhole.

second possibility is that it reflects ultrafiltration by compacted clays (Matsuhisa and Matsumoto, 1986). The third explanation for the positive $Cl^-$ gradient in shallow samples is that it reflects nonsteady-state conditions induced by glacial-interglacial salinity variations (McDuff, 1985; Schrag and DePaulo, 1993). We cannot exclude any of these explanations with available information. However, the first explanation implies that an in situ salinity greater than that of seawater exists at depths >12 mbsf. Meaningful interstitial-water samples from the WSTP (see "Downhole Tools and Sampling" section, this chapter) at future sites during Leg 164 could be used to evaluate this explanation.

The overall significance of the general downhole $Cl^-$ profile at Site 994 is discussed in the "Synthesis and Significance" section (this chapter). Decreased $Cl^-$ values in interstitial water below 12.30 mbsf likely reflect a complex interplay between gas hydrate dissociation during core recovery, gas hydrate dissociation at the base of the gas hydrate stability zone, ion diffusion, and fluid movement over the geologic history of the Blake Ridge. Also, alternative means of freshening water (e.g., mineral dehydration) in Blake Ridge sediment cannot be rigorously dismissed with present information (see discussion in Kastner et al., 1990).

The $Cl^-$ excursions between 196 and 456 mbsf are zones of freshening and are interpreted as intervals where the greatest concentrations of gas hydrate occur. High-resolution sampling (one interstitial-water sample per section) at Hole 994D shows significant $Cl^-$ variations between adjacent samples. Such concentration contrasts (as

much as 60 mM) over short distances would be eliminated by diffusion. Thus, the $Cl^-$ excursions apparently are caused by the decomposition of locally concentrated gas hydrate during core retrieval (e.g., Hesse et al., 1985). Seventeen of the 34 interstitial waters randomly sampled between 196 and 456 mbsf contain anomalously low $Cl^-$ concentrations. The vertical distribution of gas hydrate at Site 994, therefore, is inferred to be heterogeneous in the interval between 196 and 456 mbsf.

No $Cl^-$ anomalies were measured below 456 mbsf. Therefore, the interstitial-water $Cl^-$ profile suggests that the deepest occurrence of gas hydrate at Site 994 lies above 456 mbsf. This inference also is consistent with the logging results (see "Downhole Logging" section, this chapter). The downhole $Cl^-$ profile (Fig. 39) further suggests that there is a depth zone between ~380 and ~420 mbsf where gas hydrate is particularly concentrated.

Gas hydrate might be expected to concentrate (1) in depth intervals of atypical lithology because of different physical properties of the sediment (e.g., porosity and permeability) or (2) at the base of the gas hydrate stability zone because of continuous formation and dissociation of gas hydrate over time. However, neither of these two mechanisms can be readily invoked to explain the apparent concentration of gas hydrate between 380 and 420 mbsf. There is no obvious lithologic or physical property change between 380 and 420 mbsf (see "Lithostratigraphy" and "Physical Properties" sections, this chapter), and the theoretical base of the gas hydrate stability zone in seawater lies at least 65 m below this depth interval. Possible explanations for this phenomenon are discussed in the "Synthesis and Significance" section (this chapter).

### *Sample Contamination by Seawater*

Seawater contamination of interstitial-water samples is not uncommon in ODP operations because seawater circulates within the borehole. In sediment columns where $SO_4^{2-}$ is depleted at shallow depth, the presence of $SO_4^{2-}$ in deep samples can be regarded as an indication of seawater contamination (e.g., Pedersen and Shimmield, 1991; Westbrook, Carson, Musgrave, et al., 1994). The irregularity of the $SO_4^{2-}$ profile below 60 mbsf would be consistent with such an interpretation. Concentrations of dissolved species can be corrected for seawater contamination in those samples that lie below the sulfate reduction zone by assuming that all $SO_4^{2-}$ comes from seawater (e.g., Westbrook, Carson, Musgrave, et al., 1994). This has been done for $Cl^-$ in Table 16. Correcting interstitial-water concentrations for seawater contamination shifts $Cl^-$ concentrations to lesser values. The shift is slight for samples at Site 994 (e.g., no $Cl^-$ concentration changes by more than 2% of absolute concentration after correction for seawater contamination). However, because deep samples are affected more than shallow samples, the shift changes the $Cl^-$ gradient between 456 and 697 mbsf from ~0.06 to 0.05 mM/m.

### *Focused Sulfate Consumption*

The linear $SO_4^{2-}$ profile in the upper 21 mbsf suggests diffusion of $SO_4^{2-}$ through the $SO_4^{2-}$ reduction zone and focused consumption of $SO_4^{2-}$ at or near the base of this zone. Of special interest to shore-based microbiology investigations is the depth of the base of the $SO_4^{2-}$ reduction zone. However, because of likely seawater contamination (discussed above), the depth at which all $SO_4^{2-}$ is consumed at Site 994 is not well defined on the basis of $SO_4^{2-}$ data alone. Borowski et al. (1994) previously have demonstrated that the depth of complete $SO_4^{2-}$ consumption in Blake Ridge sediment coincides (to within 1.5 m) with a rapid increase in the volume of $CH_4$. The increase in $CH_4$ volume in sediment at Site 994 (Table 10) begins at ~20.5 mbsf (Fig. 41) and is consistent with the inferred base of the $SO_4^{2-}$ reduction zone (~21 mbsf).

### *Storage Effects*

Discrepancies are observed between certain values at Holes 994C and 994D from the same depth interval. Water samples from Hole 994D have higher pH, $PO_4^{3-}$, and $K^+$ and lower $Ca^{2+}$, $Mg^{2+}$, $Sr^{2+}$, and $H_4SiO_4$ values than samples from Hole 994C. We assume that such interstitial-water variability does not exist between the sediment columns only 20 m apart and, therefore, must be an artifact of sample collection, processing, and storage.

Similar chemical changes were observed by Manheim and Sayles (1974) in experiments in which cores were squeezed at 4°C and resqueezed after warming to 22°C. Although Manheim and Sayles (1974) ascribed the changes to the effect of temperature on the relative cation exchange capacity of sediment, we suggest that storage is the cause of observed chemical differences between water samples at Site 994 because all samples were squeezed at the same (room) temperature. A likely mechanism for certain variability is precipitation of carbonate due to degassing of $CO_2$ (e.g., Manheim and Sayles, 1974). That is, during extended storage of samples from Hole 994D, $CO_2$ was released and carbonate precipitation was observed. This mechanism would explain the increase in pH and decrease in $Ca^{+2}$, $Sr^{+2}$, and $Mg^{+2}$ in water samples from Hole 994D relative to Hole 994C. Differences in $PO_4^{3-}$ and $K^+$ between water samples from the two holes might be related to the change in pH because the surface charge of natural particles generally is governed by the pH of the solution. The decrease in $SiO_2$ values is puzzling; Manheim and Sayles (1974) observed an increase in $SiO_2$ concentration by warming samples.

The above interpretation does not imply that the chemistry of water samples from Hole 994C is not affected by degassing. Indeed, if release of $CO_2$ is the correct interpretation for observed variability between the chemistry of waters from Holes 994C and 994D, then the chemistry of all samples collected with high $CO_2$ concentrations will be affected by $CO_2$ degassing. Samples from Hole 994D were affected more than samples from Hole 994C only because they were squeezed after a longer holding time.

## PHYSICAL PROPERTIES

The shipboard physical properties program conducted at Hole 994C included nondestructive, high-resolution measurements of GRAPE wet bulk density, bulk magnetic susceptibility, *P*-wave velocity, and NGR activity on most recovered whole-round core sections. Thermal conductivity data were collected for unsplit sections in which the sediment directly contacted the liner, including nearly all APC cores and a few XCB cores recovered close to in situ temperature measurements. Low-resolution *P*-wave velocity data were collected using a DSV at discrete locations on split sections recovered at depths shallower than 55 mbsf.

Index properties, which are summarized in Table 17, were measured on longitudinally split sections. Where sediment properties permitted, such as within intact biscuits from XCB cores, shear strength and unconfined compressive strength also were measured. Although estimation of in situ behavior was a major goal of the laboratory test program, gas expansion, drilling and coring disturbance, and perhaps gas hydrate dissociation all reduced the effectiveness of some measurements. Because of these testing difficulties, some measurements either were not performed or their results were excluded from the site summary report. However, most data are available on CD-ROM (included in the back pocket of this volume).

Cores recovered from Holes 994A, 994B, and 994D were analyzed using only the MST. Because of the incomplete nature of these data, the results for these holes are not presented here but are available on CD-ROM (back pocket).

**Table 17. Index properties of sediment samples from Hole 994C.**

| Core, section, interval (cm) | Depth (mbsf) | Water content (wet%) | Water content (dry%) | Density | | | Porosity (%) | Void ratio |
|---|---|---|---|---|---|---|---|---|
| | | | | Bulk ($g/cm^3$) | Grain ($g/cm^3$) | Dry ($g/cm^3$) | | |
| 164-994C- | | | | | | | | |
| 1H-1, 11–13 | 0.13 | 57.03 | 132.74 | 1.42 | 2.86 | 0.61 | 79.27 | 3.71 |
| 1H-1, 35–37 | 0.37 | 61.61 | 160.45 | 1.38 | 2.89 | 0.53 | 82.75 | 4.52 |
| 1H-1, 101–103 | 1.03 | 51.29 | 105.30 | 1.49 | 2.95 | 0.73 | 74.69 | 3.03 |
| 1H-2, 53–55 | 2.05 | 44.39 | 79.81 | 1.61 | 2.86 | 0.90 | 69.91 | 2.23 |
| 1H-3, 64–66 | 3.66 | 54.63 | 120.40 | 1.48 | 2.84 | 0.67 | 78.89 | 3.34 |
| 2H-1, 133–135 | 5.75 | 44.29 | 79.49 | 1.60 | 2.84 | 0.89 | 69.32 | 2.21 |
| 2H-2, 98–100 | 6.88 | 43.05 | 75.59 | 1.56 | 2.79 | 0.89 | 65.57 | 2.06 |
| 2H-3, 92–94 | 8.32 | 42.43 | 73.71 | 1.65 | 2.69 | 0.95 | 68.43 | 1.93 |
| 2H-5, 58–60 | 10.98 | 31.74 | 46.49 | 1.85 | 2.70 | 1.26 | 57.30 | 1.22 |
| 2H-6, 92–94 | 12.82 | 44.71 | 80.86 | 1.64 | 2.85 | 0.91 | 71.56 | 2.25 |

**Only part of this table is produced here. The entire table appears on the CD-ROM (back pocket).**

## Index Properties

Wet bulk density, which varies between 1.37 and 2.04 $g/cm^3$, generally increases with depth below the seafloor although major reversals of this trend occur near 50, 100, and 180 mbsf (Fig. 42). The two independent methods used to obtain wet bulk density (GRAPE and index properties) yield nearly the same values. Bulk density increases systematically from 220 to ~610 mbsf and increases more rapidly between ~610 and ~630 mbsf.

Water contents vary from 25% to 61% and from 33% to 160% based on the results of the wet and dry methods, respectively (Fig. 42). The values are highest in the uppermost 5 m of the hole, vary from 40 to 50 mbsf, and decrease to 120 mbsf. Below this depth, the wet and dry water-content values increase to 175 mbsf. Water content gradually decreases between 175 mbsf and the bottom of the hole. The porosity curve mimics the water-content data obtained using the wet method. Values vary from a maximum of 83% to a minimum of 49%. Grain density (dry method) ranges from 2.51 to 2.94 $g/cm^3$ with an average of 2.71 $g/cm^3$.

## Acoustic Velocity

Compressional acoustic velocities were measured on unsplit sections only where the sediment completely filled the liner. In most cases, the sensor recorded only the liner velocity, and the majority of the measurements were discarded. DSV measurements were only made on split sections in the uppermost 60 m of the hole, where transducers could be inserted without fracturing the sediments or where signals could be transmitted, without attenuation, from the split surface through the intact half of the core. As shown in Figure 43, the measured velocities range from 1.36 to 1.54 km/s in the interval of 0–35 mbsf. In the interval of 460–520 mbsf, scattered data yielded an estimated velocity of 1.8 km/s.

## Undrained Shear Strength

Vane shear strength of the sediment varies from 1 to 379 kPa along the hole, with a marked increase in strength at ~50 mbsf. The change in undrained shear strength at this depth correlates with changes in other index properties (e.g., water content and grain density). Below this depth, the average shear strength increases gradually, although there is considerable scatter in the data.

## Natural Gamma Radiation

NGR data obtained from whole-round sections were filtered using a 5-m-wide boxcar function where sufficient data were present. The values range from 1 to 23 counts/30 s, with an abrupt decrease in magnitude occurring in the interval 30–50 mbsf (Fig. 42). Below 50 mbsf, the curve remains practically linear with increasing depth, with a slight peak at ~360 mbsf.

## Thermal Conductivity

Thermal conductivity values, shown in Figure 44, range from 0.78 to 1.2 W/(m·K) and form two distinct groupings: Shallower than 40 mbsf the readings average 1.1 W/(m·K), whereas below that depth the average is 0.9 W/(m·K). The reduction in thermal conductivity at 40 mbsf coincides with changes in a number of other physical properties (Fig. 42).

## Physical Properties Units

On the basis of the major trends observed in the measured physical properties, five units were identified in Hole 994C (Fig. 42). Unit A, extending from 0 to 40 mbsf, is characterized by a decrease in wet bulk density, a gradual change in water content and strength, and a distinctive NGR signature. Unit B lies between 40 and 120 mbsf and is identified mainly on the basis of a progressive decrease in water content with depth and an accompanying increase in wet bulk density. Unit C (120–180 mbsf) is characterized by a linear increase in water content (wet and dry) as a function of depth and is underlain by Unit D, which extends from 180 to 610 mbsf and makes up most of the recovered core. Sediments within Unit D show a nearly linear increase in bulk density with depth and a corresponding linear decrease in water content and porosity. The boundary between Units D and E (610–703 mbsf) correlates with the change in slope of the wet bulk density curve and an accompanying change in water content and porosity.

## Discussion

Although physical properties units delineated for Hole 994C do not correlate with lithostratigraphic boundaries, both data sets show a continuous, uniform section deeper than 160–180 mbsf. This section accounts for most, if not all, of the sediments recovered between that depth and the bottom of the hole. Consistently linear trends in bulk density, water contents, and porosity in Unit D agree with the lack of clear reflectors at those depths seen in high-resolution seismic profiles of the area.

Physical properties data also indicate several other significant trends. Because grain density is nearly constant, the increase in bulk density with depth is caused by a reduction in porosity associated with overburden stress rather than an increase in the relative mass of individual mineral grains. In addition, high water content and low shear strength at the seafloor indicate that Site 994 is in an environment of normal sedimentation, unlike Site 993, which is located in an area of mass wasting.

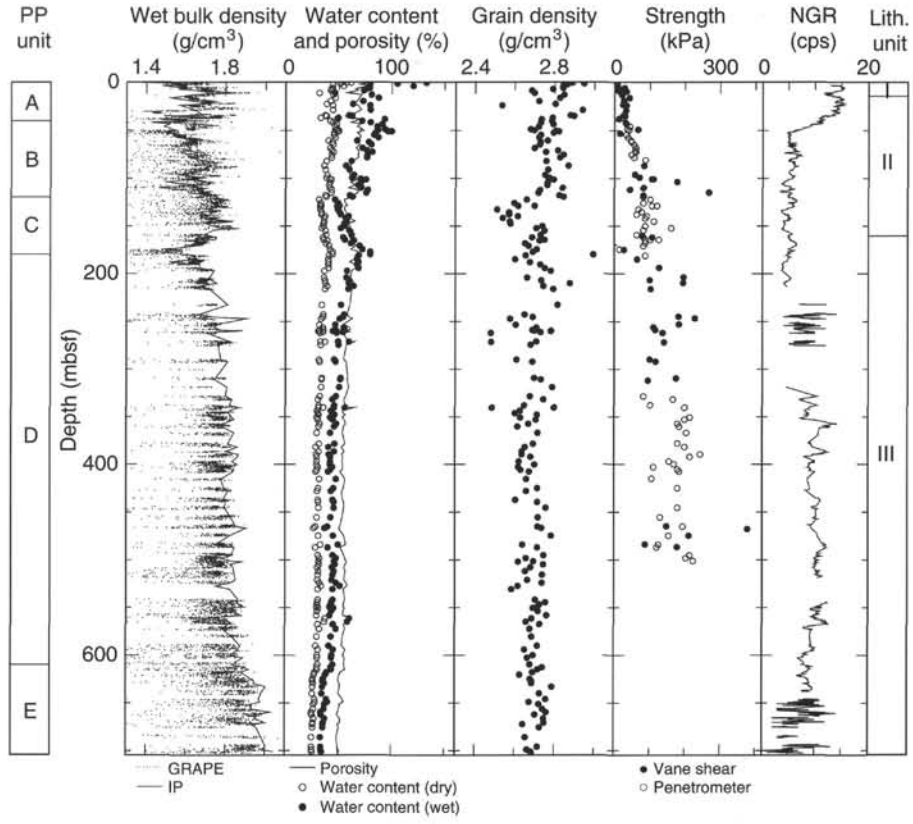


Figure 42. Summary of physical properties measurements in Hole 994C. IP = index properties data. GRAPE = gamma-ray attenuation porosity evaluator data. Grain density values have been determined using the dry method (see "Physical Properties" section, "Explanatory Notes" chapter, this volume). NGR = natural gamma radiation in average counts per second. NGR data have been smoothed with a boxcar filter at depths where sufficient data are available. NGR results plotted at depths of 240–270 mbsf and at >650 mbsf are raw data. Physical properties units delineated on the basis of variations in one or more measured parameters are shown on the left; lithostratigraphic units, on the right.

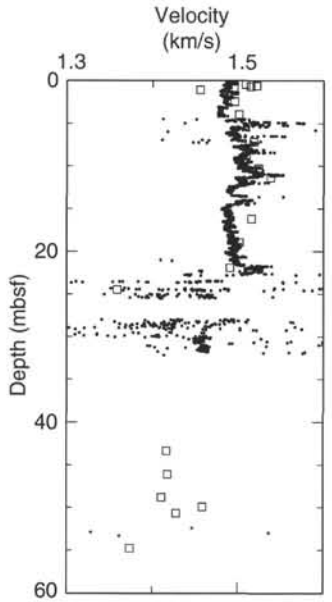


Figure 43. Acoustic velocity measurements from the uppermost part of Hole 994C. Solid circles = velocity obtained on whole-round core sections with the PWL. Open squares = measurements obtained with the DSV on split sections. For both data sets, the trend from 0 to 25 mbsf appears nearly the same as a function of depth, with both measurements showing a maximum in velocity at 12 mbsf.

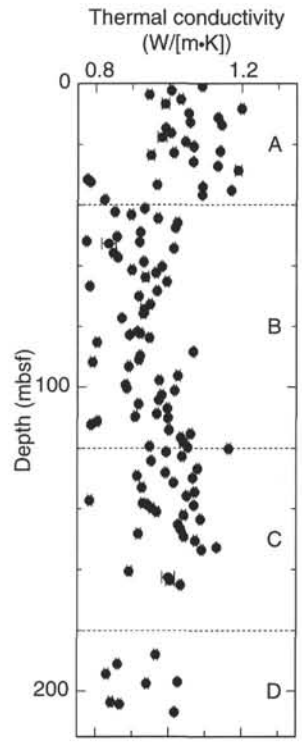


Figure 44. Thermal conductivity data obtained on sediments recovered in APC and some XCB cores from Hole 994C. The designations A through D refer to the physical properties units shown in Figure 39. These data have not been corrected for the effects of pressure or temperature. Analytical uncertainties are indicated by vertical bars.

Lithostratigraphic Unit II is characterized by higher $CaCO_3$ content relative to Unit III, and this variation in $CaCO_3$ at 180–200 mbsf may be related to some of the variations observed at the boundary between physical properties Units C and D. Trends in physical properties have often been attributed to changes in the carbonate content of sediment (Mayer, 1979; Lee, 1982).

Notably, Unit C is characterized by an increase in water contents and porosity. A breakdown of progressively greater amounts of gas hydrate in the cores with depth could account for the trend. Increasing porosity with depth also is noticed at similar depths in the well-log data at this site (see "Downhole Measurements" section, this chapter).

## GEOPHYSICS

### Vertical Seismic Profile Experiment Design

ZO- and W-VSP data were acquired in Hole 994D in five lowerings of the modified Geospace Model WLS three-component borehole seismometers (see "Operations" section, this chapter). Two W-VSPs were acquired at 482 and 650 mbsf, and one 34-station ZO-VSP was acquired at 110–650 mbsf (Table 18). Difficulties with the clamping arm drives of the tools dictated an unusual experimental procedure from 571 to 110 mbsf in which the sonde was suspended without clamping at 20-m intervals in the hole. Real-time monitoring of geophone channels on the oscilloscope in the Underway Geophysics Lab confirmed that, during interludes of low ambient noise, downgoing signals were readily discernible on the unclamped geophone.

Figure 45 shows the design of the VSP experiment. The source depths of 5 m for the 300-in$^3$ Bolt Model PAR1500 air gun and 3 m for the 400-in$^3$ Seismic Systems Model P400 water gun provide optimal pulse shape (Shipboard Scientific Party, 1989). The guns were fired alternately during acquisition of the ZO-VSP; a suspended single-element hydrophone was used to record the downgoing waveform. W-VSPs recorded a 150-in$^3$ SSI generator-injector gun fired at 15-s intervals from the *Cape Hatteras*.

**Table 18. Depths of vertical seismic profile stations, type of clamp, and number of traces picked for traveltime calculations.**

| Depth (mbsf) | Clamp | Number of traces |
|---|---|---|
| 110 | Suspended | 0 |
| 130 | Suspended | 0 |
| 150 | Suspended | 0 |
| 170 | Suspended | 0 |
| 190 | Suspended | 0 |
| 210 | Suspended | 0 |
| 230 | Suspended | 0 |
| 250 | Suspended | 2 |
| 270 | Suspended | 5 |
| 290 | Suspended | 1 |
| 310 | Suspended | 5 |
| 330 | Suspended | 4 |
| 350 | Suspended | 6 |
| 370 | Suspended | 10 |
| 390 | Suspended | 10 |
| 410 | Suspended | 8 |
| 430 | Suspended | 11 |
| 450 | Suspended | 11 |
| 470 | Suspended | 16 |
| 482 | Clamp | 24 |
| 490 | Suspended | 3 |
| 493 | Clamp | 2 |
| 510 | Suspended | 4 |
| 530 | Suspended | 2 |
| 550 | Suspended | 3 |
| 571 | Suspended | 1 |
| 585 | Clamp | 10 |
| 594 | Clamp | 19 |
| 605 | Clamp | 7 |
| 607 | Bridge | 8 |
| 627 | Bridge | 10 |
| 635 | Clamp | 10 |
| 645 | Clamp | 9 |
| 650 | Clamp | 9 |

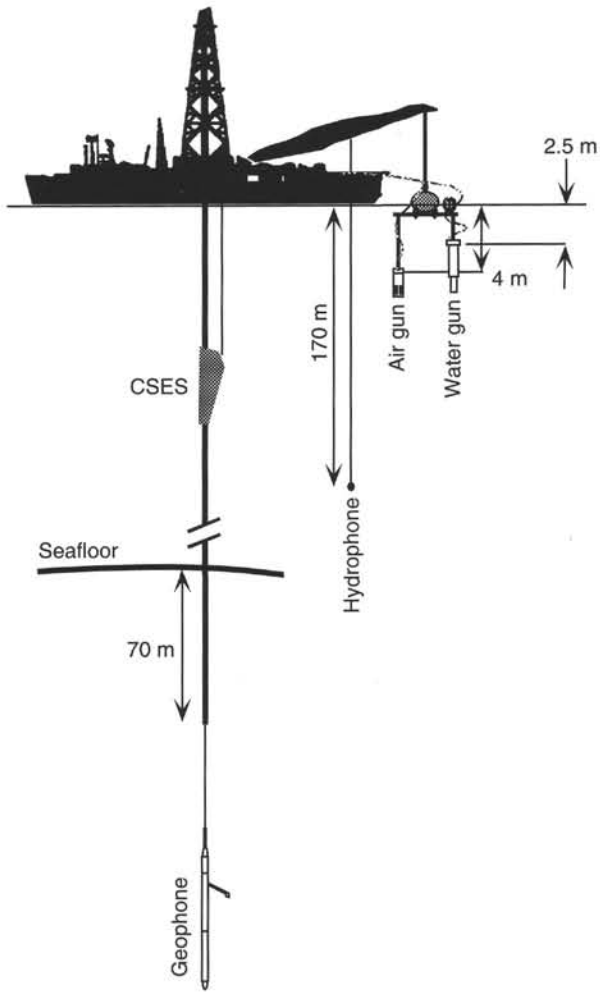


One-way time from water surface =

$$\text{event time} + \frac{\text{gun depth}}{\text{water velocity}} - \text{trigger delay (10 ms)}$$

Station depth (mbsf) = wire out (m) – water depth (m)

Figure 45. Schematic layout of a ZO-VSP experiment. Both the air and water guns were suspended from a float to maintain consistent depth. The number 3 crane near the port stern was used to tether the floated sources and support the source monitor hydrophone. CSES = conical side-entry sub.

At Site 994, difficulty was encountered in getting the tool down to the bottom of the hole, presumably because of the hole closing in and/or rock debris in the hole. Installing the CSES in the drill string allowed us to lower the drill pipe with the tool inside the pipe to the bottom of the hole. The tool was then lowered out of the bottom of the drill string, assisted by pumping, and the pipe was raised at least 30 m above the tool. The tool was then clamped and raised at the prescribed intervals, with the pipe being raised a stand at a time as required to stay above the tool. Although the drill pipe is generally a source of noise and, therefore, usually kept as far up the hole from the tool as feasible, in this case it provided the needed mechanism for getting the tool to depth and did not appear to be a significant source of noise. This suggests that the hole was filled with material that kept the pipe from "rattling."

### Data and Processing

The data were recorded on Reftek Model 72A-08/G digital acquisition systems (see "Geophysics" section, "Explanatory Notes" chapter, this volume) and archived on Exabyte tape in both Reftek refdump and SEG-Y format. Record sections were constructed by pulling 10 s of data from the recorded time series beginning at each shot instant. Data from clamped stations show high signal-to-noise ratios (Fig. 46); data from unclamped stations are considerably noisier, but downgoing arrivals are clear nonetheless (Fig. 47).

All data were contaminated with a strong bias and 60- and 180-Hz noise, which were removed with appropriate filters. The periodic components stacked across traces because the shot time randomization procedure resulted in shot times at multiples of 0.1 s, exactly six cycles at 60 Hz. The source of this noise was unclear; the ship's generators use time-varying frequencies, which typically are slightly higher than 60 Hz. There was less than a 1 mV root-mean-square (RMS) ripple on the pre-amplifier and Reftek power supplies. On the next VSP program at Site 995, we took steps to better randomize the shot times and eliminate this problem. Hydrophone data were additionally contaminated with noise at multiples of 15 Hz throughout the frequency spectrum. Because the hydrophone was close to the sources, this noise was several orders of magnitude smaller than the signal and was ignored.

After filtering, low-noise traces from each station were selected and stacked (Fig. 48). A 60-Hz notch filter and predictive deconvolution with a prediction length of 0.0167 s were applied to the stacked section. The downgoing first arrival is clear.

### Preliminary Results

Individual arrival times were picked before stacking to provide some statistics on the standard error of picked arrival times. Picking errors were ±0.0012 s (1 standard deviation) for both clamped and unclamped stations. The two stations at 607 and 627 mbsf, where the tool appeared to rest unclamped on "bridges" in the hole, were deemed to have unreliable depths and were excluded from the velocity inversion, as were data from <250 mbsf, which have low signal-to-noise ratios. A preliminary velocity-depth function was produced by inverting the first-arrival times using a weighted, damped, least-squares inversion that weights mean traveltimes by the inverse of their standard error. The velocity-depth curve in Figure 49 was produced by assigning equal weight to fitting the traveltime data and to producing a smooth velocity-depth function. The two principal features of the velocity model are a rapid velocity increase at 300–330 mbsf from ~1600 to 1800 m/s and a prominent low-velocity zone at 560–650 mbsf in which velocity decreases from ~1850 to 1550 m/s. This anomalously low velocity is almost certainly due to the presence of free gas in this interval.

A plot of two-way traveltime vs. depth (Fig. 50) for Site 994 was produced by doubling the observed one-way traveltimes of first arrivals on the stacked VSP section and adding 4 ms to account for the depth of the guns. The resulting plot provides a direct means of relating two-way traveltime on surface seismic data to depth.

## DOWNHOLE LOGGING

### Introduction

The primary objective of the downhole logging program at Site 994 was to obtain in situ physical property and geochemical data from an area where gas hydrate may exist but no BSR is observed. Site 994 was selected as a "baseline" location from which the effects of gas hydrate occurrence could be evaluated along the Blake Ridge transect. The presence of gas hydrate in the recovered cores (see "Gas Hydrate" section, this chapter), however, reduced the value of Site

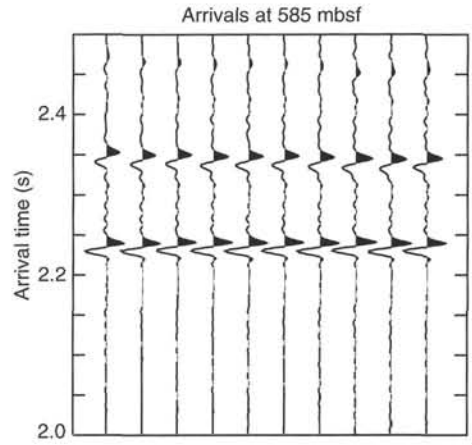


Figure 46. Air gun shots recorded on the vertical component of a clamped geophone at 575 mbsf in Hole 994D, showing clear downgoing arrivals. Second and third events are bubble pulses.

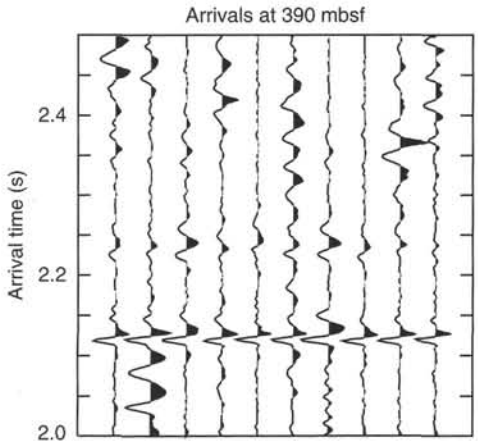


Figure 47. Air gun shots recorded on the vertical component of an unclamped geophone at 390 mbsf in Hole 994D. Despite the lower signal-to-noise ratio of unclamped traces, first-arrival times can be accurately measured.

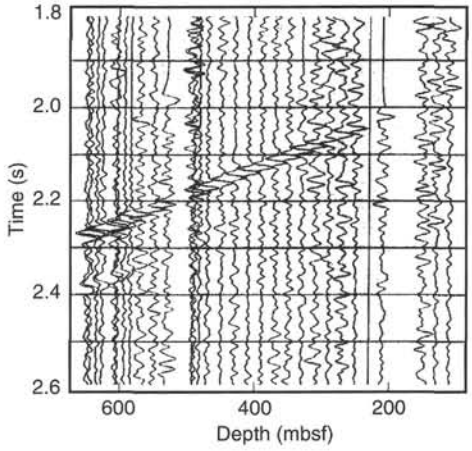


Figure 48. Stacked VSP section from Hole 994D created by selecting traces with low ambient noise, stacking common depth gathers, notch filtering at 60 Hz, and applying a noise-reduction filter that zeroes sample values in windows in which RMS amplitudes exceed a selected threshold value. First-arrival trajectory is clearly visible.

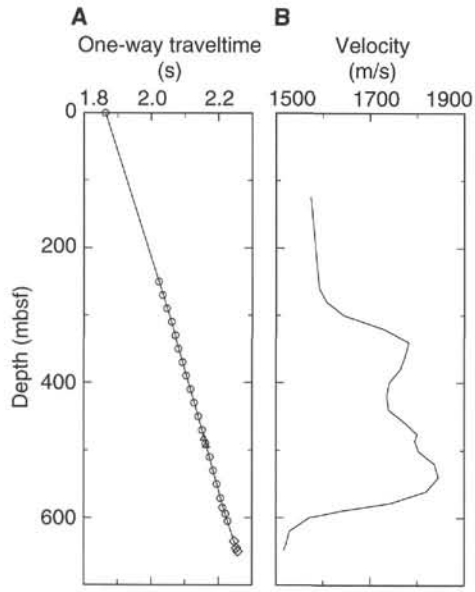


Figure 49. **A.** Observed traveltimes of downgoing first arrivals (open symbols) and traveltime fit calculated from velocity-depth model (solid line) in Hole 994D. Different symbols represent data acquired during different lowerings of the WHOI VSP tools. **B.** Velocity-depth function for Hole 994D computed by weighted, damped least-squares inversion of first-arrival times using a smoothness constraint. Velocities increase markedly from 290 to 340 mbsf and decrease sharply at 590 mbsf.

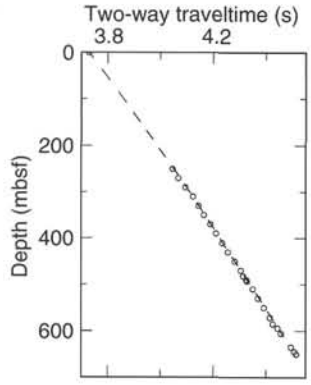


Figure 50. Two-way traveltime vs. depth from VSP measurements (open circles) and from integrated sonic log velocities (dashed line) for Hole 994D. This plot provides a means of correlating two-way traveltime on vertical-incidence seismic sections to depth.

994 as a "baseline" data source, but it has made it an invaluable source of direct gas hydrate data.

At Site 994, Holes 994C and 994D were logged with several different tool strings (see "Operations" section, this chapter). Hole 994C was logged with a Schlumberger Quad-combo tool over the interval from 76.0 mbsf (base of drill pipe) to 450.0 mbsf, and the depth interval between 52.0 mbsf (base of drill pipe) to 320.0 mbsf was logged with the geochemical combination tool. In addition to the normal acquisition of capture-$\tau$ neutron geochemical data, a series of 13 inelastic neutron geochemical measurements was made in a suspected gas hydrate–bearing stratigraphic section. The LDEO-TLT was run with the Quad-combo tool string. A second run (run 2) of the Quad-combo tool was attempted in Hole 994C, but the tool failed to pass a bridge near 510 mbsf; only temperature data were collected. Bridging of the borehole prevented the Quad-combo from going below 462.0 mbsf on run 1 in Hole 994C. The GLT was unable to pass the depth of 330.0 mbsf in Hole 994C. Borehole conditions prevented us from logging the entire hole (total penetration of 703.5 mbsf) or conducting additional surveys (see "Operations" section, this chapter).

Because of borehole stability problems in Hole 994C, the CSES was deployed before logging Hole 994D (total penetration of 670.0 mbsf). Borehole bridging prevented logging in Hole 994D below 630.0 mbsf. In Hole 994D, a modified Quad-combo tool string was run over the interval from 114.0 to 618.0 mbsf. However, the CNT-G was removed from the tool string and the SDT device was replaced with the LSS. The new LDEO-SST was deployed at the end of the logging program in Hole 994D. This was the first ever ODP deployment of the LDEO-SST, and the depth interval from 191 to 613 mbsf was logged successfully.

## Log Quality

The quality of the log measurements at Site 994 was significantly degraded by the size and rugosity of the borehole. The caliper logs in Holes 994C and 994D (Fig. 51) show borehole diameters greater than the 43.7-cm (17.2 in) maximum range of the caliper for a large portion of both holes. The upper 200 m of each hole is similar in size, with borehole diameters exceeding the maximum caliper opening. Below 200 m, however, Hole 994C is characterized by a more severe rugosity problem.

The NGT, HLDT, and CNT-G tools are particularly susceptible to adverse effects from large and irregular hole diameters. The NGT logs from Holes 994C and 994D are highly degraded because of borehole size and rugosity, so their use has been limited to depth corrections between log runs and to interpret general lithologic trends. The HLDT, which is an excentered device, has a caliper arm that forces the tool against the wall of the borehole. However, if the hole is larger than the maximum reach (43.7 cm) of the caliper arm, the density tool may lose contact with the formation. The density log was degraded in both Holes 994C and 994D because of poor tool contact with the borehole wall. Data from the density log have been used to assess general lithologic trends but not for porosity calculations (see "Porosity Calculations," this section). The CNT-G is severely affected by enlarged boreholes and has been disregarded in our initial interpretation (see "Porosity Calculations," this section). The sonic (SDT/LSS) and resistivity (DITE-SFL) logs provided useful information in both holes; however, both of these devices may be affected by the presence of gas hydrate. The GLT provides useful information; however, the GLT measurements also have been degraded by the enlarged borehole conditions. Data from the GLT have been used sparingly in our initial interpretation because of data-quality concerns and the need for standard shore-based processing. The "modified" Quad-combo surveys in Holes 994C and 994D were recorded at a cable speed of 457 m/hr, which yields standard-resolution data. Whereas the GLT was run at a cable speed of 183 m/hr, the LDEO-SST was recorded at a 270 and 335 m/hr cable speed. A summary of the logging tool strings used during Leg 164 and discussion of their measurement principles are provided in the "Downhole Logging" section in the "Explanatory Notes" chapter (this volume).

The "modified" Quad-combo logs for Holes 994C and 994D are shown at the end of this chapter. In comparison, the log data from Hole 994D are of superior quality; therefore, we decided to focus our initial interpretive efforts on the data from Hole 994D.

Shipboard data editing was limited to depth shifting and the removal of some out-of-range data. Establishing consistent depths for each of the logs was accomplished by correlating the natural gamma-ray logs. The absolute depths, relative to seafloor, for all logs were fixed by identifying the gamma-ray signal associated with the seafloor and depth shifting the log data appropriately. The natural

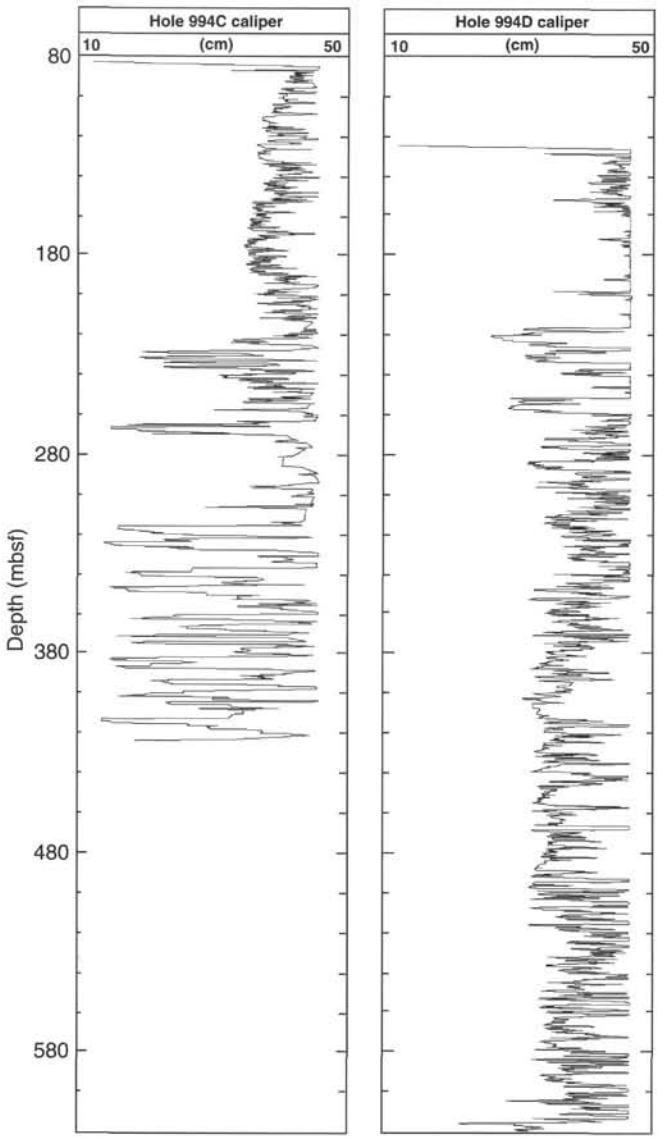


Figure 51. Caliper logs recorded from the HLDT in Holes 994C and 994D.

gamma-ray log pick for the seafloor in Holes 994C and 994D are 2810 and 2809 mbsl, respectively. Because the logs were measured from the dual elevator stool, which is located 11.4 m above sea level, the actual log-determined water depth at Holes 994C and 994D was 2798.6 and 2797.6 mbsl, respectively, which is 0.5 and 1.5 m less than the water depth of 2799.1 m (zero core depth) determined by the drillers. Out-of-range log measurements were removed from our working log database. These deletions were limited to data from within the drill pipe or near the bottom of the hole.

## Logging Units

The description of the logged interval in Hole 994D is divided into three logging units on the bases of obvious changes in the natural gamma ray (NGT), bulk density (HLDT), sonic velocity (LSS/SDT), and electrical resistivity measurements (DITE-SFL) (Fig. 52). The elemental yield data from the Hole 994C geochemical log (GLT) was also evaluated for lithologic changes (Fig. 53). Elemental yield data (uranium, thorium, and potassium) from the NGT have been used to assess the mineralogy of the sediments in the delineated logging units (Fig. 54).

### *Log Unit 1 (114.0 mbsf [base of pipe] to 212.0 mbsf)*

This interval between the base of the pipe (114.0 mbsf) and 212.0 mbsf is characterized by relatively low gamma-ray, density, velocity, and resistivity log values. All of the recorded logs are affected by the enlarged borehole, which exceeds the maximum recording size (43.7 cm) of the caliper throughout most of Unit 1. The gamma-ray log shows an abrupt upward step in value at the boundary between Unit 1 and Unit 2. The caliper log (Fig. 51) shows that the hole diameter is greatly reduced across the boundary from Unit 1 to Unit 2. We interpret the gamma-ray log to indicate that the hole is much larger than 43.7 cm just above the boundary between Units 1 and 2. We also note that the natural gamma-ray log and caliper log are inversely correlated. An expanded display of the logs shows that at a fine scale the caliper and gamma-ray logs both change at this boundary but that the other logs are constant or change smoothly across this boundary. The bulk density and acoustic velocity ramp up more gradually across the boundary between Units 1 and 2. The gamma-ray logs from the GLT in Hole 994C (Fig. 53) do not show the abrupt upward step in value at the boundary between Units 1 and 2 (depth of 212.0 mbsf). The caliper log (Fig. 51) from Hole 994C does not show a significant change in hole size at the boundary between Units 1 and 2, unlike the dramatic change in Hole 994D (Fig. 51).

Elemental yield data depicted in Figure 53 reveal no significant changes at the boundary between Units 1 and 2. Within Unit 1, the weight percentage of potassium (K) and aluminum (Al) are relatively low and remain constant. The elemental lithology indicator ratios LIR [Si/(Si+Ca)] and IIR [Fe/(Si+Ca)] are used to assess the relative amounts of carbonate, silica, and clay. Decreases in LIR suggest the increasing presence of carbonates, whereas increasing values indicate more silica. Increases in IIR suggest the presence of more clays. Within Unit 1, IIR remains relatively constant, suggesting little changes in clay content. LIR in Unit 1 shows a gradual increase with depth, thus indicating a relative decrease in the carbonate content of the sediments. There are several anomalous LIR values that need to be further evaluated near 100 mbsf. K and thorium (Th) elemental yields (Fig. 54) reveal that the clays in Unit 1 of Hole 994C are predominately montmorillonites and some illites. Photoelectric data from the formation density device in Hole 994C indicate the presence of mostly montmorillonites.

### *Log Unit 2 (212.0–428.8 mbsf)*

Unit 2 is characterized by increasing velocities (1.65 km/s at the top to 1.80 km/s at the bottom) with depth. The natural gamma-ray, bulk density, and electrical resistivity values are nearly constant throughout Unit 2, except for three conspicuous high electrical resistivity intervals between 216 and 264 mbsf. Both the acoustic velocity and resistivity logs are characterized by a distinct baseline shift to relatively higher values throughout Unit 2. At the base of Unit 2, across the boundary into Unit 3, the acoustic velocity and resistivity logs step down to lower values.

Relative to Unit 1, the gamma-ray logs (Fig. 53) from Unit 2 in Hole 994C reveal a more variable lithologic section. Within the depth interval from ~225 to ~240 mbsf, the gamma-ray logs reveal an interval of higher gamma-ray values. The relative amounts of K and Al also are elevated within the interval between 225 and 240 mbsf. The increase in Al concentrations may suggest the presence of relatively more clay; however, the IIR elemental ratios for this interval do not support this interpretation. The borehole caliper from Hole 994C shows the interval from 225 to 240 mbsf to be relatively constricted, which is a characteristic of "swelling" clays with a high cation-exchange capacity such as montmorillonite. Analyses of the LIR elemental ratios suggest that there is an increase in the relative carbonate content of the sediments in Unit 2 with the highest amounts being detected at 255 mbsf, which is near the depth where gas hydrate was recovered in a core (see "Gas Hydrate" section, this chapter). Analy-

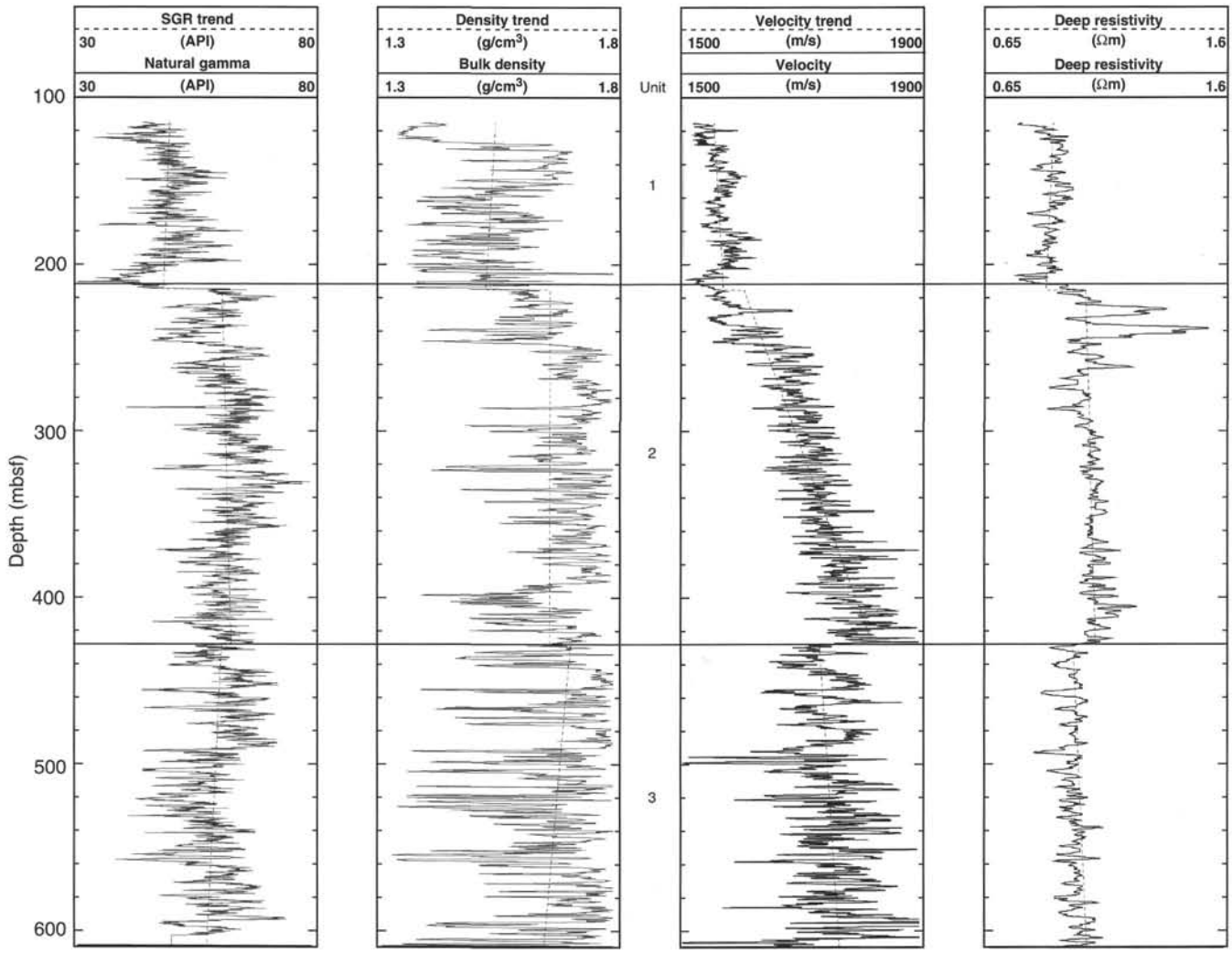


Figure 52. Log data from Hole 994D. Data shown include the natural gamma-ray log from the NGT, bulk density data from the HLDT, acoustic velocity data from the LSS, and deep-reading electrical resistivity data from the DITE. Also shown are the depths of logging Units 1, 2, and 3. Linear trends have been projected for the displayed log data.

ses of K and Th elemental yields (Fig. 54) suggest that the clays are mostly montmorillonites.

### *Log Unit 3 (428.8–618 mbsf [end of log run])*

Unit 3 is characterized by consistently lower velocities and resistivities with respect to Unit 2. An anomalous low velocity interval is seen from 492 to 508 mbsf; velocities within this anomalous interval decrease to 1.5 km/s, which suggests the presence of a highly attenuating, low-velocity region. The natural gamma-ray and density logs show decreasing values with depth in Unit 3, which is opposite the normal sediment consolidation trend. Electrical resistivity in Unit 3 slightly increases with depth, which is more characteristic of a normal compacting sedimentary section.

## Porosity Calculations

Sediment porosities can be calculated from numerous borehole measurements. At Site 994 we have attempted to use data from the neutron porosity (CNT-G), bulk density (HLDT), acoustic velocity (LSS/SDT), and electrical resistivity (DITE-SFL) logs to calculate sediment porosities. Most standard techniques for calculating log-derived porosities have been developed for lithified "clean" sandstone and carbonate systems with little or no clay fraction. Log porosity calculations in unconsolidated clay-rich marine sediments are often severely hampered by adverse borehole conditions and the lack of previous quantitative studies.

### *Neutron Porosity Calculations*

The neutron porosity log (CNT-G) measures the amount of hydrogen within the pore space of a sedimentary sequence, which is largely controlled by the amount of water that is present. The CNT-G has two pairs of detectors that indirectly measure both epithermal (intermediate energy level) and thermal (low energy) neutrons, which provide two porosity measurements. The display of both epithermal and thermal porosity logs from Hole 994C in Figure 55 reveals an average thermal porosity of ~50%, whereas the epithermal porosity averages

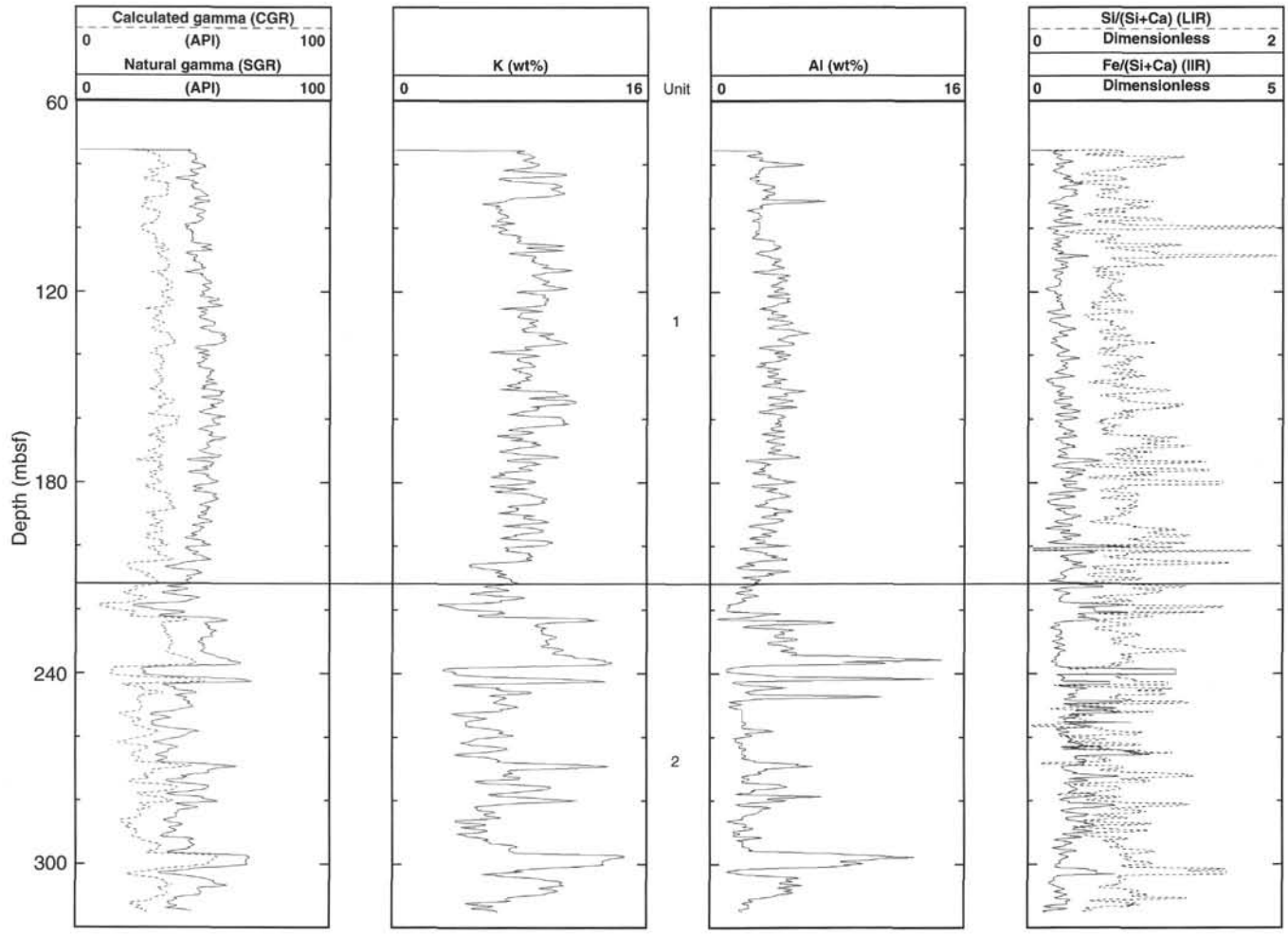


Figure 53. GLT data from Hole 994C (74.0–320.0 mbsf). Data shown include the total natural gamma-ray (SGR) and computed gamma-ray (CGR = SGR – uranium concentration) measurements. Potassium and aluminum concentrations are shown in weight percentage. LIR and IIR are lithology indicator ratios. Also shown is the depth of the boundary between logging Units 1 and 2.

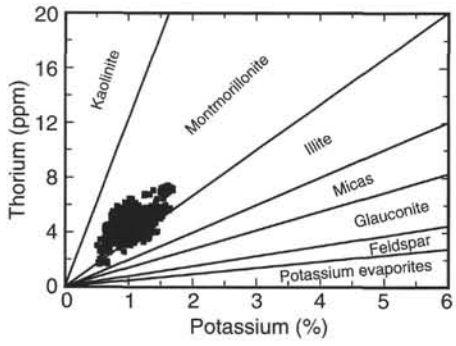


Figure 54. Lithology crossplot (modified from Schlumberger, 1989) of potassium and thorium elemental concentrations from the GLT in Hole 994C. All of the K-Th data from the logged interval (74.0–320.0 mbsf) are shown.

~100%. The thermal and epithermal porosity logs are calibrated to read 50% and 100%, respectively, in water (no sediment). Therefore, it is likely that the neutron log in Hole 994D only detected the hydrogen in the borehole waters, and the porosity data from the neutron log is of no value. In standard industry applications, the CNT-G is run with a bowspring that keeps the tool near the wall of the hole, thus reducing the effects of an enlarged borehole. Because of the size limitation of running the logs through the drill pipe, it is impossible to use a bowspring on the CNT-G in ODP holes.

### *Density Porosity Calculations*

The density log (HLDT) measurements of bulk density ($\rho_b$) from Hole 994D (Fig. 56) were used to calculate sediment porosities ($\varnothing$) using the standard relationship $\varnothing = (\rho_b - \rho_m)/(\rho_w - \rho_m)$ (Schlumberger, 1989). Water density ($\rho_w$) and grain density ($\rho_m$) were assumed to be 1.05 and 2.75 g/cm$^3$, respectively, based on index measurements of recovered core (see "Physical Properties" section, this chapter). The resulting porosity calculations yielded unreasonably high values ranging from 60% to 80%, which appear to be caused by the enlarged borehole. Sensitivity to variations in grain density ($\rho_m$) were evaluated over the range from 2.70 to 2.85 g/cm$^3$; calculated porosities varied by less than 5% and remained out of the range of expected values. The effect of the borehole can be removed from the measured density data, but this correction requires an additional porosity data source that is not available; therefore, the density log was not used to calculate porosities.

### *Acoustic Velocity Porosity Calculations*

The empirical Wyllie time-average equation (Schlumberger, 1989) was used to calculate porosities ($\varnothing$) from the measured acoustic well-log velocities ($t_{log}$) (Fig. 56). In the standard time-average re-

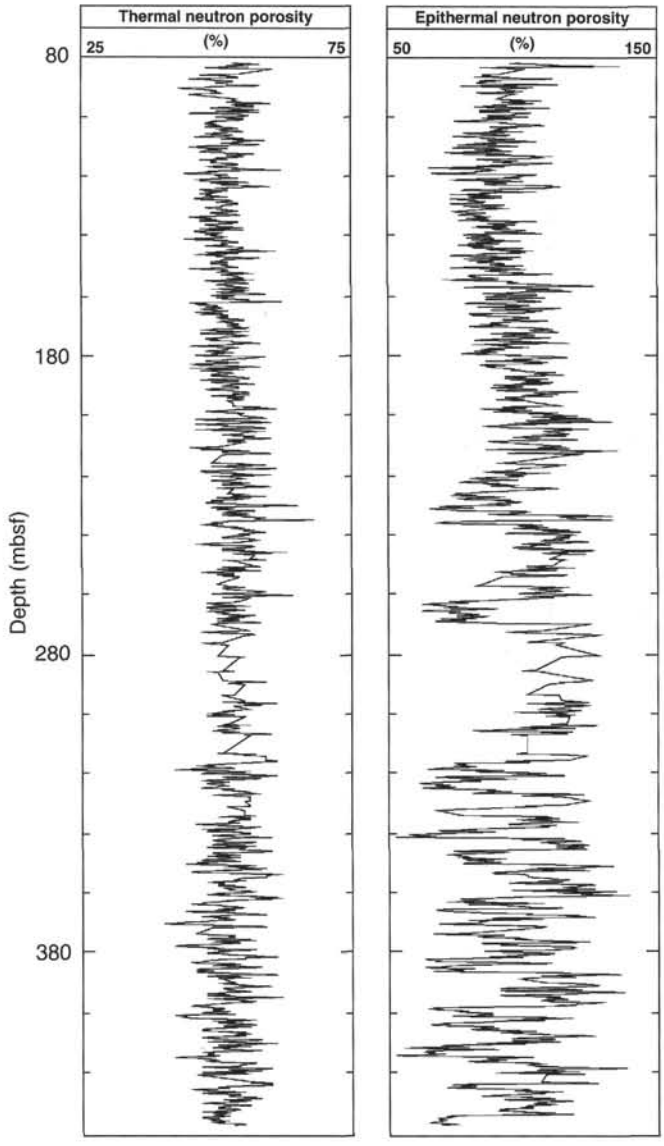


Figure 55. Thermal and epithermal porosity data from the CNT-G in Hole 994C.

lationship, $\varnothing = (t_{log} - t_m)/(t_w - t_m)$, where water velocity ($t_w$) and matrix velocity ($t_m$) were assumed to be 1.50 and 3.40 km/s, respectively. The resulting velocity porosity calculations yielded unreasonably high values ranging from 70% to 90%. Sensitivity to variations in matrix velocity ($t_m$) was evaluated over the range of 3.40–4.37 km/s; calculated porosities varied by less than 2% and remained out of the range of expected values. Several workers have shown that the observed velocity behavior of unlithified marine sediments is not always consistent with the prediction of the time-average equation. As discussed in the "Downhole Logging" section in the "Explanatory Notes" chapter (this volume), the Wood acoustic equation, which is a good approximation for matrix particles in suspension, could be used to overcome the limitation of the time-average equation. However, the Wood acoustic equation is dependent on reliable bulk density log measurements, which are not available at Site 994. An additional concern at Site 994 is the presence of gas hydrate, which often is associated with significantly higher acoustic velocities and "apparent" decreases in porosities calculated from the acoustic data. Because of the limitations of available velocity-porosity mathematical relations and because of the potential occurrence of gas hydrate, we have not used the acoustic velocity data from Site 994 to calculate porosities.

### *Electrical Resistivity Porosity Calculations*

One approach to obtaining porosities from well logs is to use the electrical resistivity logs (deep-reading resistivity device [RILD]) and Archie's relationship between the resistivity of the formation ($R_t$) and porosity ($\varnothing$): $R_t/R_w = a\,\varnothing^{-m}$, where $a$ and $m$ are parameters to be determined and $R_w$ is the resistivity of the pore waters (Archie, 1942). We have used this relationship by assuming a pore-water salinity of seawater (32 ppt) and calculating the resistivity of seawater ($R_w$) as a function of temperature in the formation using Arp's formula (Schlumberger, 1989) and a geothermal gradient of 3.85°C/100 m (seabed temperature of 3°C). To determine the parameters $a$ and $m$, we used the measured log resistivities and the porosities measured in the Physical Properties Laboratory (Fig. 57) for the depth intervals 100–200 mbsf (Unit 1) and 500–600 mbsf (Unit 3). We determined linear trends for the log resistivities and core-derived porosities in these two intervals from which we calculated representative resistivities and porosities. From these representative values, we calculated the slope, $m$, and the intercept, $\ln a$, of the function $\ln (R_t/R_w) = -m \ln \varnothing + \ln a$. Given these parameters ($a = 0.1$; $m = 6.5$), we then calculated porosity from the resistivity log using Archie's relationship. The result of this calculation is the porosity log shown in Figure 56. The calculated resistivity porosities should be considered "apparent" porosity values because we have assumed that all of the void spaces within the sediments are filled with water with the same salinity as seawater (32 ppt), which may not be true. The Archie parameters ($a$ and $m$) calculated for Hole 994D are not within the normal range of expected values (Schlumberger, 1989). The limited range of reported core-derived porosities have made it difficult to statistically constrain the calculated Archie parameters ($a$ and $m$); however, the resultant resistivity-derived porosities appear to be valid.

In Hole 994D, we see decreasing porosity with depth (Fig. 56), although this is not the normal exponential consolidation trend that would be expected if the pore space were decreasing with depth primarily from the weight of increasing overburden; instead, we see an almost linear decrease with depth in Units 1, 2, and 3. Relative to Units 1 and 3, Unit 2 exhibits a baseline shift to higher resistivities and lower calculated resistivity porosities. The assumption that all of the pore space within the sediments of Unit 2 is filled with water with the same salinity as seawater (32‰) may be invalid. Some of the pore space in Unit 2 may be occupied by gas hydrate, which exhibits very high electrical resistivities and would contribute to an "apparent" reduction in resistivity derived porosities. A comparison between core and log measurements of bulk density and porosity was made with the data from Site 994 (Fig. 57). Core measurements from Hole 994C and log measurements from Hole 994D of bulk density are similar; however, the core-measured densities are generally greater than the downhole measurements. In most cases, downhole measurements of bulk density yield values greater than the laboratory-derived values. The reason for the lower laboratory values is usually attributed to core disturbance during recovery and "core rebound." The apparent low downhole-measured bulk densities are likely caused by the enlarged hole sizes encountered at Site 994. Core porosities also are similar to the log-derived porosities. However, within the upper part of the hole (above 200 m), the core porosities are consistently greater than the log values. The resistivity derived porosities shown in Figure 56 are relatively less affected by poor borehole conditions. Thus, the resistivity-derived log and core-derived porosities agree more closely than the bulk density data. Thus, the resistivity porosity log in Figure 56 is the best downhole-derived porosity log from Site 994.

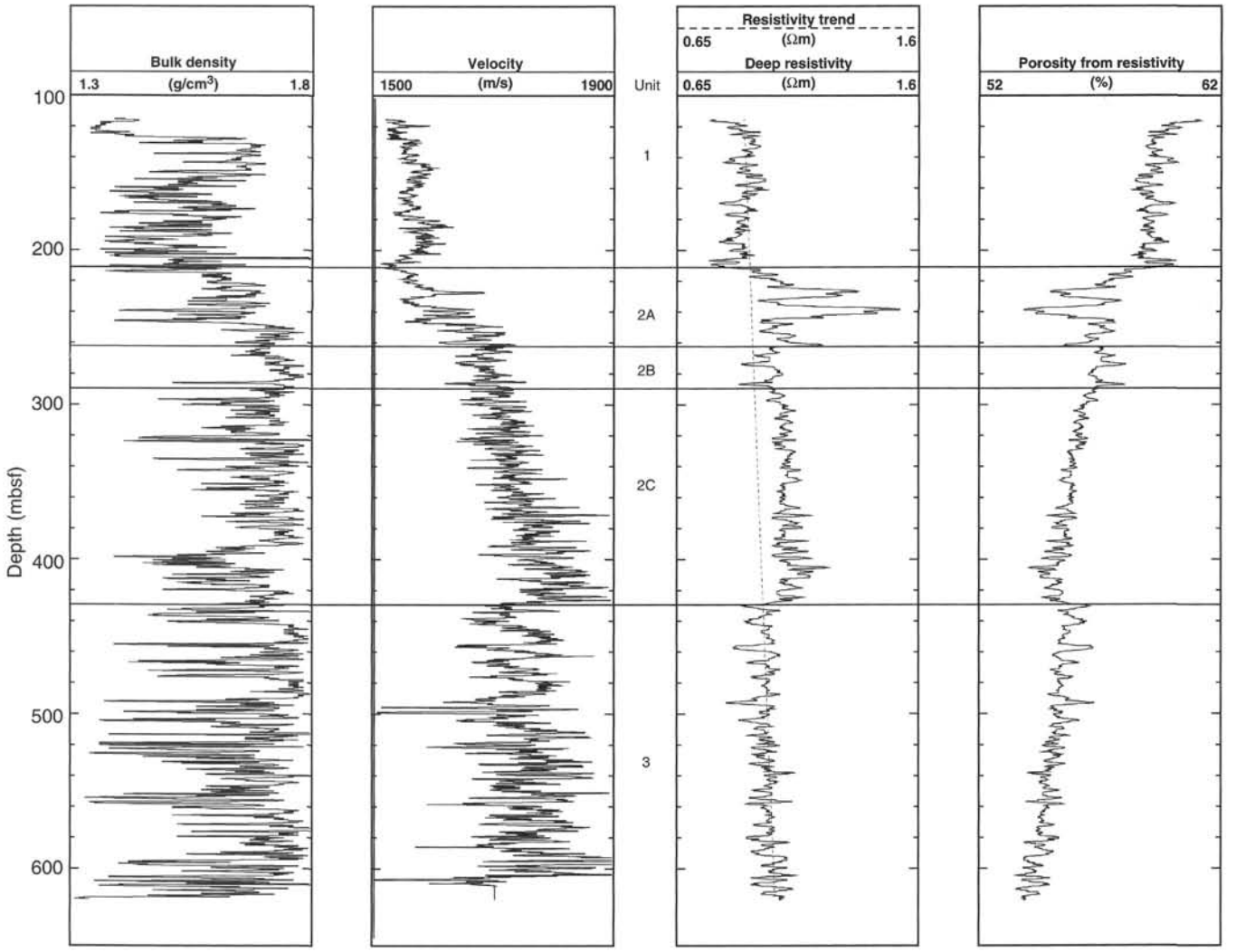


Figure 56. Log data used to calculate porosities in Hole 994D. Data shown include bulk density data (RHOB) from the HLDT, acoustic velocity data from the LSS, deep-reading, electrical resistivity data (IDPH) from the DITE, and porosity as calculated from the resistivity log. Also shown are the depths of logging Units 1, 2, and 3.

## Gas Hydrate

Collett et al. (1984; 1988), Mathews (1986), and Prensky (1995) have provided a comprehensive review of gas hydrate well-log evaluation techniques. Confirmed natural gas hydrate occurrences are generally characterized by the release of unusually large concentrations of methane during drilling and an increase in log-measured acoustic velocities and electrical resistivities. Gas hydrate–bearing stratigraphic sections exhibit relatively high electrical resistivities because some of the available pore space is filled with a solid nonconductor (i.e., gas hydrate) (Pearson et al., 1983). Because hydrate is an electrical insulator, its presence in a stratigraphic section can be electrically detected and quantified. Gas hydrate–bearing horizons also exhibit rapid acoustic velocities because some volume of the pore space is occupied by solid gas hydrate that is characterized by acoustic velocities nearly twice that of water (reviewed by Prensky, 1995). As discussed in the "Downhole Logging" section of the "Explanatory Notes" chapter (this volume), other well-log measurements, including bulk density, neutron porosity, and natural gamma ray, are not significantly affected by the presence of gas hydrate.

In comparison to logging Units 1 and 3 in Hole 994D, logging Unit 2 (212.0–428.8 mbsf) is characterized by a distinct stepwise increase in both electrical resistivity (increase of ~0.1 Ωm) and acoustic velocity (increase of ~0.1 km/s) (Fig. 58). In addition, the RILD reveals a series of three anomalously high resistivity units from 216 to 264 mbsf. Within this interval of anomalously high resistivities, gas hydrate was recovered (see "Gas Hydrate" section, this chapter). For the purpose of this discussion, we have further subdivided logging Unit 2 into three additional units: 2A, 2B, and 2C (Fig. 58). The three anomalously high resistivity units have been identified as logging Units $2A_1$, $2A_2$, and $2A_3$ (Fig. 58). In comparison, the resistivity log values are almost constant throughout logging Units 2B and 2C, whereas the acoustic velocities increase with depth over the same interval. Further comparisons show that the high electrical resistivity nature of Units $2A_1$, $2A_2$, and $2A_3$ do not correlate to any apparent velocity anomalies. Examination of the natural gamma-ray and bulk density logs (Fig. 52) reveals no apparent lithologic causes for the observed velocity and resistivity increases in Unit 2. As previously discussed, the log break in the recorded gamma-ray and density logs at the top of Unit 2 (212.0 mbsf) is caused by a dramatic change in the size of the borehole. The above observations are consistent with a material of increased resistivity and acoustic velocity, but similar density, that replaces some of the pore water in Unit 2. The depth of the boundary between Units 2 and 3 (428.8 mbsf) is in rough accord

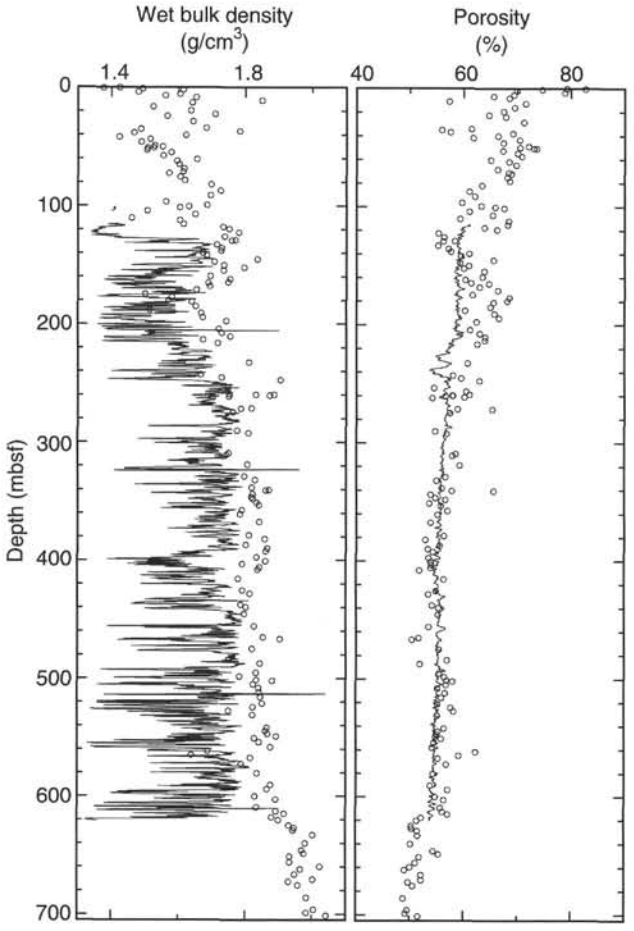


Figure 57. Comparisons of laboratory-derived index property measurements with downhole bulk density measurements and electrical resistivity-derived porosity calculations. The continuous line plots represent the downhole data. The laboratory data are shown as discrete point measurements.

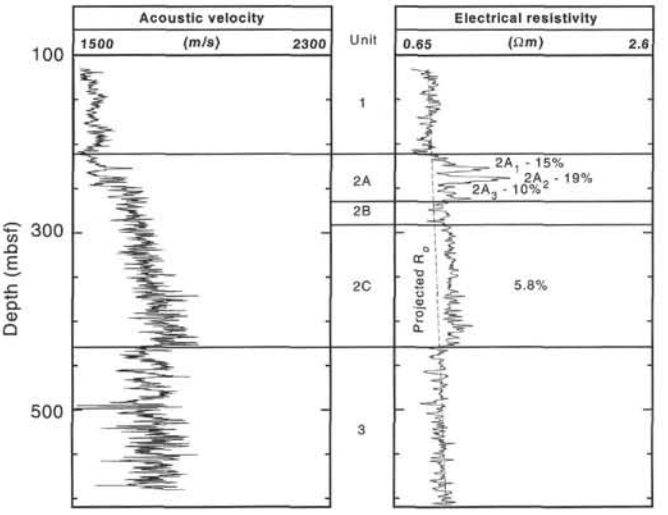


Figure 58. Log data used to calculate potential gas hydrate saturations in Hole 994D. Data shown include acoustic velocity data from the LSS and deep-reading electrical resistivity data from the DITE. Also shown are the depths of logging Units 1, 2 (2A, $2A_1$, $2A_2$, $2A_3$, 2B, and 2C), and 3. Listed beside the electrical resistivity log trace are the calculated gas hydrate saturations (percentage of pore space occupied by gas hydrate).

with the predicted base of the methane hydrate stability zone (see "Gas Hydrate" section, this chapter).

One conclusion that can be made is that logging Unit 2 in Hole 994D contains some amount of gas hydrate. However, an alternative hypothesis suggests that pore-water "salinity" changes could account for the observed electrical resistivity log responses. Geochemical analyses of recovered cores at Site 994 have revealed the presence of pore water with relatively low chloride concentrations (see "Inorganic Geochemistry" section, this chapter). This may indicate that logging Unit 2 contains waters with relatively low salt concentrations that will contribute to an increase in the measured electrical resistivities. However, because the acoustic log is not affected by changes in pore-water salinities it appears to refute the hypothesis that salinity changes are contributing to the anomalous acoustic velocity and resistivity properties of logging Unit 2. To further evaluate the effect of pore-water salinity on the measured log values at Site 994, we have attempted to quantify the observed changes in electrical resistivity in Unit 2 with respect to potential pore-water salinity changes. We have determined that to account for the high resistivities (1.40 Ωm) observed in Unit $2A_1$ (Fig. 58) would require the pore waters to be diluted, relative to a seawater baseline of 32 ppt, by almost 70% (to ~10 ppt NaCl). The resistivity response observed in Unit 2C would require a 30% reduction of the pore-water salt relative to an assumed seawater-salinity baseline (to ~22 ppt NaCl). These required pore-water salinity changes of 30% and 70% are greater than the maximum observed chloride changes measured in the recovered cores (see "Inorganic Geochemistry" section, this chapter).

Electrical resistivity log data can be used to quantify the amount of gas hydrate in a stratigraphic sequence (see "Downhole Logging" section, "Explanatory Notes" chapter, this volume). For the purpose of discussion, we have assumed that the anomalously high resistivities and velocities measured in logging Unit 2 of Hole 994D are due to the presence of in situ gas hydrate. The DITE-SFL measurements of deep electrical resistivity ($R_t$) from Hole 994D (Fig. 58) were used to calculate water saturations ($S_w$) [gas hydrate saturation ($S_h$) is equal to $(1.0 - S_w)$] using the following modified Archie relationship: $R_t/R_o = S_w^{-n}$ (Schlumberger, 1989), where $R_o$ is the resistivity of the sedimentary section if it contained only water ($S_w = 1.0$), $R_t$ is the resistivity of the hydrocarbon-bearing intervals (log values), and $n$ is an empirically derived parameter. This modified Archie relationship is based on the following logic: If the pore space of a sediment is 100% saturated with water, the RILD will measure the resistivity of the 100% water-saturated sedimentary section ($R_o$). This measured $R_o$ value is considered to be a relative baseline from which hydrocarbon saturations can be determined within nearby hydrocarbon-bearing intervals. To determine $R_o$ for logging Unit 2 in Hole 994D, we have used the measured deep resistivities from Units 1 and 3, which are assumed not to contain any hydrocarbons ($S_w = 1.0$), to project a $R_o$ trend line for Unit 2 (Fig. 58). Laboratory experiments of different sediment types have yielded a pooled estimate for $n$ of 1.9386 (reviewed by Pearson et al., 1983). Now knowing $R_t$, $R_o$, and $n$, it is possible to use the modified Archie relationship to estimate gas hydrate saturation ($S_h$ fraction of the total pore space that is occupied by gas hydrate). We calculated $S_h$ for subunits $2A_1$, $2A_2$, and $2A_3$ to be ~15%, 19%, and 10%, respectively (Fig. 58). The resistivity-derived $S_h$ for Unit 2C averages 5.8%, which probably accounts for the baseline resistivity log shift observed throughout all of Unit 2. There is no apparent resistivity-derived gas hydrate saturation gradient within Unit 2C.

Carbon (C) and oxygen (O) elemental yield data were obtained with the GLT in Hole 994C for the purpose of calculating gas hydrate saturations. Inelastic neutron measurements were made at a series of 13 stations (5-min stationary measurements) in Hole 994C (Table

19). All of the inelastic stations were within logging Unit 2. The measured C/O ratios, which ranged from 0.005 to 0.0420, are within the expected range for a gas hydrate–bearing marine sediment (Table 19). Further analyses of this data is beyond the scope of this initial log interpretive phase.

### Temperature

The LDEO-TLT was deployed on both Quad-combo logging runs (runs 1 and 2) in Hole 994C (Fig. 59). During the process of drilling, cold seawater is circulated in the hole cooling the formation surrounding the borehole. Once drilling ceases, the temperature of the formation gradually rebounds to its equilibrium temperature. The temperature data from run 2 of the Quad-combo tool string cannot be used to directly assess the nature of the thermal rebound in Hole 994C because there was a period of additional drilling and circulation between runs 1 and 2. In addition, during run 2 the Quad-combo tool failed to completely exit the drill pipe, the bottom of which was at 510 mbsf. The plot of vertical temperature gradients in Figure 59 reveals several abrupt gradient changes that were caused by borehole temperature anomalies. The logging speed indicator shows that most of the borehole temperature fluctuations are not an artifact of logging. These anomalous temperature zones in Hole 994C may indicate gas flowing into the well bore.

### Acoustic Velocities

The LSS from Hole 994D was integrated over the range of the logging run (114–618 mbsf) to produce a graph of two-way traveltime vs. depth (Fig. 60). A two-way traveltime for the water bottom of 3.73 s was determined from site survey seismic records, and velocities were linearly interpolated between the seafloor velocity of 1500 m/s and the first log velocity at 114 mbsf. The resultant traveltime depth curve (Fig. 60) is coincident with one obtained independently from the VSP data (see "Geophysics" section, this chapter).

### Lamont-Doherty Dipole Shear Tool

The deployment of the new Lamont-Doherty dipole shear tool in Hole 994D yielded acoustic waveforms from both compressional and shear wave receivers. Examples of the waveforms are presented in Figure 61. Table 20 contains several determinations of compressional and shear wave velocities. Since this is the first deployment of the LDEO-SST, the selection of shear wave arrivals has not yet been automated. Therefore, the results in Table 20 are a small sample of the data that will be forthcoming after shore-based processing.

## IN SITU TEMPERATURE MEASUREMENTS

The in situ temperature program at Site 994 was designed to provide direct constraints on thermal conditions within the hydrate stability zone at a location lacking a BSR. Secondary goals of the temperature-measurement program were to validate the results of traditional heat-flow studies (Ruppel et al., 1995), to determine the contribution of advection to heat transport through the system, and to constrain the amount of heat available to drive low-temperature diagenesis.

### Sampling Strategy

The Adara tool was used to measure in situ temperatures at 25–30 m vertical spacing during APC operations between 30 and 140 mbsf. The WSTP tool was deployed from 200 to 450 mbsf, with measurements obtained at an average spacing of 50 m. A total of 13 Adara and WSTP measurements were attempted in Hole 994C, of which eight were fully successful, four resulted in anomalous temperatures, and one ended with the loss of the WSTP water filter and probe tip. Table 21 summarizes the measurements and results obtained by the in situ temperature program in Hole 994C.

**Table 19. Carbon/oxygen elemental ratios as measured with the GLT in Hole 994C.**

| Depth (mbsf) | Well-log depth (mbrf) | Carbon/ oxygen ratio |
|---|---|---|
| 228.0 | 3038.0 | 0.017 |
| 233.0 | 3043.0 | 0.042 |
| 238.1 | 3048.1 | 0.017 |
| 243.1 | 3053.1 | 0.028 |
| 248.1 | 3058.1 | 0.019 |
| 253.1 | 3063.1 | 0.005 |
| 258.0 | 3068.0 | 0.027 |
| 263.0 | 3073.0 | 0.012 |
| 268.0 | 3078.0 | 0.025 |
| 273.1 | 3083.1 | 0.017 |
| 278.1 | 3088.1 | 0.025 |
| 283.0 | 3093.0 | 0.022 |
| 288.1 | 3098.1 | 0.014 |

### APC Adara Measurements

The Adara tool was used to obtain a stable reading of bottom-water temperature (BWT) at the mudline before retrieval of Core 164-994C-2H. Each of the five subsequent runs for in situ temperatures included a 5-min mudline stop and 10–12 min in formation. As a check on the continued stability of the electronics, short (~3–5 min) mudline temperature readings also were obtained after withdrawal of the APC.

The portion of the Adara records including the mudline stops, penetration, and pullout is shown in Figure 62. Frictional heating on penetration ranged from 1° to 5°C, with the frictional pulse generally increasing with the depth of the measurements. For most of the Adara measurements, the thermal equilibration curve was overprinted by small temperature perturbations attributed to minor operational problems holding the core in the formation during the 10- to 12-min equilibration time.

### WSTP Measurements

In situ measurements deeper than 170 mbsf were obtained using the WSTP instrument in combined water-sampling and thermal mode (except for Core 164-994C-52X, which was run in thermal mode only). Most WSTP runs included a descending mudline stop of 2–3 min duration and a 10-min thermal equilibration interval at the bottom of the hole. The pressure valve for sampling of pore fluids was activated 10 min into the thermal equilibration interval, causing a minor temperature perturbation that sometimes rendered the remainder of the record unusable for determining equilibrium values. As a check on thermistor drift during the deployment, a second mudline temperature reading was typically obtained during ascent.

Figure 63 shows WSTP records obtained in Hole 994C. A strong frictional heating pulse was recorded at penetration of the WSTP tool only for Cores 164-994C-30X, 35X, and 47X. Despite the lack of a frictional heat pulse in the remaining records, pullout forces were sufficiently high to infer that the tool was probably firmly embedded in the bottom of the hole during the runs.

### Equilibrium Temperatures

The in situ temperature records for Hole 994C were processed using standard ODP software that first converts recorded resistances to temperatures and then fits synthetic temperature vs. time functions to the recorded data. The fitting procedure is dependent on the choice of a thermal conductivity value, which was fixed at 1.0 W/(m·K) for processing data from this hole. The equilibrium temperature value

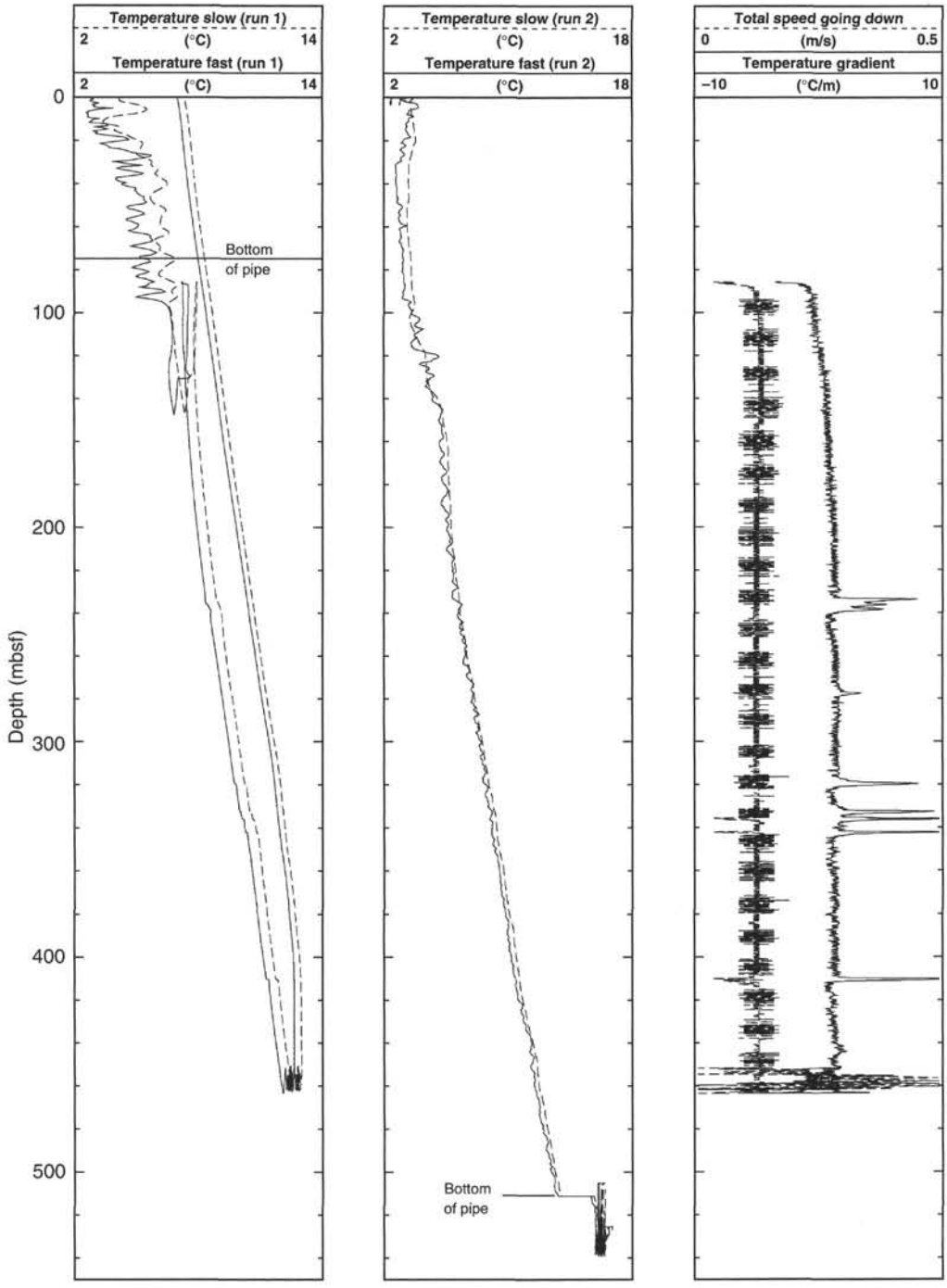


Figure 59. Temperatures recorded with the LDEO-TLT on the Quad-combo tool in Hole 994C. Logs from both runs 1 and 2 are shown. Also plotted are the vertical temperature gradient and the logging speed of the tool for the downward portion of run 1.

obtained as a result of processing is far more sensitive to the choice of the initial and final records of the equilibration interval than to deviations from the assumed nominal thermal conductivity value.

Table 21 lists equilibrium temperature values based on the best match (lowest standard deviation) between the synthetic curves and the observations for various choices of penetration records and equilibration intervals. Reported errors on the equilibrium values were estimated based on a number of subjective factors, including the stability of the equilibration curve, tool performance, and the magnitude of the correction that must be applied to the WSTP data. The equilibrium temperatures for WSTP data were shifted by –0.3°C to account for the difference between the BWT recorded at the mudline by the Adara and WSTP instruments. Because of the nonlinear relationship between thermistor resistance and temperature, correction of the WSTP data using a constant temperature offset represents only a first-order approximation to the true correction, which must be done in resistance space.

For the eight high-quality in situ measurements, the temperature data are asymptotic to the equilibrium temperature. The four anomalous measurements noted in Table 21 lack a normal thermal equilibration curve and are, instead, characterized by heating at a constant rate of 0.05°C/min while the tool was in the sediments. Although so-

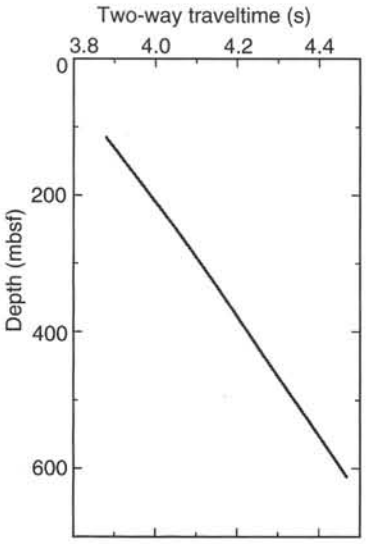


Figure 60. Two-way traveltime calculated from the acoustic velocity log in Hole 994D.

called equilibrium temperatures for these records were estimated using the normal analytical procedure, the equilibrium values should be interpreted with caution because the in-bottom records show no evidence for thermal equilibration.

Equilibrium temperatures obtained from the in situ measurements are shown as a function of depth in Figure 64A. If the anomalous measurements are disregarded, the remaining data fit an average geothermal gradient of 36.4 ± 1.3 mK/m. The regression equation for the best-fit line is $T = (3.68° \pm 0.21°C) + (0.0364° \pm 0.013°C/m)z$, where $T$ is temperature in °C and $z$ is depth in meters.

### Heat Flow

Heat flow, given by the product of thermal conductivity and the geothermal gradient, can be estimated from the in situ equilibrium temperature measurements by using thermal conductivity values measured on board (Fig. 44). The thermal conductivity data obtained from core sections recovered within 10 m of the in situ temperature measurements were first averaged and then corrected to in situ temperature and hydrostatic conditions using the formulation of Ratcliffe (1960). Based on the observed homogeneity of physical properties deeper than 180 mbsf (see "Physical Properties" section, this chapter), the average thermal conductivity value determined for the interval from 180 to 210 mbsf was adopted for all the WSTP data obtained deeper than 210 mbsf.

By converting depths to resistances using the formulation of Bullard (1939), the thermal conductivity variations with depth can be explicitly incorporated when determining heat flow. The slope of the temperature vs. resistance curve (Fig. 64B) yields a direct measure of heat flow, which averages 35.4 ± 1.3 mW/m$^2$ between the seafloor and 318.6 mbsf. The measured heat flow is not constant with depth, averaging 44.3 ± 4.1 mW/m$^2$ in the uppermost 110 m of the section, but only 33.4 ± 2.0 mW/m$^2$ between 109.9 and 318.6 mbsf. The heat-flow value determined from the in situ measurements at depths shallower than 110 mbsf is less than 10% lower than a heat-flow value previously determined 1.2 km from Hole 994C (48.4 ± 1.7 mW/m$^2$, Ruppel et al., 1995).

### Anomalous Temperature Measurements

The four anomalous temperature measurements (Table 21) were obtained from a WSTP deployment at 299.4 mbsf and from three consecutive WSTP runs deeper than 345 mbsf. An equilibrium temperature value obtained at an intervening depth (318.6 mbsf) lay on the geothermal gradient constrained by measurements shallower than 140 mbsf. The anomalous temperature records range from 5.5° to 8.3°C and show a pattern of constantly increasing temperature with time during the equilibration interval (Fig. 63).

Although precautions were taken to circulate water continuously until just before the emplacement of the WSTP, the low temperatures recorded in Cores 164-994C-35X, 42X, 47X, and 52X may be partially explained by the penetration of the probe into fill in the bottom of the hole. Cracking of the formation or the seepage of borehole water into the area around the probe tip may also account for the anomalous temperatures. Similar temperature records obtained within the gas hydrate stability zone during Leg 146 on the Cascadia Margin were discarded because of poor hole conditions and high drift during the equilibration interval. However, high drift is an unlikely explanation for the anomalous equilibration records obtained for Cores 164-994C-35X, 42X, and 47X because the rate of temperature change during the equilibration interval is small, averaging 0.05°C/min for each of the three records.

The anomalous temperature data may alternately be explained by a phenomenon related to the presence of gas hydrate within the sediments. An in situ equilibrium temperature of 12.1°C was measured within 10 m of the depth from which solid hydrate was recovered (Core 164-994C-31X; see "Gas Hydrate" section, this chapter), but most of the measurements at greater depths within the hydrate stability zone were anomalous. The anomalous measurements might be explained by the dissociation of gas hydrate upon the addition of frictional heat to the system at probe emplacement. This endothermic phase transition could significantly lower temperatures in the immediate vicinity of the probe tip. Measurements taken on the catwalk during recovery of hydrate from Core 164-994C-31X recorded markedly cooler temperatures (6°–8°C) near gas hydrate nodules than in other parts of the core (11°–13°C). These 6°–8°C temperatures near the sampled hydrate roughly agree with "equilibrium" temperatures estimated using the anomalous in situ records.

## SYNTHESIS AND SIGNIFICANCE

Site 994, located on the southern flank of Blake Ridge at a water depth of 2797.6 m, enabled us to assess the occurrence, amounts, and composition of natural gas hydrate formed in hemipelagic clays. Site 994 also provided clues about the relationship between the theoretically determined base of the gas hydrate stability zone and the seismic expression of gas hydrate–bearing sediments.

### Sedimentation and Diagenesis

#### *Lithology and Sedimentation Rates*

An essentially continuous section of upper Miocene through Holocene sediments consisting of a homogeneous hemipelagic accumulation of terrigenous clays and nannofossils, with subordinate amounts of diatoms and foraminifers, occurs at Site 994. Significant hiatuses were not detected. Contour-current deposition is indicated in the upper part of the section by a few ≤10-cm-thick winnowed beds of ungraded coarse-grained foraminifer ooze and a bed of reddish mud that was presumably derived from Canada (see "Lithostratigraphy" section, this chapter). Only a modest amount of redeposition and reworking was indicated by the sedimentary structures; however, a remarkable amount of reworking/redeposition is recorded by the mixed nannofossil assemblages from the upper upper Pliocene section.

Pleistocene to uppermost Pliocene sequences (lithostratigraphic Units I and II; 0–160 mbsf) are characterized by alternating decimeter- to meter-thick interbeds of dark greenish gray nannofossil-rich clay and more carbonate-rich greenish gray nannofossil clay. The beds differ subtly in their biogenic carbonate contents (ranging

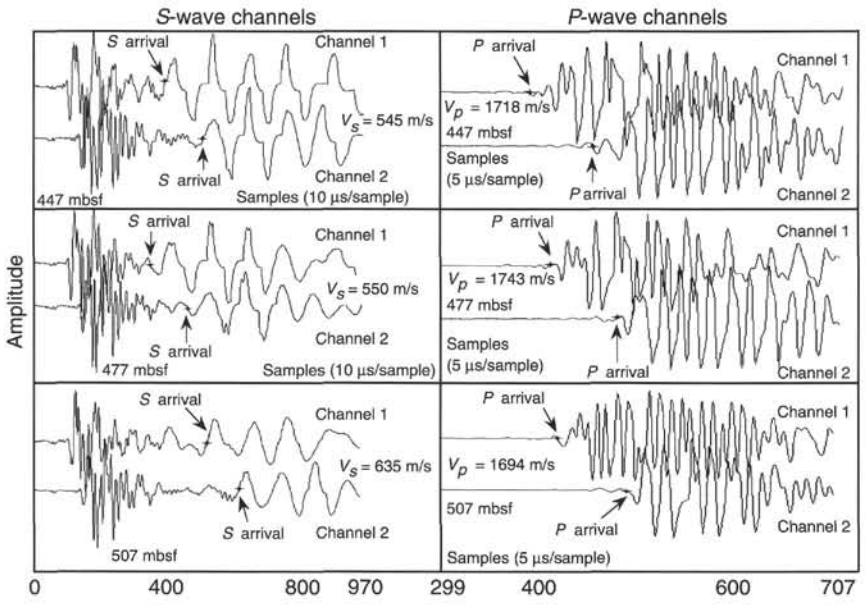


Figure 61. Examples of waveforms recorded from the compressional (*P*) and shear (*S*) wave receivers on the LDEO-SST. Waveforms similar to these examples were recorded every 15 cm over the depth range from 191 to 613 mbsf in Hole 994D. The arrival time and the offset between the source and receiver for channel 1 and channel 2 are used to determine the velocity of a particular acoustic wave.

**Table 20. Compressional and shear wave acoustic data measured with the LDEO-SST in Hole 994C.**

| Depth (mbsf) | $V_p$ (m/s) | $V_s$ (m/s) | $V_p/V_s$ | Poisson's ratio |
|---|---|---|---|---|
| 447 | 1718 | 545 | 3.15 | 0.44 |
| 477 | 1743 | 550 | 3.17 | 0.44 |
| 507 | 1694 | 635 | 2.67 | 0.42 |

**Table 21. In situ temperature measurements in Hole 994C.**

| Core | Depth (mbsf) | Tool | Equil. T[a] (°C) | K[b] (W/[m·K]) | Comments |
|---|---|---|---|---|---|
| 2H | 0 | Adara | 3.1 ± 0.5 | | Mudline temperature stop |
| 4H | 32.9 | Adara | 4.6 ± 0.5 | 1.01 | |
| 6H | 51.9 | Adara | 5.7 ± 0.25 | 0.89 | |
| 10H | 81.4 | Adara | 6.9 ± 0.5 | 0.88 | |
| 13H | 109.9 | Adara | 8.2 ± 0.25 | 1.08 | |
| 16H | 139.4 | Adara | 8.5 ± 0.5 | 0.95 | |
| 25X | 203.3 | WSTP | 11.2 ± 0.3 | 0.98 | Switch to XCB coring |
| 30X | 241.7 | WSTP | 12.2 ± 0.3 | 0.98 | |
| 35X | 299.4 | WSTP | 5.6 | 0.98 | Anomalous |
| 39X | 318.6 | WSTP | 15.4 ± 0.3 | 0.98 | |
| 42X | 347.6 | WSTP | 6.4 | 0.98 | Anomalous |
| 47X | 386.1 | WSTP | 6.6 | 0.98 | Anomalous; bent probe |
| 52X | 424.5 | WSTP | 8.3 | 0.98 | Anomalous; thermistor malfunction during equilibration interval |
| 55X | 443.7 | WSTP | — | — | Broke probe tip |

Notes: Adara = Adara APC temperature shoe, and WSTP = water-sampling temperature probe.

[a]The equilibrium temperature reported here was obtained by minimizing the standard deviation between the synthetic equilibration curve and the recorded data during multiple processing runs. The value of equilibrium temperature for the anomalous runs actually represents the baseline value recorded during this equilibration interval. Errors are estimated based on factors discussed in the text.

[b]K indicates the average, corrected thermal conductivity value used to convert from depth to resistance. No laboratory thermal conductivity data were obtained in cores recovered from deeper than 210 mbsf, and 0.98 W/(m·K) was adopted for all in situ temperature measurements deeper than Core 164-994C-25X.

from 25 to 35 wt% $CaCO_3$), which may reflect a rhythmic change of depositional environments and/or paleoceanography and climate. The sedimentation rate for the Pleistocene and uppermost Pliocene interval is estimated to be 3–10 m/m.y. (see below), indicating that the average bed took 10–30 k.y. to be deposited. The upper reflective zone (approximately the upper 0.15 s) in seismic reflection profiles (Fig. 1) coincides with the weakly stratified Pleistocene and uppermost Pliocene sequences.

Pliocene to Miocene sediments below 160 mbsf (Unit III) are homogeneous, dark greenish gray clays composed of moderately bioturbated terrigenous clays with nannofossils. Biogenic carbonate content is generally less than 20 wt%. This Pliocene to Miocene sequence (Unit III) corresponds with both the blanking zone (0.15–0.61 s below seafloor) and the moderately reflective zone (below 0.61 s) observed on seismic reflection profiles across Site 994 (Fig. 1). Sediments of Unit III are so uniform in their lithology and laboratory-determined physical properties that the origin of the reflections below 0.61 s cannot be attributed to physical property or lithologic changes in the recovered sediments. Sedimentation rates estimated from nannofossil zonations consistently increased from 68 m/m.y. during the Quaternary to 303 m/m.y. during the late Miocene (Fig. 24).

Unit III spans the sediment interval in which the BSR occurs at nearby sites (e.g., 0.55 s at Site 995). Phase data suggest the base of the gas hydrate stability should occur within Unit III. The uniform character of the stratigraphic section made Site 994 an ideal reference site to observe phenomena related to gas hydrate formation and dissociation without the added complications of sediment composition, texture, and fabric changes.

### *Sediment Accumulation Rates*

Mass accumulation rates (MARs) for both carbonate and noncarbonate fractions are shown in Figure 65. The MAR of the carbonate fraction was relatively constant at ~2–5 g/cm$^2$ per $10^3$ yr, whereas the noncarbonate fraction MAR increased to 12–14 g/cm$^2$ per $10^3$ yr in the Pliocene and to 30–35 g/cm$^2$ per $10^3$ yr in the late Miocene. Enhanced contour-current deposition in late Miocene and Pliocene times is indicated by the high influxes of terrigenous matter.

The range of TOC at Site 994 shows a modest increases from 0.3%–1.1% in the Pleistocene section to 0.9%–1.8% in the lower Pliocene and upper Miocene sequence (Fig. 66). However, the mass accumulation rates of TOC increased ~25 times downcore, from <0.02 cm$^2$/k.y. in the latest Pleistocene to 0.6 cm$^2$/k.y. during the late Miocene. The downhole trend for the MAR of TOC is almost parallel to that of the noncarbonate influx.

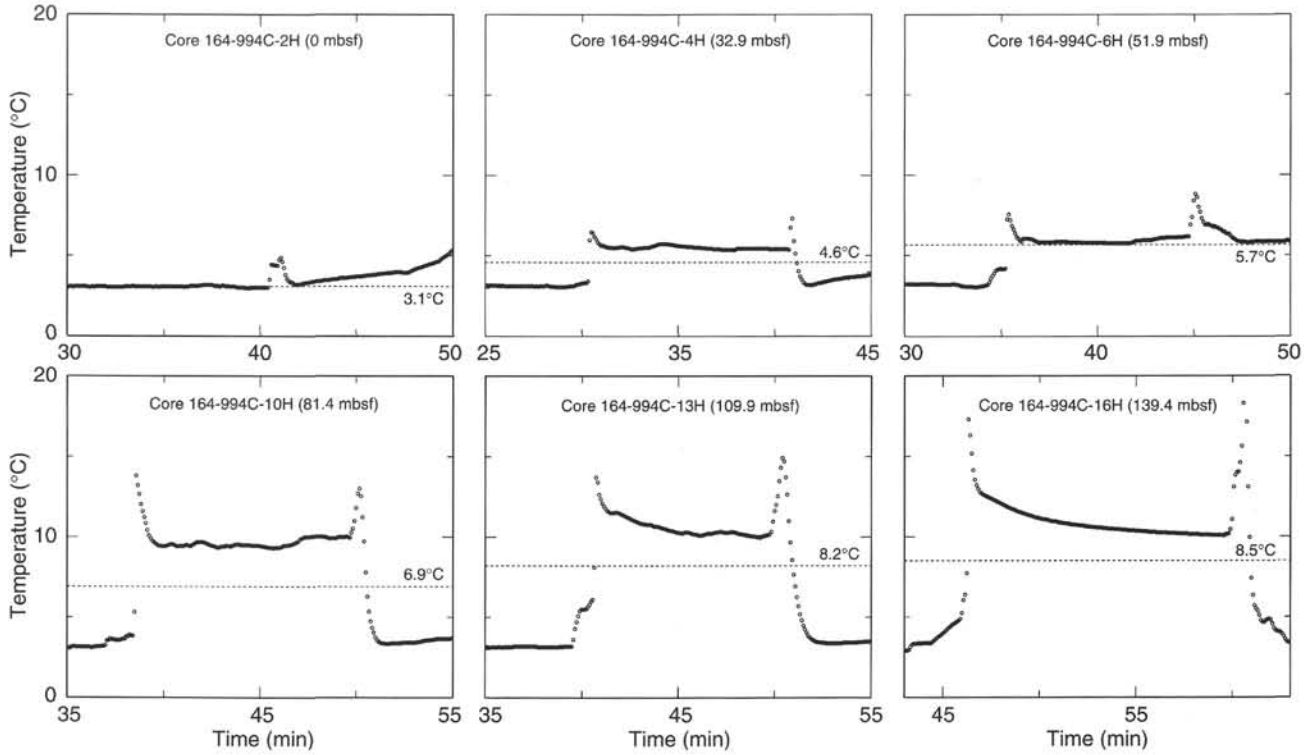


Figure 62. Raw temperature vs. time records from the Adara tool for the period between the descending and ascending mudline stops in Hole 994C. Dashed lines = equilibrium temperatures determined by fitting synthetic curves to the equilibration record, assuming thermal conductivity of 1 W/(m·K).

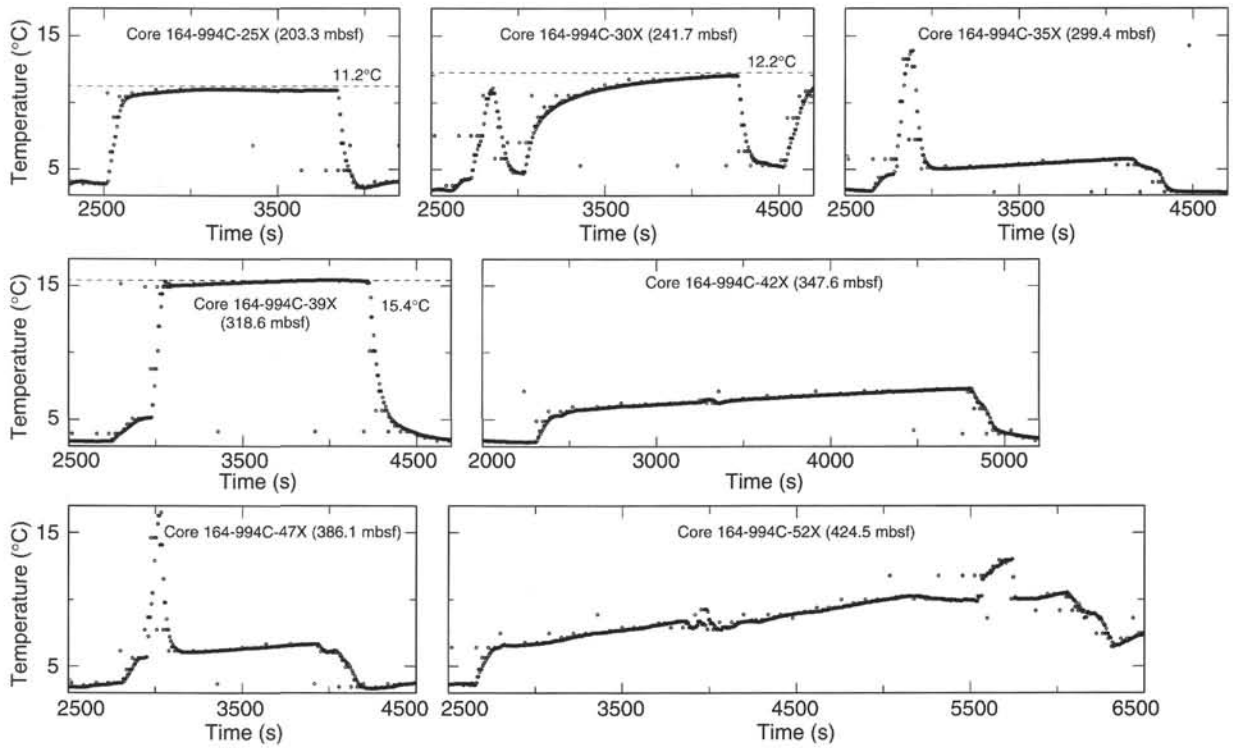


Figure 63. Raw temperature vs. time records from the WSTP for the period between the ascending and descending mudline stops. Dashed lines = equilibrium temperatures determined by fitting synthetic curves to the equilibration record, assuming thermal conductivity of 1 W/(m·K). No equilibrium temperatures are shown for the data labeled anomalous in Table 21.

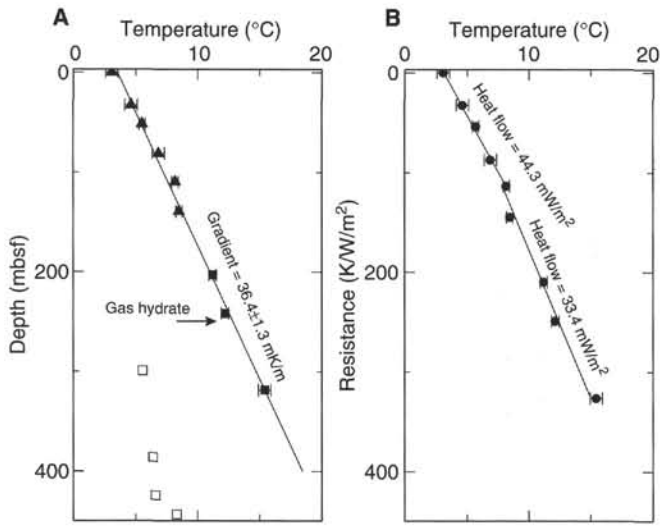


Figure 64. **A.** Equilibrium temperatures as a function of depth. Solid symbols = reliable results, open symbols = the anomalous data, triangles = Adara tool results, and squares = WSTP results. The average geothermal gradient determined from the high-quality data is 36.4 ± 1.3 mK/m. Error bars indicate uncertainties based on factors discussed in the text. The depth at which gas hydrate was recovered in the core is indicated. **B.** Equilibrium temperature as a function of resistance. The pressure- and temperature-corrected thermal conductivity from the interval immediately above the in situ temperature measurements was used to calculate resistances from depth. The slope of the data in resistance space is a direct measure of the heat flow. Average heat flow may be 20% greater in the uppermost 110 m than over the entire depth range spanned by the in situ measurements.

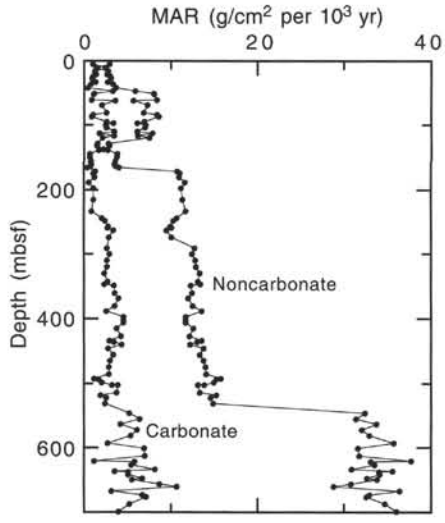


Figure 65. Mass accumulation rates for both carbonate and noncarbonate fractions calculated from the sedimentation rates, shipboard density, and porosity measurements for Hole 994C. Carbonate contents were determined from an XRD peak of calcite so that diagenetic dolomite and siderite were excluded from the carbonate fraction.

### *Diagenetic Dolomite and Siderite*

Diagenetic dolomite is rather common throughout the Pleistocene to uppermost Pliocene sections (164-994C-5H-5, 6H-1, 6H-3, 6H-6, 10H-2, 10H-4). It occurs as rhombohedral crystals disseminated within host clays, irregularly shaped semi-indurated nodules, and

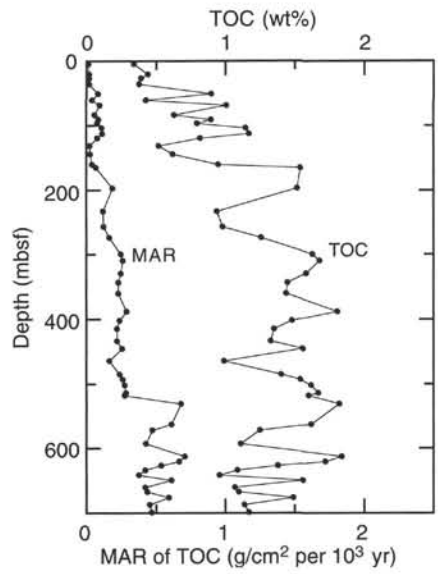


Figure 66. Total organic carbon and mass accumulation rates for Site 994.

heavily dolomitized beds. The shallowest occurrence of a dolomite bed (containing more than 50% dolomite) was at about 40 mbsf, which is below the base of sulfate reduction zone (~21 mbsf) and within the zone of methanogenesis. $Ca^{+2}$ and $Mg^{+2}$ contents of interstitial waters decrease rapidly over the first 20 mbsf. These observations suggest that some of this dolomite authigenesis occurs at the base of the sulfate reduction zone, potentially related to anaerobic methane oxidation (see "Inorganic Geochemistry" section, this chapter).

The occurrence of dolomite-rich beds and nodules is largely restricted to Pleistocene to uppermost Pliocene strata, and the amount of dolomite becomes nominal below 120 mbsf in the Pliocene and Miocene units. If the supply of methane from below has remained nearly constant, the lower sedimentation rate during the Pleistocene to latest Pliocene would have enhanced the total amount of methane that is oxidized within the sediments at the base of the sulfate reduction zone. Thus, the lower sedimentation rate may focus diagenesis on the units at the base of the sulfate reduction zone for a longer time period.

Diagenetic siderite first occurs at 120 mbsf and increases in abundance with increasing depth to a maximum at 636.7 mbsf (164-994C-78X-1, 46 cm) in the upper Miocene strata. The origin of siderite at Site 994 is not evident, but the distribution at Site 994, coupled with the carbon and oxygen isotopic values of siderite recovered from Site 533 on the Blake Outer Ridge (Matsumoto, 1983, 1989), suggests that siderite occurrence may be related to the formation and dissociation of gas hydrate.

## Detection and Implications of the Presence of Gas Hydrate

### *Direct Sampling*

The presence of gas hydrate at Site 994 was documented by direct sampling (see "Gas Hydrate" section, this chapter). This site was intentionally located in an area where a BSR is not observed to provide a reference section for comparison with Site 995, which is associated with a strong BSR. The recovery of gas hydrate samples at Site 994, therefore, confirms that gas hydrate may be present despite the absence of a BSR.

Volumetric calculations based on a controlled decomposition experiment using a gas hydrate nodule recovered from Section 164-994C-31X-7 (259.90 mbsf) indicate that this sample was composed

of structure I methane hydrate with at least 80% of its cages occupied by $CH_4$. Comparison with gases evolved from the surrounding sediments indicates that the gas hydrate had lower concentrations of ethane, propane, and higher molecular weight hydrocarbons, and correspondingly higher concentrations of $CO_2$ (see "Gas Hydrate" section, this chapter).

### *Proxy Measurements*

Gas hydrate was not directly sampled in other parts of the sedimentary section at Site 994. However, the presence of gas hydrate within the sediments between ~210 and ~430 mbsf is inferred on the basis of the following observations (Table 22):

1. The cores were observed to evolve large amounts of gas. Many cores extruded material onto the rig floor before the liners were pulled out of the core barrel (Cores 164-994C-35X, 43X, 54X through 59X, 63X through 65X, and 73X through 75X). An extreme was Core 164-994C-64X, from which 15-cm-long pieces of core material shot out of the core barrel and landed 5 m away on the deck. On one occasion (Core 164-994C-30X; 241.7 to 251.3 mbsf), the whole core liner shot out of the core barrel and landed on the deck below. Most cores continued to expand on the catwalk until holes were drilled through the liners to release gas.

Gas evolution was thought to be responsible for the low core recovery. Core recovery was generally >80% down to 200 mbsf but decreased to 20%–60% for the interval 200–500 mbsf, with several short intervals of high recovery. Below this level, the recovery appears to increase to 60%–100%, with short intervals of low recovery (Fig. 67). The low-recovery cores typically contained numerous gas-filled voids between the pieces of core that remained within the liners. Gas samples from these voids indicated the voids were largely filled with methane (see "Organic Geochemistry" section, this chapter). Thus, the expansion was related to gas evolution within the cores. Significant amounts of sediment apparently were extruded from the top of the core barrel, through the check valve, and into the pumps above. Apparently, the low core recovery was partly a consequence of core loss during core recovery as gas evolved from the samples, rather than just from core loss during the drilling process.

These qualitative indicators of the presence of gas do not require that gas hydrate was present in the sediment before coring, but they do indicate that significant amounts of gas were in the sediments. Assuming that sediment porosity was 50% and that interstitial waters were saturated with respect to methane (~4 L of $CH_4$ per liter of water), the entire core may evolve about 54 L of $CH_4$ under STP conditions, as it comes to the surface. Clearly, having pore waters that are at or close to methane saturation is capable of causing a significant amount of core expansion. Moreover, if the core contains 5% gas hydrate, the total volume of $CH_4$ becomes three to five times as much as in hydrate-free sediments.

2. Pore water in the sediments from below 568 mbsf were gas saturated before recovery. Core 164-994C-70P from 568.7 to 569.9 mbsf evolved 640 mL of methane from a 20-cm-long core. Using a porosity of 50%, the measured gas volume implies that about 5 L of methane evolved per liter of water. This is more $CH_4$ than can be dissolved in the pore water under in situ conditions. The ZO-VSP data from Site 994 indicate that *P*-wave velocities decreased to a minimum of 1530 m/s at 610 mbsf. This drop in velocity is presumably caused by the presence of free gas.

The above observations suggest that sediment pore waters are gas saturated at depths below which the theoretical calculations and empirical evidence indicate the presence of gas hydrate. This, in turn, implies that there is an adequate supply of methane available in the sedimentary sequence to form gas hydrate in overlying zones in which gas hydrate is stable.

3. Both the general trend of the interstitial-water chloride concentrations and the intersample variation in chloride concentrations (chloride anomalies) between 200 and 450 mbsf suggest the presence of gas hydrate throughout this interval. Gas hydrate decomposition during recovery releases water and methane into the interstitial pores, resulting in a freshening of the pore waters. The general chloride profile may represent a combination of several processes, including increases in interstitial-water salinities associated with gas hydrate formation, diffusive and advective transport within the sedimentary sequence that alters the distribution of interstitial salinities, and the natural decomposition of gas hydrate at the base of the gas hydrate stability field, that should freshen the pore waters. Moreover, other hydrologic and diagenetic reactions (e.g., expulsion of pore waters by compaction and clay mineral transformation) that may influence interstitial-water chloride concentrations. All these effects operate over long time scales and may be in disequilibrium with current conditions. Thus, it is difficult to predict the present in situ interstitial-water chloride profile. Although nine attempts were made to sample in situ interstitial salinities (seven WSTP tool runs and two Fisseler tool runs), none produced uncontaminated pore waters to unequivocally establish the in situ value (see "Downhole Tools and Sampling" section, this chapter).

Interstitial-water compositions are naturally modified by diffusion so that in a relatively static sedimentary sequence only small

**Table 22. Top and base of gas hydrate distribution.**

| | Chloride anomaly depth (mbsf) | Logging depth (mbsf) | Experimental depth (mbsf) |
|---|---|---|---|
| Site 994 (depth of water = 2799.1 mbsl): | | | |
| Top | 194.95–209.2 | 212.0 | |
| Base | 427.37–439.5 | 428.8 | 497 (SW)–529 (PW) |

Note: SW = based on experiments in seawater, and PW = based on experiments in pure water.

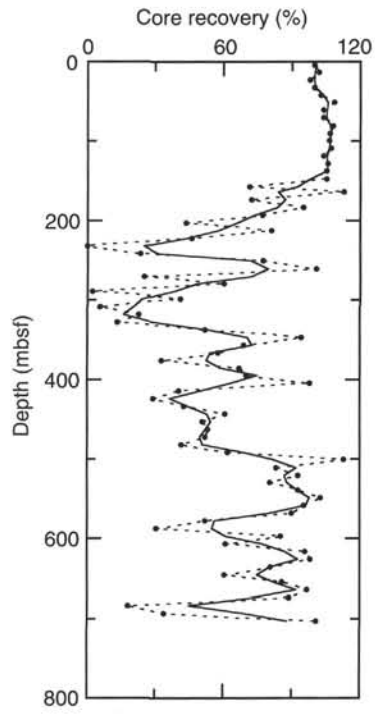


Figure 67. Plot showing the percentage of recovery from APC and XCB coring (circles and dashed line) in Hole 994C smoothed with a five-point average (solid line).

changes in chloride occur between nearby sediments. Thus, the negative spikes of chloride concentrations that were measured at Site 994 between 209 and 427 mbsf can best be explained as artifacts of gas hydrate decomposition during core recovery, and the relative amplitudes of the anomalies are proportional to the amount of gas hydrate that dissociated within the sample during core recovery.

4. Core temperatures upon recovery on the catwalk were quite variable. Small areas of surprisingly low temperatures within individual core sections also were carefully documented. Low temperature anomalies are interpreted as indicating areas where gas hydrate decomposition had occurred recently or where large volumes of gas evolved and expanded during core recovery.

In most cases, these anomalously cool spots were observed to be warming, indicating that gas hydrate was not decomposing as the catwalk temperature measurements were being made. However, in a few cases, these anomalously cool spots continued to cool while the temperature measurements were being made. These continued cooling trends could indicate either that (1) gas hydrate was decomposing while the measurements were being made or that (2) ice had formed in the sediments as a consequence of gas hydrate decomposing during core recovery, and the ice was in the process of melting while the temperatures were being measured.

Figure 21 (see "Gas Hydrate" section, this chapter) shows a downhole trend of core temperatures measured immediately after recovery either on the catwalk or in the gas-collection chambers. Although the measured core temperatures show considerable scatter with depth, anomalously low temperatures are observed only in the interval between 200 and 430 mbsf. The lowest temperature measurements appear to correspond to the horizon from which solid gas hydrate samples were recovered and the horizons characterized by strong negative chloride anomalies.

5. Data from downhole logs also are interpreted as indicating the presence of gas hydrate in the interval between 212.0 and 428.8 mbsf. Both the *P*-wave velocity and resistivity logs are distinctly offset in this zone (higher values); however, there are no obvious changes in either the lithology or physical properties data from this interval that could account for these offsets. Thus, the in situ observations made with the downhole logs and the analysis of the recovered core material suggest the presence of in situ gas hydrate.

### *Defining the Zone of Gas Hydrate Occurrence*

The depth to the top and base of the zone of gas hydrate occurrence at Site 994 was measured using both interstitial-water chloride anomalies and downhole logs (Table 22; Fig. 68). These data are in general agreement considering the different resolution of the techniques. Interstitial-water chloride anomalies established whether gas hydrate occurred within a given sample. The occurrence of the highest and lowest chloride anomalies establish the minimum range of the zone of gas hydrate occurrence. Because the data on the temperatures of the recovered cores indicate that the distribution of gas hydrate is rather patchy, the lack of an interstitial-water chloride anomaly in individual samples does not confidently determine the limit of the zone. Thus, the top of this zone might be higher and its base lower because of the distribution of the samples (see "Gas Hydrate Estimates" section below). Downhole logging estimates of the position of the top and bottom of the gas hydrate–bearing zone are picked as discrete boundaries. The largest error with the logging pick probably involves the subjectivity of establishing the uppermost occurrence within what is probably a gradation boundary (see "Downhole Logging" section, this chapter). In Table 22, we indicate that the boundaries of the gas hydrate–bearing zone as extending from the last distinct chloride anomaly to the next sample that lies along the chloride base line.

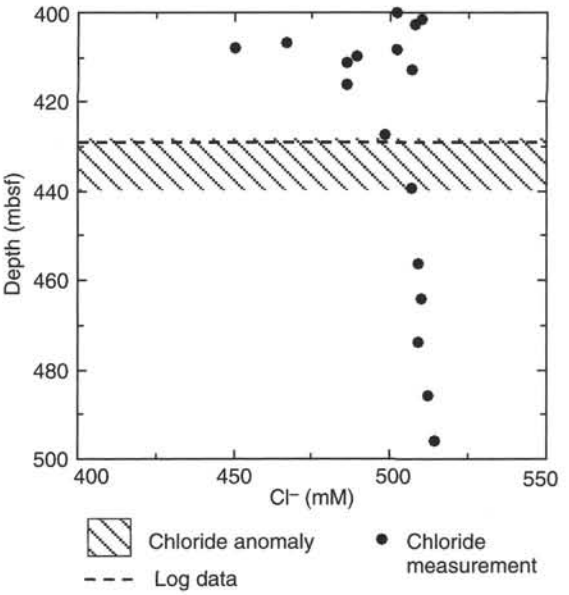


Figure 68. Plot of the depth to the base of gas hydrate occurrence at Site 994 as estimated by interstitial-water chloride anomalies and by downhole logging.

### *Discrepancy Between Observed and Predicted Base of Gas Hydrate Stability*

Eight successful in situ temperature measurements through the upper 320 mbsf reveal that the temperature gradient is 36.4° ± 0.13°C/km (see "In Situ Temperature Measurements" section, this chapter). Knowing the temperature gradient at Site 994 allows the base of gas hydrate stability (BGHS) to be predicted from experimental data. Assuming that the pore fluid has a salinity between seawater and pure water, the predicted BGHS is between 497 and 529 mbsf (Fig. 69).

No distinct change in sediment velocities is seen in the depth range that would correspond with the experimentally predicted BGHS (i.e., 497 to 529 mbsf). At Site 994, ZO-VSP data indicate that sediment *P*-wave velocities range between 1730 and 1820 m/s in the interval between 350 and 550 mbsf. However, a distinct low-velocity zone occurs below 550 mbsf, reaching a minimum velocity of 1520 m/sec at 605 mbsf. This decrease in sediment *P*-wave velocity suggests the presence of free-gas bubbles and correlates well with a strong reflector at 0.61 s sub-bottom (see Fig. 1). However, this reflector is clearly well below the predicted BGHS.

The direct sampling, shipboard temperature measurements, interstitial-water chloride anomalies, and downhole-logging data only suggest that gas hydrate occurred within a zone between 209 and 429 mbsf (Table 22; Fig. 68). The inferred gas hydrate–bearing zone does not extend to the predicted base of gas hydrate stability (497–529 mbsf; Fig. 69) as estimated from experimental data and using the measured geothermal gradient at Site 994 (see "In Situ Temperature Measurements" section, this chapter). Why the discrepancy exists is unclear.

### *Gas Hydrate Estimates*

Preliminary estimates of the amount of gas hydrate in the sediments at Site 994 were made in the following ways:

1. Estimates of the amounts of gas hydrate that existed in the sediments before recovery are made by assuming that diffusive equilibration prohibits significant and nonsystematic interstitial-water chloride concentrations from occurring between closely spaced samples. Thus, chloride spikes are only a result of gas hydrate decomposition during sample recovery. To produce an estimate of the interstitial-water salinity through the zone between 200 and 450 mbsf (Fig. 70A), where erratic chloride values were measured, a polynomial was fit to the relatively smooth chloride data above 200 mbsf and below 450 mbsf. All but one of the measured chloride concentrations in the zone between 200 and 450 mbsf have lower values than the calculated values, some significantly lower. The differences between the calculated in situ chloride concentrations and the measured chloride concentrations were used to establish the relative chloride anomaly that is associated with each sample (Fig. 70B).

The calculated chloride anomalies enable the amount of gas hydrate that was present in these samples to be estimated. Corrections for the porosity of the samples were made using the shipboard physical properties data (see "Physical Properties" section, this chapter). The estimated percentage of the sediment samples that was occupied by gas hydrate had a skewed distribution, ranging as much as 7 vol% (at 391 mbsf), with a mean value of 1.3 ± 1.8 vol% and a median value of 1 vol% for all the interstitial-water samples that were collected between 200 and 450 mbsf (Fig. 70C). However, these are considered to be minimum estimates because the baseline chlorinities used to calculate these values may be lower than the actual in situ interstitial-water chlorinities and because gas expansion during core recovery may result in lower core recovery from the more gas hydrate-rich samples.

2. Calculations of the percentage of gas hydrate that is required to explain the observed change in the downhole-logging electrical resistivity (Fig. 58) indicate that the general trend through the interval between 212.0 and 428.8 mbsf can be explained by the pervasive addition of as much as 2.9 vol% gas hydrate. The same calculation indicates that the most concentrated horizon (~239 mbsf) contains as much as 9.5 vol% gas hydrate. It is remarkable that independent estimation of the amounts of gas hydrate from different data sets (chloride anomalies and logging data) yields similar values of a few percent gas hydrate disseminated in the sediments.

### *Habit of Natural Gas Hydrate Occurrences*

The distribution of gas hydrate within the sediments is rather heterogeneous. The recovered pieces of gas hydrate apparently were concentrated in zones that are ~2–10 cm thick. However, most of the hydrate in Site 994 sediments are thought to be fine-grained crystals that are disseminated in clay and claystone pore spaces. High-resolution temperature measurements of slab samples (see "Gas Hydrate" section, this chapter) indicate that an individual thermal anomaly was produced from a discrete zone <2 $cm^3$ in size. The distribution of shipboard core temperature measurements and the interstitial-water chloride contents indicate that large variations in the amount of gas hydrate occur at the meter scale.

## Conclusions

Although very little gas hydrate was recovered from Site 994, the downhole interstitial-water chloride anomalies, temperature anomalies in recovered cores, and patterns in the downhole log data indicate that gas hydrate typically occupies between 1 and 3 vol% of the sedimentary section from 220 to 430 mbsf, with several intervals containing as much as 9.5 vol% gas hydrate. The hydrate is inferred to occur as finely dispersed crystals within homogenous sediments. All of the inferred hydrate occurs well above the experimentally predicted base of gas hydrate stability at this site.

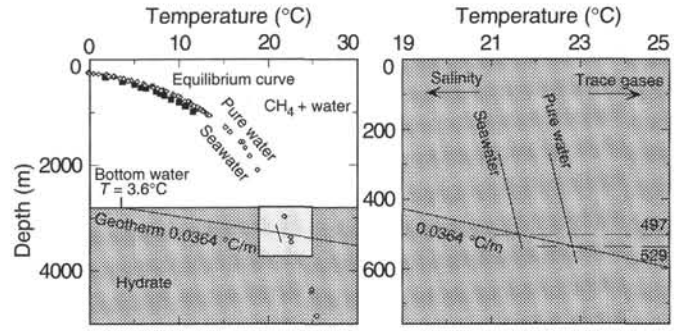


Figure 69. The zone of $CH_4$ hydrate stability in the marine environment lies between the sediment-water interface and the intersection of the geotherm and the $CH_4$ hydrate–water equilibrium curve (after Kvenvolden and McMenamin, 1980). At Site 994, the sediment-water interface is 2799 mbsl; the geotherm is 3.6° + 0.0364°C/mbsf. The depth of intersection for the $CH_4$ hydrate–water equilibrium curve in pure water (compiled in Sloan, 1990) occurs at ~529 mbsf; the depth of intersection for the $CH_4$ hydrate–water equilibrium curve in seawater (Dickens and Quinby-Hunt, 1994) occurs at ~497 mbsf. Depths along the equilibrium curves assume a hydrostatic pressure gradient of 0.010 MPa/m (1.467 psi/m). Note that dissolved ions shift the $CH_4$ hydrate–water equilibrium curve such that the zone of $CH_4$ hydrate stability is shallower than expected from consideration of the $CH_4$-pure water system and that incorporation of trace gases (e.g., $CO_2$, $H_2S$, and $C_2$) into the hydrate lattice has the opposite effect.

## REFERENCES

Archie, G.E., 1942. The electrical resistivity log as an aid in determining some reservoir characteristics. *J. Pet. Technol.,* 5:1–8.

Behrmann, J.H., Lewis, S.D., Musgrave, R.J., et al., 1992. *Proc. ODP, Init. Repts.,* 141: College Station, TX (Ocean Drilling Program).

Borowski, W.S., Paull, C.K., and Ussler, W., III, 1994. Influence of methane flux from gas hydrates on pore water sulfate profiles. *Eos,* 75:331–332.

Bullard, E.C., 1939. Heat flow in South Africa. *Proc. R. Soc. London A,* 173:474–502.

Cande, S.C., and Kent, D.V., 1995. Revised calibration of the geomagnetic polarity timescale for the Late Cretaceous and Cenozoic. *J. Geophys. Res.,* 100:6093–6095.

Collett, T.S., Bird, K.J., Kvenvolden, K.A., and Magoon, L.B., 1988. Geologic interrelations relative to gas hydrates within the North Slope of Alaska. *Open-File Rep.—U.S. Geol. Surv.,* 88–389:150.

Collett, T.S., Godbole, S.P., and Economides, C.E., 1984. Quantification of in-situ gas hydrates with well logs. *Proc. Annu. Tech. Meet. Petrol. Soc. CIM,* 35:571–582.

Collot, J.-Y., Greene, H.G., Stokking, L.B., et al., 1992. *Proc. ODP, Init. Repts.,* 134: College Station, TX (Ocean Drilling Program).

Damuth, J.E., 1977. Late Quaternary sedimentation in the western equatorial Atlantic. *Geol. Soc. Am. Bull.,* 88:695–710.

Davis, E.E., Mottl, M.J., Fisher, A.T., et al., 1992. *Proc. ODP, Init. Repts.,* 139: College Station, TX (Ocean Drilling Program).

Dickens, G.R., and Quinby-Hunt, M.S., 1994. Methane hydrate stability in seawater. *Geophys. Res. Lett.,* 21:2115–2118.

Duan, Z., Møller, N., Greenberg, J., and Weare, 1992. The prediction of methane solubility in natural waters to high ionic strengths from 0° to 250°C and from 0 to 1600 bar. *Geochim. Cosmochim. Acta,* 56:1451–1460.

Froelich, P.N., Kvenvolden, K.A., Torres, M.E., Waseda, A., Didyk, B.M., and Lorenson, T.D., 1995. Geochemical evidence for gas hydrate in sediment near the Chile Triple Junction. *In* Lewis, S.D., Behrmann, J.H., Musgrave, R.J., and Cande, S.C. (Eds.), *Proc. ODP, Sci. Results,* 141: College Station, TX (Ocean Drilling Program), 279–286.

Gartner, S., 1977. Calcareous nannofossil biostratigraphy and revised zonation of the Pleistocene. *Mar. Micropaleontol.,* 2:1–25.

Gradstein, F.M., and Sheridan, R.E., 1983. Introduction. *In* Sheridan R.E., Gradstein, F.M., et al., *Init. Repts. DSDP,* 76: Washington (U.S. Govt. Printing Office), 5–18.

Heezen, B.C., Hollister, C.D., and Ruddiman, W.F., 1966. Shaping of the continental rise by deep geostrophic contour currents. *Science,* 152:502–508.

Hesse, R., and Harrison, W.E., 1981. Gas hydrates (clathrates) causing pore-water freshening and oxygen isotope fractionation in deep-water sedimentary sections of terrigenous continental margins. *Earth Planet. Sci. Lett.,* 55:453–462.

Hesse, R., Lebel, J., and Gieskes, J.M., 1985. Interstitial water chemistry of gas-hydrate-bearing sections on the Middle America Trench slope, Deep-Sea Drilling Project Leg 84. *In* von Huene, R., Aubouin, J., et al., *Init. Repts. DSDP,* 84: Washington (U.S. Govt. Printing Office), 727–737.

Housen, B.A., and Musgrave, R.J., 1996. Rock-magnetic signature of gas hydrates in accretionary prism sediments. *Earth Planet. Sci. Lett.,* 139:509–519.

Jenden, P.D., and Gieskes, J.M., 1983. Chemical and isotopic composition of interstitial water from Deep Sea Drilling Project Sites 533 and 534. *In* Sheridan, R.E., Gradstein, F.M., et al., *Init. Repts. DSDP,* 76: Washington (U.S. Govt. Printing Office), 453–461.

Kastner, M., Elderfield, H., Martin, J.B., Suess, E., Kvenvolden, K.A., and Garrison, R.E., 1990. Diagenesis and interstitial-water chemistry at the Peruvian continental margin—major constituents and strontium isotopes. *In* Suess, E., von Huene, R., et al., *Proc. ODP, Sci. Results,* 112: College Station, TX (Ocean Drilling Program), 413–440.

Katz, B.K., 1983. Organic geochemical character of some Deep Sea Drilling Project cores from Legs 76 and 44. *In* Sheridan, R.E., Gradstein, F.M., et al., *Init. Repts. DSDP,* 76: Washington (U.S. Govt. Printing Office), 463–468.

Katzman, R., Holbrook, W.S., Paull, C.K., and Collins, J.A., 1994. A combined verticle incidence and wide-angle seismic study of a gas hydrate zone, Blake Outer Ridge. *J. Geophys. Res.,* 99:17975–17995.

Klitgord, K.D., and Behrendt, J.C., 1979. Basin structure in the U.S. Atlantic margin. *In* Watkins, J.S., Montadert, L., and Wood-Dickerson, P., *Geological and Geophysical Investigations of Continental Margins.* AAPG Mem., 29:85–112.

Kvenvolden, K.A., 1988. Methane hydrate—a major reservoir of carbon in the shallow geosphere? *Chem. Geol.,* 71:41–51.

Kvenvolden, K.A., and Barnard, L.A., 1983. Gas hydrates of the Blake Outer Ridge, Site 533, Deep Sea Drilling Project Leg 76. *In* Sheridan, R.E., Gradstein, F.M., et al., *Init. Repts. DSDP,* 76: Washington (U.S. Govt. Printing Office), 353–365.

Kvenvolden, K.A., Barnard, L.A., and Cameron, D.H., 1983. Pressure core barrel: application to the study of gas hydrates, Deep Sea Drilling Project Site 533, Leg 76. *In* Sheridan, R.E., Gradstein, F.M., et al., *Init. Repts. DSDP,* 76: Washington (U.S. Govt. Printing Office), 367–375.

Kvenvolden, K.A., Ginsburg, G.D., and Solovyev, V.A., 1993. Worldwide distribution of subaquatic gas hydrates. *Geo-Mar. Lett.,* 13:32–40.

Kvenvolden, K.A., and Kastner, M., 1990. Gas hydrates of the Peruvian outer continental margin. *In* Suess, E., von Huene, R., et al., *Proc. ODP, Sci. Results,* 112: College Station, TX (Ocean Drilling Program), 517–526.

Kvenvolden, K.A., and McMenamin, M.A., 1980. Hydrates of natural gas: a review of their geologic occurrence. *Geol. Surv. Circ. (U.S.),* 825.

Langford, F.F., and Blanc-Valleron, M.M., 1990. Interpreting Rock-Eval pyrolysis data using graphs of pyrolizable hydrocarbons vs. total organic carbon. *AAPG Bull.,* 74:799–804.

Lee, H.J., 1982. Bulk density and shear strength of several deep-sea calcareous sediments. *In* Demars, K.R., and Chaney, R.C. (Eds.), *Geotechnical Properties, Behavior, and Performance of Calcareous Soils.* ASTM Spec. Tech. Publ., 777:54–78.

Manheim, F.T., and Sayles, F.L., 1974. Composition and origin of interstitial waters of marine sediments, based on deep sea drill cores. *In* Goldberg, E.D. (Ed.), *The Sea* (Vol. 5): *Marine Chemistry: The Sedimentary Cycle:* New York (Wiley), 527–568.

Markl, R.G., and Bryan, G.M., 1983. Stratigraphic evolution of the Blake Outer Ridge. *AAPG Bull.,* 67:663–683.

Markl, R.G., Bryan, G.M., and Ewing, J.I., 1970. Structure of the Blake-Bahama Outer Ridge. *J. Geophys. Res.,* 75:4539–4555.

Mathews, M., 1986. Logging characteristics of methane hydrate. *The Log Analyst,* 27:26–63.

Matsuhisa, Y., and Matsumoto, R., 1986. Oxygen isotope ratios of interstitial waters from the Nankai Trough and the Japan Trench, Leg 87. *In* Kagami, H., Karig, D.E., Coulbourn, W.T., et al., *Init. Repts. DSDP,* 87: Washington (U.S. Govt. Printing Office), 853–856.

Matsumoto, R., 1989. Isotopically heavy oxygen-containing siderite derived from the decomposition of methane hydrate. *Geology,* 17:707–710.

Matsumoto, R., 1983. Mineralogy and geochemistry of carbonate diagenesis of the Pliocene and Pleistocene hemipelagic mud on the Blake Outer Ridge, Site 533, Leg 76. *In* Sheridan, R.E., Gradstein, F.M., et al., *Init. Repts. DSDP,* 76: Washington (U.S. Govt. Printing Office), 411–427.

Mayer, L.A., 1979. Deep sea carbonates: acoustic, physical, and stratigraphic properties. *J. Sediment. Petrol.,* 49:819–836.

McDuff, R.E., 1985. The chemistry of interstitial waters, Deep Sea Drilling Project Leg 86. *In* Heath, G.R., Burckle, L.H., et al., *Init. Repts. DSDP,* 86: Washington (U.S. Govt. Printing Office), 675–687.

Molfino, B., and McIntyre, A., 1990. Precessional forcing of nutricline dynamics in the Equatorial Atlantic. *Science,* 249:766–769.

Mountain, G.S., Miller, K.G., Blum, P., et al., 1994. *Proc. ODP, Init. Repts.,* 150: College Station, TX (Ocean Drilling Program).

Needham, H.D., Habib, D., and Heezen, B.C., 1969. Upper Carboniferous palynomorphs as a tracer of red sediment dispersal patterns in the Northwest Atlantic. *J. Geol.,* 77:113–120.

Paull, C.K., Ussler, W., III, and Borowski, W., 1994. Sources of biogenic methane to form marine gas-hydrates: in situ production or upward migration? *Ann. N.Y. Acad. Sci.,* 715:392–409.

Paull, C.K., Ussler, W., and Dillon, W.P., 1991. Is the extent of glaciation limited by marine gas-hydrates? *Geophys. Res. Lett.,* 18:432–434.

Pearson, C.F., Halleck, P.M., McGuire, P.L., Hermes, R., and Mathews, M., 1983. Natural gas hydrate deposits: a review of in-situ properties. *J. Phys. Chem.,* 87:4180–4185.

Pedersen, T.F., and Shimmield, G.B., 1991. Interstitial water chemistry, Leg 117: contrasts with the Peru Margin. *In* Prell, W.L., Niitsuma, N., et al., *Proc. ODP, Sci. Results,* 117: College Station, TX (Ocean Drilling Program), 499–513.

Prensky, S., 1995. A review of gas hydrates and formation evaluation of hydrate-bearing reservoirs. *Proc. SPWLA Annu. Logging Symp.,* 36:GGG.

Ratcliffe, E.H., 1960. Thermal conductivities of ocean sediments. *J. Geophys. Res.,* 65:1535–1541.

Reynolds, R.L., Tuttle, M.L., Rice, C.A., Fishman, N.S., Karachewski, J.A., and Sherman, D.M., 1994. Magnetization and geochemistry of greigite-bearing Cretaceous strata, North Slope Basin, Alaska. *Am. J. Sci.,* 294:485–528.

Roberts, A.P., 1994. Sedimentary greigite ($Fe_3S_4$): formation, identification, and magnetic characteristics. *Eos,* 75:124. (Abstract)

Ruppel, C., Von Herzen, R.P., and Bonneville, A., 1995. Heat flux through an old (~175 Ma) passive margin: offshore southeastern United States. *J. Geophys. Res.,* 100:20037–20057.

Schaefer, R.G., and Leythaeuser, D., 1984. $C_2$–$C_8$ hydrocarbons in sediments from Deep Sea Drilling Project Leg 75, Holes 530A, Angola Basin, and 532, Walvis Ridge. *In* Hay, W.W., Sibuet, J.-C., et al., *Init. Repts. DSDP,* 75 (Pt. 2): Washington (U.S. Govt. Printing Office), 1055–1067.

Schlumberger, 1989. *Log Interpretation Principles/Applications:* Houston, TX (Schlumberger Educational Services).

Schoell, M., 1980. The hydrogen and carbon isotopic composition of methane from natural gases of various origins. *Geochim. Cosmochim. Acta,* 44:649–662.

Schrag, D.P., and DePaolo, D.J., 1993. Determination of $\delta^{18}O$ of seawater in the deep ocean during the last glacial maximum. *Paleoceanography,* 8:1–6.

Sheridan, R.E., Gradstein, F.M., et al., 1983. *Init. Repts. DSDP,* 76: Washington (U.S. Govt. Printing Office).

Shipboard Scientific Party, 1972. Sites 102-103-104—Blake-Bahama Outer Ridge (northern end). *In* Hollister, C.D., Ewing, J.I., et al., *Init. Repts. DSDP,* 11: Washington (U.S. Govt. Printing Office), 135–218.

———, 1989. Site 735. *In* Robinson, P.T., Von Herzen, R., et al., *Proc. ODP, Init. Repts.,* 118: College Station, TX (Ocean Drilling Program), 89–222.

———, 1994. Sites 889 and 890. *In* Westbrook, G.K., Carson, B., Musgrave, R.J., et al., *Proc. ODP, Sci. Results,* 146: College Station, TX (Ocean Drilling Program), 127–239.

Shipley, T.H., Houston, M.H., Buffler, R.T., Shaub, F.J., McMillen, K.J., Ladd, J.W., and Worzel, J.L., 1979. Seismic evidence for widespread possible gas hydrate horizons on continental slopes and rises. *AAPG Bull.,* 63:2204–2213.

Sloan, E.D., 1990. *Clathrate Hydrates of Natural Gases:* New York (Marcel Dekker).

Thompson, R., and Oldfield, F., 1986. *Environmental Magnetism:* London (Allen and Unwin).

Tucholke, B.E., Bryan, G.M., and Ewing, J.I., 1977. Gas hydrate horizon detected in seismic reflection profiler data from the western North Atlantic. *AAPG Bull.,* 61:698–707.

Tucholke, B.E., and Carpenter, G.B., 1977. Sediment distribution and Cenozoic sedimentation patterns on the Agulhas Plateau. *Geol. Soc. Am. Bull.,* 88:1337–1346.

Tucholke, B.E., and Mountain, G.S., 1979. Seismic stratigraphy, lithostratigraphy, and paleosedimentation patterns in the North American Basin. *In* Talwani, M., Hay, W., and Ryan, W.B.F. (Eds.), *Deep Drilling Results in the Atlantic Ocean: Continental Margins and Paleoenvironment.* Am. Geophys. Union, Maurice Ewing Ser., 3:58–86.

Westbrook, G.K., Carson, B., Musgrave, R.J., et al., 1994. *Proc. ODP, Init. Repts.,* 146 (Pt. 1): College Station, TX (Ocean Drilling Program).

**Ms 164IR-107**

**NOTE: Core-description forms ("barrel sheets") and core photographs can be found in Section 4, beginning on page 337. Forms containing smear-slide data can be found in Section 5, beginning on page 599.**

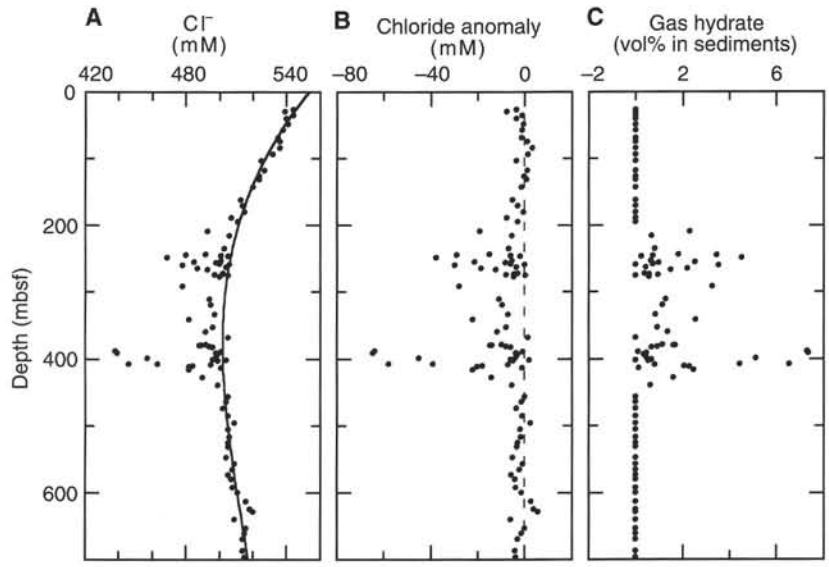


Figure 70. **A.** Interstitial-water chloride profiles at Site 994 indicate a distinct freshening with depth that is highlighted by a zone of low and erratic values between 200 and 450 mbsf. A polynomial fit to the data above and below the 200–450 mbsf zone is indicated. **B.** Chloride anomalies are interpreted with respect to the polynomial. **C.** The percentage of gas hydrate by volume is calculated by assuming that the chloride anomalies (B) are solely produced by gas hydrate decomposition during core recovery and are corrected by porosity using a linear fit to the porosity data (see "Physical Properties" section, this chapter).

# SHORE-BASED LOG PROCESSING
# HOLE 994C

**Bottom felt:** 2810.1 mbrf
**Total penetration:** 703.5 mbsf
**Total core recovered:** 501.5 m (71.3%)

## Logging Runs

Logging string 1: DITE/SDT/HLDT/CNT-G/NGT/LDEO-TLT (2 runs)
Logging string 2: AACT/GST/NGT
A wireline heave compensator was used to counter ship heave.

## Bottom-Hole Assembly Depths

The following bottom-hole assembly depths are as they appear on the logs after differential depth shift (see "Depth Shift" section) and depth shift to the seafloor. As such, there might be a discrepancy with the original depths given by the drillers on board. Possible reasons for depth discrepancies are ship heave, the use of the wireline heave compensator, and drill string and/or wireline stretch.

DITE/SDT/HLDT/CNT-G/NGT: Bottom-hole assembly at ~77.5 mbsf.
AACT/GST/NGT: Bottom-hole assembly at ~74.5 mbsf.

## Processing

**Depth shift:** Original logs have been interactively depth shifted with reference to the NGT from DITE/SDT/HLDT/CNT-G/NGT run and to the seafloor (–2809.5 m). This amount corresponds to the depth of the seafloor as seen on the logs and differs 0.6 m from the "bottom felt" depth given by the drillers.

**Gamma-ray processing:** Data have been processed to correct for borehole size and type of drilling fluid.

**Acoustic data processing:** The array sonic tool was operated in the standard depth-derived borehole compensated mode including long (8-10-10-12 ft) and short-spacing mode (3-5-5-7 ft). The long-spacing logs have been processed to eliminate some of the noise and cycle skipping experienced during the recording.

**Geochemical processing:** The elemental yields recorded by the GST tool represent the relative contribution of only some of the rock-forming elements (iron, calcium, chlorine, silicon, sulfur, hydrogen, gadolinium, and titanium—the last two computed during geochemical processing) to the total spectrum. Because other rock-forming elements are present in the formation (such as aluminum, potassium, and so on), caution is recommended in using the yields to infer lithologic changes. Instead, ratios (see file acronyms.doc on CD-ROM in back pocket, this volume) are more appropriate to determine changes in the macroscopic properties of the formation. A list of oxide factors used in geochemical processing includes the following:

$SiO_2$ = 2.139
$CaO/CaCO_3$ = 1.399–2.497
FeO* = 1.358
$TiO_2$ = 1.668
$K_2O$ = 1.205
$Al_2O_3$ = 1.889

FeO* Computed using an oxide factor that assumes a 50:50 combination of $Fe_2O_3$ and FeO factors.

VARCA = variable Ca oxide/carbonate factor used in $CaO/CaCO_3$ calculation.

## Quality Control

The quality of the density data was greatly impaired by the degraded hole conditions, which yielded bulk density values as low as 1.2 g/cm$^3$ in the 215 mbsf–TD interval. Invalid density spikes were observed at 395–405, 410–413, 426–428, and 442–450 mbsf.

Data recorded through the bottom-hole assembly, such as the NGT data above 77.5 mbsf, should be used qualitatively only because of the attenuation on the incoming signal. Invalid gamma-ray data were recorded at 63–77.5 mbsf during the DITE/SDT/HLDT/CNT-G/NGT run.

The quality of the acoustic data was greatly impaired by the degraded hole conditions and by the presence of gas hydrate, which yielded original transit time values in excess of 220 µs/ft. The processing produced acceptable results that should be regarded from a qualitative standpoint only; invalid data are still present at 85 and 205–214.5 mbsf.

The results of geochemical processing are presented along with the calcium carbonate measurements performed on board. FACT = quality control curve in geochemical processing. Accuracy of the estimates is inversely proportional to the magnitude of the curve.

Details of standard shore-based processing procedures are found in the "Explanatory Notes" chapter (this volume). For further information about the logs, please contact:

Cristina Broglia
Phone: 914-365-8343
Fax: 914-365-3182
E-mail: chris@ldeo.columbia.edu

Elizabeth Pratson
Phone: 914-365-8313
Fax: 914-365-3182
E-mail: beth@ldeo.columbia.edu

Hole 994C: Natural Gamma Ray Logging Data

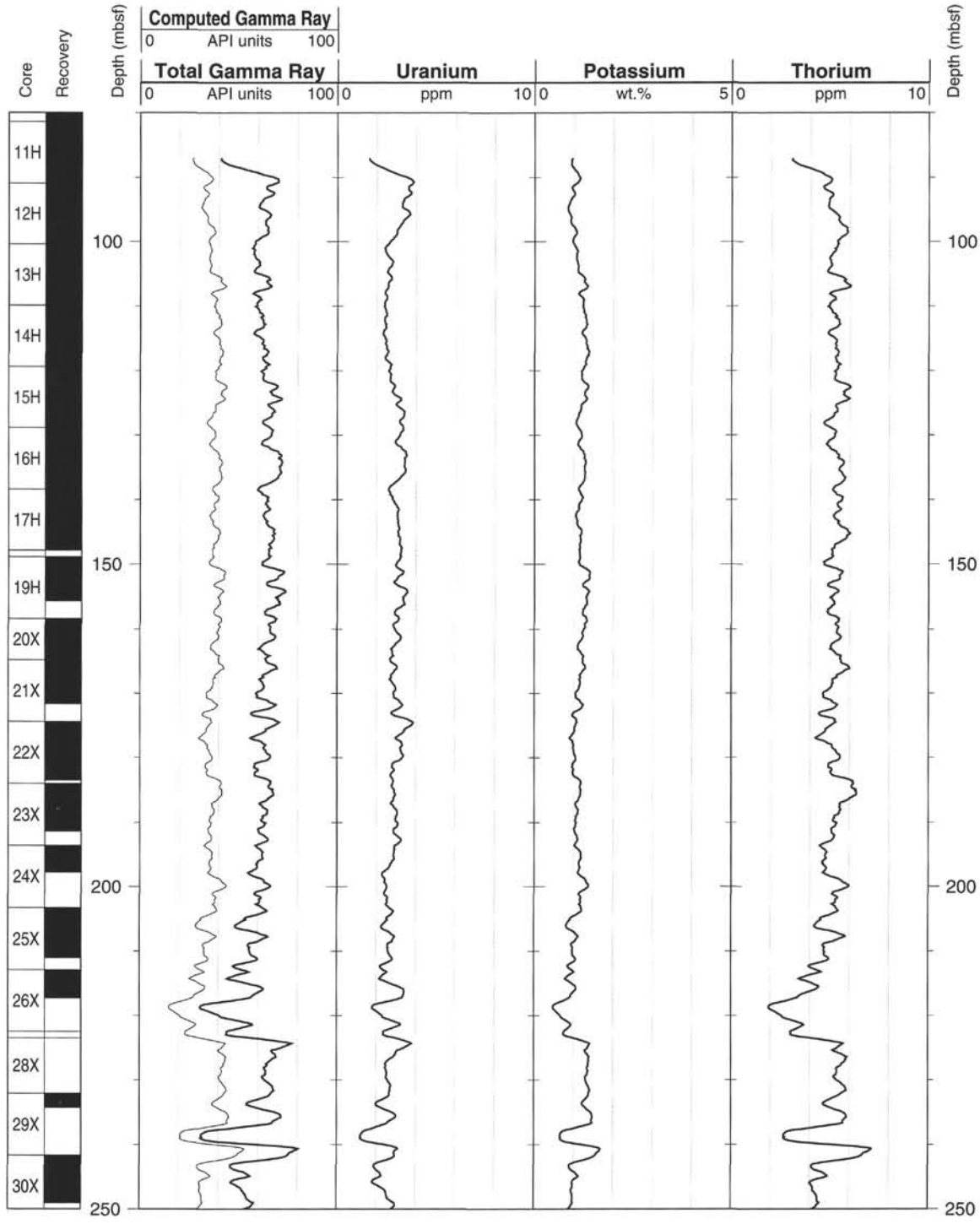

Hole 994C: Natural Gamma Ray Logging Data (cont.)

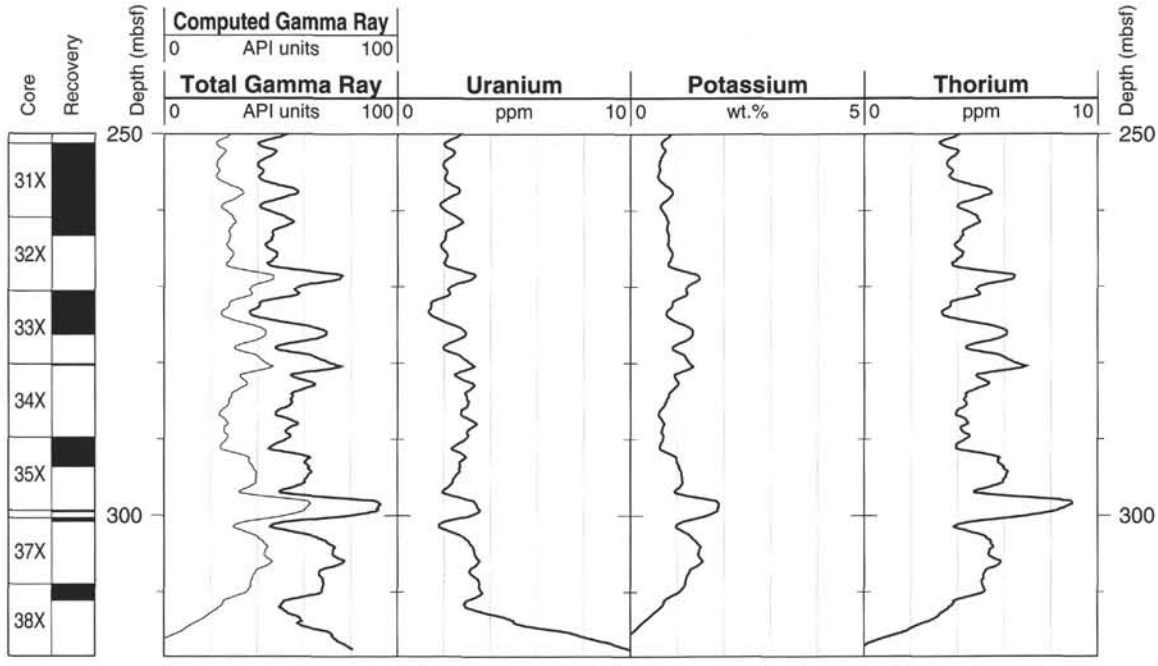

Hole 994C: Natural Gamma Ray-Density-Porosity Logging Data

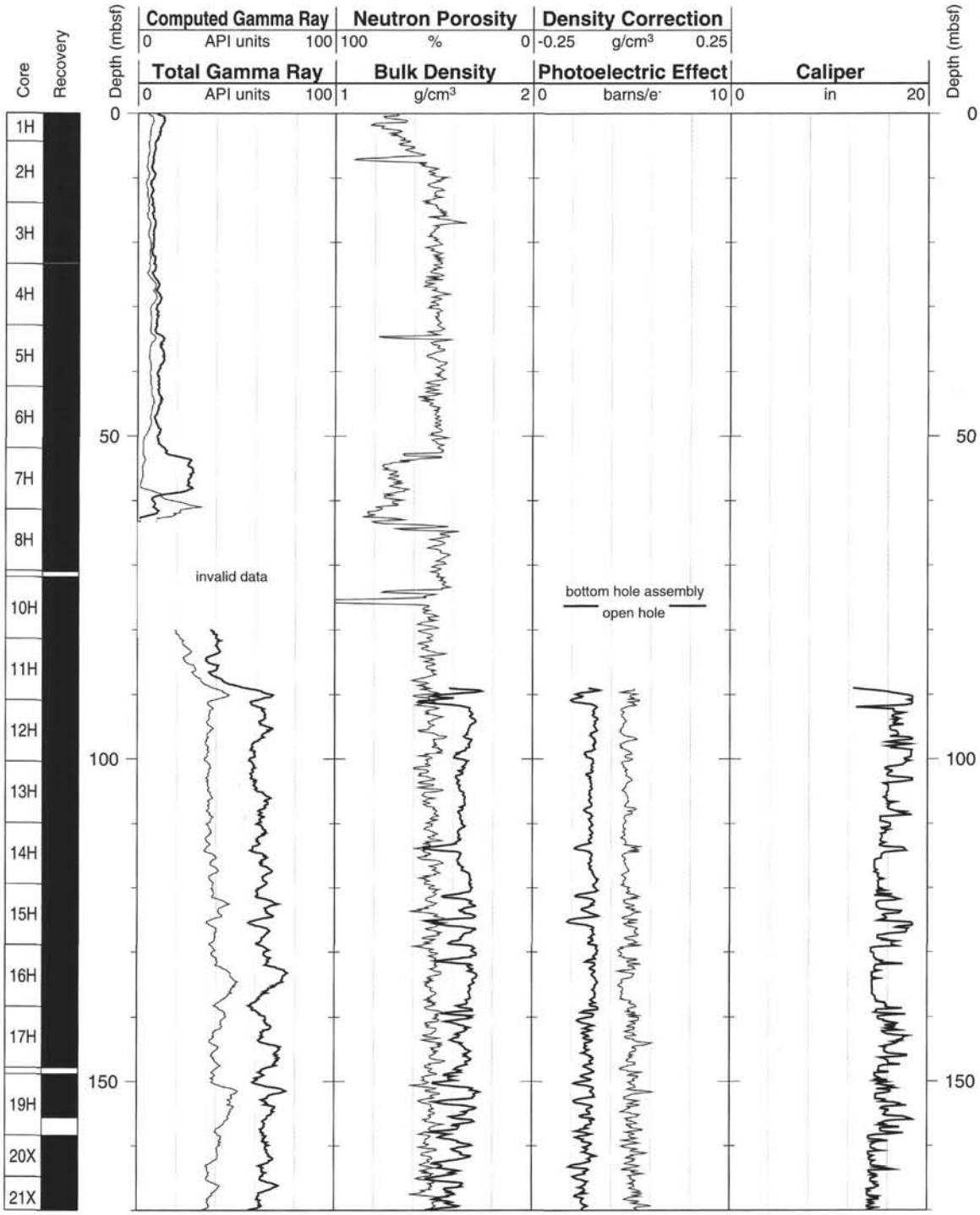

Hole 994C: Natural Gamma Ray-Density-Porosity Logging Data (cont.)

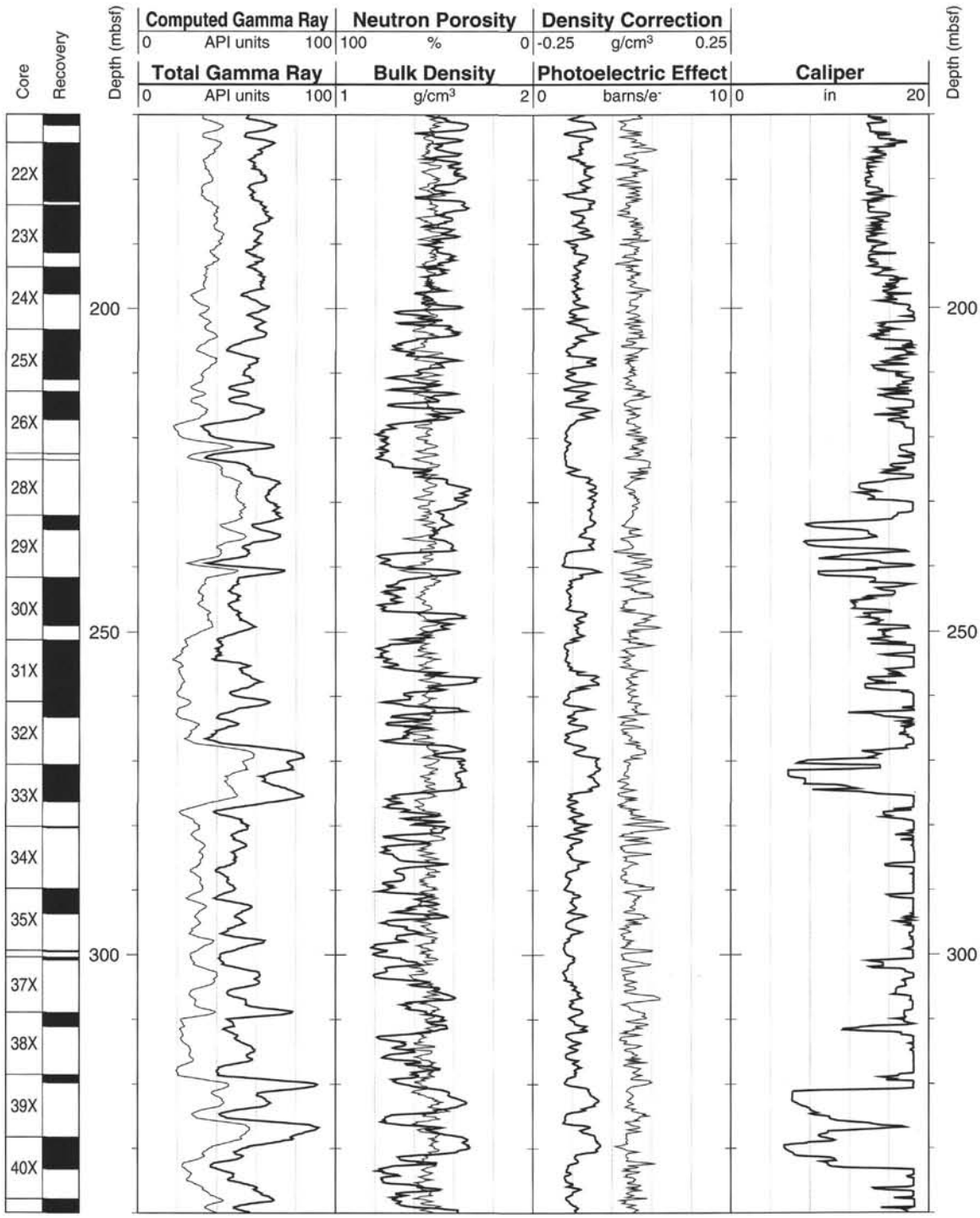

Hole 994C: Natural Gamma Ray-Density-Porosity Logging Data (cont.)

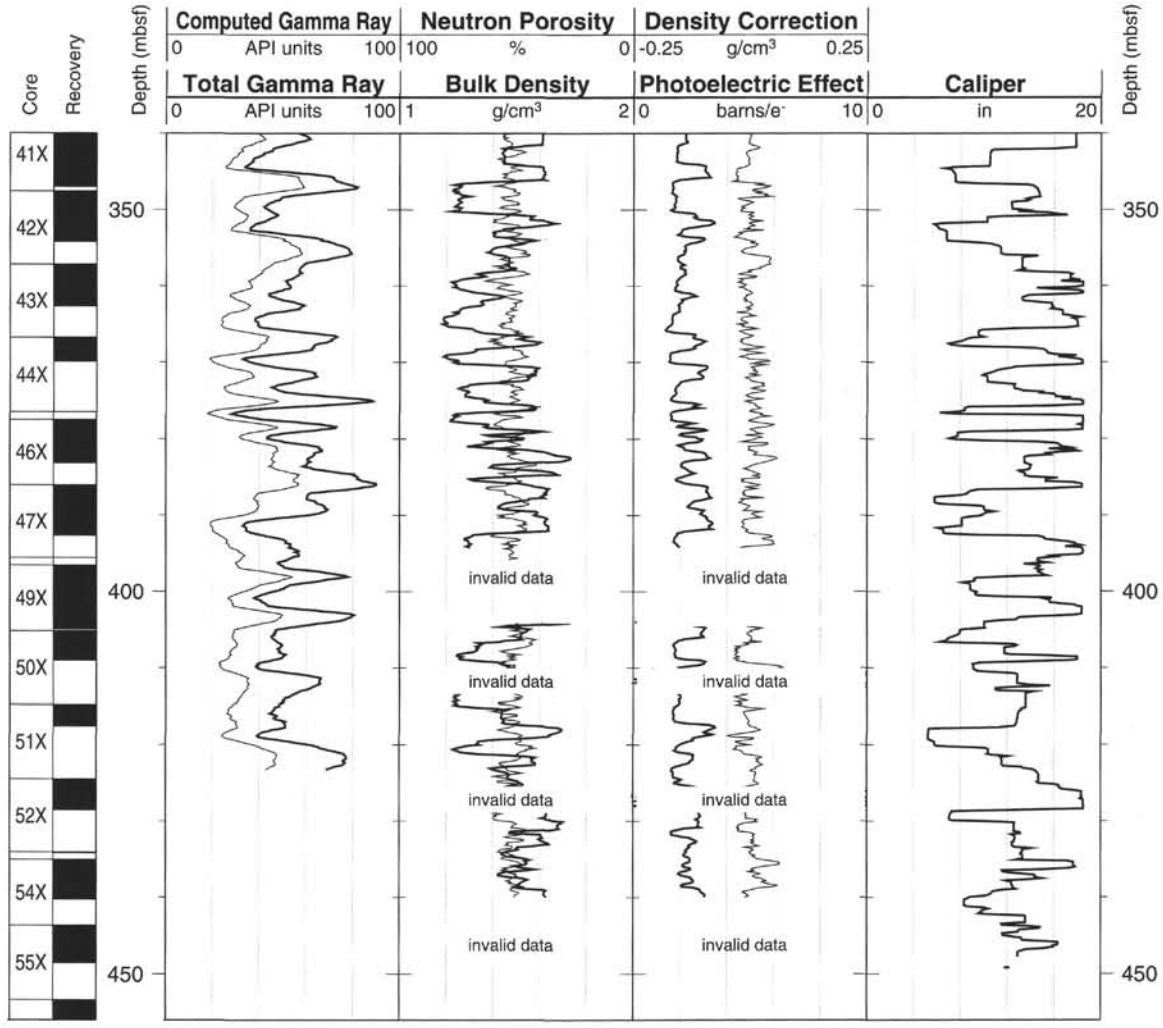

Hole 994C: Natural Gamma Ray-Resistivity-Sonic Logging Data

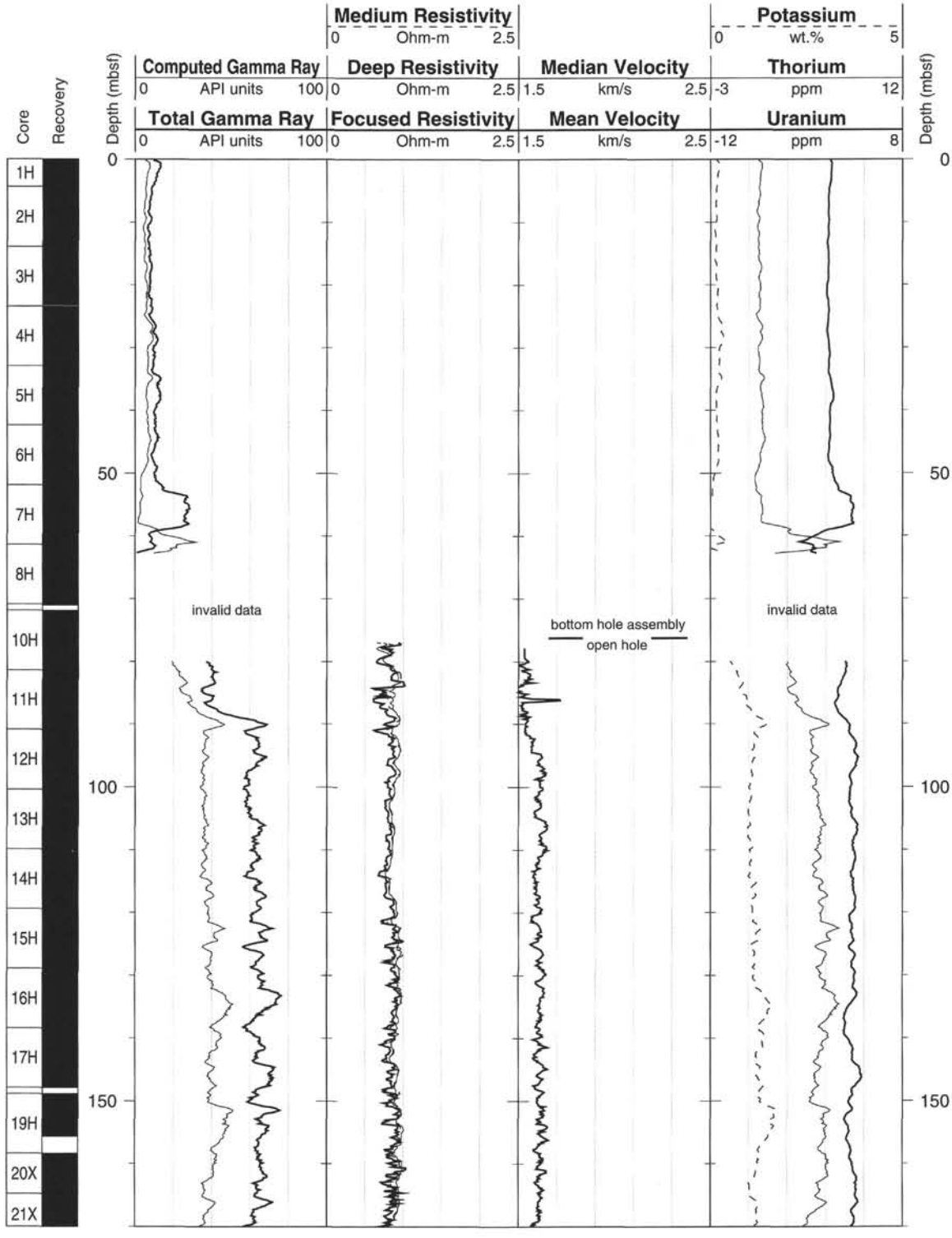

Hole 994C: Natural Gamma Ray-Resistivity-Sonic Logging Data (cont.)

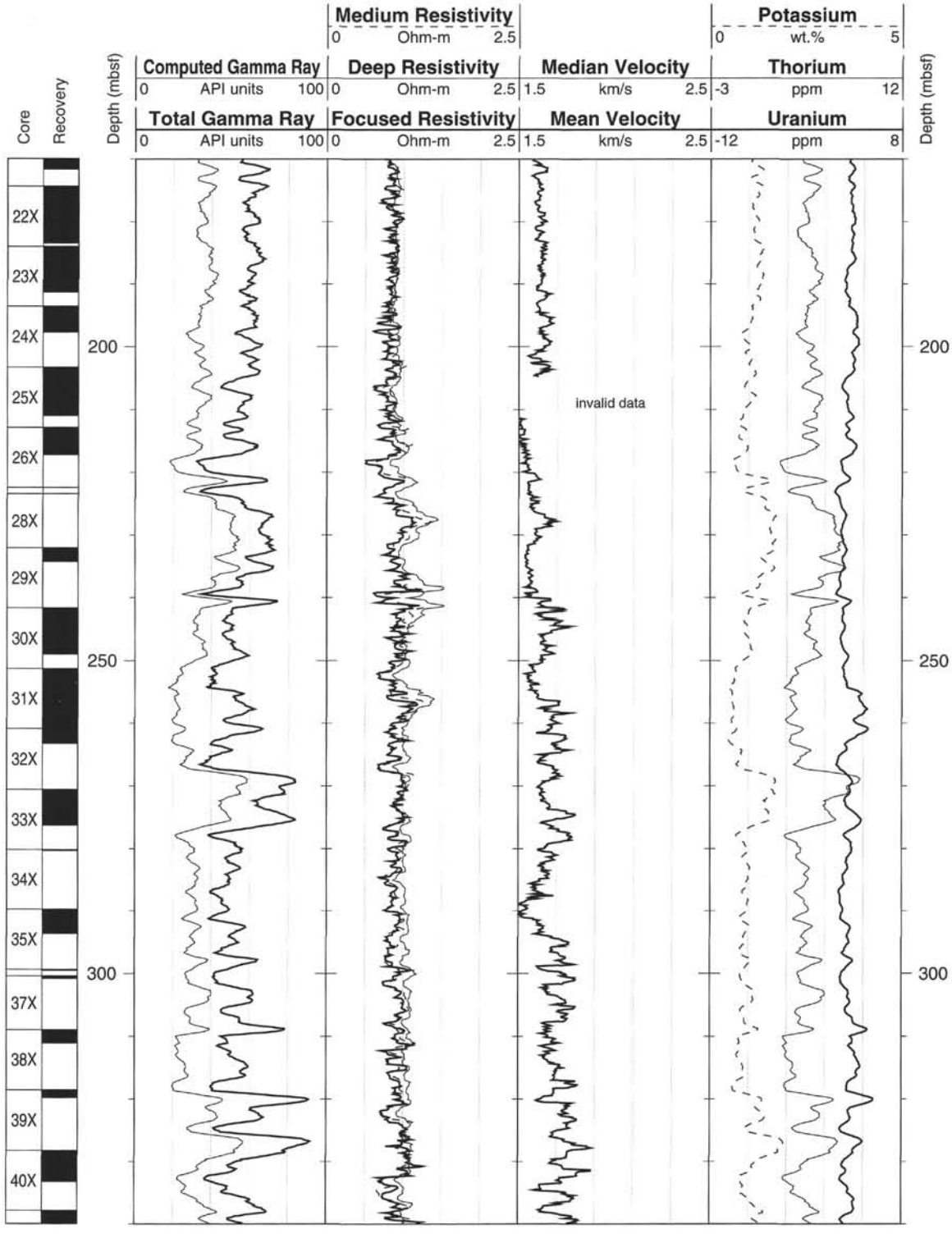

Hole 994C: Natural Gamma Ray-Resistivity-Sonic Logging Data (cont.)

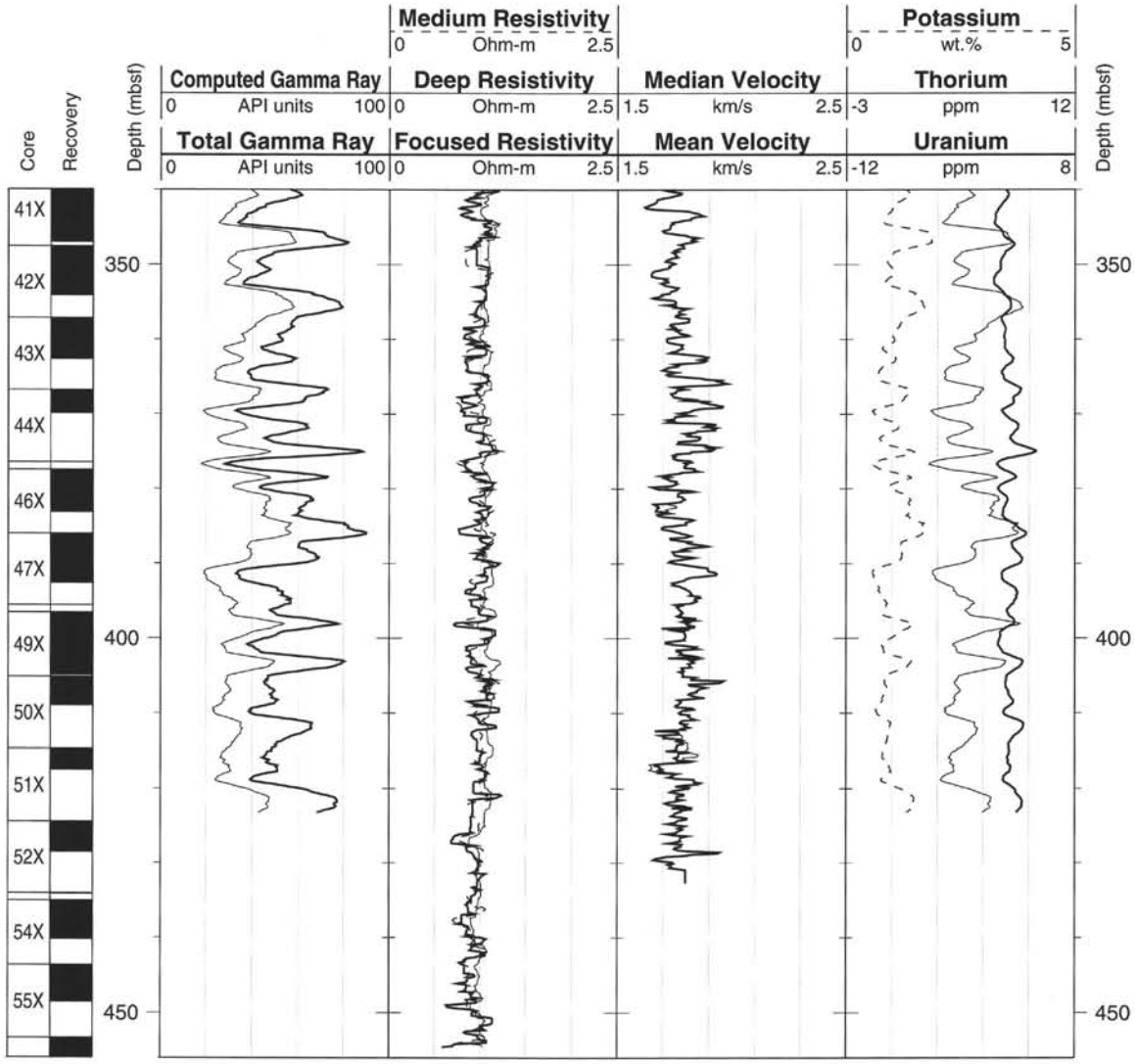

Hole 994C: Geochemical Logging Data

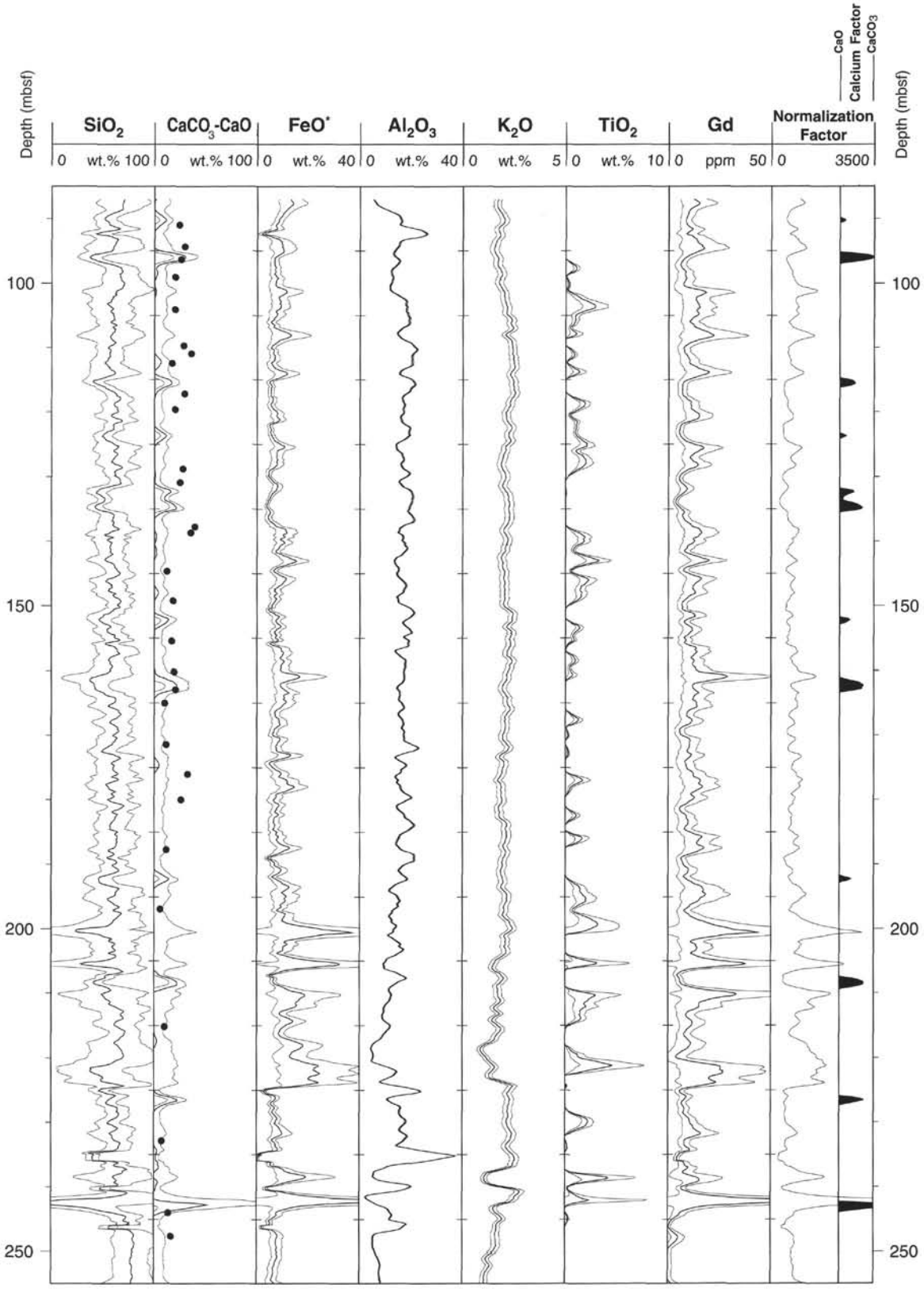

Hole 994C: Geochemical Logging Data (cont.)

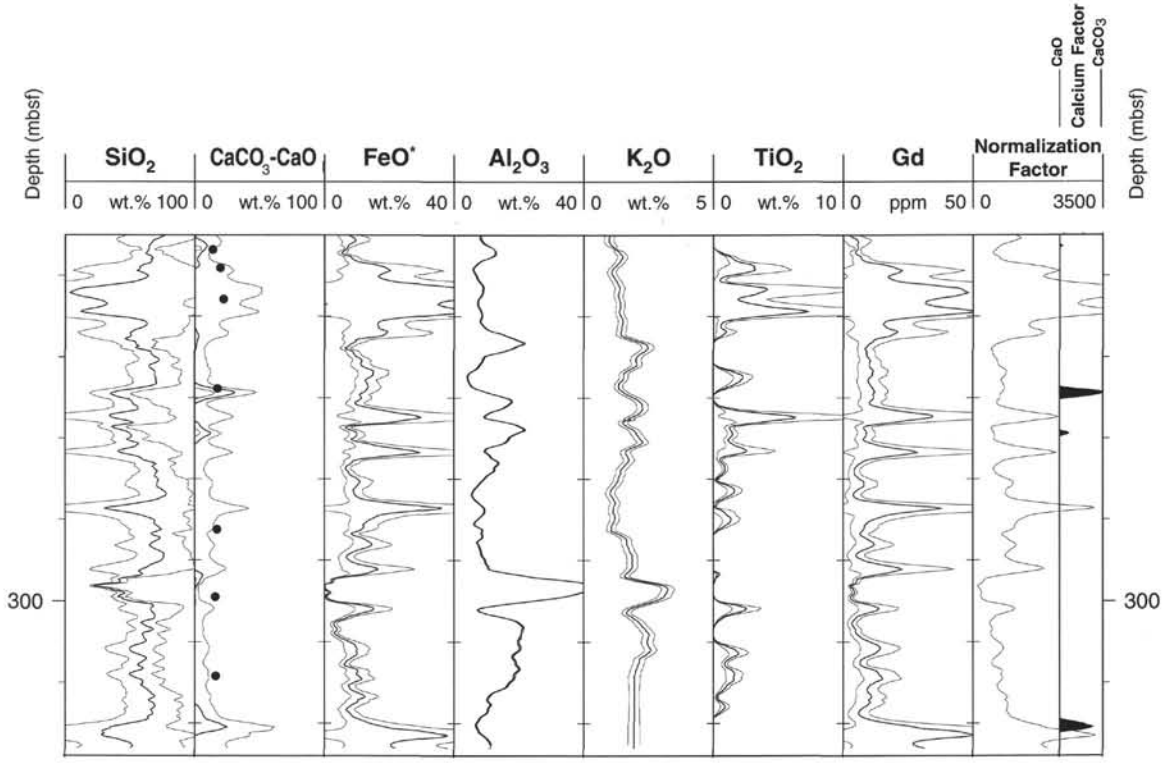

# SHORE-BASED LOG PROCESSING
# HOLE 994D

**Bottom felt:** 2810.1 mbrf
**Total penetration:** 670 mbsf
**Total core recovered:** 69.4 (80.5%)

## Logging Runs

Logging string 1: DITE/SDT/HLDT/NGT
Logging string 2: LDEO-SST

A wireline heave compensator was used to counter ship heave.

## Bottom-Hole Assembly

The following bottom-hole assembly depths are as they appear on the logs after differential depth shift (see "Depth Shift" section) and depth shift to the seafloor. As such, there might be a discrepancy with the original depths given by the drillers on board. Possible reasons for depth discrepancies are ship heave, the use of the wireline heave compensator, and drill string and/or wireline stretch.

DITE/SDT/HLDT/NGT: Bottom-hole assembly at ~114 mbsf.

## Processing

**Depth shift.** No depth shift necessary.

**Gamma-ray processing:** Data have been processed to correct for borehole size and type of drilling fluid.

**Acoustic data processing:** The array sonic tool was operated in standard depth-derived, borehole compensated, long spacing mode (8-10-10-12 ft). The long-spacing logs have been processed to eliminate some of the noise and cycle skipping experienced during the recording.

## Quality Control

The quality of the density data was affected by the degraded hole conditions that caused frequent low density (<1.5 g/cm$^3$). Invalid density/photoelectric effect spikes were observed at 203–211, 246, 324, 435, 467.5, 505, 523, 697.5, and 611.5 mbsf.

Data recorded through bottom-hole assembly, such as the NGT data above 114 mbsf, should be used qualitatively only because of the attenuation on the incoming signal. Invalid gamma-ray data were recorded at 94–100 and 108–117 mbsf.

Details of standard shore-based processing procedures are found in the "Explanatory Notes" chapter (this volume). For further information about the logs, please contact:

Cristina Broglia
Phone: 914-365-8343
Fax: 914-365-3182
E-mail: chris@ldeo.columbia.edu

Elizabeth Pratson
Phone: 914-365-8313
Fax: 914-365-3182
E-mail: beth@ldeo.columbia.edu

Hole 994D: Natural Gamma Ray-Density-Porosity Logging Data

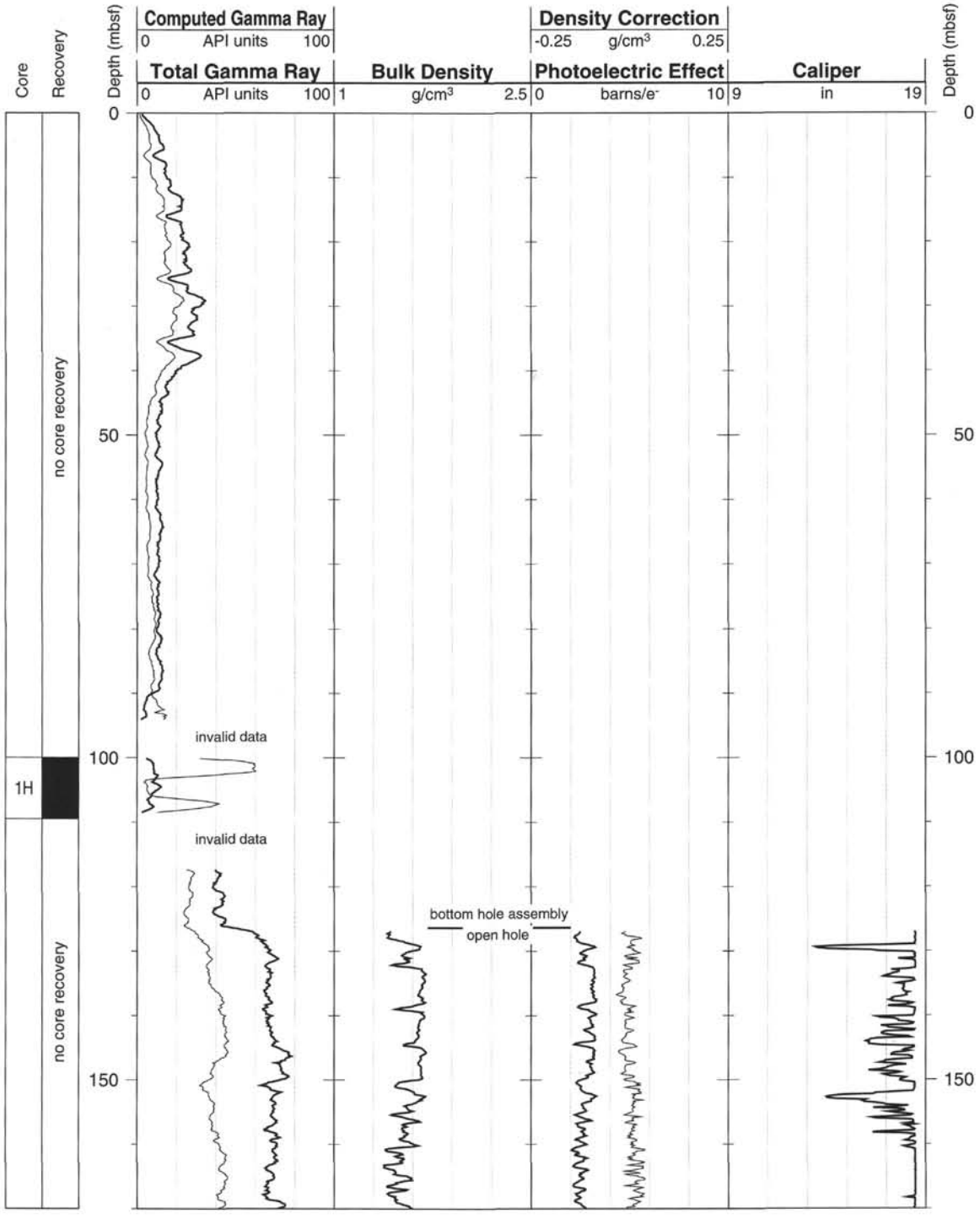

Hole 994D: Natural Gamma Ray-Density-Porosity Logging Data (cont.)

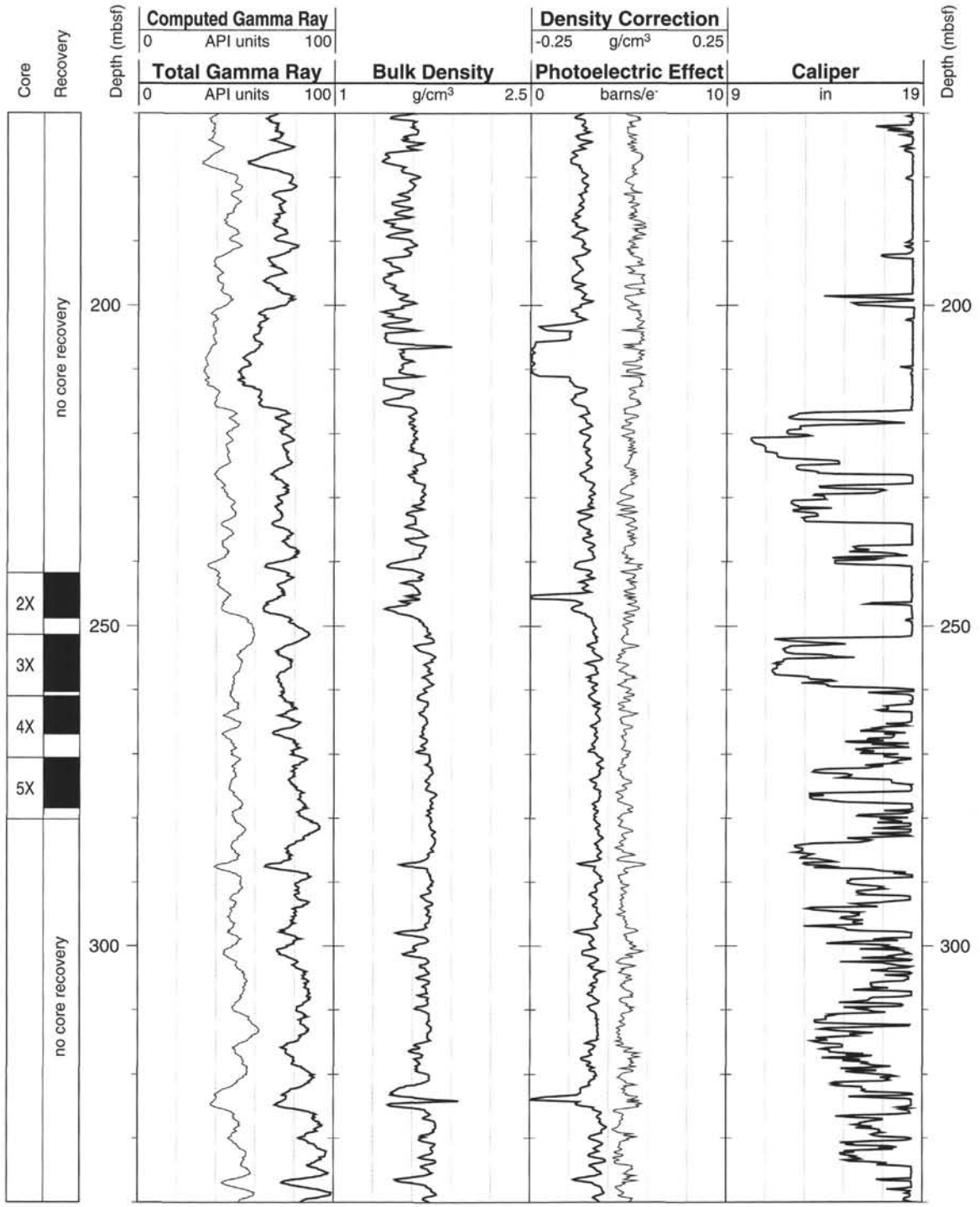

Hole 994D: Natural Gamma Ray-Density-Porosity Logging Data (cont.)

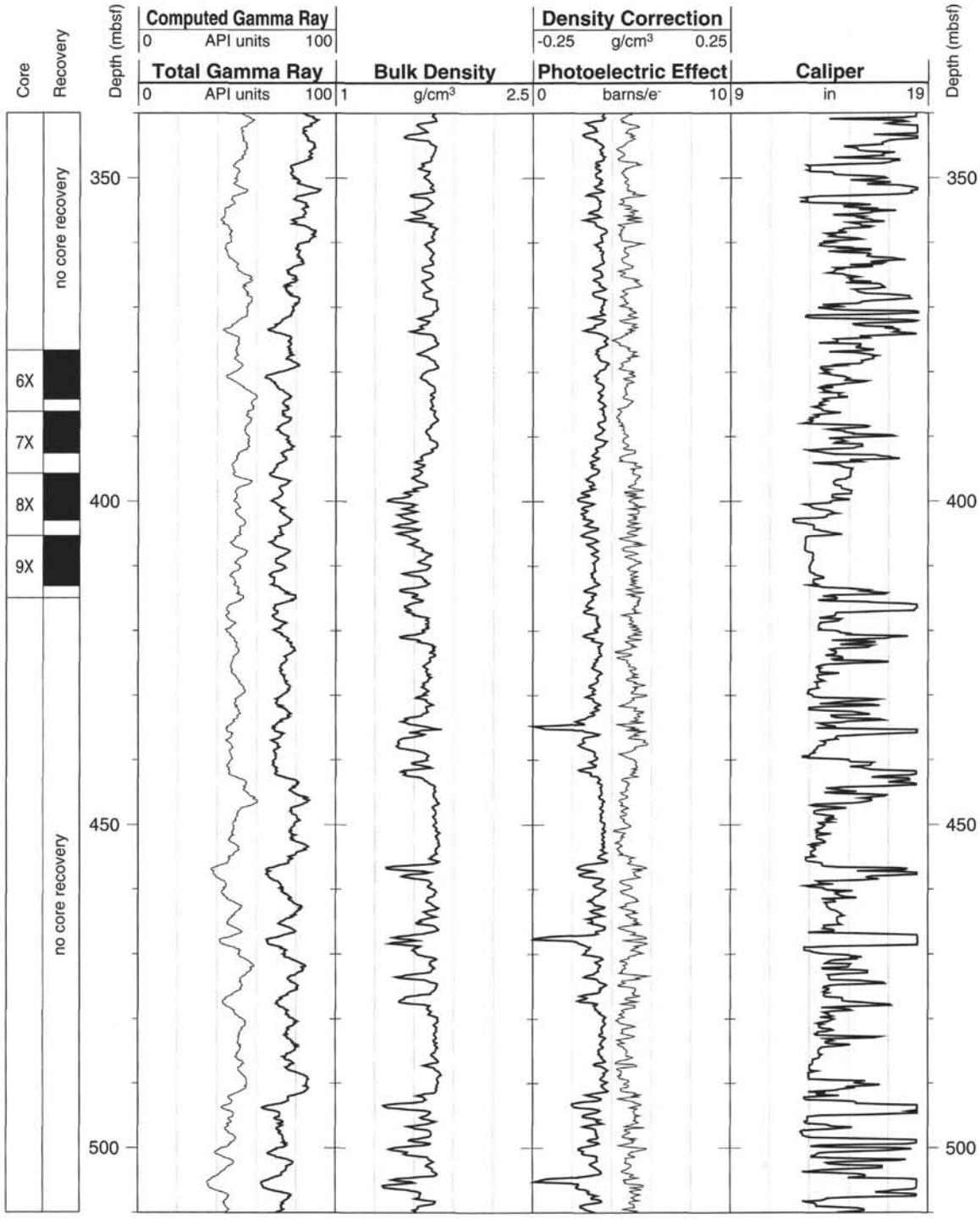

Hole 994D: Natural Gamma Ray-Density-Porosity Logging Data (cont.)

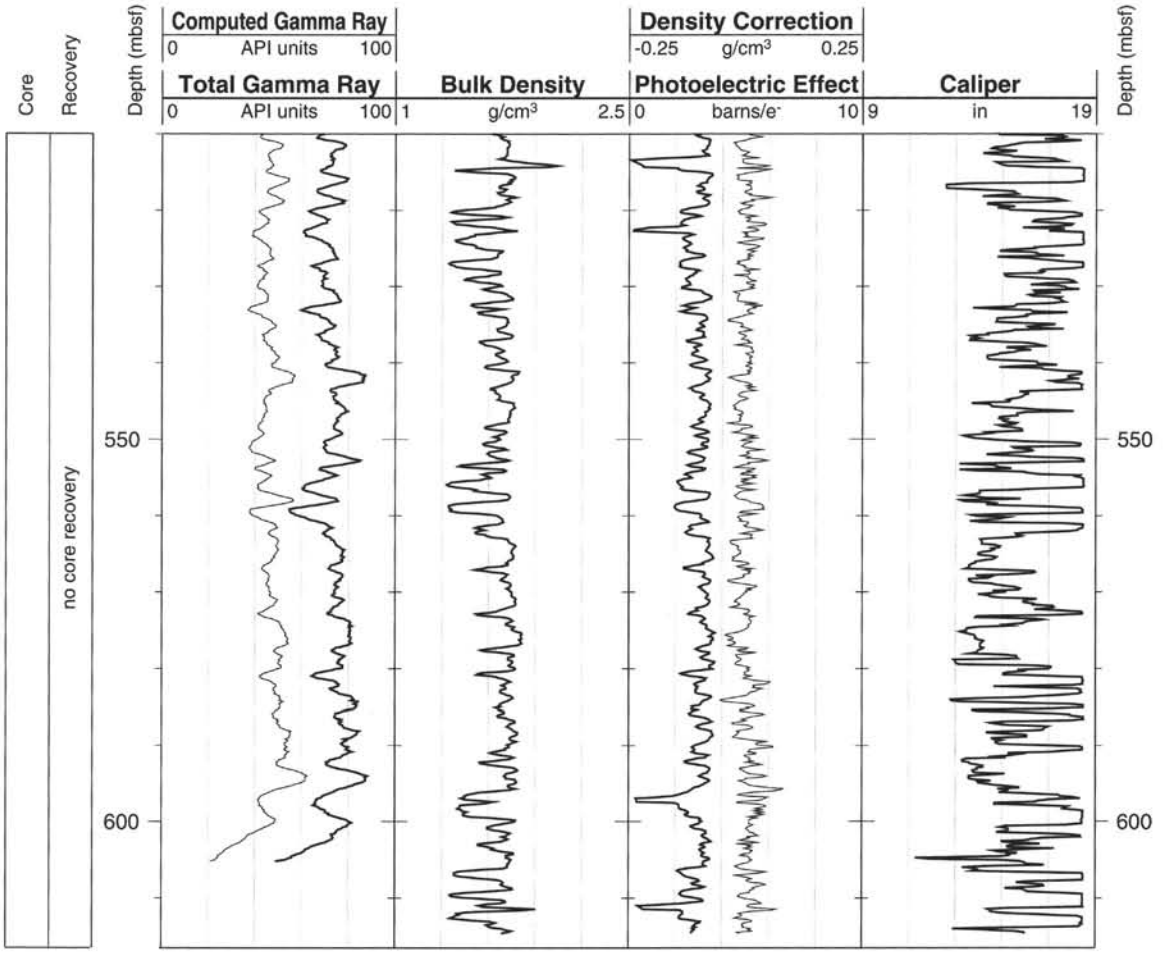

Hole 994D: Natural Gamma Ray-Resistivity-Sonic Logging Data

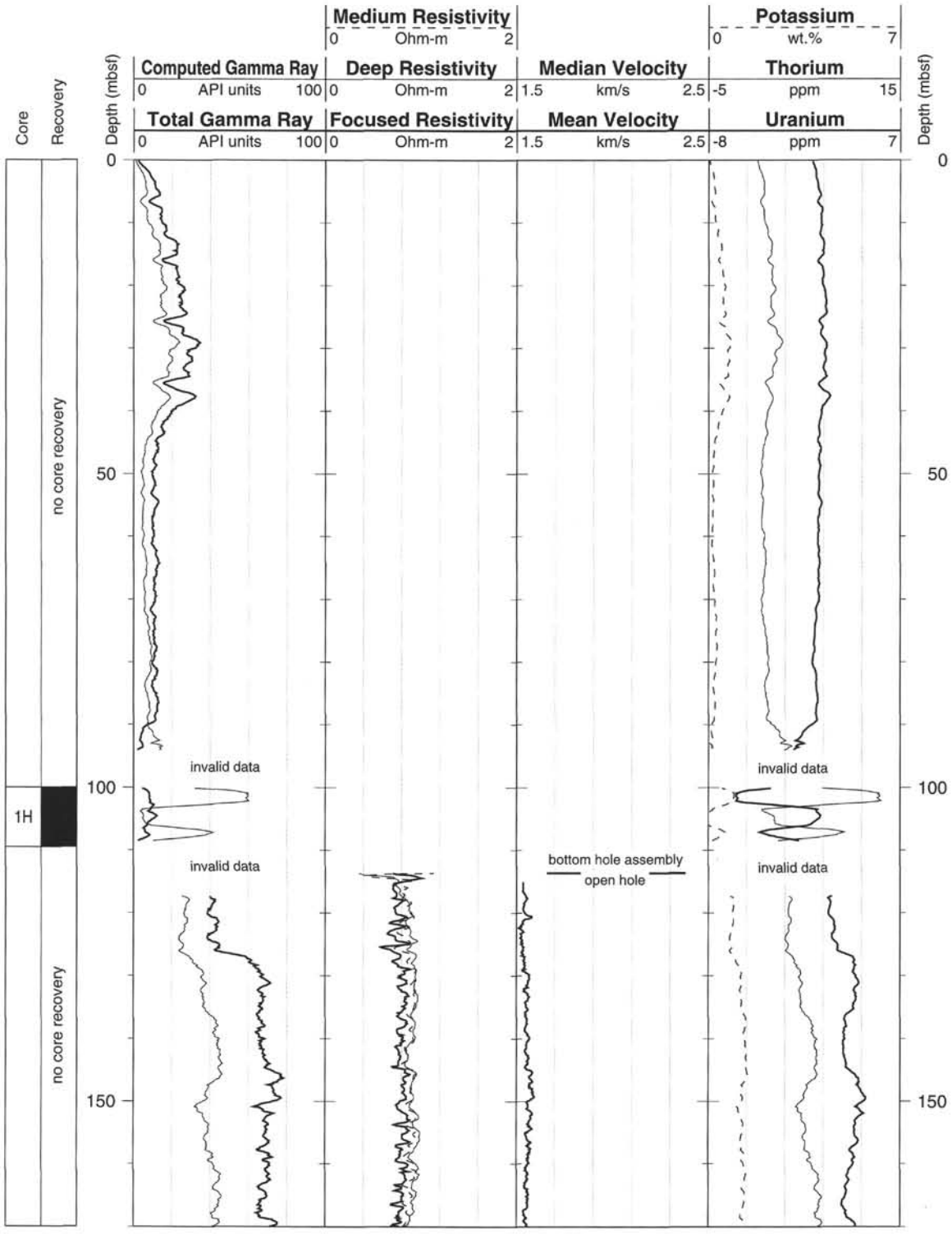

Hole 994D: Natural Gamma Ray-Resistivity-Sonic Logging Data (cont.)

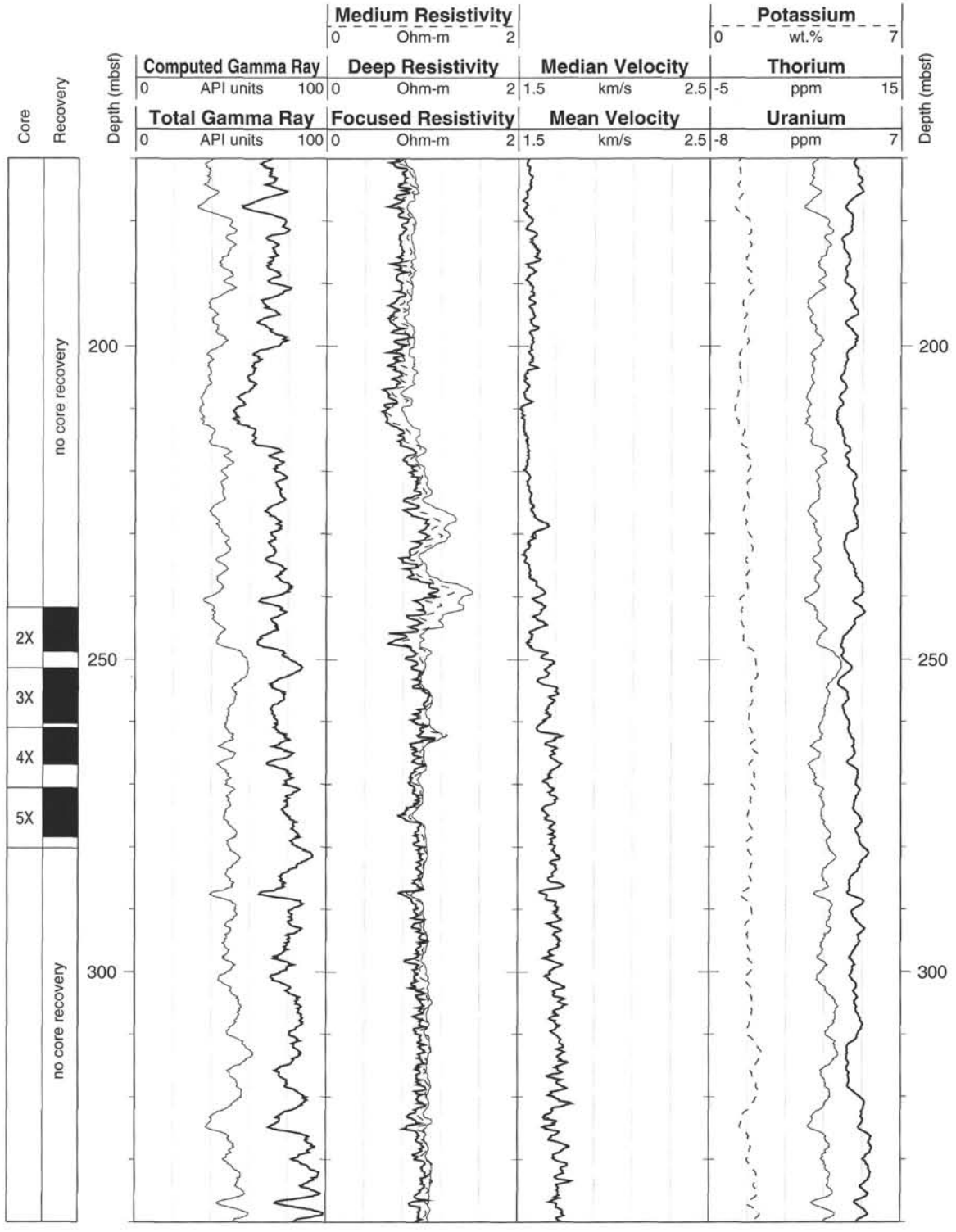

Hole 994D: Natural Gamma Ray-Resistivity-Sonic Logging Data (cont.)

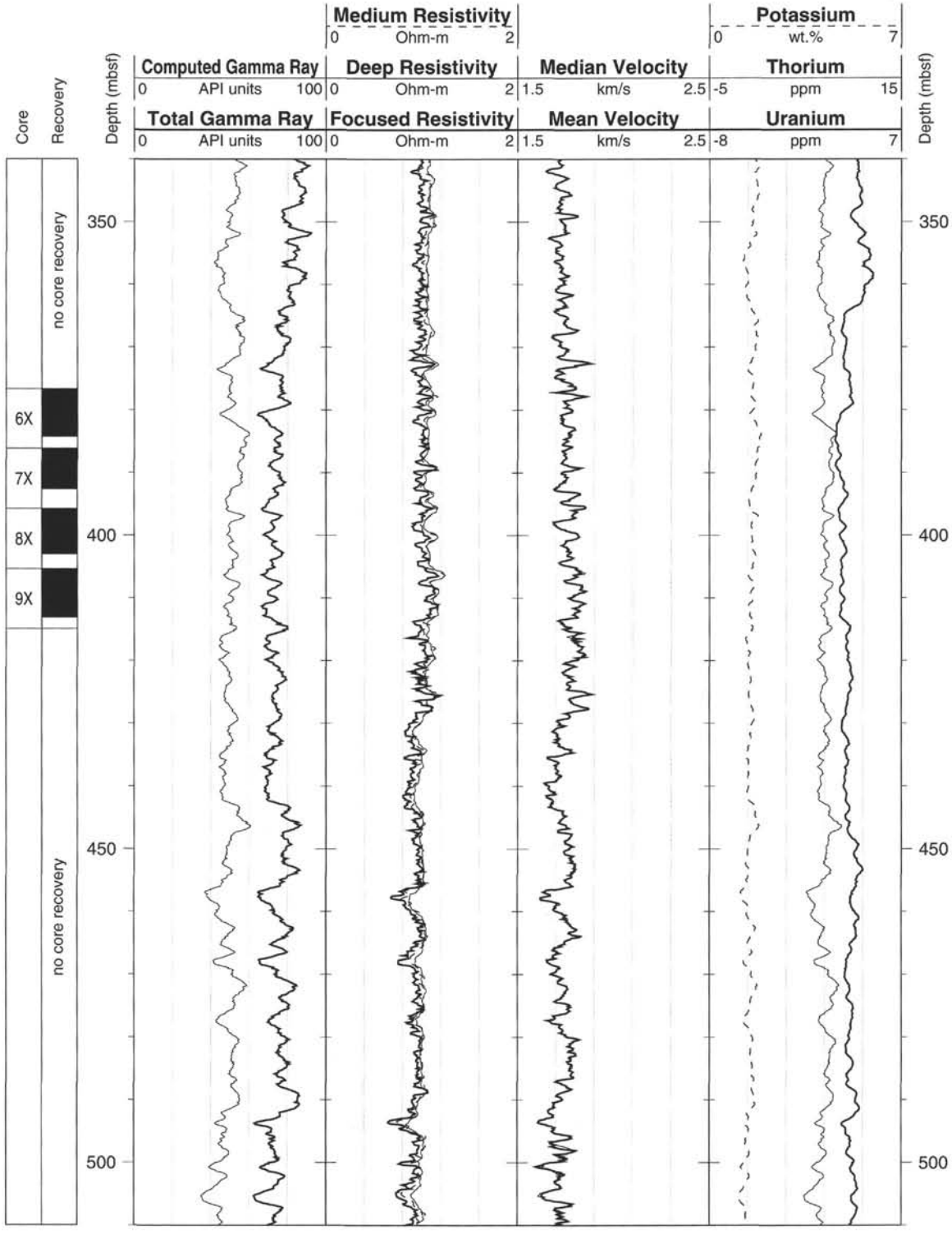

Hole 994D: Natural Gamma Ray-Resistivity-Sonic Logging Data (cont.)